UNIVERSITY OF CALIFORNIA,
IRVINE

Synthesis, Characterization, and Electronic Structure of Heteromultimetallic Complexes Incorporating a Redox-Active Metalloligand

DISSERTATION

submitted in partial satisfaction of the requirements
for the degree of

DOCTOR OF PHILOSOPHY
in Chemistry

by

Michael Kenneth Wojnar

Dissertation Committee:
Professor Alan F. Heyduk, Chair
Professor Andrew S. Borovik
Professor William J. Evans

2019

DEDICATION

To

My family, my friends, and Ryan

TABLE OF CONTENTS

LIST OF FIGURES

Page

LIST OF TABLES

Page

LIST OF SCHEMES

Page

ACKNOWLEDGEMENTS

Obtaining a Ph.D. is not only about learning how to think critically and independently, but also about recognizing those that have helped you along the way. There is not a doubt in my mind that, without the mentorship and encouragement that I have been given, I would certainly not be where I am today. So, these acknowledgements are here in an attempt to express the gratitude and love I have in my heart for all of these people. You have helped me accomplish my dreams and I can't thank you enough.

Of course, I want to thank my advisor, Alan Heyduk. It has been incredibly special to work in your lab on ideas that continue to inspire me to this day. The way you approach problems in chemistry, and how you taught me to view chemistry through this lens, is what I think makes our relationship so amazing. You have pushed me beyond what I ever thought I could handle, and you helped me get to places that, to this day, I don't feel like I deserve. There are certainly not enough pages to thank you, so, instead, I am going to keep working hard to make you proud.

I want to thank my thesis committee members, Andy Borovik and Bill Evans. Andy, I want you to know that I have always been aware of how supportive you have been of me. From second-year reports to my candidacy exam, as well as the various presentations I have given over the years, you were always the first one to come up to me with words of encouragement. Thank you for believing in me when I didn't believe in myself. Bill, out of all of the professors at UCI, I am thankful that I had the opportunity to learn the most from you, as you taught the majority of my classes. I wanted you on my committee because, every time I came to you to talk about research, you expressed such an interest in what I was doing. It made me feel like the chemistry was important and worthwhile, which I sometimes forgot along the way.

The scientific community at UCI has been supportive throughout this process as well. I want to thank Jenny Yang - I am so happy that you came to UCI when you did. Watching you start a research lab has been really great to see. I have to thank Joe Ziller - I will never forget my days in the X-ray Facility. Thank you for teaching me those skills, and for putting up with me for all of that time

(it was also great to have a colleague during the troubling times of the 2016 presidential election). I also need to thank the inorganic chemistry community, from the Borovik, Yang, and Evans labs, as well as Mike Green. This department is truly special and I am happy to have been a part of it.

Heyduk lab members, past and present: I love you so much. Wes, Janice, Elaine, Aaron, Kyle, and Lindsay, you shaped me to be the scientist I am today. I won't forget it. One of the things I am most proud of is the fact that I get to leave the Heyduk lab in the hands of two of the most intelligent and capable female scientists that I have had the privilege of mentoring and working with: Claudia and Bronte. You both know that we are family - it has been so rewarding to see you both grow over the past several years. I can't wait to see what the world has in store for the both of you. You deserve the best.

I don't have the words for how grateful I am for my family. It certainly has been rough being away from you all for so long. I hope I have made you proud. I just want you to know that, although I have been so far, you have always been in my mind and in my heart. The beautiful thing about it all is, when I look at myself and my work here at UCI, I don't see me. I only see all of you.

Lastly, none of this work would have been possible without the love of my life, Ryan. I do not know many people who strive to help others achieve their dreams, seemingly at the expense of their own. We met my first week of classes in graduate school and, in retrospect, I have come to realize that you were my guardian angel all along. As you know, this past year has been incredibly hard on me. Without you, I am not sure I would have made it. This thesis is a testament to us, and just one single chapter in our life together. Now, it's time to take our babies, Patriot and Pepper, and begin writing the next chapter. Here is to that next chapter.

CURRICULUM VITAE

Michael K Wojnar

Graduate Student Researcher
University of California, Irvine 1102 Natural Sciences II Irvine, CA 92697-2025
Work: 949-824-7479 Cell: 708-369-9211 Email: mwojnar@uci.edu

Education

2013-Present	Chemistry Ph.D. Candidate (Expected: Fall 2018) University of California, Irvine *Advisor: Alan F. Heyduk*
2009-2013	BS in Chemistry, Minor in Hispanic Studies Boston College *Advisor: Jeffery A. Byers*

Research Experience

Chemistry Department, University of California, Irvine September 2013 – Present

- Synthesis and characterization of heteromultimetallic systems and multi-electron reactivity
  - Designed heterobimetallic and heterotrimetallic systems incorporating a redox-active metalloligand and investigated the electronic structures via spectroscopic, electrochemical, and computational methods.
  - Synthesized a library of metalloligands and investigated their optical and electronic properties.
  - Generated heterotrimetallic mixed-valent molecules featuring a bridging metalloligand and studied the metal-metal electronic communication.

- Investigation of Group 9 metals with redox-active amidophenolate ligands for the storage of electron and proton equivalents.
  - Synthesized Group 9 complexes $[M(isq)_2]^{0/-}$ (isq = iminosemiquinonate; M = Co, Rh) and demonstrated that upon reaction with hydrogen storage material, NH_3BH_3, that the electrons and protons migrate to and are stored on the organic ligands, as opposed to the metal center, in the case of cobalt.

- X-ray Crystallography Facility Fellowship
  - Specific duties of the X-ray Fellow included screening and mounting crystals provided by the users, initiating data collection, solving structures, completing data packets, training new users, and maintaining the low temperature systems.

Chemistry Department, Boston College, Chestnut Hill, MA September 2011 – January 2013

- Studied the mechanism and utility of transition metal-mediated Brook rearrangements toward the rapid synthesis of small complex molecules.

Publications

1. **Wojnar, M. K.**; Ziller, J. W.; Heyduk, A. F. “Heterobimetallic and Heterotrimetallic Clusters Containing a Redox-Active Metalloligand” *Eur. J. Inorg. Chem.* **2017**, 5571–5575.
2. Rosenkoetter, K. E.; **Wojnar, M. K.**; Charette, B. J.; Ziller, J. W.; Heyduk, A. F. “Hydrogen-Atom Non-Innocence of a Tridentate [SNS] Pincer Ligand" *Inorg. Chem*. **2018**, *57*, 9728–9737.
3. **Wojnar, M. K.**; Rosenkoetter, K. E.; Ziller, J. W.; Heyduk, A. F. “Ancillary Ligand Effects on Heterobimetallic $M[SNS]_2CuL_2$ Complexes (M = Mo, W)" In preparation.
4. **Wojnar, M. K.**; Ziller, J. W.; Heyduk, A. F. “Synthesis of a Library of $M[SNS]_2$ Redox-Active Metalloligands Incorporating Group 4, 5, and 6 Metals” In preparation.
5. **Wojnar, M. K.**; Ziller, J. W.; Heyduk, A. F. “A Mixed-Valent Heterotrimetallic Complex Bridged by a Redox-Active Metalloligand” In preparation.
6. **Wojnar, M. K.**; Ziller, J. W.; Heyduk, A. F. “Redox-Active Amidophenolate Ligands Acting as both Proton and Electron Reservoirs” In preparation.

Notable Honors and Positions

X-ray Crystallography Facility Fellowship	2017 - 2018
UCCS (University of California Chemical Symposium) Organizing Committee	2016 - 2017
Graduate Assistance in Areas of National Need (GAANN) Fellowship	2014 - 2015
Graduate Assistance in Areas of National Need (GAANN) Fellowship	2013 - 2014
Undergraduate Research Fellowship	2012 - 2013
Honors Chemistry Program at Boston College	2009 - 2013

Contributed Presentations

1. **Wojnar, M. K.**; Heyduk, Alan F. “Electronic Communication in Heteromultimetallic Systems Incorporating the Redox-Active $M[SNS]_2$ Metalloligand” 255th American Chemical Society National Meeting, LGBTQ+ Graduate Student & Postdoctoral Scholar Research Symposium, March 19th, 2018, New Orleans, LA, poster presentation
2. **Wojnar, M. K.**; Heyduk, Alan F. “Exploration of the $M[SNS]_2$ (M = W, Mo) as Redox-Active Metalloligands in Heteromultimetallic Systems”. Southern California Bioinorganic Meeting, December 2nd, 2017, Irvine, CA, oral presentation.
3. **Wojnar, M. K.**; Heyduk, Alan F. “Exploration of $M[SNS]_2$ (M = W, Mo) as Redox-Active Metalloligands in Heteromultimetallic Systems”. 253rd American Chemical Society National Meeting, April 6th, 2017, San Francisco, CA, oral presentation.
4. **Wojnar, M. K.**; Heyduk, Alan F. “Investigation of $Mo[SNS]_2$ as a Redox-Active Metalloligand in Heteromultimetallic Systems”. UC Symposium for the Chemical Sciences, March 27th, 2017, Lake Arrowhead, CA, poster presentation.
5. **Wojnar, M. K.**; Heyduk, Alan F. “Electron Transfer and Mixed Valency in Heteromultimetallic Systems” SoCal Undergraduate Research Symposium, July 15th, 2016, Irvine, CA, oral presentation.
6. **Wojnar, M. K.**; Heyduk, Alan F. “Investigation of $Mo[SNS]_2$ as a Redox-Active Metalloligand in Heteromultimetallic Systems”. UC Symposium for the Chemical Sciences, March 21st, 2016, Lake Arrowhead, CA, poster presentation.
7. **Wojnar, M. K.**; Heyduk, Alan F. “Exploring the $Mo[SNS]_2$ Complex as a Redox-Active Cofactor in Heteromultimetallic Systems”. 251st American Chemical Society National Meeting, March 13th, 2016, San Diego, CA, oral presentation.
8. Reiner, Benjamin R.; **Wojnar, M. K.** “Transition Metal-Catalyzed Brook Rearrangement for the Rapid Assembly of Complex Small Molecules”. Boston College Chemistry Department

Seminar. Chestnut Hill, MA; December, 2012, oral presentation.

Teaching Experience

- Lab Instructor - Inorganic Chemistry, Organic Chemistry
  - Trained senior level students in advanced inorganic techniques and principles (Schlenk line and glove box use of air-sensitive chemicals), and sophomore level students in introductory organic laboratory techniques.

- X-ray Crystallography Facility Fellowship
  - Trained graduate students how to mount and solve structures.

- Mentorship
  - Mentored an undergraduate who is currently a graduate student at the University of Minnesota Twin Cities.

References

Prof. Alan F. Heyduk
Department of Chemistry
University of California
Irvine, CA 92697
949-824-8806
aheyduk@uci.edu

Prof. Andrew S. Borovik
Department of Chemistry
University of California
Irvine, CA 92697
949-824-1510
aborovik@uci.edu

Prof. William J. Evans
Department of Chemistry
University of California
Irvine, CA 92697
949-824-5174
wevans@uci.edu

ABSTRACT OF THE DISSERTATION

Synthesis, Characterization, and Electronic Structure of Heteromultimetallic Complexes Incorporating a Redox-Active Metalloligand

By

Michael Kenneth Wojnar

University of California, Irvine, 2018

Professor Alan F. Heyduk, Chair

The theme of this dissertation centers around the synthesis and characterization of heteromultimetallic systems incorporating a redox-active metalloligand, a metal complex that acts as a ligand toward other metal centers. The redox-active metalloligand is comprised of two tridentate non-innocent ligands coordinated to a redox-active metal center.

Chapter 2 describes the synthesis and characterization of heterobimetallic $Mo[SNS]_2Ni(dppe)$ and heterotrimetallic $Mo[SNS]_2\{Ni(dppe)\}_2$ complexes that include $Mo[SNS]_2$ as the metalloligand ([SNS] = bis(2-mercapto-p-tolyl)amine). These systems involve molybdenum-nickel metal-metal bonds, through a two-center two-electron bond in the bimetallic systems, and through a three-center four-electron bonding scheme in the trimetallic complex. Electrochemistry, supported by density functional theory (DFT) calculations, is in agreement with nickel-localized oxidations, making the heterotrimetallic $Mo[SNS]_2\{Ni(dppe)\}_2$ a viable molecular study of mixed valency in linear trinuclear systems.

Chapter 3 discusses the installation of a copper center on the the $Mo[SNS]_2$ metalloligands. Considered as a one-electron-reduced form of $Mo[SNS]_2Ni(dppe)$, these bimetallic systems are best described as copper in its monovalent form coordinated to the monoanion of the metalloligand, $Mo[SNS]_2^{-1}$. Variation of the ligand on the copper centers leads to distinct changes in the metal-metal bond distance via X-ray crystallography, while spectroscopic techniques confirm almost identical electronic structures that are unperturbed by the ancillary ligand identity. Solid-state- and solution-based characterization methods lead to electronic structure assessment of these bimetallic molybdenum–copper systems as dynamic Mo(V)–Cu(I) ions in solution.

Chapter 4 revolves around a library of trimetallic systems incorporating the late transition metal centers cobalt, nickel, and copper, with the general formula, $Mo[SNS]_2\{M(dppe)\}_2$ (M= Co, Ni, Cu). As these trimetallic cluster compounds incorporate three-center bonding schemes, variation of the metal center from cobalt to nickel to copper leads to distinct variations in the coordination geometry of the metalloligand bridge, as well as metal-metal bond length.

Chapter 5 focuses on a library of metalloligands of the general formula, $K_x[M[SNS]_2]$. Electrochemical, spectroscopy, structural, and computational studies measure the HOMO-LUMO gaps of these compounds. Based on these methods, the covalency of these systems can be tuned through judicious choice of metal ion.

Chapter 6 describes the synthesis and characterization of a mixed-valent molecule, $V[SNS]_2\{Ni(dppe)\}_2$, which is the one-electron oxidized version of $[K][V[SNS_2\{Ni(dppe)\}_2]$. Oxidation of these trimetallic systems leads to metal-metal bond scission and localization of valence on the metalloligand. It is hypothesized that the energetic and spatial mismatch between the nickel and vanadium metal centers (as seen through the dative character of the metal-metal bonds) leads to valence trapping

Chapter 1

Introduction

Redox-Active Sulfur-Containing Ligands

In the early 1960s began a period of chemistry known as the "dithiolene dawn"[1] in which unique electronic structures and geometries of metal complexes, comprised of sulfur-containing redox non-innocent ligands, were synthesized and investigated. These bidentate ligands, introduced by McCleverty as dithiolenes[2], included *cis*-1,2-diphenyl-ethene-1,2-dithiolate (pdt) and 1,2-ethylenedithiolate (edt) and were explored by three different research groups at the time (Schrauzer and Mayweg; Gray; Davison, Edelstein, Holm, and Maki).[3-5] Neutral four-coordinate homoleptic nickel complexes were studied and the square-planar environments of these systems were rationalized as one-electron oxidation of the ligands yielding a divalent nickel ion (Figure 1.1, top). These molecules also demonstrated multiple one-electron transfer events at mild potentials; the electrochemistry was consistent with strongly covalent systems that delocalized charge over the entire molecule with minimal geometric rearrangement of the M-S_4 coordination environment. Additionally, tris homoleptic complexes of the dithiolene ligands (mentioned above) were shown to adopt trigonal prismatic coordination geometries, one of the first times this geometry was observed in a molecular metal complex.[6-8] The stability of this obscure geometry was attributed to several π interactions between the ligand p orbitals and metal d orbitals (i.e. covalency). Through a battery of techniques, that became more refined with time, from X-ray crystallography, electrochemistry, spectroscopy, and computations, it became evident that significant metal AND ligand contributions dominated the frontier molecular orbitals of these compounds. This energetic reordering of metal and ligand orbitals reached a point that Solomon and coworkers described as "inverted" electronic structures (Figure 1.1, bottom), in which the lower energy bonding orbitals were metal-based, while the corresponding antibonding orbitals had more ligand character (the opposite of how molecular orbitals schemes are typically constructed).[9] Although not the first examples of redox non-innocent ligands, the dithiolenes provided elegant examples of how to discuss oxidation state assignments and the location of redox in these systems.

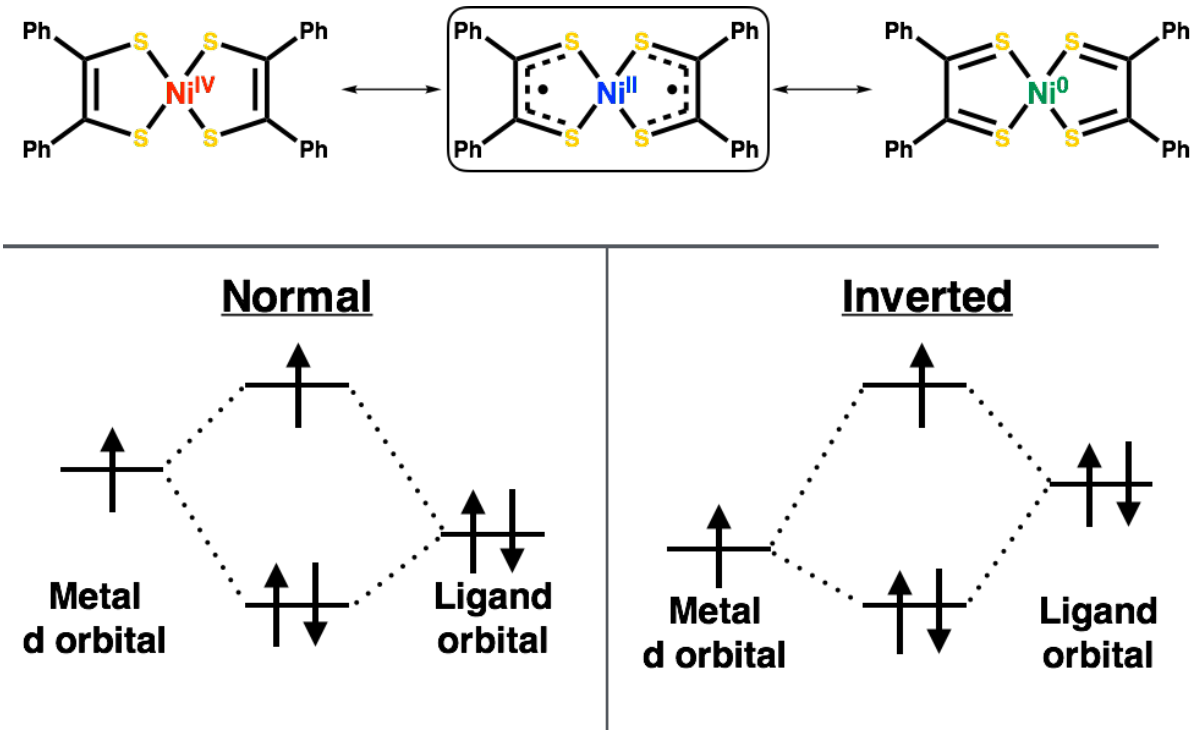

Figure 1.1. Resonance structures of $Ni(dtb)_2$ (dtb = dithiobenzil) (top); normal vs. inverted bonding scheme invoked in bis dithiolene chemistry, adapted from reference 9.

Electron Transfer and Mixed Valency

At the heart of oxidation state assignment lies the topic of electron locality, determined by interactions between redox sites. One method to probe electronic interactions is to connect identical redox sites and introduce an odd electron to the system, a molecular model of intramolecular charge transfer. Given theoretically equivalent redox sites, this setup is intriguing because it forces the system to "reveal" where a solitary electron would choose to reside amongst two identical locations. By definition, this encompasses the field of mixed valency, in which identical redox sites are in different oxidation states. The amount of electron exchange (also known as valence detrapping or electron delocalization) dictates the electrical, magnetic, and optical properties of the compounds, and allows for the classification of mixed-valent complexes. According to the Robin-Day classification system, mixed-valent molecules can be broken up into three distinct classes.[10] Class I mixed-valent systems consist of zero electron exchange due to negligible interaction between redox sites. As a result, the properties of the mixed-valent complex are similar to those of the disparate unperturbed sites. Class III mixed-valent systems denote a fully valence-detrapped system in which the itinerant electron is delocalized;

the system exhibits properties different from those of the individual redox sites. Class II systems lie in the regime between these two boundaries. Although there are three different classifications for mixed-valent molecules, determination of class is not as simple as choosing Robin-Day Classes I-III; similar to oxidation state, there is a "grey" area, the borderlines where chemistry remains abstract.

As mixed valency is a model of intramolecular electron transfer, an accurate representation of this comes about from Marcus-Hush theory (Figure 1.2).[11,12] Parabolas represent the potential energy wells for the reactants and products of electron transfer (i.e. the identical redox sites). The location on the x-axis of the parabolas (the reaction coordinate of the electron transfer i.e. the sum of the changes in the positions of all the atoms involved in the reaction) and the location on the y-axis (energy) relay information about how fast these redox reactions occur (or if they occur at all). While this essentially describes transition state theory, Marcus and Hush further developed this theory to make it applicable to electron transfer reactions, which incorporates a new element (H_{ab}) to describe the electron transfer.[13] H_{ab} refers to the electronic coupling between redox centers and λ to the photoinduced intervalence charge transfer (IVCT).

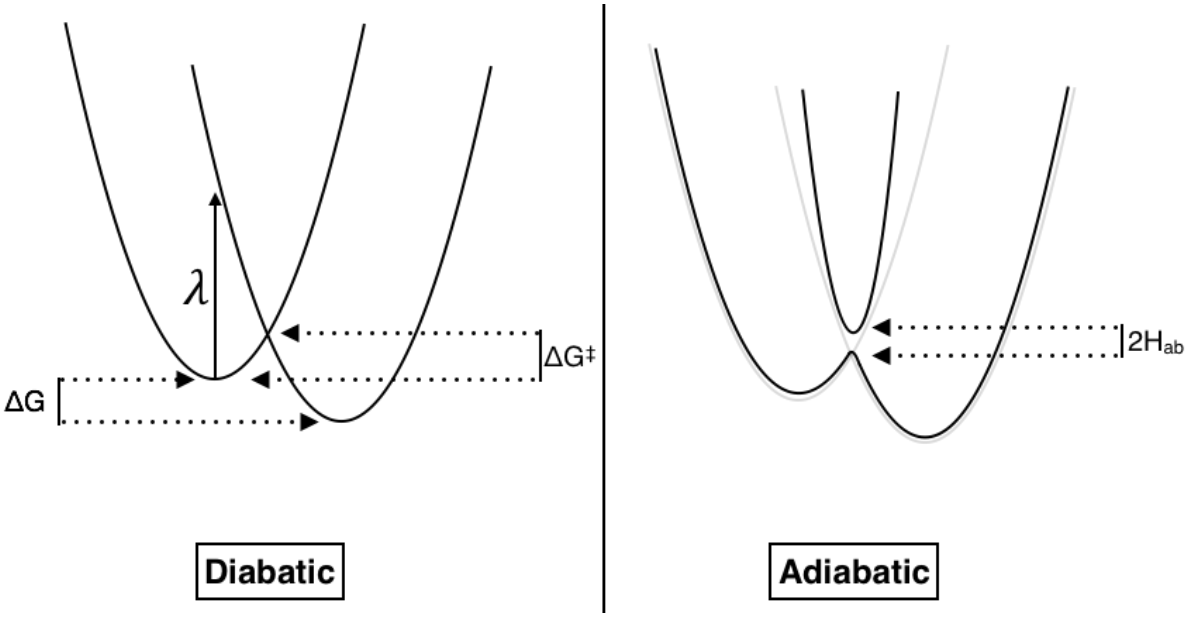

Figure 1.2. Two-state electron transfer model of Hush and Marcus.[14-16]

In conjunction with Marcus theory and IVCT analysis, the three-center model has also been employed to more accurately describe the electronic structure of these mixed-valent systems.[17-20] In the most general form, many mixed-valence systems involve three centers: two identical redox sites

and a bridge. According to molecular orbital theory, the identical redox species can be made into linear combinations through symmetry that form bases for irreducible representations of a symmetry group. These symmetry-adapted linear combinations (SALCs) of atomic orbitals can interact with the molecular orbitals on the bridge to generate a three-center interaction (Figure 1.3). These generated molecular orbitals are, in many instances, considered to be better representations of electron transfer in these delocalized systems in that they demonstrate a delocalized viewpoint of electron transfer. This bonding scheme has been invoked to rationalize the localization and delocalization in mixed-valent systems: contributions from the bridge orbitals to the molecular orbital on the redox site dictates valence trapping vs. detrapping in the systems.

The most heavily cited example of mixed valency is that of the Creutz-Taube ion, a bimetallic system comprised of two ruthenium metal centers bridged by the organic linker, pyrazine.[21,22] Upon oxidation of the bimetallic Ru^{II} coordination complex, the resulting unpaired electron exhibits delocalization onto both metal centers via the pi system of the organic bridge. This is one of the most extensively studied mixed-valent systems and, according to the Robin-Day classification system, lies on the border between Class II and Class III. Since then, a great deal of synthetic work has been undertaken to generate symmetric systems with redox-active centers to see what factors lead to valence trapping vs. valence detrapping.[23] Marcus theory states that the distance between the redox-active locations mediates the electronic coupling – the smaller the distance, the greater the coupling. It has also been shown that energetic overlap (energetic proximity of orbitals) is essential for electronic delocalization.

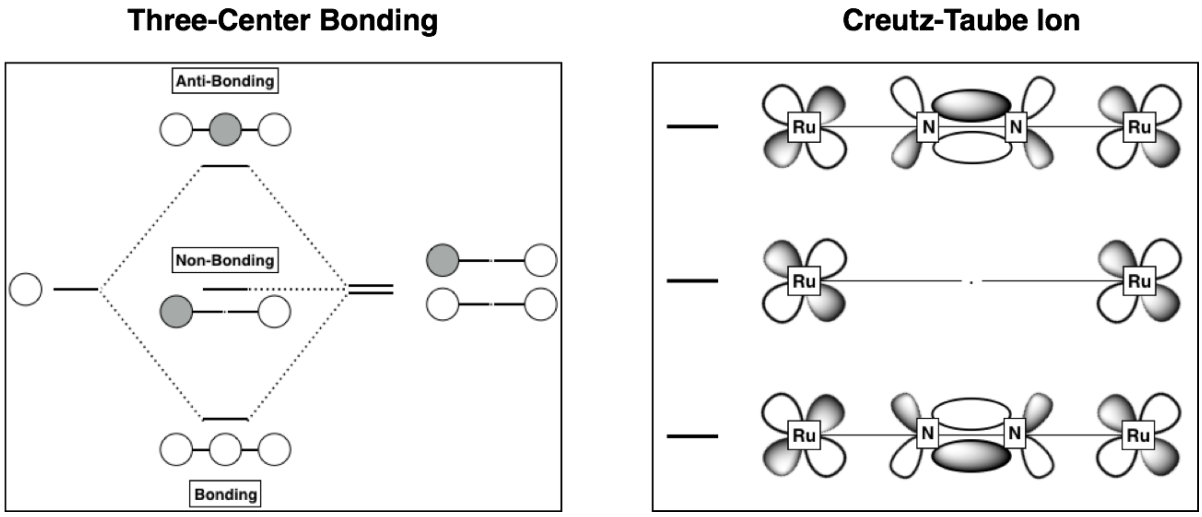

Figure 1.3. Three-state model in a general system (left) and the three-state model of the Creutz-Taube ion (right).

Mixed-Valence Motifs

The field of mixed valency is dominated by the motif of two redox-active metal centers bridged by a ligand, "metal–ligand–metal" (Figure 1.4, left). The opposite arrangement has also been explored: "ligand–metal–ligand", where two redox-active ligands are bridged by a metal ion (Figure 1.4, middle). Redox-active ligands bridged by an organic moiety have also been investigated, "ligand–ligand–ligand" (Figure 1.4, right). Lastly, and what encompasses a large part of this dissertation, is the following manifold: two-redox active metal centers bridged by a redox-active metal (via a metalloligand linker approach) supported through metal-metal bonds, "metal–metal–metal".

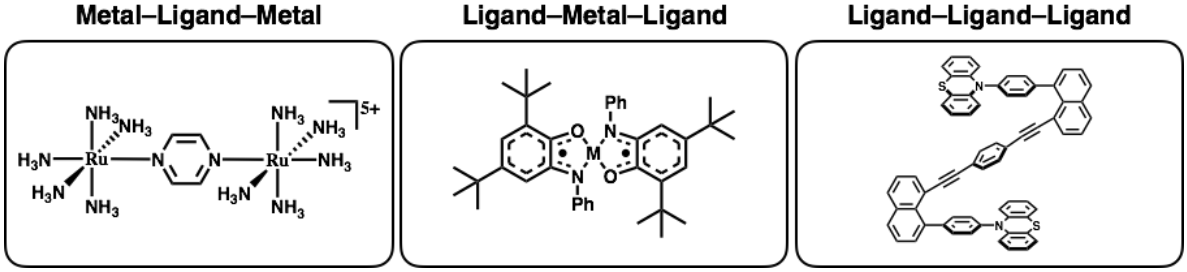

Figure 1.4. Examples of metal–ligand–metal (left), ligand–metal–ligand (middle), and ligand–ligand–ligand mixed-valent architectures.

Metal-Metal Communication through an Organic Linker

The most common scenario in synthetic mixed valency exploration is two metals communicating through an organic bridge. This motif dates back to what is considered one of the first synthetic coordination compounds, Prussian Blue (Figure 1.5, left). The intense color of this blue pigment can

be attributed to the different valences of the iron-based coordination complex and the associated inter-valence charge transfer transition, in which the electron "hops" or is delocalized over both the ferric and ferrous centers.[24,25] Kubiak and coworkers utilized a set of mixed-valent complexes of the type $\{[Ru_3O(OAc)_6(CO)(L)]^{2-}BL\}^-$ (L = a pyridyl ligand; BL = pyrazine or 4,4′-bipyridine) and observed coalescence of CO ligand stretches, demonstrating delocalization on the IR time-scale.[26] More recent work has shifted the focus of electronic communication from coordinate covalent bonds (metal–pyrazine–metal) to non-covalent hydrogen bonding interactions (Figure 1.5, right).[27,28]

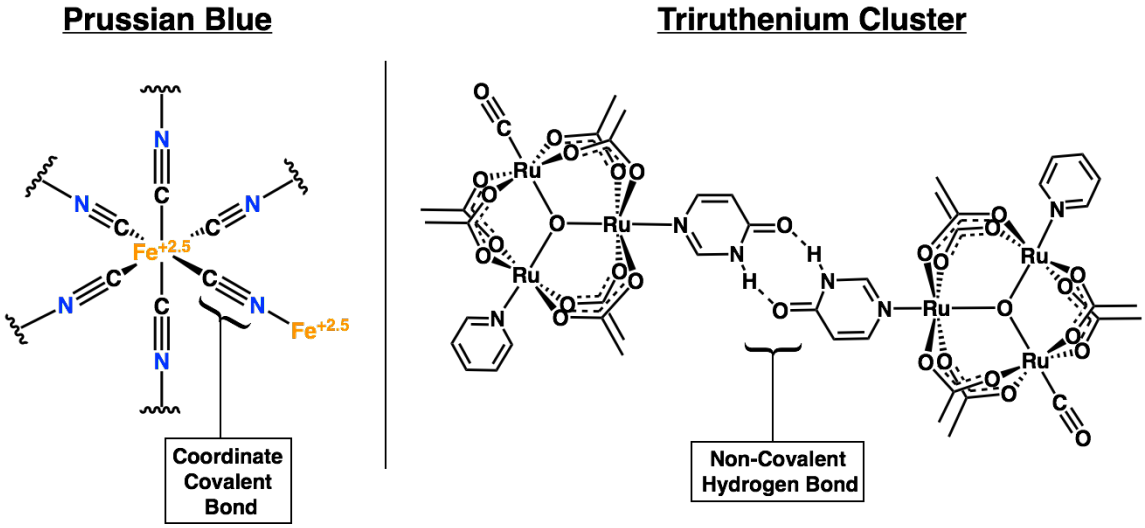

Figure 1.5. Examples of mixed-valent systems involving different bonding "metal–ligand–metal" motifs: coordinate covalent bonds in Prussian Blue (left)[24,25] and non-covalent hydrogen bonding in ruthenium dimers (right)[27,28].

This "metal–ligand–metal" motif has been utilized to explore a variety of other topics, from the magnetic exchange interactions between spin carriers toward single-molecule magnetism and information storage to the understanding of electron transfer in metalloenzyme active sites. Harris and co-workers incorporated a formally redox-active diiminobenzoquinone bridge to modulate magnetic coupling between iron centers.[29,30] The organic bridge not only allows for spatial and energetic overlap between the two metal centers but having an unpaired electron on the bridge allows for strong magnetic coupling through an electron hopping mechanism. This strong magnetic coupling engenders isolation of the ground state from the excited states, thereby preventing thermal relaxation and/or quantum tunneling.[31] Mixed-valent multimetallic systems bridged by organic/atomic linkers are also prevalent in biology, where metal ions bridged by endogenous and/or exogenous ligands leads to

mixed-valent motifs.[32] These mixed-valent systems not only comprise iron-sulfur clusters but also extend to other iron metalloenzyme active sites, like hemerythrin and uterroferrin, as well as copper-containing sites, like tyrosinase and hemocyanin. Understanding the factors that lead to valence trapping/de-trapping and how it extends to the reactivity of those enzymes is of fundamental interest in emulating their behavior.[33]

Ligand-Ligand Communication through a Metallic Linker

While the most prominent motif is that of two redox-active metals bridged by an organic linker, the reverse motif has also been extensively studied: two redox-active ligands coupled by a metal bridge. Thomas and coworkers synthesized a library of Group 10 metals (Ni^{II}, Pd^{II}, Pt^{II}) coordinated to the bis(2-amino-3,5-di-tert-butylphenyl)amine, in which the ligand coordinates to the metal in a bidentate fashion in its diiminosemiquinonate radical form.[34] From analysis of the IVCT transition of the three metal anionic complexes, it was shown that the energy of the transition is tuned by the identity of the metal: the metal d orbital has the correct symmetry and energy to mix with the ligand antibonding orbitals (Figure 1.6). For this reason, Pd shows the lowest energy IVCT, followed by nickel, and platinum having the highest energy band. Brown and coworkers confirmed this non-periodic phenomenon through interrogation of the singlet-triplet gaps of the Group 10 bis(iminosemiquinone) complexes.[35]

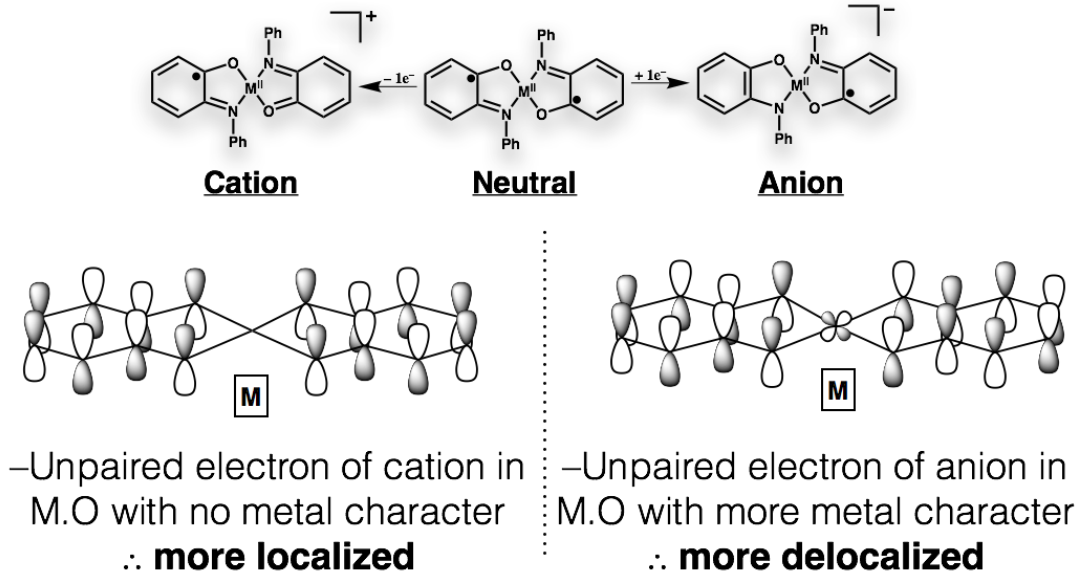

Figure 1.6. Valence trapping vs. detrapping in monocation (left) and monoanionic (right) complexes of the

Group 10 bis(iminosemiquinone) due to metal contributions to the molecular orbital of interest.

Ligand-Ligand Communication through an Organic Linker

Another motif in donor-acceptor systems investigating electron transfer (ET) is comprised of completely organic fragments. Wenger and coworkers connected two redox-active phenothiazine (PTZ) moieties through a naphthalene linker to generate "molecular triple deckers" in which the PTZ substrates are stacked on top of an arene bridge.[36] Mixed-valent species were generated via one-electron-oxidation, and the systems were classified as Class II species, based on cyclic voltammetry, UV-vis-NIR spectroscopy, EPR spectroscopy, and computational studies. Due to the connectivity of the napthalene bridge, it is hypothesized that communication/charge transfer proceeds through a combination of through-bond and through-space interactions.

D'Alessandro et. al. observed a similar charge transfer pathway in aromatic stacks involving Zn(II) frameworks containing cofacial thiazolo[5,4-*d*]thiazole (TzTz) units in a metal-organic framework (MOF).[37] The goal of these MOF systems is to utilize the through-space interactions to lead to long-range delocalization and, as a result, conductivity in the framework. Upon reduction of the MOF, low energy IVCT bands emerge, which computations (coupled with experimental results) identify as a through-space charge transfer transition. Marcus-Hush theory was applied to analyze the band shapes of the IVCT bands, leading to classification of these systems under the Class II mixed valency designation.

Methods of Determining Electronic Communication

Half-Wave Potential Splittings in Voltammetry Studies

A common, though convoluted, method to determine electronic communication between redox sites is through the splitting of the half-wave potentials in the cyclic voltammograms. The logic behind this technique is: if two identical redox-active centers exhibit zero electronic interaction between them, the potential at which their redox events occur will be the same (i.e. no potential splitting) because they are the exact same redox-active moiety.[38] This can be likened to the ferrocene/ferrocenium redox couple – each ferrocene molecule is identical in solution but is far enough apart to

experience zero electronic communication. Thus, a single redox event is observed in the voltammogram. On the other hand, if the two redox centers do communicate electronically, after the initial redox event, the second redox center "feels" this redox process and is pushed to a different potential (half-wave potential splitting occurs).

Spectroscopic Transitions

With the inability of electrochemistry to differentiate resonance contribution from electrostatic, magnetic, and inductive contributions, potential splitting is an ineffective method of determining electronic coupling.[39,40] On the other hand, spectroscopic transitions benefit from small time-scales close to the rate of electron transfer (electronic transitions ~ 10^{-15} s^{-1}; EPR transitions ~ 10^{-8} s^{-1}). Spectroscopic characterization provides more accurate information on the electronic coupling and can aid in mapping out kinetics of charge transfer.[41] Specifically, hyperfine splitting in EPR spectroscopy details where the charge is distributed in paramagnetic systems incorporating nuclear spins. Vibrational spectroscopy also provides electron transfer location. For example, resonance Raman experiments of the Creutz-Taube ion feature vibrational modes associated with the pyrazine bridge, confirming its participation in valence detrapping.[42]

Structural and Computational Analysis

In some cases, X-ray structures can provide information about valence trapping/detrapping in mixed-valent systems. If the redox sites are indeed equivalent, the asymmetric unit of the compound should only include one redox moiety, with the other being generated through symmetry operations. This demonstrates that the redox sites are equivalent in the solid state. However, the situation can become more complicated due to choice of crystallization solvents and/or crystal packing, which may desymmetrize the complex in the solid state versus solution-based measurements.

Computations also provide information about mixed-valent systems. Several groups (previously mentioned) confirm the identity of their IVCT bands through computational analysis, which serves to provide the molecular orbitals that dictate the transition. These theoretical results also confirm vibrational modes that are analyzed via IR/resonance Raman spectroscopy.

Metalloligands in Inorganic Synthesis

Metalloligands in inorganic synthesis emerged in the 1960s, with the isolation of the Busch-Jicha complex, with two bis-ethylmercaptoamine nickel complexes bound to a divalent nickel ion (Figure 1.7, left).[43] The N_2S_2 coordination environment around nickel also demonstrated structural similarity to the active site of acetyl-coenzyme A synthase (ACS). The dinickel active site, in which an N_2S_2 nickel metalloligand binds a secondary nickel ion through bridging thiolates, reacts carbon monoxide, methane cation (CH_3^+), and CoA, to generate acetyl-CoA (Figure 1.7, right). Since then, the motif has been explored in terms of CO/ethylene copolymerization, in which the Ni(N_2S_2) metalloligand stabilizes a palladium metal center that performs the chemistry.[44] In this metalloligand system, the combination of divalent nickel with strong-field ligands in a square planar environment means that the nickel center is not actively interacting with the secondary metal centers that it stabilizes.[45]

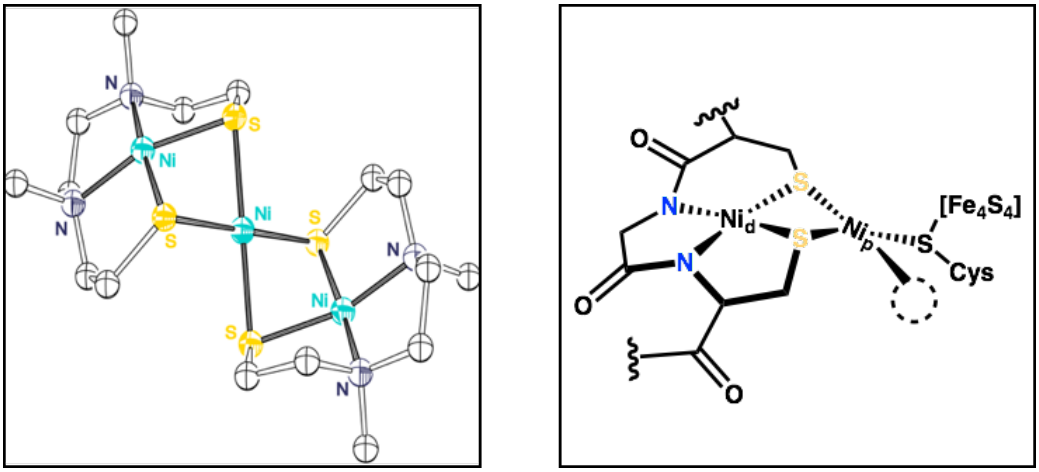

Figure 1.7. The Busch-Jicha complex (left) and the active site of acetyl-coenzyme A synthase (ACS).

Metal-Metal Bonding in Heteromultimetallic First-Row Transition Metal Systems

While the field of metal-metal bonding gained popularity after the discovery of the delta bond in a compound involving third-row metal ions, $[Re_2Cl_8]^{2-}$, the field has grown to include first-row transition metals. 3d transition metals involving multiple metal-metal bonds are elusive in that poor orbital overlap was originally thought to preclude extensive bonding schemes. The availability of the first-row metals, in conjunction with the unique spin states and cooperative interactions with other metal ions, renders this suite of multimetallic systems ripe for investigation.[46] The primary means of

identification and characterization of interactions between metal centers is through X-ray crystallography – the distance between ions acts as a gauge of metal-metal bond order, with the shorter distances aligning with a greater bond order.[47] Although external chemical effects, such as the nature of the ligand environment and/or crystal packing effects, may complicate metal-metal bond identity and assignment, solid-state characterization in tandem with spectroscopic and computational analysis, can further confirm the presence of metal-metal bonds.

The groups of Thomas and Lu have systematically varied metal identity (thereby tuning d orbital energies and electron counts) to corroborate bond orders in multimetallic bonding platforms.[48-51] Aligning with chemical intuition, it was observed that metal-metal bond order decreased as d orbital energy differences (between the two distinct metal ions, vanadium–M (M = Fe, Co, Ni)) increased. Different metal ions with larger d electron counts concomitantly led to further reductions in bond order, due to the filling of metal-metal antibonding orbitals. The ability of these double-decker amido-phosphine ligand architectures to accommodate a wide range of metal-metal bond distances also supports stabilizing interactions between metal centers through direct overlap, as opposed to ligand scaffolds "forcing" close proximities of the ions (Figure 1.8).

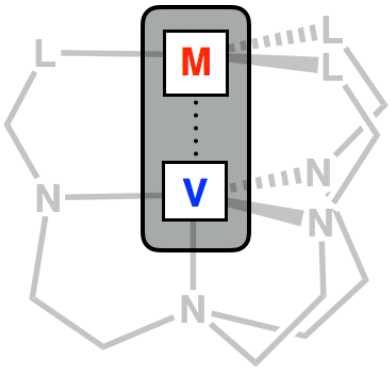

M	Fe	Co	Ni
V	V	V	V
B.O.	2.5	1.5	0.5

Figure 1.8. Variation in vanadium–metal bond order as a function of metal identity and d electron count (L = $^{i}Pr_2$), adapted from reference 49.

Metal-Metal Communication through a Redox-Active Metalloligand and Metal-Metal Bonds

While systems with metal-metal bonds represent a major area of investigation in mixed valency, most examples center around binuclear systems or trinuclear systems in a triangular framework (Figure 1.9, left).[52-55] In many of these cases, the presence of metal-metal bonds provides a pathway

for electron delocalization, and as a result, Class III behavior. Prominent examples of linear, trinuclear systems incorporating metal-metal interactions are Cotton's coordination complexes that utilize the ligand, di(2-pyridyl)amine (dpa) (Figure 1.9, right).[56-59] These homometallic systems, of the form $[M_3(dpa)_4Cl_2]$, range in electronic localization/delocalization depending on metal identity, as well as oxidation state. In all cases, class designation is directly impacted by the presence of metal-metal bonds. As was discussed previously, metal-metal bonds favor valence detrapping, while bond scission localizes the charge. These systems are examples of extended metal atom chains (EMACS), directly relevant to the properties of molecular metal wires and switches.[60,61] Due to the synthesis of this class of compounds, there is a lack of control around the heterometallic derivatives of these linear systems.

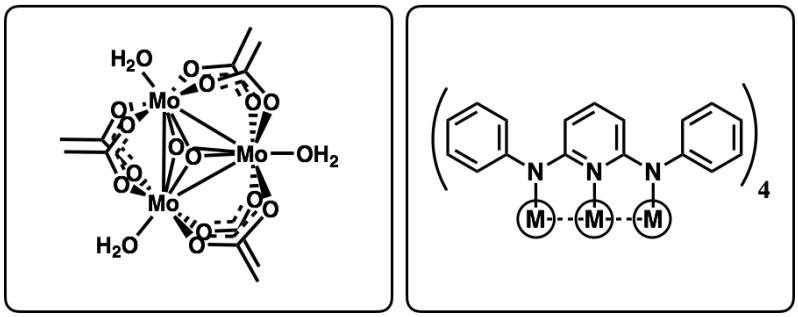

Figure 1.9. "Metal–Metal–Metal" mixed valency motif incorporating metal-metal bonds.

Mixed-valent metal clusters connected through direct metal-metal bonds are sought after not only for their structural properties but also their magnetic behavior. Betley and coworkers synthesized a triiron mixed-valent system in which a fully delocalized manifold was achieved via overlap of the iron d orbitals.[62] A high spin system was achieved through a double exchange mechanism, mediated by the direct overlap of d orbitals.

Previous work in the Heyduk lab that led to the synthesis of $M[SNS]_2\{M(dppe)\}_2$ heteromultimetallic clusters started with the discovery of $M[ONO]_2$ complexes as metalloligands ([SNS] = bis(2-mercapto-*p*-tolyl)amine; dppe = 1,2-bis(diphenylphosphino)ethane; [ONO] = bis(3,5-di-*tert*-butyl-2-phenol)amine). Under reducing conditions and in weakly coordinating solvents, it was discovered that $[ONO^{q}]FeCl_2$ assembles into the bimetallic $Fe_2[ONO]_3$ (Figure 1.10, top).[63] Magnetic data confirmed an S=7/2 ground state, attributed to an S=3/2 $Fe[ONO]_2$ metalloligand (one $[ONO^{sq\cdot}]$ radical ligand antiferromagnetically coupled to a high-spin Fe(II) center) which is ferromagnetically

coupled to a second S=2 high-spin Fe(III) center (antiferromagnetic coupling of high-spin Fe(III) center, S=5/2, to a [ONO$^{sq\cdot}$] radical ligands yields an S=2 spin state). This electronic structure description was supported by substitution of one of the iron centers for the redox-inactive zinc analogue (FeZe[ONO]$_3$). This yielded an S=3/2 ground state, which stems directly from the metalloligand, as described above. Interestingly enough, the pathway of exchange is not mediated by metal-metal interactions, as X-ray diffraction experiments confirmed a long Fe–Fe/Fe–Zn bond distance of 3.07 Å/3.05 Å; these distances fall outside the sum of the covalent radii of the two distinct ions.[64]

The effect of substituting the "hard" oxygen atom donors of the bis(phenol)amine ligand for "soft" sulfur donor atoms was also investigated in our lab. Bis [ENE] (E=O, S) complexes were synthesized incorporating the Group VI metal center, tungsten (to afford neutral complexes when both [ENE] ligands are utilized in their trianionic, catecholate form).[65] The substitution of oxygen for sulfur led to milder reduction potentials and red-shifted absorption profiles. This was attributed to the covalency of W[SNS]$_2$, in which close energetic and spatial proximity of [SNS] ligand π orbitals and metal d orbitals led to orbital mixing and redistribution of electron density among the entire molecule. It was hypothesized that the larger thiolate donors in the M[SNS]$_2$ framework would promote multimetallic architectures, as the sulfur donors harken to their ubiquity in multimetallic biological systems (i.e. iron-sulfur clusters, acetyl-coenzyme A synthetase).

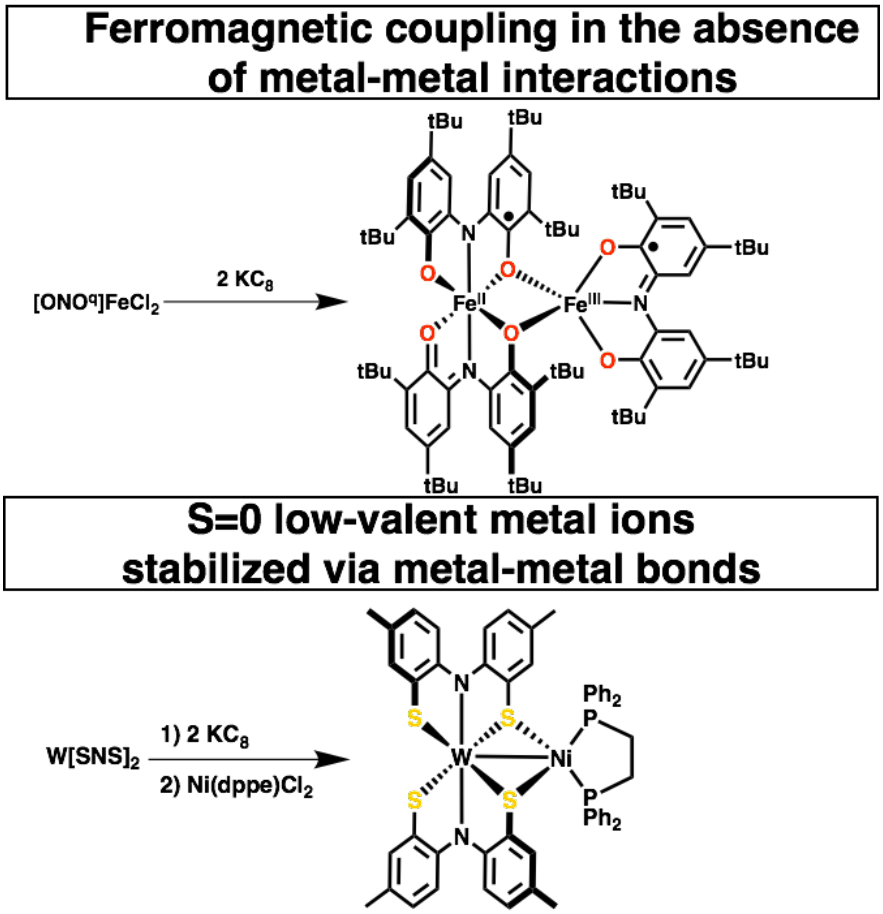

Figure 1.10. Previous work with six-coordinate metalloligands: ferromagnetic coupling in $Fe_2[ONO]_3$ in the absence of direct Fe–Fe bonds (top) and an S=0 $W[SNS]_2Ni(dppe)$ with a formal W–Ni bond (bottom).

Recently, it was demonstrated that $W[SNS]_2$ can act as a redox-active metalloligand to Group X metal ions (M = Ni, Pd, Pt) (Figure 1.10, bottom).[66] These bimetallic frameworks featured metal-metal interactions between the two ions and displayed electronic complexity not observed by the solitary metals. These "reduced" complexes also displayed proton reduction catalytic activity in the presence of the organic acid 4-cyanoanilinium tetrafluroborate.[67]

Contributions of This Work

This work fits into the scheme of mixed valency through the thiolate-supported connection of metal ion redox sites to a metal ion bridge ("metal–metal–metal"), which allows for the direct interaction between the metal centers via metal-metal bonds (Figure 1.11). Due to the oxidation state ambiguity and covalency of metal-[SNS]-ligand systems, it was imperative to first fully understand the electronic structure of the redox-active metalloligand, $M[SNS]_2$, with characterization of the met-

alloligands accomplished through variation of metal choice (Chapter 5). This information was crucial to our understanding of the electronic structure of the $Mo[SNS]_2$ heterobimetallic systems, incorporating Group X and XI metals ions. Chapter 2 will examine the electronic structure and mixed valency potential of the $Mo[SNS]_2$ metalloligand upon coordination of Ni(dppe) synthons. Chapter 3 focuses on heterobimetallic systems with $Mo[SNS]_2$ coordination to copper ions. Metal-metal bond length is interrogated upon variation of the ancillary ligand ligated to the Group XI metal. With these two areas of information understood, the work was then extended to heterotrimetallic systems, in which the exterior metal ions were swapped from cobalt, to nickel, and copper (Chapter 4). Electronic structure and metal-metal bonding are understood utilizing the three-center model. Chapter 6 investigates metal-metal interactions and mixed valency as the 4d-metal-based $Mo[SNS]_2$ metalloligand bridge is changed for the 3d analogue, $V[SNS]_2$.

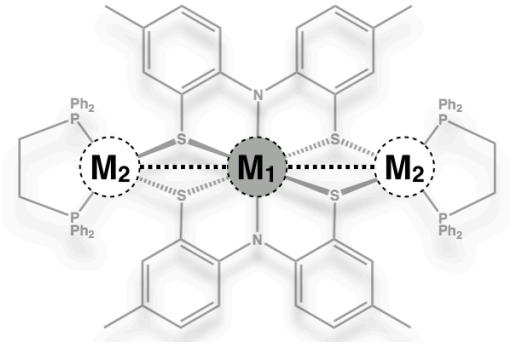

Figure 1.11. "Metal–Metal–Metal" architecture in $M[SNS]_2\{M(dppe)\}_2$ heteromultimetallic systems.

References

(1) Eisenberg, R.; Gray, H. B. *Inorg. Chem.* **2011**, *50*, 9741–9751.
(2) McCleverty, J. A. *Prog. Inorg. Chem.* **1968**, 49–221.
(3) Schrauzer, G. N.; Mayweg, V. *J. Am. Chem. Soc.* **1962**, *84*, 3221–3221.
(4) Gray, H. B.; Williams, R.; Bernal, I.; Billig, E. *J. Am. Chem. Soc.* **1962**, *84*, 3596–3597.
(5) Davison, A.; Edelstein, N.; Holm, R. H.; Maki, A. H. *Inorg. Chem.* **1963**, *2*, 1227–1232.
(6) Stiefel, E. I.; Eisenberg, R.; Rosenberg, R. C.; Gray, H. B. *J. Am. Chem. Soc.* **1966**, *88*, 2956–2966.
(7) Stiefel, E. I.; Dori, Z.; Gray, H. B. *J. Am. Chem. Soc.* **1967**, *89*, 3353–3354.
(8) Bennett, M. J.; Cowie, M.; Martin, J. L.; Takats, J. *J. Am. Chem. Soc.* **1973**, *95*, 7504–7505.
(9) Szilagyi, R. K.; Lim, B. S.; Glaser, T.; Holm, R. H.; Hedman, B.; Hodgson, K. O.; Solomon, E. I. *J. Am. Chem. Soc.* **2003**, *125*, 9158–9169.
(10) Robin, M. B.; Day, P. *Adv. Inorg. Chem. Radiochem.* **1968**, *60*, 247–422.
(11) Sutin, N. *Acc. Chem. Res.* **1982**, *15*, 275–282.
(12) Sutin, N. *Prog. Inorg. Chem.* **1983**, 441–498.
(13) Brunschwig, B. S.; Creutz, C.; Sutin, N. *Chem. Soc. Rev.* **2002**, *31*, 168–184.

(14) Marcus, R. *Can. J. Chem.* **1959**, *37*, 155–163.
(15) Marcus, R. A. *Annu. Rev. Phys. Chem.* **1964**, *15*, 155–196.
(16) Hush, N. S. *Prog. Inorg. Chem.* **1967**, 391–444.
(17) Zhang, L. T.; Ko, J.; Ondrechen, M. J. *J. Am. Chem. Soc.* **1987**, *109*, 1666–1671.
(18) Ondrechen, M. J.; Ko, J.; Zhang, L. T. *J. Am. Chem. Soc.* **1987**, *109*, 1672–1676.
(19) Ernst, S.; Haenel, P.; Jordanov, J.; Kaim, W.; Kasack, V.; Roth, E. *J. Am. Chem. Soc.* **1989**, *111*, 1733–1738.
(20) Chisholm, M. H.; Lear, B. J. *Chem. Soc. Rev.* **2011**, *40*, 5254–5265.
(21) Creutz, C.; Taube, H. *J. Am. Chem. Soc.* **1969**, *91*, 3988–3989.
(22) Creutz, C.; Taube, H. *J. Am. Chem. Soc.* **1973**, *95*, 1086–1094.
(23) Kaim, W.; Klein, A.; Glöckle, M. *Acc. Chem. Res.* **2000**, *33*, 755–763.
(24) Buser, H. J.; Schwarzenbach, D.; Petter, W.; Ludi, A. *Inorg. Chem.* **1977**, *16*, 2704–2710.
(25) Ferlay, S.; Mallah, T.; Ouahes, R.; Veillet, P.; Verdaguer, M. *Nature* **1995**, *378*, 701–703.
(26) Kubiak, C. P. *Inorg. Chem.* **2013**, *52*, 5663–5676.
(27) Porter, T. M.; Heim, G. P.; Kubiak, C. P. *Chem. Sci.* **2017**, *8*, 7324–7329.
(28) Porter, T. M.; Heim, G. P.; Kubiak, C. P. *J. Am. Chem. Soc.* **2018**, *140*, 12756–12759.
(29) Jeon, I.-R.; Park, J. G.; Xiao, D. J.; Harris, T. D. *J. Am. Chem. Soc.* **2013**, *135*, 16845–16848.
(30) Gaudette, A. I.; Jeon, I.-R.; Anderson, J. S.; Grandjean, F.; Long, G. J.; Harris, T. D. *J. Am. Chem. Soc.* **2015**, *137*, 12617–12626.
(31) Demir, S.; Jeon, I.-R.; Long, J. R.; Harris, T. D. *Coord. Chem. Rev.* **2015**, *289*, 149–176.
(32) Solomon, E. I.; Xie, X.; Dey, A. *Chem. Soc. Rev.* **2008**, *37*, 623–638.
(33) Gamelin, D. R.; Bominaar, E. L.; Kirk, M. L.; Wieghardt, K.; Solomon, E. I. *J. Am. Chem. Soc.* **1996**, *118*, 8085–8097.
(34) Leconte, N.; Moutet, J.; Constantin, T.; Molton, F.; Philouze, C.; Thomas, F. *Eur. J. Inorg. Chem.* **2018**, *2018*, 1752–1761.
(35) Conner, K. M.; Perugini, A. L.; Malabute, M.; Brown, S. N. *Inorg. Chem.* **2018**, *57*, 3272–3286.
(36) Schmidt, H. C.; Guo, X.; Richard, P. U.; Neuburger, M.; Palivan, C. G.; Wenger, O. S. *Angew. Chem. Int. Ed.* **2018**, *130*, 11862–11865.
(37) Hua, C.; Doheny, P. W.; Ding, B.; Chan, B.; Yu, M.; Kepert, C. J.; D'Alessandro, D. M. *J. Am. Chem. Soc.* **2018**, *140*, 6622–6630.
(38) Zanello, P. *Inorganic electrochemistry: theory, practice and application*; Royal Society of Chemistry: **2007**.
(39) D'Alessandro, D. M.; Keene, F. R. *Dalton Trans.* **2004**, 3950–3954.
(40) Winter, R. F. *Organometallics* **2014**, *33*, 4517–4536.
(41) Demadis, K. D.; Hartshorn, C. M.; Meyer, T. J. *Chem. Rev.* **2001**, *101*, 2655–2686.
(42) Petrov, V.; Hupp, J. T.; Mottley, C.; Mann, L. C. *J. Am. Chem. Soc.* **1994**, *116*, 2171–2172.
(43) Wei, C. H.; Dahl, L. F. *Inorg. Chem.* **1970**, *9*, 1878–1887.
(44) Rampersad, M. V.; Zuidema, E.; Ernsting, J. M.; van Leeuwen, P. W. N. M.; Darensbourg, M. Y. *Organometallics* **2007**, *26*, 783–792.
(45) Denny, J. A.; Darensbourg, M. Y. *Chem. Rev.* **2015**, *115*, 5248–5273.
(46) Eisenhart, R. J.; Clouston, L. J.; Lu, C. C. *Acc. Chem. Res.* **2015**, *48*, 2885–2894.
(47) Cotton, F. A.; Murillo, C. A.; Walton, R. A. *Multiple bonds between metal atoms*; Springer Science & Business Media: **2005**.
(48) Clouston, L. J.; Siedschlag, R. B.; Rudd, P. A.; Planas, N.; Hu, S.; Miller, A. D.; Gagliardi, L.; Lu, C. C. *J. Am. Chem. Soc.* **2013**, *135*, 13142–13148.
(49) Clouston, L. J.; Bernales, V.; Cammarota, R. C.; Carlson, R. K.; Bill, E.; Gagliardi, L.; Lu, C.

C. *Inorg. Chem.* **2015**, *54*, 11669–11679.

(50) Thomas, C. M. *Comm. Inorg. Chem.* **2011**, *32*, 14–38.

(51) Greenwood, B. P.; Rowe, G. T.; Chen, C.-H.; Foxman, B. M.; Thomas, C. M. *J. Am. Chem. Soc.* **2009**, *132*, 44–45.

(52) Babonneau, F.; Henry, M.; King, R. B.; El Murr, N. *Inorg. Chem.* **1985**, *24*, 1946–1949.

(53) Jeffery, J. C.; Riis-Johannessen, T.; Anderson, C. J.; Adams, C. J.; Robinson, A.; Argent, S. P.; Ward, M. D.; Rice, C. R. *Inorg. Chem.* **2007**, *46*, 2417–2426.

(54) Powell, G.; Richens, D. T. *Dalton Trans.* **2006**, 2959–2963.

(55) Houston, J. R.; Richens, D. T.; Casey, W. H. *Inorg. Chem.* **2006**, *45*, 7962–7967.

(56) Cotton, F. A.; Daniels, L. M.; Murillo, C. A.; Pascual, I. *J. Am. Chem. Soc.* **1997**, *119*, 10223–10224.

(57) Clerac, R.; Cotton, F. A.; Dunbar, K. R.; Murillo, C. A.; Pascual, I.; Wang, X. *Inorg. Chem.* **1999**, *38*, 2655–2657.

(58) Clerac, R.; Cotton, F. A.; Daniels, L. M.; Dunbar, K. R.; Kirschbaum, K.; Murillo, C. A.; Pinkerton, A. A.; Schultz, A. J.; Wang, X. *J. Am. Chem. Soc.* **2000**, *122*, 6226–6236.

(59) Berry, J. F.; Cotton, F. A.; Daniels, L. M.; Murillo, C. A.; Wang, X. *Inorg. Chem.* **2003**, *42*, 2418–2427.

(60) Cotton, F. A.; Chao, H.; Murillo, C. A.; Wang, Q. *Dalton Trans.* **2006**, 5416–5422.

(61) Wang, W.-Z.; Ismayilov, R. H.; Lee, G.-H.; Liu, I. P.-C.; Yeh, C.-Y.; Peng, S.-M. *Dalton Trans.* **2007**, 830–839.

(62) Hernández Sánchez, R.; Bartholomew, A. K.; Powers, T. M.; Ménard, G.; Betley, T. A. *J. Am. Chem. Soc.* **2016**, *138*, 2235–2243.

(63) Wong, J. L.; Higgins, R. F.; Bhowmick, I.; Cao, D. X.; Szigethy, G.; Ziller, J. W.; Shores, M. P.; Heyduk, A. F. *Chem. Sci.* **2016**, *7*, 1594–1599.

(64) Cordero, B.; Gómez, V.; Platero-Prats, A. E.; Revés, M.; Echeverría, J.; Cremades, E.; Barragán, F.; Alvarez, S. *Dalton Trans*. **2008**, 2832–2838.

(65) Shaffer, D. W.; Szigethy, G.; Ziller, J. W.; Heyduk, A. F. *Inorg. Chem.* **2013**, *52*, 2110–2118.

(66) Rosenkoetter, K. E.; Ziller, J. W.; Heyduk, A. F. *Dalton Trans.* **2017**, *46*, 5503–5507.

(67) Rosenkoetter, K. E.; Ziller, J. W.; Heyduk, A. F. *Inorg. Chem.* **2016**, *55*, 6794–6798.

Chapter 2

Heterobimetallic and Heterotrimetallic Clusters Containing a Redox-Active Metalloligand

Portions of this work have been reported previously:

Wojnar, M. K.; Ziller, J. W.; Heyduk, A. F., Heterobimetallic and Heterotrimetallic Clusters Containing a Redox-Active Metalloligand, *European Journal of Inorganic Chemistry* **2017**, 5571–5575.

2.1 Introduction

Multimetallic coordination complexes and clusters have long garnered interest for their promise as mediators in small-molecule-activation reactions[1] and other multi-electron redox processes.[2-6] Hetero-multimetallic complexes are of further interest as structural and functional models of metalloenzyme active sites found in nature, as well as derivatives of molecular wires.[7-9] Whereas biology utilizes the residues inherent to proteins to encapsulate multiple metal centers in close proximity and maintain the integrity of these clusters, in synthetic systems, multidentate ligand platforms and cluster self-assembly strategies are commonly employed to prepare model complexes and clusters.[10,11] Another approach to the synthesis of heteromultimetallic complexes is through the use of metalloligands, comprising a well-defined coordination complex that can serve as a ligand towards another metal ion, typically through one or more bridging donor atoms.

The most prominent metalloligand platform, owing to its stability as well as its role in biological systems, is the so-called Ni(N_2S_2) family of complexes, which incorporate *cis*-dithiolate *S*-donors. The lone pairs of the thiolate sulfur atoms show a strong propensity to bridge to secondary or even tertiary metal centers.[12-14] A wide range of Ni(N_2S_2) complexes have been reported and have been used as metalloligands for a variety of transition metal ions. The Ni(N_2S_2) metalloligands are electron-rich and strongly donating thanks to the combination of the d^8 nickel(II) center and the thiolate bridging atoms. While Ni(N_2S_2) metalloligands allow for a systematic investigation into their ligand steric factors and donor abilities, the robust four-coordinate environment limits the ability of the nickel center to interact with the adjacent metal in multimetallic complexes. In this chapter is reported the synthesis of heterobimetallic and heterotrimetallic cluster complexes incorporating a redox-active Mo[SNS]$_2$ metalloligand ([SNS]H_3 = bis-(2-mercapto-*p*-tolyl)amine). These complexes show dynamic bonding between the molybdenum and nickel metal centers and rich redox activity. In the case of the heterotrimetallic derivative, electrochemical experiments show evidence for mixed valency within the trimetallic core.

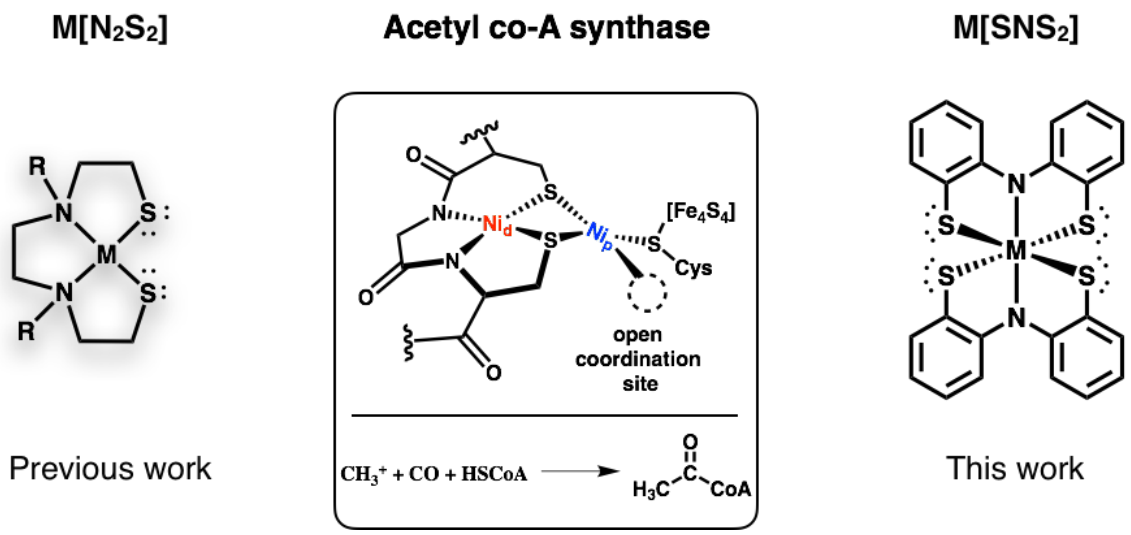

Figure 2.1. Active site of acetyl co-A synthase (middle) and M(N_2S_2) metalloligand (left) used to mimic this site synthetically. In comparison, M[SNS]$_2$ (right) allows for the bridging of two metal centers and metal-metal interactions.

2.2 Results

2.2.1 Synthesis of Mo[SNS]$_2$ (1), Mo[SNS]$_2$Ni(dppe) (2) and Mo[SNS]$_2${Ni(dppe)}$_2$ (3)

The Mo[SNS]$_2$ (**1**) metalloligand was prepared by the reaction of [SNS]H_3 with $MoCl_5$ under oxidizing conditions. When a toluene mixture of the molybdenum(V) starting material $MoCl_5$ and two equivalents of [SNS]H_3 were heated to reflux under air the solution turned dark purple signalling the formation of Mo[SNS]$_2$ (**1**) as shown in Scheme 2.1. The complex was isolated as a purple microcrystalline solid in 65% yield. The diamagnetic product was readily characterized by ^{1}H NMR spectroscopy and electrospray mass spectrometry. Single crystals of **1** were grown from diffusion of diethyl ether into a saturated solution of **1** in toluene and used to determine the solid-state structure of the complex, which is isostructural to the previously-reported tungsten derivative.[15]

The Mo[SNS]$_2$ complex was readily incorporated as a metalloligand in the heterobimetallic complex Mo[SNS]$_2$Ni(dppe) (**2**) under reducing conditions. In a typical reaction, a cold THF solution of **1** was treated first with two equivalents of KC_8 followed by a single equivalent of (dppe)$NiCl_2$ (Scheme 2.1). The targeted heterobimetallic complex was isolated as a diamagnetic black microcrystalline solid in 81% yield. Complex **2** is diamagnetic and was characterized by a parent ion peak at 1070.1 *m/z* in the electrospray mass spectrum. In solution, **2** is C_2-symmetric and showed one

singlet in the $^{31}P\{^{1}H\}$ NMR spectrum at 43 ppm. Given that the $Mo[SNS]_2$ metalloligand of **2** retained two "free" thiolate donors, we targeted the synthesis of a symmetric trimetallic cluster complex. Following the same strategy used to prepare **2**, reduction of $Mo[SNS]_2Ni(dppe)$ (**2**) with two equivalents of KC_8 in THF followed by the addition of one equivalent of $(dppe)NiCl_2$, afforded the trimetallic complex $Mo[SNS]_2\{Ni(dppe)\}_2$ (**3**) as a green solid in 81% yield as summarized in Scheme 2.1. Complex **3** is diamagnetic and was readily characterized by a parent ion peak at 1526.20 *m/z* in the electrospray mass spectrum. In solution, **3** showed one singlet in the $^{31}P\{^{1}H\}$ NMR spectrum at 37 ppm. The ^{1}H NMR spectrum is consistent with a D_2-symmetric complex, with all four methyl groups of the $[SNS]^{3-}$ ligands resonating as a sharp singlet at 1.9 ppm.

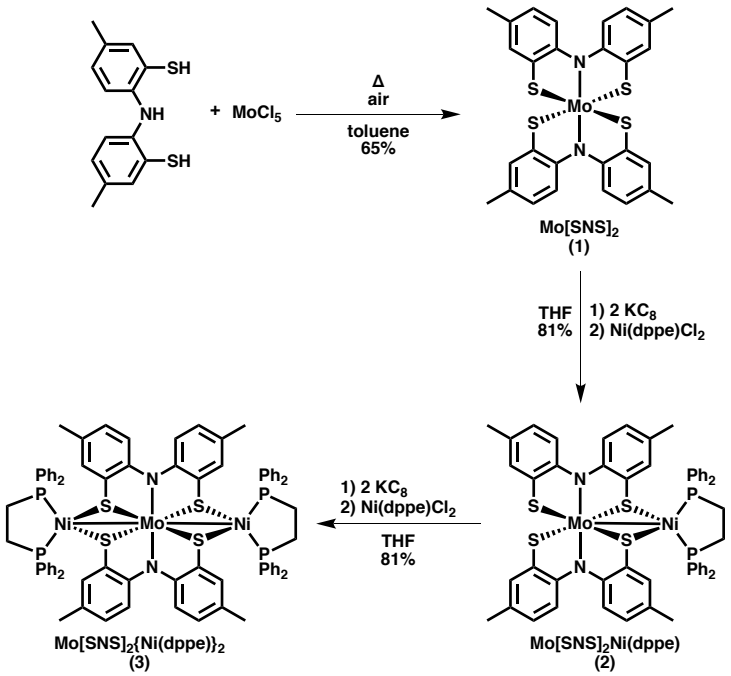

Scheme 2.1. Synthesis of $Mo[SNS]_2$ (**1**), $Mo[SNS]_2Ni(dppe)$ (**2**), and $Mo[SNS]_2\{Ni(dppe)\}_2$ (**3**).

2.2.2 Structural Characterization of $Mo[SNS]_2\{Ni(dppe)\}_x$

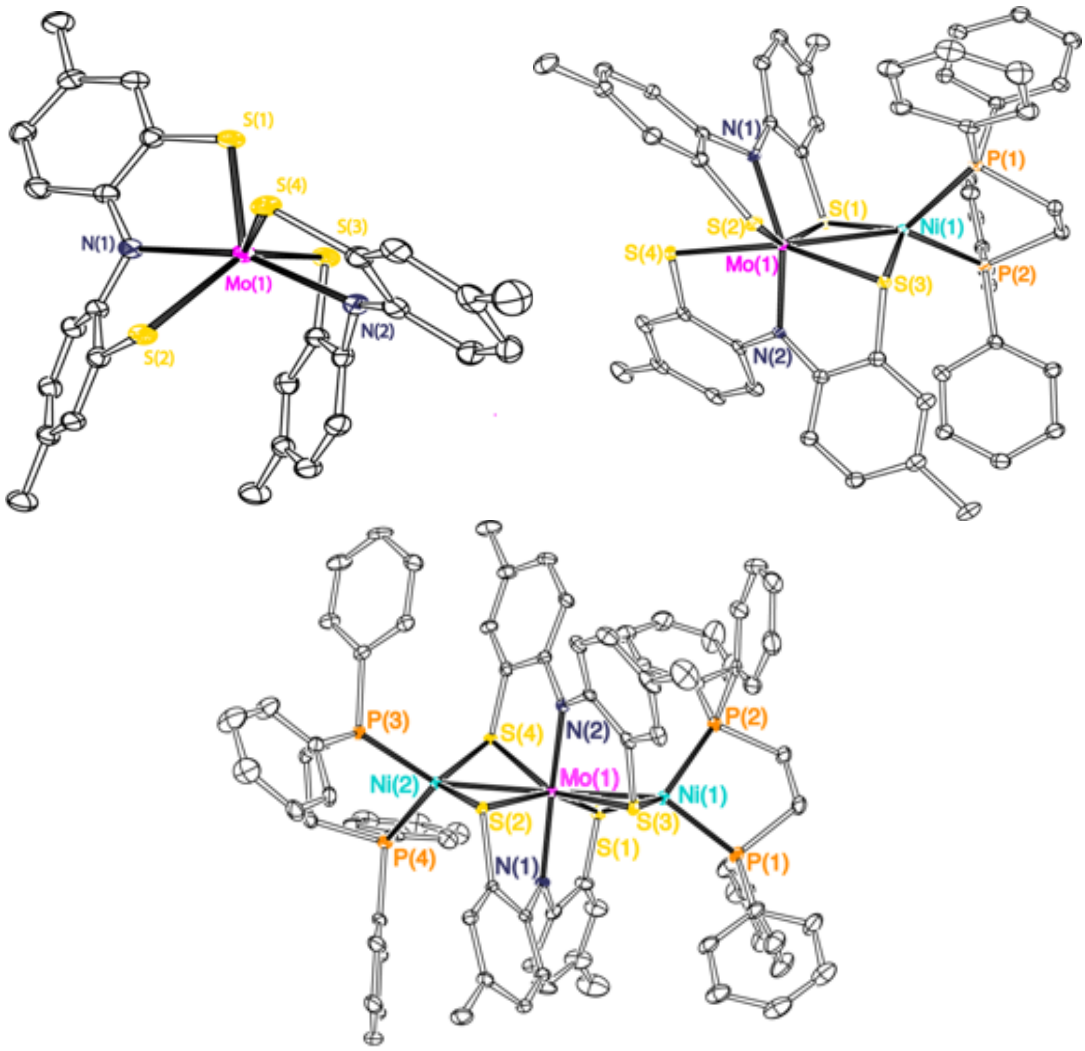

Figure 2.2. ORTEP diagram of $Mo[SNS]_2$ (**1**), $Mo[SNS]_2Ni(dppe)$ (**2**), $Mo[SNS]_2\{Ni(dppe)\}_2$ (**3**). Ellipsoids are shown at 50% probability. Hydrogen atoms (and a pentane solvent molecule in **3**) have been omitted for clarity.

Figure 2.2 (top left) shows an ORTEP diagram of **1** and selected bond angles and distances can be found in Tables 2.1 and 2.2. The molybdenum derivative **1** has a six-coordinate metal center that is intermediate between standard octahedral and trigonal prismatic geometries. The structural data for **1** suggest that the complex is best described as comprising a d^0 molybdenum(VI) and two trianionic $[SNS]^{3-}$ ligands. This will be discussed in more detail in a later chapter, but the long C–S_{avg} and C–N_{avg} bonds, at 1.741 Å and 1.388 Å, respectively, are in agreement with carbon–sulfur and carbon–nitrogen single bonds.[16-20]

In the solid state, single-crystal X-ray diffraction experiments showed **2** to be a heterobimetallic complex with a bond between the molybdenum and nickel centers, isostructural with the W–Ni derivative.[21] Complex **2** crystallized in the primitive space group $P2_1/c$. An ORTEP diagram of **2** is presented in Figure 2.2. The overall symmetry of **2** is approximately C_2, with the rotation axis defined by the two metal atoms. A short intermetallic distance of 2.56 Å between the nickel and molybdenum is significantly smaller than the sum of their covalent radii (2.78 Å), suggesting the presence of a metal-metal bond.[22] There are several examples of Mo–Ni complexes with bridging thiolates in the literature, but they typically have metal-metal distances that are significantly longer.[23-25] Additionally, seven-coordinate molybdenum complexes with non-innocent pincer ligands have been observed previously.[26,27] The Mo–S bonds of **2** are elongated slightly compared to those in **1** at 2.41 Å for the bridging thiolates and 2.40 Å for the non-bridging thiolates. Notably, for the bridging thiolate donors, the Ni–S bond distances (2.18 Å) are shorter than is typically observed for nickel(II) with bridging thiolates, likely due to the presence of metal-metal bonding in **2**.[28,29] An average Ni–P bond distance of 2.23 Å is longer than typically observed for nickel(II) phosphine complexes and falls in line with the values reported for nickel(I) complexes containing the dppe ligand and *cis*-dithiolate donors.[30] The bond distances within the SNS ligand backbone are all consistent with those measured in $Mo[SNS]_2$, suggesting that these ligands remain in the trianionic $[SNS]^{3-}$ form.

Table 2.1. Selected bond distances for $Mo[SNS]_2$ (**1**), $Mo[SNS]_2Ni(dppe)$ (**2**),and $Mo[SNS]_2\{Ni(dppe)\}_2$ (**3**).

Distances / Å	$Mo[SNS]_2$ (**1**)	$Mo[SNS]_2Ni(dppe)$ (**2**)	$Mo[SNS]_2\{Ni(dppe)\}_2$ (**3**)
Mo(1)–Ni(1)	–	2.5579(5)	2.6755(6)
Mo(1)–Ni(2)	–	–	2.6635(6)
Mo(1)–S(1)	2.3411(6)	2.4002(8)	2.409(1)
Mo(1)–S(2)	2.3975(6)	2.3705(7)	2.419(1)
Mo(1)–S(3)	2.3816(6)	2.4175(9)	2.412(1)
Mo(1)–S(4)	2.3791(6)	2.4291(9)	2.414(1)
Mo(1)–N(1)	2.099(2)	2.118(3)	2.120(4)
Mo(1)–N(2)	2.048(2)	2.073(2)	2.109(3)
Ni(1)–S(1)	–	2.1871(9)	2.176(1)
Ni(1)–S(3)	–	2.1833(8)	2.196(1)
Ni(1)–P(1)	–	2.2312(9)	2.182(1)
Ni(1)–P(2)	–	2.2211(8)	2.229(1)
Ni(2)–S(2)	–	–	2.199(1)
Ni(2)–S(4)	–	–	2.170(1)
Ni(2)–P(3)	–	–	2.185(1)
Ni(2)–P(4)	–	–	2.211(1)
Angles / °			
S(1)–Mo(1)–S(3)	88.32(2)	101.46(3)	98.41(4)
S(2)–Mo(1)–S(4)	86.13(2)	97.71(3)	98.97(4)
S(1)–Ni(1)–S(2)	–	117.17(3)	113.19(4)
S(2)–Ni(2)–S(4)	–	–	114.49(5)
P(1)–Ni(1)–P(2)	–	87.78(3)	90.75(5)
P(3)–Ni(2)–P(4)	–	–	91.27(5)

Table 2.2. Average intraligand bond distances for $Mo[SNS]_2$ (**1**), $Mo[SNS]_2Ni(dppe)$ (**2**), and $Mo[SNS]_2\{Ni(dppe)\}_2$ (**3**).

	$Mo[SNS]_2$ (1)	**$Mo[SNS]_2Ni(dppe)$ (2)**	**$Mo[SNS]_2\{Ni(dppe)\}_2$ (3)**
$S–C_{avg}$	1.74	1.75	1.76
$N–C_{avg}$	1.39	1.41	1.41
$(\Delta C–C)_{avg}$	0.043	0.025	0.030

The solid-state molecular structure of the heterotrimetallic complex $Mo[SNS]_2\{Ni(dppe)\}_2$ (**3**) is analogous to the heterobimetallic derivative, $Mo[SNS]_2Ni(dppe)$ (**2**). X-ray quality crystals of **3** were grown by diffusion of pentane into a saturated solution of the complex in THF at room temperature, and crystallized in the triclinic space group, P-1. Figure 2.2 (bottom) displays the molecular structure of **3** as an ORTEP diagram and selected structural metrics are presented in Tables 2.1 and 2.2. As shown in Figure 2.2, the $Mo[SNS]_2$ metalloligand of **3** functions as a chelating ligand to two different nickel centers, acting as a metallic bridge.[31] Intermetallic distances of 2.66 Å and 2.68 Å in the structure of **3**, while longer than those observed in **2**, are still consistent with the presence of Mo–Ni bonds. Again, in **3**, the average Mo–S distance is long at 2.41 Å while the average Ni–S distance is short at 2.18 Å. The average Ni–P distance of 2.20 Å in **3** is again consistent with dppe bound to a reduced nickel center[30,32], and the SNS ligand bond lengths are consistent with an $[SNS]^{3-}$ formulation.

2.2.3 Spectroscopic Characterization of $Mo[SNS]_2\{Ni(dppe)\}_x$

Solution NMR spectra of **2** are consistent with the heterobimetallic structure observed in the solid state. In the $^{31}P\{^1H\}$ NMR spectrum, a single phosphorous resonance was observed at 43 ppm for the chelating dppe ligand. In the ^1H NMR spectrum at 298 K, the proton resonances associated with the methyl groups of the $[SNS]^{3-}$ ligands appeared as broad singlets at 2.06 and 2.24 ppm. Cooling the ^1H NMR sample to 268 K caused these broad resonances to sharpen into well-resolved singlets at 2.09 and 2.31 ppm, while warming the sample to 318 K resulted in coalescence into one singlet at 2.24 ppm. Based on the solid-state structure, two distinct resonances would be expected for

the methyl groups of the $[SNS]^{3-}$ ligands. The peak positions and shapes of these methyl resonances were fit over a temperature range of 278 K-308 K, allowing the extraction of activation parameters $\Delta H^{\ddagger} = 4 \pm 1$ kcal mol^{-1} and $\Delta S^{\ddagger} = 20 \pm 5$ eu for the dynamic process (Figure 2.3).

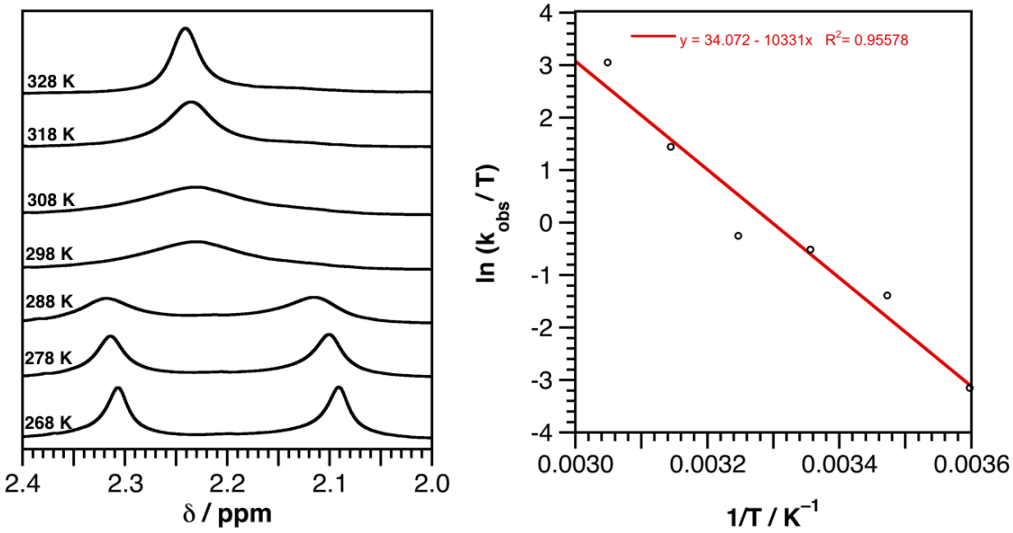

Figure 2.3. ^{1}H VT NMR spectra in tetrachloroethane-d_2 (left) and Eyring plot (right) for Mo[SNS]$_2$Ni(dppe) (**2**).

Addition of external trapping reagents led to isolation of the monometallic ions. When **2** was exposed to 1,2-bis(diphenylphosphino)ethane (dppe), the heterobimetallic system was quantitively converted into the monomeric Mo[SNS]$_2$ (**1**) and Ni^0(dppe)$_2$, confirmed by both ^{1}H and ^{31}P{^{1}H} NMR (Scheme 2.2).

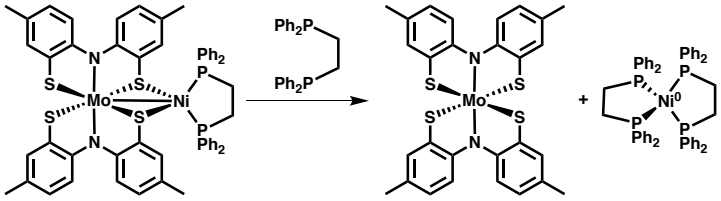

Scheme 2.2. Dissociation of Ni(dppe) synthon facilitated by phosphine ligand.

2.2.4 Voltammetric Investigations of Mo[SNS]$_2${Ni(dppe)}$_x$

Cyclic voltammetry experiments were used in an attempt to better resolve the possible electronic structures of **1**, **2**, and **3**. Figure 2.4 shows the cyclic voltammograms for Mo[SNS]$_2$Ni(dppe) (**2**) and Mo[SNS]$_2${Ni(dppe)}$_2$ (**3**), respectively, under the same conditions used to study **1**. Table 2.3 collects the reduction potentials referenced to $[Cp_2Fe]^{+/0}$ for the reversible processes. Cyclic voltammetry experiments on **1** revealed two reversible ($i_{pc}/i_{pa} \cong 1$), one-electron

reductions at potentials of –0.50 V and –1.34 V vs. $[Cp_2Fe]^{+/0}$ (glassy carbon working electrode, 0.1 M $[Bu_4N][PF_6]$ in THF). Opening up the potential window revealed two oxidations at more positive potentials (>0.5 V vs. $[Cp_2Fe]^{+/0}$) that were only partially reversible.

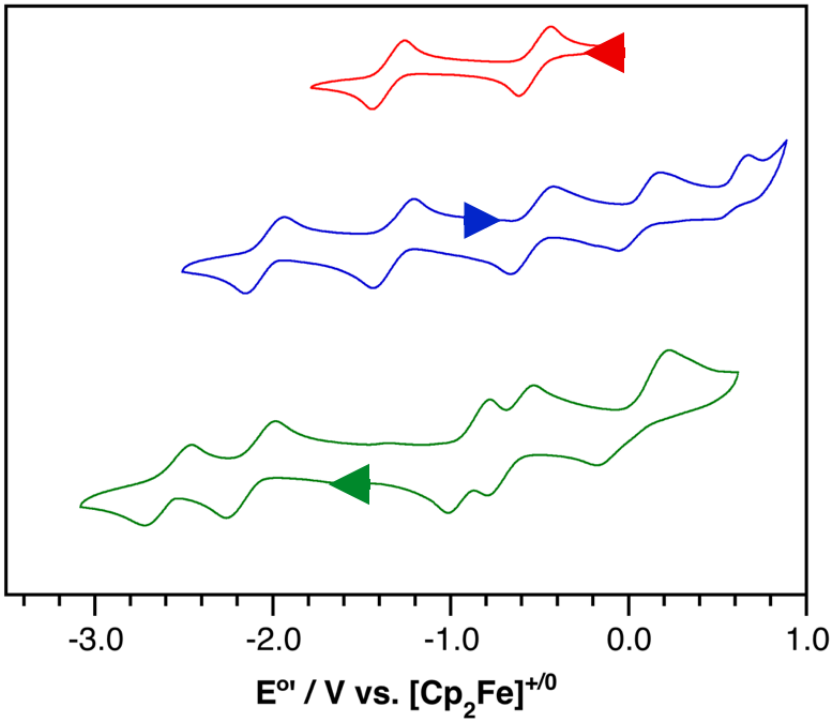

Figure 2.4. Cyclic voltammograms of (a) $Mo[SNS]_2$ (**1**), (b) $Mo[SNS]_2Ni(dppe)$ (**2**),and (c) $Mo[SNS]_2\{Ni(dppe)\}_2$ (**3**) dissolved in THF. Measurements were made under N_2 using a scan rate of 200 mV sec^{-1} on 1.0 mM analyte solutions containing 0.10 M $[Bu_4N][PF_6]$ as the supporting electrolyte. Potentials were referenced to $[Cp_2Fe]^{+/0}$ using an internal standard. The asterisk (arrowhead) denotes the open circuit potential. Voltammetric data were collected using three electrodes: glassy carbon working, platinum counter, and silver wire pseudo-reference.

Table 2.3. Reduction potentials for $Mo[SNS]_2$ (**1**), $Mo[SNS]_2Ni(dppe)$ (**2**), and $Mo[SNS]_2\{Ni(dppe)\}_2$ (**3**), referenced to $[Cp_2Fe]^{+/0}$ in THF.

	$[M]^{-1/-2}$	$[M]^{0/-1}$	$[M]^{0/+1}$	$[M]^{+1/+2}$	$[M]^{+2/+3}$
$Mo[SNS]_2$ (**1**)	–1.34	–0.50	+0.51	+0.91	–
$Mo[SNS]_2Ni(dppe)$ (**2**)	–2.05	–1.32	–0.54	+0.06	+0.57
$Mo[SNS]_2\{Ni(dppe)\}_2$ (**3**)	–2.50	–2.12	–0.80	–0.50	+0.03

Despite the reductive conditions used to prepare **2** and **3**, both complexes retain two reversible one-electron reductions, though in each case these processes shift to progressively more negative potentials, consistent with a more reduced molecule. Concomitant with the cathodic shift, the

separation between the two reductions shrinks from 840 mV in **1** to 730 mV in **2** to 440 mV in **3**.

In addition to two reductions, complexes **2** and **3** show multiple, reversible oxidative processes. Complex **2** shows two, one-electron oxidations, with a good degree of reversibility, at –0.54 V and +0.06 V. A third, pseudo-reversible oxidation for **2** is apparent near the edge of the solvent window at +0.57 V. For complex **3**, two closely-spaced oxidations appear at –0.80 V and –0.50 V with a third oxidation visible at +0.03 V. The initial oxidations of **2** and **3** are interesting in that it seems likely that they are localized on the low-valent nickel center (or rather within the Mo–Ni bond). The first one-electron oxidation of **2** is at –0.54 V and it appears that the addition of a second nickel center to form **3** results in the appearance of a second one-electron oxidation in the same region. The contention that these oxidations are nickel-localized suggests that the first oxidation of **3** may result in the formation of a mixed-valent, $[Ni–Mo–Ni]^+$ species. In this case, the separation between $E_3^{\circ\prime}$ and $E_4^{\circ\prime}$ processes can be used to calculate a comproportionation constant (K_c) of 10^5,[33,34] indicative of a mixed-valence cation, $[Ni–Mo–Ni]^+$, that is stable with respect to disproportionation.[35] This stability can be attributed to both electrostatic and electronic contributions.[36,37]

2.2.5 Computational Investigations of $Mo[SNS]_2\{Ni(dppe)\}_x$

Complexes **1**, **2**, and **3** represent the "building up" of molecular complexity, with the introduction of additional redox centers that can interact with the redox-active molybdenum metalloligand. To investigate the interaction that the Ni(dppe) synthon has with $Mo[SNS]_2$, density functional theory (DFT) calculations were performed on these systems, utilizing the TPSS functional at the TZVP level of theory. Geometry optimization yielded a molybdenum–nickel bond length of 2.64 Å for **2,** and 2.71 Å for both metal–metal bond lengths in **3**. As will be discussed in depth in a later chapter, **1** consists of a molybdenum ion in a distorted trigonal prismatic geometry. As a result of the covalency in this sytem, the highest occupied molecular orbital (and the filled orbitals that are lower in energy) are primarily ligand-based, with the lowest unoccupied molecular orbital (and the unfilled orbitals that are higher in energy) being Mo-based. In a pseudo-octahedral geometry, the

Mo(VI) ion has three almost degenerate orbitals, $d_{Z}2 \leq d_{xy}$, $d_{x^2-y^2}$.[38] It is these orbitals that the formal Ni(0) metal center (generated in situ) interacts with to generate the heterobimetallic **2** (Figure 2.5). Figure 2.6 illustrates the interaction between the sites – a sigma bonding combination localized in between the two metal ions that is doubly occupied. Located in the bonding orbitals of **2** are four orbitals that are predominantly localized on nickel. In the antibonding orbitals are four orbitals that are molybdenum-based (Figure 2.6). This suggests that, upon homolytic cleavage of the Mo–Ni metal-metal bond, the formal oxidation state assignment of **2** is Mo(V) (d^1) and Ni(I) (d^9). According to Mulliken population analysis (MPA), the bond has a polarity with the "negative" end localized on nickel (39%) and the "positive" end localized on molybdenum (19%), which is attributed to the differing electronegativities of the metal centers. The MPA also shows that another relevant resonance structure is Mo(VI) (d^0) and Ni(0) (d^{10}), which would yield a dative metal-metal bond. In either case, introduction of a redox-rich transition metal ion forms a two-center two-electron bonding motif, with the two electrons being placed in a molecular orbital with both molybdenum and nickel character.

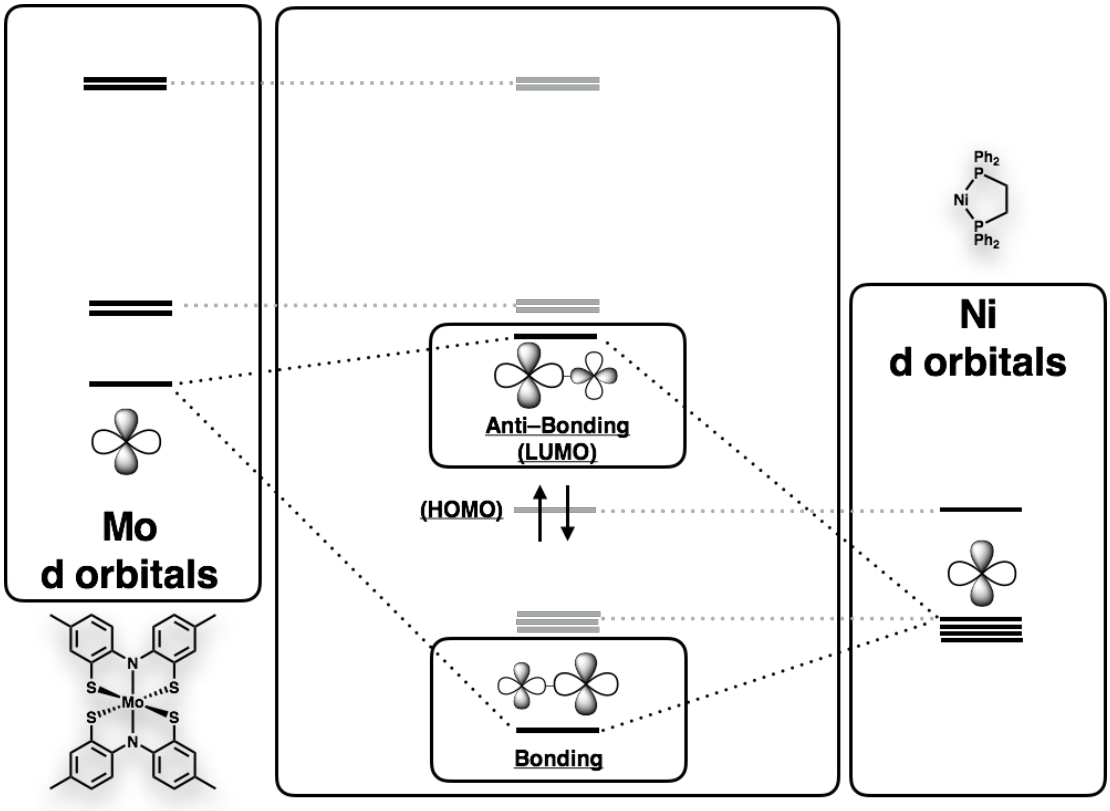

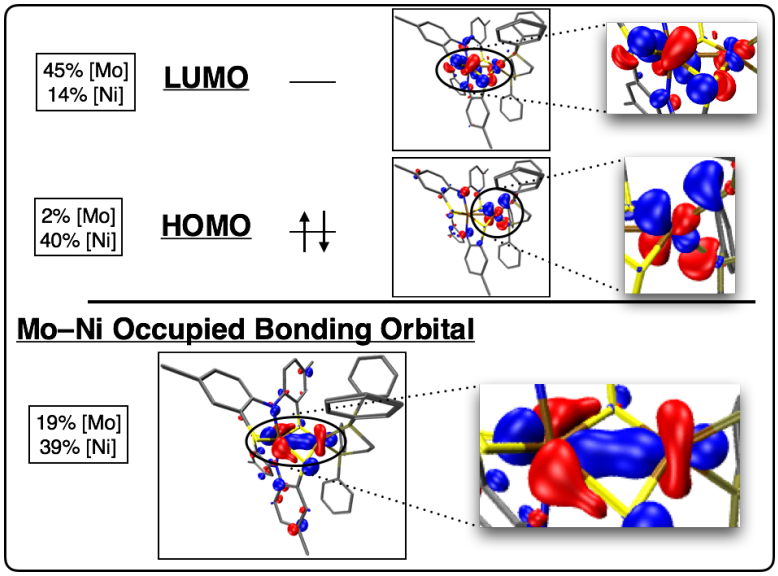

Figure 2.5. General molecular orbital diagram (top) and frontier molecular orbital diagram with Kohn-Sham molecular orbitals for **3** (bottom). Orbital rendering was performed using VMD.

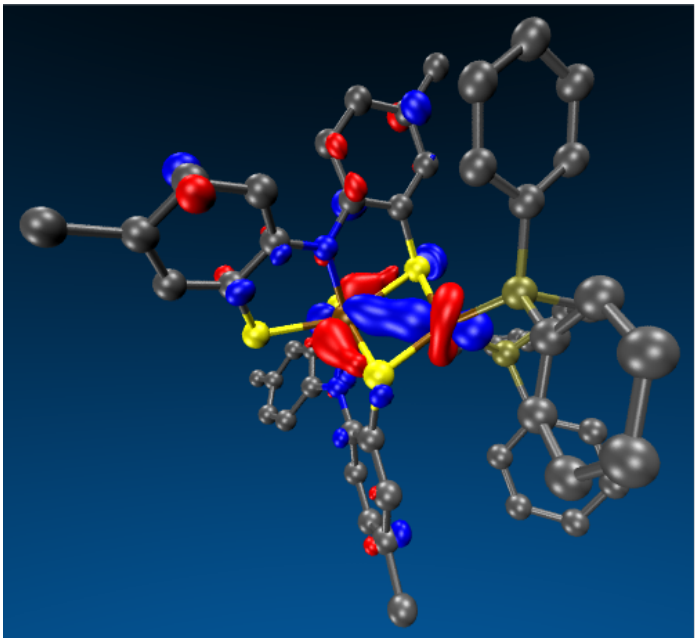

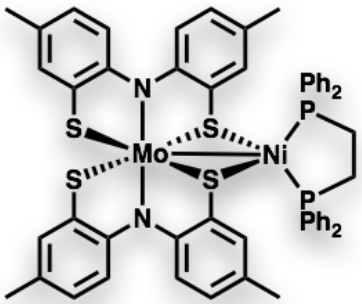

Figure 2.6. Metal-metal σ bond between molybdenum and nickel for Mo[SNS]$_2$Ni(dppe) (**2**).

For the electronic structure of **3**, which is synthesized via two-electron reduction with addition of a second metal center, the heterotrimetallic system can be viewed as the storage of four electrons among three transitions metal ions. This "three-center four-electron" bonding is further exemplified in the frontier molecular orbital scheme for **3**, in which the bonding, non-bonding, and anti-bonding orbitals are all observed in the computational experiment. In terms of electron

configuration, a formal [Ni^{I}–Mo^{IV}–Ni^{I}] ↔ [Ni^{0}–Mo^{VI}–Ni^{0}] affords 20 d electrons, which populate the bonding (Figure 2.7) and non-bonding orbitals, the nickel-localized symmetry-adapted linear combinations (SALC) of atomic orbitals. As with any three-center system, the contributions from each atom depend on the energy of their orbitals, typically dictated by electronegativity. Delineated in Figure 2.8, the contributions for the bonding and non-bonding orbitals are dominated by the nickel ions (37% for the metal-metal bond, 52% for the non-bonding molecular orbitals), while the anti-bonding orbital is localized on the molybdenum metalloligand (43% molybdenum contribution to the LUMO). This is consistent with the relative electronegativities of the two transition metal centers, with the nickel d orbitals being lower in energy (more electronegative atom) than the molybdenum d orbitals (less electronegative).

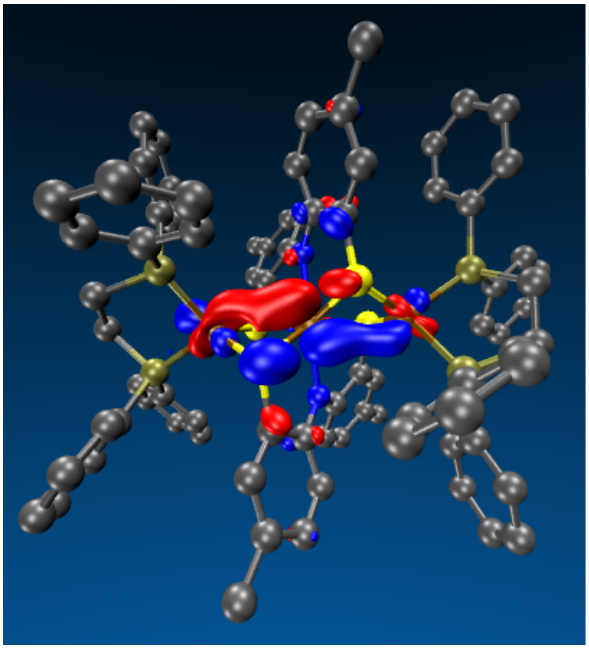

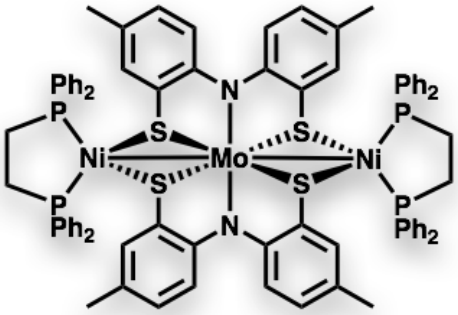

Figure 2.7. Three-center four-electron metal-metal bond between molybdenum and nickel ions for $Mo[SNS]_2\{Ni(dppe)\}_2$ (**3**).

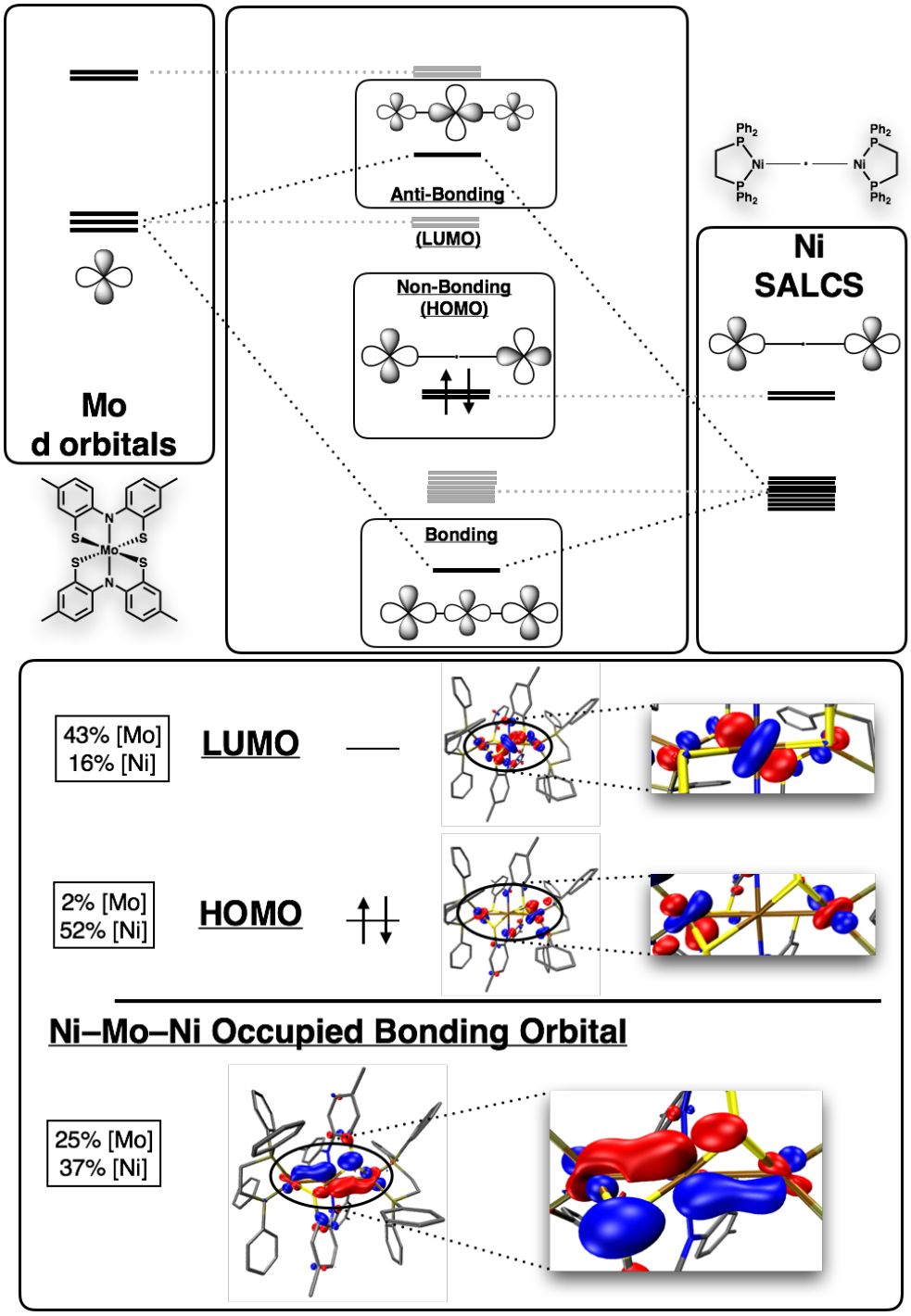

Figure 2.8. General molecular orbital diagram (top) and frontier molecular orbital diagram with Kohn-Sham molecular orbitals for **3** (bottom). Orbital rendering was performed using VMD.

2.3 Discussion

$Mo[SNS]_2$ was shown to act as a metalloligand to stabilize low-valent nickel ions through a reduction/salt-metathesis, a common strategy in heteromultimetallic systems. Although it will be discussed in detail in a later chapter, **1** can best be described as $Mo^{VI}[SNS^{cat}]^{3-}{}_2$, in which the ligands

are fully-reduced and "innocent" in the chemistry to generate **2** and **3**. Due to the close proximity of metal and ligand orbitals in the case of **1**, partial oxidation (i.e. covalency or π backbonding) is observed, so that the "true" oxidation state assignment would be a non-integer value between $Mo^{V}([SNS^{cat}]^{3-})([SNS^{sq.}]^{2-}) \leftrightarrow Mo^{VI}([SNS^{cat}]^{3-})_2$. A formal two-electron reduction generates $Mo[SNS]_2Ni(dppe)$ (**2**) and a four-electron reduction yields $Mo[SNS]_2\{Ni(dppe)\}_2$ (**3**).

Complex **2** demonstrated dynamic behavior in solution, as observed via VT NMR experiments, and was in agreement with trapping of the $[Ni^0]$ synthon by addition of phosphine ligand. Based on the ^1H NMR data, there must be a dynamic process in solution that equilibrates the different chemical environments of the coalescing methyl groups on the [SNS] ligand backbone. The small $\Delta H^{\ddagger}$ value (4 ± 1 kcal mol^{-1}) suggests a transition state that does not include a significant bond-breaking component, or at least that any bond breaking in the transition state is compensated for by a nearly equivalent bond making. The positive $\Delta S^{\ddagger}$ value (20 ± 5 eu) is indicative of a transition state that is less ordered than the ground state. These two activation parameters are consistent with a dynamic process in which the (dppe)Ni fragment "walks" around the $Mo[SNS]_2$ metalloligand, exchanging one thiolate donor for the next, without invoking dissociation of the cluster. No dynamic behavior was observed in **3**. For this metalloligand platform, it was previously confirmed crystallographically that one of the thiolate arms was hemilabile for the second- and third-row Group X metals.[39] It is hypothesized that the molybdenum–thiolate hemilability allows for the association of exogenous ligands, like dppe. This dynamic behavior is common in heterobimetallic systems incorporating Lewis acid/base sites.[40,41]

Based on the solid- and solution-based characterization methods for **2**, the heterobimetallic complex can be described by two resonance structures: $[Mo^{V}–Ni^{I}] \leftrightarrow [Mo^{VI}–Ni^{0}]$. Based on the structural data, two electronic arrangements seem plausible for complex **2**: either molybdenum(V)–nickel(I) or molybdenum(VI)–nickel(0). Within the context of two interacting metal centers, these two oxidation state assignments represent different extremes for the description of the metal-metal bond. In the former case, one electron from a Ni^{I} and one electron from a Mo^{V} are shared equally to form

the metal-metal bond.[42] In the latter case, two electrons from a Ni^0 are shared with a Mo^{VI} to form the metal-metal bond. Given that the oxidation state formalism was not developed to account for covalent interactions, the two possibilities recognized here amount to the extremes of a perfectly covalent metal-metal bond and a dative metal-metal bond. The real nature of the metal-metal bond in **2** lies somewhere in between these two extremes.[43,44] The prevalence of both resonance structures underscores the covalency in **2**, which is best represented computationally in Figure 2.5. The two electrons are not localized on either metal ion, but rather distributed in a molecular orbital that has contributions from both the molybdenum metalloligand (19%) and the nickel ion (37%); the difference in these contributions reflects the inherent energetic differences in the metal d orbitals of molybdenum and nickel. These population analyses also suggest that the resonance structure, [Mo^{VI}–Ni^0], has more contribution toward the complete electronic structure description of **2**. As such, **2** also fits into the category of a (frustrated) Lewis-acid/base pair.[45] The electronic complexity of **2**, denoted by the multiple reversible redox events found in the voltammograms, can also be rationalized through this metal-metal bonding scheme. The two oxidations refer to the two electrons deposited into the metal-metal bonding orbital via the reduction/salt-metathesis strategy. While calculations illustrate a HOMO that involves electrons in a nonbonding orbital on the nickel center, it is hypothesized that the oxidation of Ni(0)/Ni(I) → Ni(I)/Ni(II) will induce a tetrahedral to square planar twist. This severe redox-induced geometric change will sever the metal-metal bond, as has been observed in these systems and other bimetallic systems incorporating Ni(dppe).[46-48] The Mo–Ni bonding combination generates an antibonding orbital as well, which explains to the two reductions at more negative potentials. Due to the relative energetic differences in the metal d orbitals, the oxidations (bonding orbital) are more polarized toward the more electronegative nickel, while the reductions (antibonding orbital) are more polarized toward the metalloligand.[49]

While the heterobimetallic **2** exemplifies a two-center two-electron bond, **3** involves the addition of two more electrons, as well as another nickel ion, making **3** a three-center four-electron system.[50,51] The heterotrimetallic system was confirmed by both ^1H and ^{31}P $\{^1H\}$ NMR

spectroscopy, and exhibited D_2 symmetry in solution, revealing that the nickel ions are in equivalent electronic and steric environments. X-ray diffraction demonstrated short molybdenum–nickel bond distances at 2.66 Å-2.68 Å. Given the similarities in the structures of **2** and **3**, we posit that **3** can be described as either a Ni^{I}–Mo^{IV}–Ni^{I} complex or a Ni^{0}–Mo^{VI}–Ni^{0} complex, where again these two descriptions represent the extremes of perfectly covalent and dative interactions between the molybdenum and nickel centers. The lengthening of the Mo–Ni bonds in **3** is in accordance with a more reduced molybdenum (larger covalent radii), as well as metal-metal interactions with more dative character (dative bonds are weaker than covalent bonds). These metal-metal interactions were confirmed computationally, with the electron density being polarized toward the more electronegative nickel ions. The electrochemistry also reflects the three-center four-electron bonding, in which the two oxidations (~300 mV apart) coincide with the two electrons populating the non-bonding orbitals localized on the nickel centers. The two cathodic features are consistent with population of the Ni–Mo–Ni antibonding orbital, and the final two-electron process at ~0 V hypothesized as the electrons occupying the Ni–Mo–Ni bonding orbital. This simplified rationalize justifies the placement and localization of the four electrons that are introduced with concomitant formational of molybdenum–nickel metal-metal bonds.

Preliminary spectroscopic analysis of the one-electron-oxidized species does not show evidence for the low-energy intervalence charge transfer (IVCT) transitions that are typically associated with delocalized electronic manifolds.[52] The absence of such intervalence charge transfer transitions is consistent with the electronic mismatch, as well as the polarization, between the 3d nickel orbitals and the 4d Mo orbitals, that results in a localized electronic structure in the $[Ni–Mo–Ni]^{+}$ cation.[53,54] Based on the comproportionation constant and the spectroscopic data, the $[Ni–Mo–Ni]^{+}$ cation is more localized than the classic Creutz-Taube ion, which is surprising given that **3** displays short metal-metal distances across the complex.[55] Typically, linear trimetallic complexes, both with and without formal metal-metal bonds, show strong Class III character with much higher comproportionation constants than estimated here for the $[Ni–Mo–Ni]^{+}$ cation.[56,57]

One hypothesis to bear in mind is that **3** is already a mixed-valent system. This heterotrimetallic complex represents the only example of $M[SNS]_2\{M(dppe)\}_2^x$ class of compounds to have low energy transitions in the UV-vis spectrum (918 nm, 4,600 M^{-1} cm^{-1}). The electronic description above invoked only two resonance structures: Ni(0)–Mo(VI)–Ni(0) and Ni(I)–Mo(IV)–Ni(I) (Scheme 2.3).

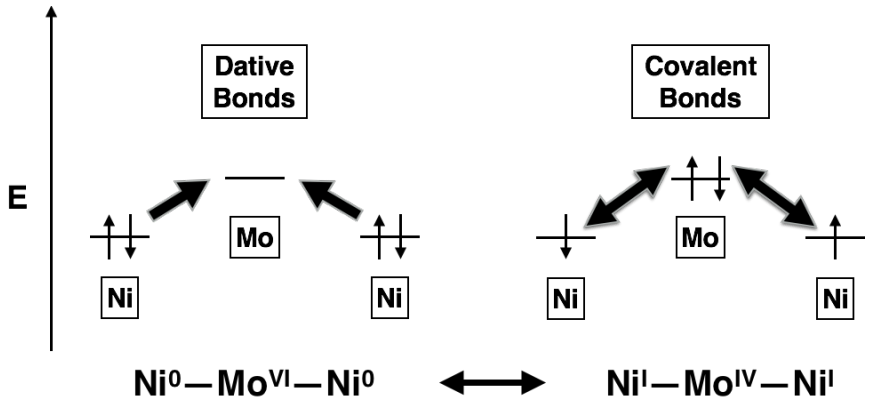

Scheme 2.3. $Mo[SNS]_2\{Ni(dppe)\}_2$ resonance structures invoking strictly dative interactions (Ni(0)–Mo(VI)–Ni(0)) and strictly covalent interactions (Ni(I)–Mo(IV)–Ni(I)).

These resonance structures were chosen specifically due to the S=0 closed-shell system of **3** and the *D*2 symmetry of the molecule. A third possible resonance structure(s) could include: Ni(I)–Mo(V)–Ni(0) and Ni(0)–Mo(V)–Ni(I) (Scheme 2.4).

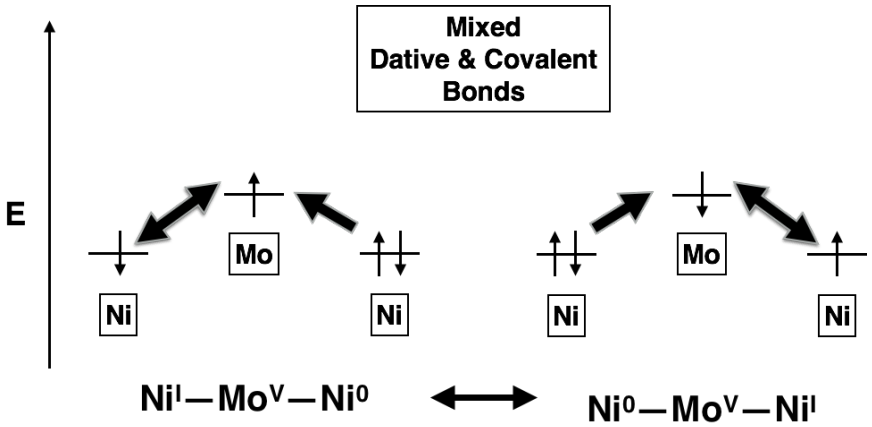

Scheme 2.4. $Mo[SNS]_2\{Ni(dppe)\}_2$ resonance structures invoking a mixed dative and covalent interaction (Ni(I)–Mo(V)–Ni(0)).

These resonance structures are consistent with the characterization measurements provided above. Inequivalent nickel ions were observed in the solid-state with distinctly different molybdenum nickel bond lengths of 2.676 Å and 2.664 Å. The D_2 symmetry of **3** (and the identical nickel environments by ^1H and ^{31}P $\{^1H\}$ NMR spectroscopy) can be attributed to the slow time scale of NMR

spectroscopy (~10^{-5} s). If this is notably much slower than the movement of the electron, it would lead to averaged signals in the spectrum.[58] The voltammetry data is also in agreement with the mixed-valence resonance structures presented above. In comparison to the electrochemistry of **1**, the open circuit potential of **3** is consistent with a formal one-electron reduction of the $Mo[SNS]_2$ bridge. In sum, this yields three electrons to be distributed among the two nickel centers. As mentioned above, **3** also displays a low energy charge transfer band. Based on the following equation, one can calculate the electronic coupling parameter, H_{ab}:

$$H_{ab}\ (cm^{-1}) = [(4.2 \times 10^{-4})\ \varepsilon_{max} \Delta \upsilon_{1/2} \lambda_{max}]^{1/2} / d$$

where ε_{max} refers to the molar extinction coefficient, $\Delta\boldsymbol{\upsilon}_{1/2}$ is the full-width-at-half-maximum, λ_{max} is the energy of the absorption maximum, and d is the separation between redox sites.[59] The calculated value of H_{ab} is 1958 cm^{-1}, in which the parameters were gathered from the electronic absorption spectroscopy data, while the value of d (5.313 Å) was gathered from the X-ray crystal structure of **3**. This value for H_{ab} is in agreement with a Robin-Day Class II system, in which the electronic coupling parameter falls within the boundaries of $0 < H_{ab} < \lambda_{max}/2$ (5447 cm^{-1}).[60,61] These data are also consistent with valence-trapping in the case of neutral **3**, which can once again be rationalized by the electronic mismatch between the Mo 4d and the Ni 3d orbitals involved in the metal-metal bonding network. One electron oxidation would yield isovalent nickel ions, which explains the bleaching of the low energy band upon oxidation of **3**. The electronic complexity of **3** makes spectroscopic analysis difficult due to the plethora of transitions afforded in a heterotrimetallic complex incorporating three redox-active metals and two non-innocent ligands. This is in stark constrast to the Creutz-Taube ion, which incorporates ancillary ammonia ligands which do not contribute to the spectroscopic features of the system.

2.4 Conclusion

In this study, the ability of the homoleptic molybdenum complex $Mo[SNS]_2$ to act as a redox-active metalloligand was demonstrated through the synthesis of heterobimetallic and heterotrimetallic complexes of nickel. As a metalloligand, the $Mo[SNS]_2$ species is unique in that it comprises an

electron-poor molybdenum center encapsulated by two trianionic azanidodithiolate ligands. This combination is distinct from the more common Ni(N_2S_2) metalloligand motif that includes both an electron-rich metal center and thiolate bridging donor atoms. The presence of the high-valent molybdenum center in both Mo[SNS]$_2$Ni(dppe) (**2**) and Mo[SNS]$_2${Ni(dppe)}$_2$ (**3**) engenders these complexes with rich reductive redox-chemistry, even though these clusters are assembled under reducing conditions. It is these reducing conditions that result in low formal oxidation states for the nickel centers in **2** and **3**, which in turn gives rise to substantive oxidative redox chemistry. Based on the electrochemical studies, bimetallic **2** is stable over five different oxidation states whereas trimetallic **3** is stable over six. The first oxidation of trimetallic **3** to the [Ni–Mo–Ni]$^+$ cation, afforded a putative mixed-valence complex with a localized electron distribution. Given the evidence for a direct communication pathway between the two nickel centers in neutral **3**, it is surprising that **3**$^+$ shows localized behavior. Current efforts are aimed at understanding the communication pathways resulting in this non-coupled mixed-valent system. The exploration of electronic communication in multimetallic systems remains relevant to a variety of chemistries, ranging from the molecular understanding of the electronic structure of metalloenzyme active sites, to the interaction between metal ions in bulk heterogeneous systems.

2.5 Experimental Section

General Considerations. All compounds and reactions reported below show varied degrees of air- and moisture-sensitivity, therefore all manipulations were carried out using standard vacuum-line, Schlenk-line and glovebox techniques. Solvents were sparged with argon before being deoxygenated and dried by passage through Q5 and activated alumina columns, respectively. To test for effective oxygen and water removal, aliquots of each solvent were treated with a few drops of a purple solution of sodium benzophenone ketyl radical in THF. $NiCl_2 \cdot 6H_2O$ (Fisher) and 1,2-bis(diphenylphosphino)ethane (dppe) (>97%, TCI) were used as received. (dppe)$NiCl_2$ was prepared according to the previously reported procedure.[62]

Spectroscopic Measurements. NMR spectra were collected at 298 K on a Bruker Avance 400 MHz

spectrometer in dry, degassed $CDCl_3$ or C_6D_6. ^1H NMR spectra were referenced to tetramethylsilane (TMS) using the residual proteo impurities of the solvent (7.26 ppm). All $^{31}P\{^1H\}$ NMR spectra were referenced with an external standard of phosphoric acid (H_3PO_4, 85%). All chemical shifts are reported using the standard δ notation in parts per million; positive chemical shifts are to a higher frequency from the given reference. Electronic absorption spectra were recorded with a Perkin-Elmer Lambda 900 UV-vis-NIR spectrophotometer or a Jasco V-670 absorption spectrometer using 1-cm path-length cells at ambient temperature (20-24 °C).

Electrochemical Methods. Electrochemical experiments were performed on a Gamry Series G300 potentiostat/galvanostat/ZRA (Gamry Instruments, Warminster, PA) using a 3.0 mm glassy carbon working electrode, a platinum wire auxiliary electrode, and a silver wire pseudo-reference electrode. Electrochemical experiments were performed at ambient temperature (20-24°C) in a nitrogen-filled glovebox. Sample concentrations were 1.0 mM in analyte in a THF solution containing 100 mM $[Bu_4N][PF_6]$ as the supporting electrolyte. All potentials are referenced to $[Cp_2Fe]^{+/0}$ using ferrocene or decamethylferrocene (−0.49 V vs $[Cp_2Fe]^{+/0}$) as an internal standard. Ferrocene and decamethylferrocene (Acros) were purified by sublimation under reduced pressure and tetrabutylammonium hexafluorophosphate (Acros) was recrystallized from ethanol three times and dried under vacuum.

Crystallographic Methods. X-ray diffraction data for all complexes were collected on single crystals mounted on a glass fiber using paratone oil. Data was acquired using a Bruker SMART APEX II diffractometer equipped with a CCD detector at 88 K using molydenum *Kα* radiation (λ = 0.71073 Å), which was wavelength selected with a single-crystal graphite monochromator. The SMART program package was used to determine unit-cell parameters and for data collection. The raw frame data were processed using SAINT and SADABS to yield the reflection data file. Subsequent calculations were carried out using the SHELXTL program suite. The structures were solved by direct methods and refined on *F*2 by full-matrix least-squares techniques. Analytical scattering factors for neutral atoms were used throughout the analyses. Hydrogen atoms were generated in calculated positions and

refined using a riding model. ORTEP diagrams were generated using ORTEP-3 for Windows.

Computational Methods. All calculations were performed employing the non-empirical tpss density functional theory using the quantum chemistry program package TURBOMOLE. For computational efficiency, initial geometry optimizations were performed using moderate split-valence plus polarization basis sets (def2-SVP).[63] Structures were refined using basis sets of triple zeta valence plus polarization (def2-TZVP) quality.[64] Crystal structures obtained from X-ray diffraction experiments were used as starting points for the geometry optimization; no molecular symmetry was imposed. Energies and minimum energy structures were evaluated self-consistently to tight convergence criteria (energy converged to 0.1 μHartree, maximum norm of the Cartesian gradient $\leq 10^{-4}$ a.u.). Linear-response time-dependent DFT was used to simulate electronic absorption spectra of the two series.

$Mo[SNS]_2$ (1). A green suspension of $MoCl_5$ (112 mg, 408 μmol, 1.00 equiv) in 10 mL of toluene was treated with a yellow solution of $[SNS]H_3$ (219 mg, 837 μmol, 2.05 equiv) in 16 mL of toluene. The resulting purple solution was heated to reflux for 8.5 h. The reaction mixture was concentrated down to 5 mL under reduced pressure and 10 mL of pentane was added to induce precipitation of the product. The solid was removed by filtration, washed with pentane (3 × 5 mL), and dried under reduced pressure to provide the product as a purple solid (250 mg, 65%). X-ray quality crystals were obtained by diffusion of diethyl ether into a saturated solution of **1** in toluene. ^{1}H NMR (400 MHz; C_6D_6) δ/ppm: 7.42 (*d*, *J* = 8.6 Hz, 4H, aryl–H), 7.06 (br *s*, 4H, aryl–H), 6.56 (*d*, *J* = 8.6 Hz, 4H, aryl–H), 1.99 (*s*, 12H, $–CH_3$). MS (ESI^+) *m/z*: calcd for $[C_{28}H_{24}N_2S_4Mo]$, 614.0; found 612.3 ($[M]^+$). UV-vis (THF) λ_{max}/nm (ε / M^{-1} cm^{-1}): 424 (7,410), 520 (10,600).

$Mo[SNS]_2Ni(dppe)$ (2). To a 100-mL Schlenk flask, potassium metal (26 mg, 0.65 mmol, 2.0 equiv.) and graphite (63 mg, 0.65 mmol, 2.0 equiv.) were heated to generate two equiv. of KC_8 as a bronze powder. The KC_8 was then suspended in 10 mL of dry THF and frozen in a liquid nitrogen cold well. Upon thawing, $Mo[SNS]_2$ (200 mg, 0.330 mmol, 1.0 equiv.) was added to stirred solution to form a dark brown mixture with a yellow hue around the rim. After 10 minutes, solid $(dppe)NiCl_2$ (173 mg,

0.330 mmol, 1.0 equiv.) was added to the mixture, which was stirred at room temperature for two hours. The solution was filtered through a Celite plug to remove graphite and KCl and yield a dark purple filtrate. The filtrate was concentrated to roughly 4 mL and a solid precipitated upon addition of 10 ml of pentane. The solid was collected by filtration filtered and washed with pentane (2 x 10 mL) and Et_2O (2 x 20 mL) to afford the product as a black powder (420 mg, 81% yield). X-ray quality crystals were obtained by diffusion of pentane into a THF solution of the complex at ambient temperature. Anal. Calcd. (Found) for $C_{54}H_{48}MoN_2NiP_2S_4$ (%): C, 60.62 (60.65); H, 4.52 (4.78); N, 2.62 (2.22). ^{1}H NMR (400 MHz; $CDCl_3$) δ/ppm: 6.36–7.5 (br, 32H, aryl–H), 2.62 (*d*, *J* = 11.6 Hz, 4H, – CH_2), 2.24 (br *s*, 6H, –CH_3), 2.06 (br *s*, 6H, –CH_3). ^{31}P{^{1}H} NMR (162 MHz, $CDCl_3$) δ/ppm: 43.1 (*s*). MS (ESI$^+$) *m/z*: calcd for [$C_{54}H_{48}MoN_2NiP_2S_4$], 1070.1; found 1070.1 ([M+H]$^+$). UV-vis (THF) λ_{max}/nm (ε / M^{-1} cm^{-1}): 488 (17,100), 724 (5,560).

Mo[SNS]$_2${Ni(dppe)}$_2$ (3). To a 100-mL Schlenk flask, potassium metal (12 mg, 0.32 mmol, 2.0 equiv.) and graphite (31 mg, 0.32 mmol, 2.0 equiv.) were heated to generate two equiv. of KC_8 as a bronze powder, which was subsequently suspended in 10 mL of dry THF before being frozen in a liquid nitrogen cold well. Upon thawing, **2** (170 mg, 0.160 mmol, 1.0 equiv.) was added to the stirred suspension causing an immediate color change to black. After 10 minutes, (dppe)$NiCl_2$ (84 mg, 0.16 mmol, 1.0 equiv.) was added and the mixture was stirred at room temperature for two hours. The mixture was filtered through a Celite plug to remove graphite and KCl to yield a green filtrate that was concentrated to roughly 4 mL. Precipitation was induced by the addition of 10 mL of pentane. The solid was collected by filtration, washed with pentane (2 x 10 mL) and Et_2O (2 x 20 mL), and dried to afford the product as a black powder (420 mg, 81%). X-ray quality crystals of the product were obtained by diffusion of pentane into a THF solution of the complex at ambient temperature. ^{1}H NMR (C_6D_6) *δ*/ppm: 7.35 (*m*, 8H, aryl–H), 7.09 (*m*, 16H, aryl–H), 7.04 (*d*, J = 7.04 Hz, 4H, aryl–H), 6.84 (*d*, J = 7.12 Hz, 4H, aryl–H), 6.77 (*d*, J = 8.24, 16H, aryl–H), 6.74 (*s*, 4H, aryl–H), 6.23 (*d*, *J* = 7.88 Hz, 4H, aryl–H), 2.57 (*m*, 4H, –CH_2), 2.33 (*m*, 4H, –CH_2), 1.85 (*s*, 12H, –CH_3). ^{31}P{^{1}H} NMR (162 MHz, C_6D_6) *δ*/ ppm: 36.8 (*s*). MS (ESI$^+$) *m/z*: calcd for [$C_{80}H_{72}MoN_2Ni_2P_4S_4$], 1526.1; found

1526.2 ([M]$^+$). UV-vis (THF) λ_{max}/nm (ε / M^{-1} cm^{-1}): 460 (30,100), 622 (10,600), 918 (4,600).

Table 2.4. Crystal data and structure refinement for $Mo[SNS]_2$ (**1**), $Mo[SNS]_2Ni(dppe)$ (**2**), and $Mo[SNS]_2\{Ni(dppe)\}_2$ (**3**).

Identity	$Mo[SNS]_2$ (**1**)	$Mo[SNS]_2Ni(dppe)$ (**2**)	$Mo[SNS]_2\{Ni(dppe)\}_2$ (**3**)
Empirical formula	$C_{28}H_{24}MoN_2S_4$	$C_{54}H_{48}MoN_2NiP_2S_4$	$C_{80}H_{72}MoN_2Ni_2P_4S_4$
Formula weight (g/mol)	612.67	1069.77	1526.87
Crystal system	Monoclinic	Monoclinic	Triclinic
Space group	$P2_{1/c}$	$P2_{1/c}$	P-1
T (K)	143(2)	133(2)	88(2)
a (Å)	12.0185(8)	19.4466(19)	14.8086(12)
b (Å)	19.4620(12)	15.6654(15)	16.5494(14)
c (Å)	10.8443(7)	16.2658(16)	16.7941(14)
α (º)	90	90	84.7003(13)
β (º)	91.4905(7)	106.8402(12)	75.1285(2)
ɣ (º)	90	90	82.7401(12)
V (Å3)	2535.7(3)	4742.7(8)	3938.3(6)
Z	4	4	2
Refl. collected	12278	53283	18460
Indep. refl.	12278	11296	18460
R1 ($I > 2\sigma$)[a]	0.0261	0.0391	0.0484
wR2 (all data)[b]	0.0656	0.0867	0.1188

[a]$R1 = \Sigma||F_o|-|F_c|| / \Sigma|F_o|$, [b]$wR2 = [\Sigma[w(F_o^2-F_c^2)^2] / \Sigma[w(F_o^2)^2]]^{1/2}$

2.6 References

(1) Thomas, C. M. *Comments Inorg. Chem.* **2011**, *32*, 14–38.

(2) Powers, T. M.; Betley, T. A. *J. Am. Chem. Soc.* **2013**, *135*, 12289–12296.

(3) Nippe, M.; Goodman, S. M.; Fry, C. G.; Berry, J. F. *J. Am. Chem. Soc.* **2011**, *133*, 2856–2859.

(4) Krogman, J. P.; Thomas, C. M. *Chem. Comm.* **2014**, *50*, 5115–5127.

(5) Heyduk, A. F.; Macintosh, A. M.; Nocera, D. G. *J. Am. Chem. Soc.* **1999**, *121*, 5023–5032.

(6) Lindahl, P. A. *J. Inorg. Biochem.* **2012**, *106*, 172–178.

(7) Cotton, F. A.; Daniels, L. M.; Murillo, C. A.; Pascual, I. *J. Am. Chem. Soc.* **1997**, *119*, 10223–10224.

(8) Clerac, R.; Cotton, F. A.; Dunbar, K. R.; Murillo, C. A.; Pascual, I.; Wang, X. *Inorg. Chem.* **1999**, *38*, 2655–2657.

(9) Clerac, R.; Cotton, F. A.; Daniels, L. M.; Dunbar, K. R.; Kirschbaum, K.; Murillo, C. A.; Pinkerton, A. A.; Schultz, A. J.; Wang, X. *J. Am. Chem. Soc.* **2000**, *122*, 6226–6236.

(10) Eisenhart, R. J.; Clouston, L. J.; Lu, C. C. *Acc. Chem. Res.* **2015**, *48*, 2885–2894.

(11) Gavrilova, A. L.; Bosnich, B. *Chem. Rev.* **2004**, *104*, 349–384.

(12) Ogo, S.; Kabe, R.; Uehara, K.; Kure, B.; Nishimura, T.; Menon, S. C.; Harada, R.; Fukuzumi, S.; Higuchi, Y.; Ohhara, T. *Science* **2007**, *316*, 585–587.

(13) Howard, K. E.; Rauchfuss, T. B.; Rheingold, A. L. *J. Am. Chem. Soc.* **1986**, *108*, 297–299.

(14) Denny, J. A.; Darensbourg, M. Y. *Chem. Rev.* **2015**, *115*, 5248–5273.

(15) Shaffer, D. W.; Szigethy, G.; Ziller, J. W.; Heyduk, A. F. *Inorg. Chem.* **2013**, *52*, 2110–2118.

(16) Herebian, D.; Bothe, E.; Bill, E.; Weyhermüller, T.; Wieghardt, K. *J. Am. Chem. Soc.* **2001**, *123*, 10012–10023.

(17) Ghosh, P.; Begum, A.; Herebian, D.; Bothe, E.; Hildenbrand, K.; Weyhermüller, T.; Wieghardt, K. *Angew. Chem. Int. Ed.* **2003**, *42*, 563–567.

(18) Sproules, S.; Banerjee, P.; Weyhermüller, T.; Yan, Y.; Donahue, J. P.; Wieghardt, K. *Inorg. Chem.* **2011**, *50*, 7106–7122.

(19) Sproules, S.; Wieghardt, K. *Coord. Chem. Rev.* **2011**, *255*, 837–860.

(20) Roy, N.; Sproules, S.; Weyhermüller, T.; Wieghardt, K. *Inorg. Chem.* **2009**, *48*, 3783–3791.

(21) Rosenkoetter, K. E.; Ziller, J. W.; Heyduk, A. F. *Inorg. Chem.* **2016**, *55*, 6794–6798.

(22) Cordero, B.; Gómez, V.; Platero-Prats, A. E.; Revés, M.; Echeverría, J.; Cremades, E.; Barragán, F.; Alvarez, S. *Dalton Tran.* **2008**, 2832–2838.

(23) Schilter, D.; Fuller, A. L.; Gray, D. L. *Eur. J. Inorg. Chem.* **2015**, 4638–4642.

(24) Adams, H.; Gardner, H. C.; McRoy, R. A.; Morris, M. J.; Motley, J. C.; Torker, S. *Inorg. Chem.* **2006**, *45*, 10967–10975.

(25) Prout, K.; Critchley, S.; Rees, G. V. *Acta Cryst., Sect. B* **1974**, *30*, 2305–2311.

(26) Shekar, S.; Brown, S. N. *Dalton Trans.* **2014**, *43*, 3601–3611.

(27) Marshall-Roth, T.; Brown, S. N. *Dalton Trans.* **2015**, *44*, 677–685.

(28) Zhu, W.; Marr, A. C.; Wang, Q.; Neese, F.; Spencer, D. J. E.; Blake, A. J.; Cooke, P. A.; Wilson, C.; Schröder, M. *Proc. Natl. Acad. Sci. U.S.A.* **2005**, *102*, 18280–18285.

(29) Carroll, M. E.; Barton, B. E.; Gray, D. L.; Mack, A. E.; Rauchfuss, T. B. *Inorg. Chem.* **2011**, *50*, 9554–9563.

(30) Chambers, G. M.; Mitra, J.; Rauchfuss, T. B.; Stein, M. *Inorg. Chem.* **2014**, *53*, 4243–4249.

(31) Jones, S. C.; Coropceanu, V.; Barlow, S.; Kinnibrugh, T.; Timofeeva, T.; Brédas, J.-L.; Marder, S. R. *J. Am. Chem. Soc.* **2004**, *126*, 11782–11783.

(32) Busby, R.; Hursthouse, M. B.; Jarrett, P. S.; Lehmann, C. W.; Abdul Malik, K. M.; Phillips, C. *J. Chem. Soc., Dalton Trans.* **1993**, 3767–3770.

(33) Richardson, D. E.; Taube, H. *Coord. Chem. Rev.* **1984**, *60*, 107–129.

(34) Kubiak, C. P. *Inorg. Chem.* **2013**, *52*, 5663–5676.

(35) Robin, M. B.; Day, P. *Adv. Inorg. Chem. Radiochem.* **1968**, *60*, 247–422.

(36) D'Alessandro, D. M.; Keene, F. R. *Dalton Trans.* **2004**, 3950–3954.

(37) Winter, R. F. *Organometallics* **2014**, *33*, 4517–4536.

(38) Stiefel, E. I.; Eisenberg, R.; Rosenberg, R. C.; Gray, H. B. *J. Am. Chem. Soc.* **1966**, *88*, 2956–2966.

(39) Rosenkoetter, K. E.; Ziller, J. W.; Heyduk, A. F. *Dalton Trans.* **2017**, *46*, 5503–5507.

(40) Karunananda, M. K.; Parmelee, S. R.; Waldhart, G. W.; Mankad, N. P. *Organometallics* **2015**, *34*, 3857–3864.

(41) Mankad, N. P. *Chem. Comm.* **2018**, *54*, 1291–1302.

(42) Esswein, A. J.; Dempsey, J. L.; Nocera, D. G. *Inorg. Chem.* **2007**, *46*, 2362–2364.

(43) Remenyi, C.; Kaupp, M. *J. Am. Chem. Soc.* **2005**, *127*, 11399–11413.

(44) Kaim, W. *Inorg. Chem.* **2011**, *50*, 9752–9765.

(45) Bauer, J.; Braunschweig, H.; Dewhurst, R. D. *Chem. Rev.* **2012**, *112*, 4329–4346.
(46) Schilter, D.; Nilges, M. J.; Chakrabarti, M.; Lindahl, P. A.; Rauchfuss, T. B.; Stein, M. *Inorg. Chem.* **2012**, *51*, 2338–2348.
(47) Huynh, M. T.; Schilter, D.; Hammes-Schiffer, S.; Rauchfuss, T. B. *J. Am. Chem. Soc.* **2014**, *136*, 12385–12395.
(48) Kang, S. K.; Albright, T. A.; Wright, T. C.; Jones, R. A. *Organometallics* **1985**, *4*, 666–675.
(49) Pauling, L. *The Nature of the Chemical Bond.*; Cornell University Press: Ithaca, NY; **1960**.
(50) Berry, J. F. *Dalton Trans.* **2012**, *41*, 700–713.
(51) Green, M. L. H.; Parkin, G. *Dalton Trans.* **2016**, *45*, 18784–18795
(52) D'Alessandro, D. M.; Keene, F. R. *Chem. Soc. Rev.* **2006**, *35*, 424–440.
(53) Clouston, L. J.; Siedschlag, R. B.; Rudd, P. A.; Planas, N.; Hu, S.; Miller, A. D.; Gagliardi, L.; Lu, C. C. *J. Am. Chem. Soc.* **2013**, *135*, 13142–13148.
(54) Clouston, L. J.; Bernales, V.; Cammarota, R. C.; Carlson, R. K.; Bill, E.; Gagliardi, L.; Lu, C. C. *Inorg. Chem.* **2015**, *54*, 11669–11679.
(55) Creutz, C.; Taube, H. *J. Am. Chem. Soc.* **1969**, *91*, 3988–3989.
(56) Toma, H. E.; Araki, K.; Alexiou, A. D. P.; Nikolaou, S.; Dovidauskas, S. *Coord. Chem. Rev.* **2001**, *219*, 187–234.
(57) Yamaguchi, T.; Imai, N.; Ito, T.; Kubiak, C. P. *Bull. Chem. Soc. Jpn.* **2000**, *73*, 1205–1212.
(58) Demadis, K. D.; Hartshorn, C. M.; Meyer, T. J. *Chem. Rev.* **2001**, *101*, 2655–2686.
(59) Brunschwig, B. S.; Creutz, C.; Sutin, N. *Chem. Soc. Rev.* **2002**, *31*, 168–184.
(60) Hush, N. S. *Prog. Inorg. Chem.* **1967**, 391–444.
(61) Hush, N. S. *Coord. Chem. Rev.* **1985**, *64*, 135–157.
(62) Standley, E. A.; Smith, S. J.; Müller, P.; Jamison, T. F. *Organometallics* **2014**, *33*, 2012–2018.
(63) Schäfer, A.; Huber, C.; Ahlrichs, R. *J. Chem. Phys.* **1992**, *97*, 2571–2577.
(64) Schäfer, A.; Huber, C.; Ahlrichs, R. *J. Chem. Phys.* **1994**, *100*, 5829–5835.

Chapter 3

Ancillary Ligand Effects on

Heterobimetallic Mo[SNS]$_2$CuL$_2$ Complexes

3.1 Introduction

Metal-metal bonds play a key role in multimetallic complexes, from electron storage to redox potential tuning. Understanding the factors that govern the formation and cleavage of metal-metal bonds is crucial toward harnessing their multi-electron capabilities and understanding their electronic structure. For example, the transience of an Fe–Ni interaction has been implicated during the reversible reduction of protons to hydrogen gas in the [FeNi] hydrogenase.[1] Similarly, an unusual molybdenum-copper system is present in the active site of carbon monoxide dehydrogenase (CODH) from the *Oligotropha carboxidovorans* and is known to perform the oxidation of CO to CO_2 (Scheme 3.1).[2] The structure of the enzyme active site suggests a weak interaction between the high-valent molybdenum(VI) center and the low-valent copper center[3,4] but the majority of synthetic model complexes for this enzyme have significantly shorter molybdenum-copper bond distances.[5,6]

Synthetic bimetallic systems containing copper typically involve weak metal-metal interactions.[7,8] Two main factors are often suggested to explain weak metal-metal bonding involving copper: 1) the metal ions are typically farther apart on the periodic table, and therefore the atomic d orbital energies are divergent 2) copper typically includes more d electrons, leading to possible population of metal-metal antibonding orbitals.[9,10] Energetically, as the metal orbitals start to move apart from one another, localization of d electrons and less mixing/covalency is observed, as has been seen in other heterobimetallic systems containing copper. In the literature, the main metal-metal interactions supported by copper(I) complexes are typically closed-shell d^{10}-d^{10} van der Waals interactions, labeled as cuprophilic interactions.[11-13] These d^{10}–d^{10} metal-metal bonding motifs are established for the second- and third-row transition metal derivatives (i.e. aurophilicity).[14-16]

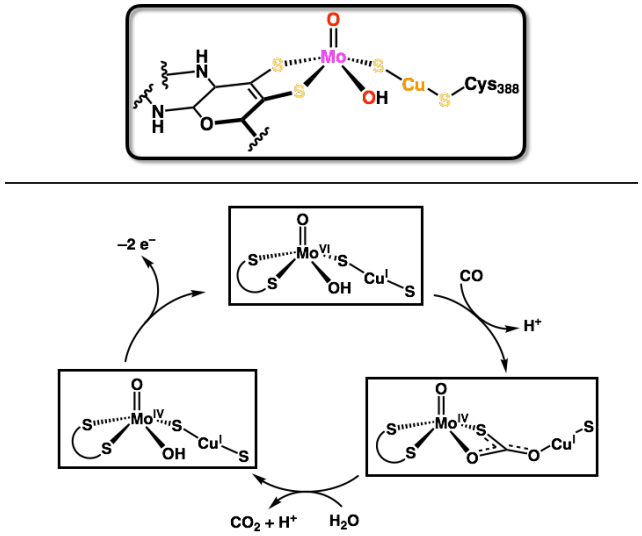

Scheme 3.1. Active site of [MoCu] carbon monoxide dehydrogenase (CODH) (top); proposed catalytic cycle for [MoCu] CODH for the oxidation of CO to CO_2.

Previously in our lab, we reported heterobimetallic complexes consisting of a M[SNS]$_2$ metalloligand (M = Mo, W) coordinated to Group 10 metal centers nickel, palladium, and platinum.[17,18] In the case of the tungsten–nickel derivatives, the intermetallic distances were the shortest ever reported, and well within the sum of the covalent radii, indicative of a formal metal-metal bond. In addition to the structural data, the presence of a metal-metal bond was supported by spectroscopic data. Electronically, the M[SNS]$_2$ metalloligand gave rise to several reversible redox processes, and as such the M[SNS]$_2$Ni(dppe) complexes were electrochemically stable over five different oxidation states, with the tungsten derivative proving to be a catalyst for the electrochemical reduction of protons to hydrogen.[19] Herein we report the synthesis and characterization of a heterobimetallic Mo[SNS]$_2$CuL$_2$ complexes (M = Mo, W; L$_2$ = bis(diphenylphoshino)ethane (dppe), 4,4'-di-tert-butyl-2,2'-bipyridine (bpyt-Bu$_2$). The solid-state structures of these complexes show that the ancillary L$_2$ ligand has a surprising impact on the structure of the complex by modulating the metal-metal interaction, without perturbing the electronics of the system.

3.2 Results

3.2.1 Synthesis of $Mo[SNS]_2Cu(dppe)$, $Mo[SNS]_2Cu(bpytBu_2)$, and $[K][Mo[SNS]_2]$.

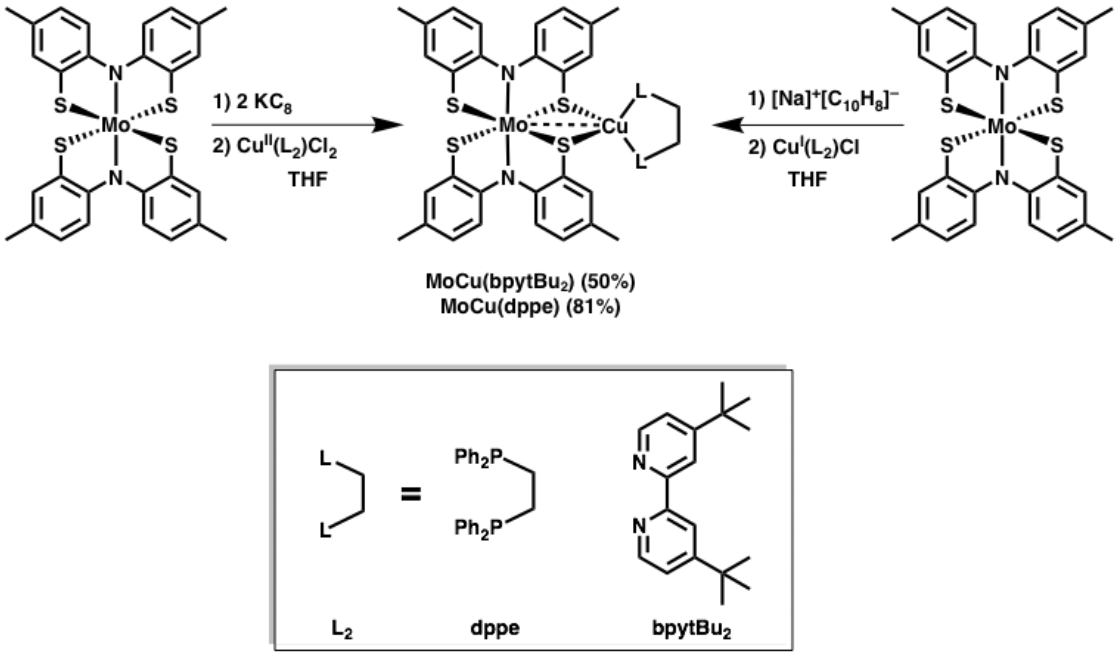

Scheme 3.2. Synthesis of complexes MoCu(dppe/$bpytBu_2$).

Heterobimetallic $Mo[SNS]_2CuL_2$ (L_2 = bis(diphenylphoshino)ethane (dppe), 4,4'-di-tert-butyl-2,2'-bipyridine ($bpytBu_2$) complexes were prepared by metathesis using both copper(I) and copper(II) salts. As previously reported, the $Mo[SNS]_2$ metalloligand exhibits two reversible reductions in the –0.50 V to –1.34 V window (vs $Cp_2Fe^{+/0}$). Thus, in a typical reaction, one equivalent of $Mo[SNS]_2$ was treated initially with two equivalents of freshly-prepared KC_8 in cold THF followed by the addition of one equivalent of $CuCl_2$(dppe). The product, $Mo[SNS]_2Cu(dppe)$ was isolated as a dark brown powder in 81% yield. When the copper source was $CuCl_2(bpytBu_2)$, the yield dropped to 50% for $Mo[SNS]_2Cu(bpytBu_2)$. (Scheme 3.2). Alternatively, the same products are accessible in similar yields using copper(I) salts, $Cu(L_2)Cl$, and one equivalent of sodium naphthalide as the reductant. The formation of the desired heterobimetallic complexes was indicated by ESI^+ mass spectrometry, which showed the correct parent ion peak and isotopic pattern for each complex (1074.69 m/z for MoCu(dppe) and 944.67 m/z for MoCu($bpytBu_2$)).

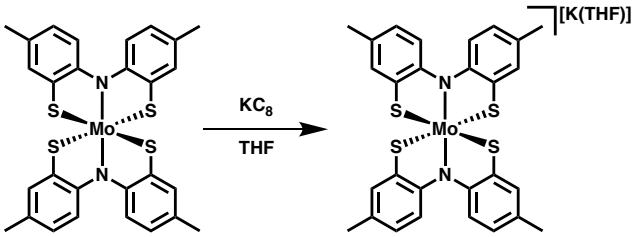

Scheme 3.3. Synthesis of $Mo[SNS]_2^-$ anion.

As a point of comparison, the $Mo[SNS]_2$ metalloligand anion was synthesized by addition of one equivalent of KC_8 reductant (Scheme 3.3). The resulting heterobimetallic Mo–K complex, incorporating a formally redox-inactive alkali metal, was isolated in quantitative yield and observed in ESI^- (negative mode) spectrometry, with the parent ion peak observed at 614.9 m/z.

3.2.2 Structural Characterization of Mo–Cu & Mo–K Complexes

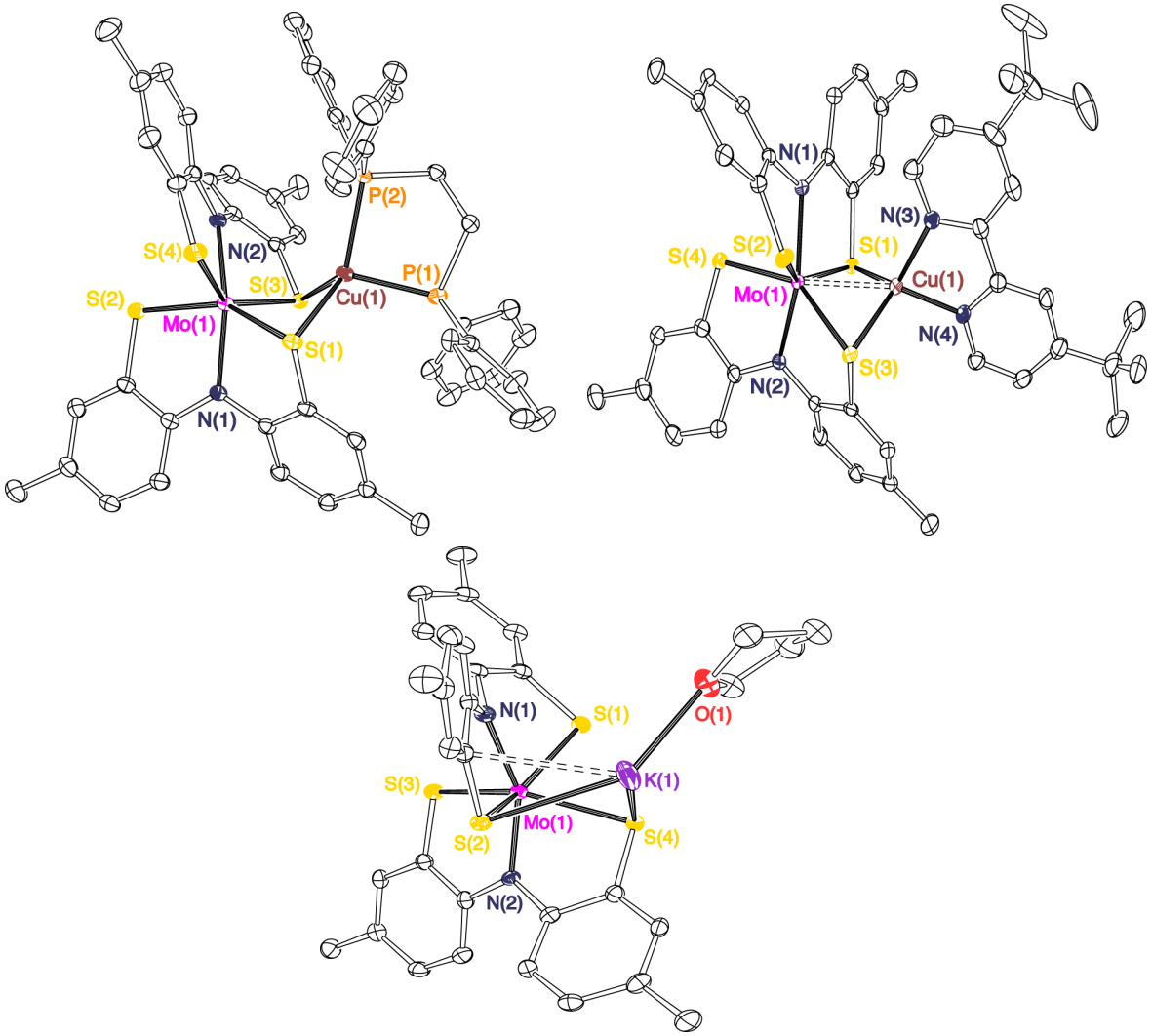

Figure 3.1. ORTEP diagrams of MoCu(dppe) (top left), $MoCu(bpytBu_2)$ (top right), and $[K(THF)][Mo[SNS]_2]$ (bottom). Ellipsoids are shown at 50% probability. Hydrogen atoms were omitted for clarity.

The heterobimetallic structures of the $Mo[SNS]_2CuL_2$ complexes, as well as the $Mo[SNS]_2^-$ anion, were determined by single-crystal X-ray diffraction experiments (Figure 3.1). Crystals of $Mo[SNS]_2Cu(bpytBu_2)$, $Mo[SNS]_2Cu(dppe)$, and $[K(THF)][Mo[SNS]_2]$ were grown by diffusion of a THF solution of the complexes into pentane, heptane, and Et_2O, respectively. The phosphine complex, $Mo[SNS]_2Cu(dppe)$, crystallized in the space group, $P2_1/c$, while the bipyridine complex, $Mo[SNS]_2Cu(bpytBu_2)$ crystallized in the space group, $I4_1/a$. $[K(THF)][Mo[SNS]_2]$ crystallized as a polymeric structure in the $Pna2_1$ space group. All three heterobimetallic complexes demonstrated pseudo-octahedral coordination geometries in the solid-state, with Bailar twist values (θ) ranging between 2°-28° ($\theta_{trigonal\ prism}$= 0°; $\theta_{octahedron}$= 60°).[20,21] To quantify the Bailar twist values, two trigonal faces need to be defined. These trigonal faces are composed of a nitrogen and sulfur atom of one [SNS] ligand, along with a sulfur atom from the second [SNS] ligand. For $Mo[SNS]_2Cu(dppe)$ and $[K(THF)][Mo[SNS]_2]$, the first trigonal face is defined by S(1), N(1), and S(3); the second trigonal face is composed of S(2), N(2), and S(4). In the case of $Mo[SNS]_2Cu(bpytBu_2)$, the two trigonal faces consist of S(1), N(2), and S(3), and S(2), N(1), S(4). The most notable differences among the $Mo[SNS]_2CuL_2$ structures are the M···Cu distances. In the phosphine complex, the Mo···Cu distance is long, at 3.01 Å. For the bipyridine complex, the Mo···Cu distance was much shorter, at 2.75 Å. To effectively compare the different metal-metal interactions, the bond distances were normalized to the sum of the covalent radii of the two respective metal centers (covalent ratio, *r*).[22] For $MoCu(bpytBu_2)$, the intermetallic distance is within the sum of the covalent radii of the two transition metal centers, affording a covalent ratio of $r = 0.96$, indicative of a metal-metal bond. These values are comparable to the heterobimetallic dithiomolybdate–copper complex ($[NEt_4][O_2MoS_2Cu(dppe)]$), which has a molybdenum–copper metal-metal bond length of 2.73 Å and a covalent ratio of 0.95.[23] In the diphosphine complex, the covalent ratio is larger, at r = 1.05, which is outside of the ratio expected for a metal-metal bond. The Cu–S bond distances correlate with the differences in metal-metal distance. Thus, for the $Mo[SNS]_2Cu(dppe)$ complex, the Cu–S distances are longer, falling in the 2.30-2.34 Å range; whereas, for the $Mo[SNS]_2Cu(bpytBu_2)$

complexes, the Cu–S distances are shorter, falling in the 2.18-2.27 Å range. These differences in the metal-metal and Cu–S distances result in "clothespin"-like distortions in the S–Cu–S bond angle, which is 91-94° in the diphosphine complexes and 103° in the bipyridine derivatives.[24,25]

Outside of the differences associated with the metal-metal interaction, the structures of the two $Mo[SNS]_2CuL_2$ complexes are remarkably similar. In both complexes, the copper centers are best described as distorted tetrahedral with τ_4 values of 0.78 (MoCu(dppe)) and 0.85 ($MoCu(bpytBu_2)$) (Table 3.3). To compare the oxidation state of the $Mo[SNS]_2$ metalloligand, the metrical data of $[K(THF)][Mo[SNS]_2]$ was investigated in conjunction with the Mo–Cu complexes. The molybdenum center of the $Mo[SNS]_2$ metalloligands displayed pseudo-octahedral geometry in all cases. The Mo–S bond distances all fall in the narrow range of 2.35-2.45 Å (Table 3.1). The [SNS] bond metrics are in agreement with a fully-reduced, trianionic $[SNS]^{3-}$ ligand set, with all three complexes demonstrating $C–S_{avg}$, $C–N_{avg}$, and $(\Delta C–C)_{avg}$ intraligand bond metrics of 1.75 Å, 1.41 Å, and 0.024-0.025 Å, respectively (Table 3.2).[26-29] The average Cu–P bond length of 2.29 Å in the diphosphine derivative is consistent with other Cu(I)–phosphine complexes incorporating dppe, which also have similar bite angles of 90-91°.[30,31] The average copper-nitrogen bond distances of 2.02 Å observed in the bipyridine derivatives is longer than is typically observed for Cu(II) complexes incorporating the $bpytBu_2$ ligand, but with a similar bite angle at 81°.[32] Additionally, the C1–C1' bond length of the bipyridine-type ligand is 1.48 Å, indicative of a $C(sp^2)–C(sp^2)$ bond length, characteristic of a neutral bipyridine ligand.[33-36]

Table 3.1. Average intraligand bond distances and angle for $Mo[SNS]_2Cu(dppe)$, $Mo[SNS]_2Cu(bpytBu_2)$, and $[K(THF)][Mo[SNS]_2]$.

Distances / Å	$Mo[SNS]_2Cu(dppe)$	$Mo[SNS]_2Cu(bpytBu_2)$	$[K(THF)][Mo[SNS]_2]$
Mo(1)–M(1)	3.0097(5)	2.750(1)	3.9745(8), 4.3490(8)
Mo(1)–S(1)	2.4336(6)	2.398(1)	2.4544(8)
Mo(1)–S(2)	2.3526(5)	2.3995(7)	2.3704(9)
Mo(1)–S(3)	2.4206(5)	2.446(1)	2.3549(9)
Mo(1)–S(4)	2.3774(5)	2.359(1)	2.4181(8)
Mo(1)–N(1)	2.078(1)	2.098(2)	2.062(2)
Mo(1)–N(2)	2.076(1)	2.071(2)	2.065(2)
M(1)–S(1)	2.3417(6)	2.2765(8)	3.152(1)
M(1)–S(3)	2.3285(5)	2.267(1)	3.293(1)
Cu(1)–L(1) (L = N,P)	2.2937(5)	2.031(2)	–
Cu(1)–L(2) (L = N,P)	2.2821(6)	2.017(2)	–
Angles / °			
S(1)–Mo(1)–S(3)	86.66(2)	94.86(3)	90.80(3)
S(2)–Mo(1)–S(4)	92.05(2)	96.10(3)	94.06(3)
N(1)–Mo(1)–N(2)	150.44(5)	152.60(8)	153.5(1)
S(1)–M(1)–S(3)	91.00(2)	103.47(3)	64.16(2)
L(1)–M(1)–L(2)	91.18(2)	81.31(8)	–

Table 3.2. Intraligand bond metrics for $Mo[SNS]_2Cu(dppe)$, $Mo[SNS]_2Cu(bpytBu_2)$, and $[K(THF)][Mo[SNS]_2]$.

	$Mo[SNS]_2Cu(dppe)$	$Mo[SNS]_2Cu(bpytBu_2)$	$[K(THF)][Mo[SNS]_2]$
S–C$_{avg}$	1.75	1.75	1.75
N–C$_{avg}$	1.41	1.41	1.41
(ΔC–C)$_{avg}$	0.024	0.024	0.025

Table 3.3. Bailar twist (θ) values and τ_4 Geometry index values for $Mo[SNS]_2Cu(dppe)$, $Mo[SNS]_2Cu(bpytBu_2)$, and $[K(THF)][Mo[SNS]_2]$.

	$Mo[SNS]_2Cu(dppe)$	$Mo[SNS]_2Cu(bpytBu_2)$	$[K(THF)][Mo[SNS]_2]$
$\theta_{S,S}$	2.5	2.2	5.3
$\theta_{N,S}$	23.4	21.5	28.5
$\theta_{N,S}$	15.4	27.0	22.0
τ_4 Cu(1)	0.78	0.85	–

3.2.3 Spectroscopic Characterization of Mo–Cu & Mo–K Complexes

In solution, both $Mo[SNS]_2CuL_2$ complexes behave as S=1/2 species and show little dependence on the identity of the L_2 ligand, as well as the identity of the secondary metal center. The X-band EPR spectrum for $Mo[SNS]_2CuL_2$ in THF at 298 K is shown in Figure 3.2 (left column). The isotropic S=1/2 spectrum displays a six-line pattern diagnostic of a single unpaired electron with hyperfine coupling to an I=5/2 molybdenum nucleus (^{95,97}Mo; 25.47% natural abundance). The spectra were readily modeled giving g = 2.00/2.01 and A = 92/97 for the bipyridine and phosphine analogues, respectively (Table 3.4). In both spectra, the hyperfine coupling broadens into the baseline and disappears at low temperature (right column). The EPR spectra at 77 K were also modeled as isotropic signals with g = 1.99-2.01 and A = 110-112 MHz. No hyperfine coupling to an I=3/2 copper is observed in any of the spectra (^{63}Cu; 69.17% natural abundance). The heterobimetallic Mo–Cu complexes also demonstrate remarkably analogous spectra to the corresponding Mo–K system incorporating the redox-inactive metal. The X-band EPR spectrum for $[K][Mo[SNS]_2]$ in THF at 298 K can be modelled as an isotropic S=1/2 system with values, g = 2.00, A = 88 MHz. At 77 K, similar to the Mo–Cu systems, the molybdenum hyperfine broadens and disappears into the baseline. The g value at 77 K remains at 2.00, while the A value slightly increases, from 88 MHz at 298 K, to 107 MHz at 77 K.

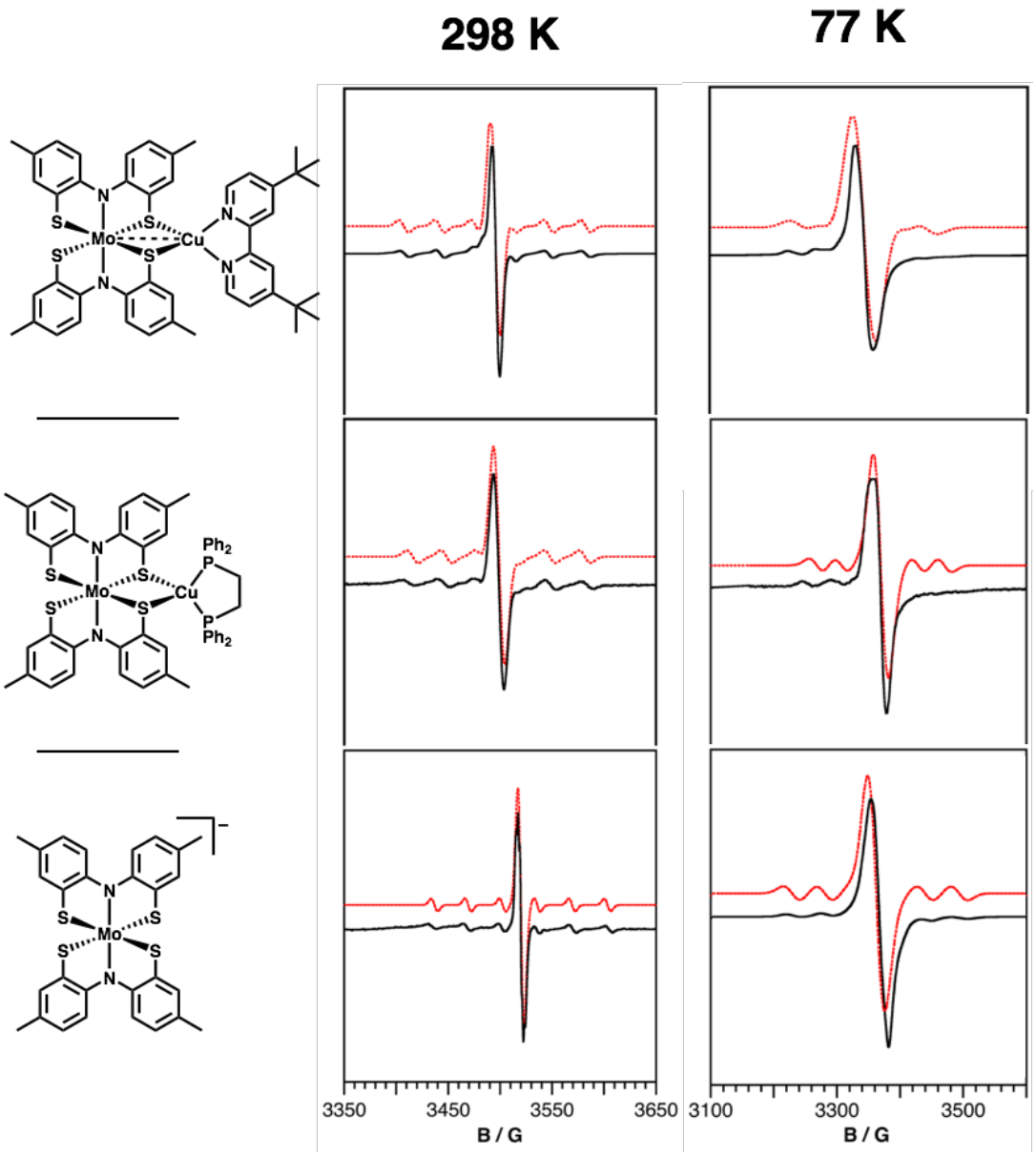

Figure 3.2. X-band EPR spectra, at 298 K (left column) and 77 K (right column) in THF, of $Mo[SNS]_2Cu(bpytBu_2)$ (top row), $Mo[SNS]_2Cu(dppe)$ (middle row), $[K(THF)][Mo[SNS]_2]$ (bottom row).

Table 3.4. EPR parameters for $Mo[SNS]_2Cu(bpytBu_2)$, $Mo[SNS]_2Cu(dppe)$, and $[K][Mo[SNS]_2]$ in THF solvent at 298 K and 77 K.

	g	A (MHz)			g	A (MHz)
$Mo[SNS]_2Cu(bpytBu_2)$ (298 K)	2.00	97		$Mo[SNS]_2Cu(bpytBu_2)$ (77 K)	2.00	110
$Mo[SNS]_2Cu(dppe)$ (298 K)	2.00	92		$Mo[SNS]_2Cu(dppe)$ (77 K)	1.99	112
$[K][Mo[SNS]_2]$ (298 K)	1.99	88		$[K][Mo[SNS]_2]$ (77 K)	2.00	107

Consistent with the EPR spectroscopic data, the electronic absorption spectra of $Mo[SNS]_2CuL_2$ complexes show a high degree of similarity with little dependence on the ancillary ligand on copper. Figure 3.3 shows the UV-vis spectra of the molybdenum bimetallic systems. Electronic absorption spectra of these complexes in THF demonstrates a single main charge-transfer transition in the UV-visible portion of the spectrum, at λ_{max}=490 nm, with a shoulder occurring at lower energy, ~ 670 nm. The spectra retain very similar features with slightly different band structure upon variation of the ancillary ligand from dppe to $bpytBu_2$. To demonstrate the minimal interaction between metal centers, and the minimal contribution of the copper(L_2) synthon to the observed transitions, spectroscopic measurements were performed on the monoanionic $[Mo[SNS]_2]^-$ complex with the redox-inactive potassium countercation ($[K][Mo[SNS]_2]$). The $Mo[SNS]_2^-$ anion exhibits one main charge transfer transition at λ_{max}=477 nm with a shoulder at lower energy, and all transitions slightly blue shifted in comparison to the Mo–Cu complexes.

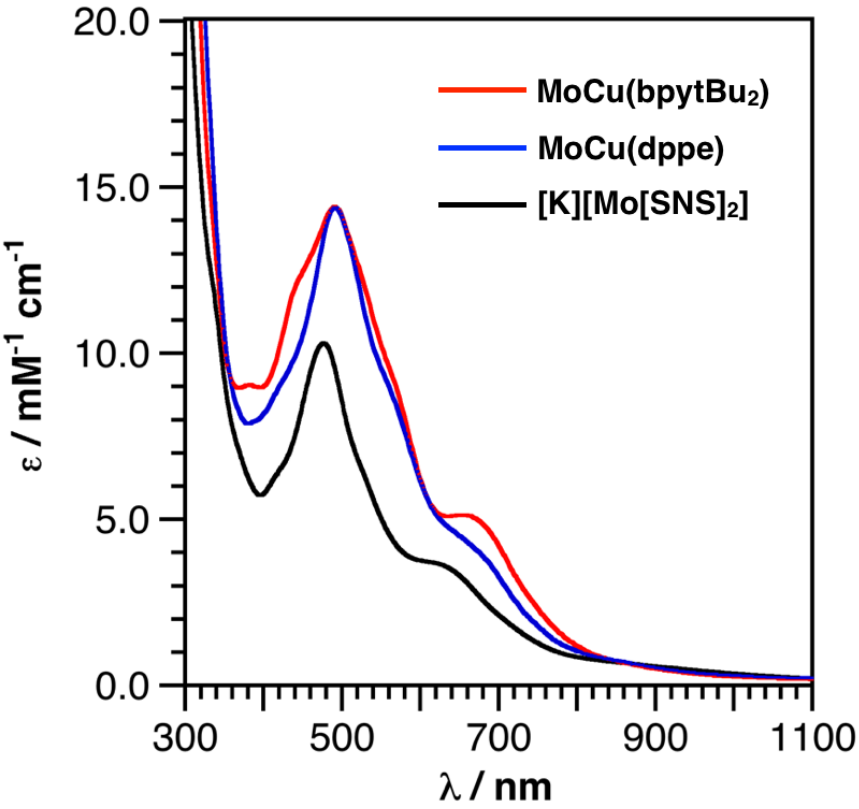

Figure 3.3. Electronic absorption spectra of $Mo[SNS]_2Cu(dppe)$ (blue), $Mo[SNS]_2Cu(bpytBu_2)$ (red), and $[K][Mo[SNS]_2]$ (black).

3.2.4 Computational Analysis of Mo–Cu & Mo–K Complexes

To reinforce the electronic structure depiction dictated by structural and spectroscopic characterization, gas-phase DFT calculations were performed on $Mo[SNS]_2Cu(dppe)$, $Mo[SNS]_2Cu(bpytBu_2)$, and $[K][Mo[SNS]_2]$. The calculations were performed as unrestricted Hartree-Fock (UHF) calculations, utilizing the TPSS functional, at the TZVP level of theory. The calculated metrical data was in good agreement with the solid-state experimental data; $Mo[SNS]_2Cu(bpytBu_2)$ demonstrated a short calculated molybdenum-copper bond distance of 2.796 Å, and $Mo[SNS]_2Cu(dppe)$ exhibited a longer Mo–Cu bond length of 3.035 Å. The potassium countercation was removed from the geometry optimization of $[Mo[SNS]_2]^{-1}$. Spin density plots of the Mo–Cu and Mo–K complexes yielded a single unpaired electron localized in a dz^2 orbital on the Mo transition metal center (75%-89% molybdenum contribution), with minimal contribution from the secondary metal (Figure 3.4). The frontier molecular orbitals for the three species also illustrate the prevalence of the $Mo[SNS]_2$ metalloligand to the overall electronic structure of these heterobimetallic

systems. Mulliken population analyses (MPA) were conducted on the three complexes, with the singly-occupied molecular orbital (SOMO) localized on the molybdenum center. The singly-unoccupied molecular orbital (SUMO), as well as the SUMO+1/SUMO+2, were also dominated by the molybdenum center in the case of Mo[SNS]$_2$Cu(dppe) and [K][Mo[SNS]$_2$]. The SUMO+1 and SUMO+2 were calculated to be comprised of a π* orbital on the bipyridine unit for Mo[SNS]$_2$Cu(bpytBu$_2$).

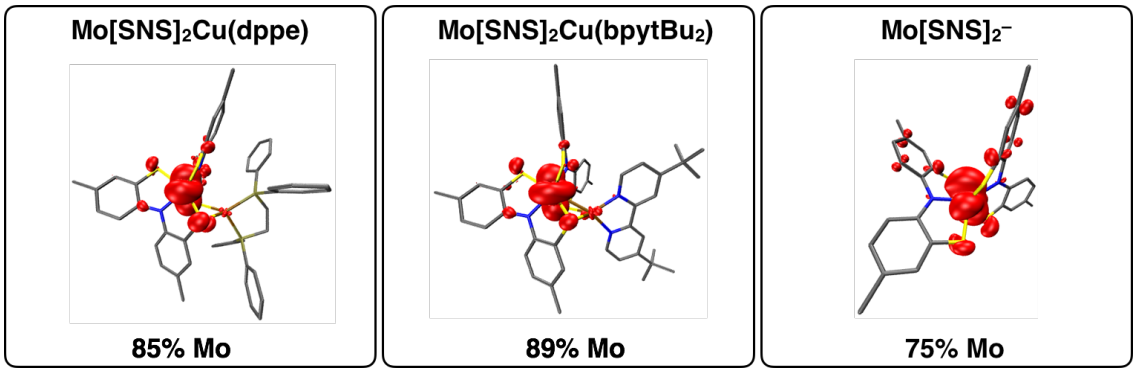

Figure 3.4. Spin density plots for Mo[SNS]$_2$Cu(dppe) (left) Mo[SNS]$_2$Cu(bpytBu$_2$) (middle), and [K][Mo[SNS]$_2$] (right) with the contribution of Mo in bold (isovalue = 0.00186).

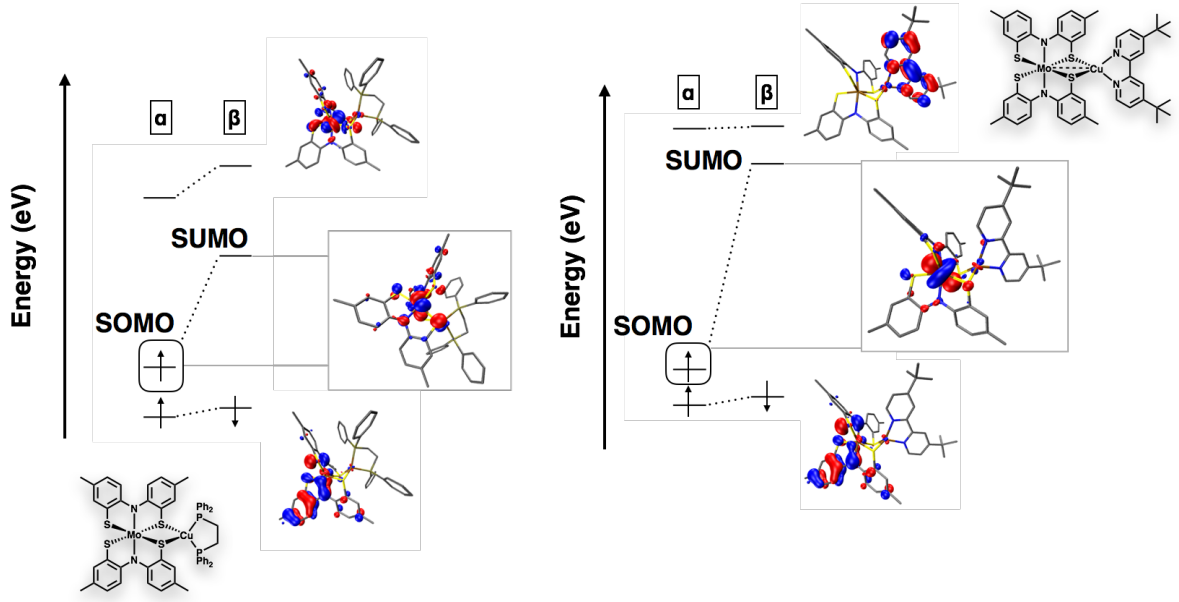

Figure 3.5. Frontier molecular orbital picture of Mo[SNS]$_2$Cu(dppe) (left) and Mo[SNS]$_2$Cu(bpytBu$_2$) (right).

The spectroscopic features of the heterobimetallic systems were also analyzed through time-dependent density functional theory (TD-DFT) calculations. Mo[SNS]$_2$Cu(dppe) demonstrated one main calculated transition with a large oscillator strength value. This transition, from the SOMO–1 to the SUMO+4, was calculated to occur from a molecular orbital of significant [SNS] ligand character

(88%) to a molecular orbital with molybdenum metal character (40%) (Figure 3.6). The SUMO+4 is high in energy, according to DFT calculations, to the point that mixing with a π* orbital on the phenyl ring of the bidentate phosphine ligand is observed, lowering the contribution of Mo. While the $Mo[SNS]_2^-$ anion displayed similar calculated spectroscopic behavior to the phosphine derivative, $Mo[SNS]_2Cu(bpytBu_2)$ demonstrated transitions to the bipyridine ligand, calculated to be lower in energy.

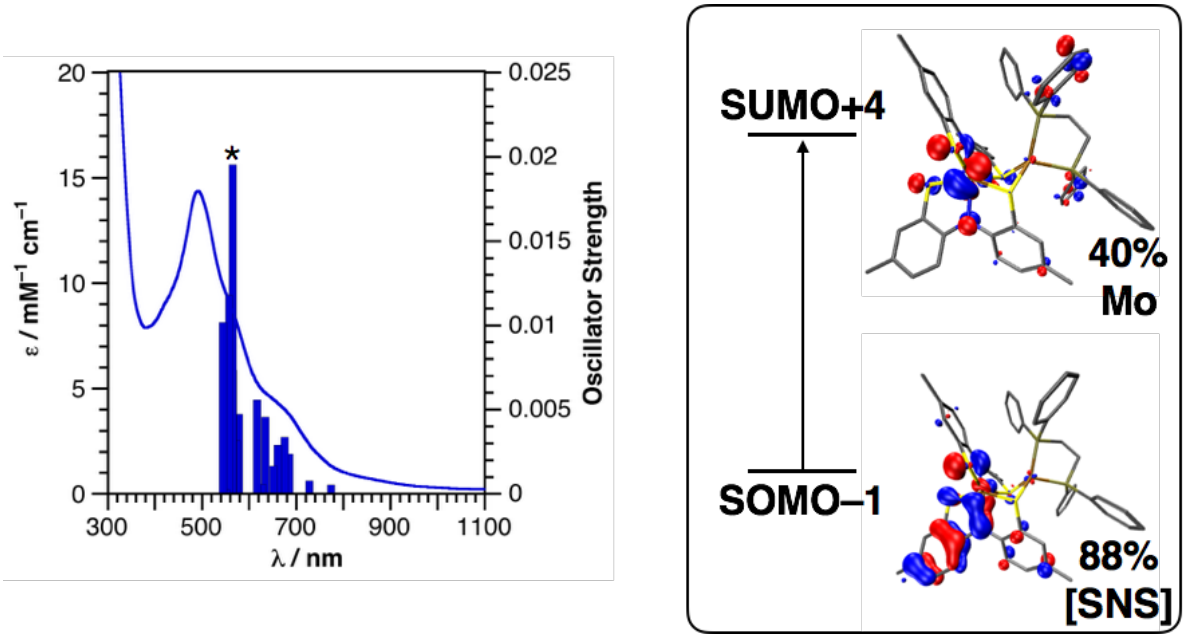

Figure 3.6. Time-dependent density functional theory (TD-DFT) calculations demonstrating the main electronic transition (denoted by *) in $Mo[SNS]_2Cu(dppe)$.

3.3 Discussion

The library of bimetallic systems that the $Mo[SNS]_2$ metalloligand can support has been expanded, with incorporation of the Group XI transition metal center, copper. A point of interest is the metal-metal bond length (and therefore, electronic interaction between metals) as a function of the ancillary ligand. To demonstrate this, $[K][Mo[SNS]_2]$ was utilized as a frame of reference, in which the redox inactivity of the alkali metal, K, and long metal-metal bond length (3.97 Å-4.34 Å, r = 1.11-1.22) confirms zero electronic interaction between the Group VI and Group I metals. The solid-state structures were determined by X-ray crystallography and formal oxidation assignment as Mo(V)–Cu(I) system for all of the complexes is supported by the structural parameters. The similar

geometries and bond distances of the $Mo[SNS]_2$ metalloligand in the copper-containing systems, to the redox-inactive potassium derivative, reinforces the oxidation state of the metalloligand as $[Mo^{V}[SNS^{3-}]_2]^{-}$ in all three cases. The average Mo–S bond distance in all three heterobimetallic systems is 2.40 Å. Additionally, the average C–S and C–N intraligand bond distances for all three systems are 1.75 Å and 1.41 Å, respectively. It has been shown previously that the oxidation state of the ligand leads to minor, but precise, fluctuations in the bond lengths of the tridentate ligand backbone, a "reporter" for ligand oxidation state.[37] While the bond parameters are consistent with the same metalloligand oxidation state, the molybdenum–copper metal-metal bond length was observed to vary drastically upon ancillary ligand identity. For the bipyridine system, the distance between the two metal centers (2.75 Å) is within the sum of their covalent radii (r = 0.96), indicative of a possible interaction between the copper center and the metalloligand central metal. For the phosphine derivative, the metal-metal bond distance is elongated to 3.01 Å (0.26 Å longer, r = 1.05), which is consistent with no formal metal-metal bond, or a weak interaction. The phenyl rings of the bidentate dppe ligand impose a more sterically-encumbered environment around the copper center, which could result in a lengthening of the metal-metal distance; the bipyridine ligand lacks these substituents. In addition to steric encumbrance, crystal packing can provide another reasonable explanation for the variation in metal-metal bond length. A common point of contention is that bridging ligands intrinsically impose short metal-metal bond lengths.[38] With these types of complexes, it is evident that the $Mo[SNS]_2$ metalloligand can accomodate a wide range of metal-metal bond distances and not bias a particular metal-metal bond distance. The fact that the metal-metal bond length can vary by ~0.25 Å by selection of ancillary ligand highlights the weakness (or lack) of metal-metal interaction, similar to bimetallic ruthenium compounds that exhibit this deformational isomerism in a single unit cell.[39]

In conjunction with the X-ray crystallographic data, the solution-based characterization consisted of a monoanionic metalloligand coordinated to a monovalent secondary metal center with negligible interaction between metal centers. EPR spectroscopy exhibited S=1/2 systems with

localization of a single unpaired electron on the $Mo[SNS]_2$ metalloligand with no delocalization of the unpaired electron onto the copper center. The simulations of these spectra (at both 298 K and 77 K) demonstrated isotropic signals with g values between 1.99-2.00, and the corresponding A values in the narrow range of 88-112 MHz. These parameters are in agreement with other Mo(V) complexes incorporating redox non-innocent dithiolene ligands. For example, the X-band EPR spectrum of $[Mo(bdt)_3]^{-1}$ (bdt = benzenedithiolate) demonstrated a g_{iso} value of 2.01 and A_{iso} value of 27.1 cm^{-1} (81 MHz).[29] For comparison, a six-coordinate molybdenum complex incorporating o-aminobenzenethiol ligands has a larger hyperfine coupling constant of ~50 cm^{-1} (150 MHz), which suggests that covalency (i.e. backbonding into the π system of the [SNS] ligand) is still prevalent in the sulfur-containing ligand platforms.[40] The lack of anisotropy, which is hypothesized to be prevalent in these monoanionic systems with the ground state electronic configuration $(dz^2)^1$, is attributed to the X-band frequency (~9.5 GHz) employed.[41] These spectra also confirm that the bipyridine and phosphine derivatives are nominally equivalent in solution, which stands in contrast to the solid-state structural data that shows significantly different metal-metal distances with the two ancillary ligands. This distinction between solid-state- and solution-based characterization suggests fluxionality of these heterobimetallic molecules in solution, previously observed for $Mo[SNS]_2Ni(dppe)$, as well as other heterobimetallic systems incorporating the late transition metal centers, nickel and copper.[42] Electrochemical analysis of these compounds yielded multiple irreversible redox events, which is hypothesized to be caused by this fluxionality (or hemilability, prevalent in Cu^+ systems[43-45]) in solution.

Electronic absorption data confirm the presence of a reduced metalloligand, $Mo[SNS]_2^{-1}$, with a weak interaction to the secondary copper center. These bimetallic compounds exhibit nearly identical UV-vis spectra upon variation of the ancillary ligand, as well as in comparison to the reduced metalloligand with an outer-sphere K countercation. Inspection of the UV-vis data indicates that the spectra consist of transitions from predominantly ligand-based orbitals to metal-based orbitals, rendering these charge transfer transitions as ligand-to-metal (LMCT) transitions. These spectra are

also similar to the neutral $Mo[SNS]_2$ metalloligand.[46] For the Mo–Cu systems, this is also consistent with a monoanionic metalloligand coordinated to copper in the monovalent oxidation state, which is expected to exhibit no transitions in the UV-visible range of the electromagnetic spectrum, as the d^{10} metal is inhibited from d-d transitions, and the corresponding MLCT transition ($Cu \rightarrow \pi^*_{dppe}$) is expected to occur at energies > 300 nm.[47-50]

DFT calculations were in agreement with the structural and spectroscopic characteristics of the heterobimetallic systems. Spin density plots of $Mo[SNS]_2Cu(dppe)$, $Mo[SNS]_2Cu(bpytBu_2)$, and $[K][Mo[SNS]_2]$ demonstrated an unpaired electron that was localized on the molybdenum center (75%-89% molybdenum contribution) of the metalloligand, consistent with the EPR data. Additionally, molecular orbital calculations on $Mo[SNS]_2Cu(dppe)$ and $[K][Mo[SNS]_2]$ illustrated the dominance of the metalloligand in the frontier molecular orbitals, with the more electronegative copper metal d orbitals being significantly lower in energy, and thus energetically inaccessible for redox chemistry. TD-DFT calculations were also in agreement, with one main transition from an [SNS]-ligand-based orbital to a predominantly Mo-based orbital. This calculation also indicates where electrons are polarized in the ground state of the metalloligand: electrons are mainly localized on the [SNS] ligand, with light providing the energy to move them to the metal. As such, the most relevant resonance structure of the monoanion metalloligand is $[Mo^{V}[SNS^{3-}]_2]^-$.

The relevance of these Mo–Cu heterobimetallic systems lies not only in the structural similarities to the [MoCu] CODH enzyme active site but also to the proposed electronic structure of its active site. Scheme 3.1 (bottom) describes the proposed catalytic cycle of carbon monoxide oxidation to carbon dioxide. During the catalysis, it is hypothesized that the oxidation state of the molybdenum metal center varies from Mo(VI) to Mo(IV) during the two-electron redox process, while the copper center maintains the monovalent oxidation state. Consistent with this trend, the analogous structural and spectroscopic properties of the Mo–Cu systems indicates that the secondary metal center remains innocent in the redox chemistry, while the molybdenum center loads and unloads the electronic equivalents. This is confirmed computationally, with the frontier molecular

orbitals containing minimal copper character. Most importantly, a method has been introduced to change the structural character of these multimetallic systems (variation of metal-metal bond distance), while the electronic structure of the heterobimetallic system (S=1/2, Mo-based radical) remains unperturbed. Future directions for these copper-containing systems will be directed toward photochemical applications. These Cu(I) systems hold promise for their photophysical properties as ^{3}MLCT emitters, with the nearby "heavier" molybdenum center possibly encouraging singlet-triplet spin flips.[51-53]

3.4 Conclusion

In the case of the Mo–Ni bimetallic complexes, a significant amount of covalency is implicated in the frontier molecular orbitals. Upon moving one element to the right on the periodic table, the Group VI and Group XI metals are now energetically farther away, leading to weaker metal-metal interactions and, as a result, localization of electron density on the disparate metal centers. This is a common motif in heterobimetallic design, in which metals that are closer on the periodic table (and with smaller total d-electron counts) show much stronger interactions between metal centers, while upon moving to copper, exhibit weaker sigma interactions only, due to poorer energetic (different electronegativity) and spatial (effective nuclear charge) overlap. These weak interactions can be controlled by judicious choice of ligand, in which metal-metal bond distance was tuned significantly as a function of ancillary ligand identity.

3.5 Experimental Section

General Considerations. All compounds and reactions reported below show varied degrees of air- and moisture-sensitivity, therefore all manipulations were carried out using standard vacuum-line, Schlenk-line and glovebox techniques. Solvents were sparged with argon before being deoxygenated and dried by passage through Q5 and activated alumina columns, respectively. To test for effective oxygen and water removal, aliquots of each solvent were treated with a few drops of a purple solution of sodium benzophenone ketyl radical in THF. $CuCl_2 \cdot 6H_2O$ (Fisher), CuCl, and 1,2-bis(diphenylphosphino)ethane (dppe) (>97%, TCI) were used as received. Cu(dppe)Cl[54-56] and

$Cu(bpytBu_2)Cl_2$[57] were synthesized following literature procedures from commercially available precursors.

Spectroscopic Measurements. Electronic absorption spectra were recorded with a Jasco V-670 absorption spectrometer UV-vis-NIR spectrophotometer using 1-cm path-length cells at ambient temperature (20-24 °C). Perpendicular-mode X-band EPR spectra were collected using a Bruker EMX spectrometer equipped with an ER041XG microwave bridge using the following spectrometer settings: attenuation = 20 dB, microwave power = 2.017 mW, frequency = 9.79 GHz, modulation amplitude = 1.02 G, gain = 2.00 × 103, conversion time = 81.92 ms, time constant = 655.36 ms, sweep width = 300 G, and resolution = 1024 points. The EPR spectra were modeled using EasySpin/ MatLab.

Crystallographic Methods. X-ray diffraction data for all complexes were collected on single crystals mounted on a glass fiber using paratone oil. Data was acquired using a Bruker SMART APEX II diffractometer equipped with a CCD detector at 88 K using molydenum *Kα* radiation (λ = 0.71073 Å), which was wavelength selected with a single-crystal graphite monochromator. The SMART program package was used to determine unit-cell parameters and for data collection. The raw frame data were processed using SAINT and SADABS to yield the reflection data file. Subsequent calculations were carried out using the SHELXTL program suite. The structures were solved by dual space methods and refined on *F*2 by full-matrix least-squares techniques. Analytical scattering factors for neutral atoms were used throughout the analyses. Hydrogen atoms were generated in calculated positions and refined using a riding model. ORTEP diagrams were generated using ORTEP-3 for Windows.

Computational Methods. All calculations were performed employing the non-empirical tpss density functional theory using the quantum chemistry program package TURBOMOLE. For computational efficiency, initial geometry optimizations were performed using moderate split-valence plus polarization basis sets (def2-SVP).[58] Structures were refined using basis sets of triple zeta valence plus polarization (def2-TZVP) quality.[59] Crystal structures obtained from X-ray diffraction experiments were used as starting points for the geometry optimization; no molecular symmetry was imposed. Energies and minimum energy structures were evaluated self-consistently to tight

convergence criteria (energy converged to 0.1 μHartree, maximum norm of the Cartesian gradient ≤10−4 a.u.). Linear-response time-dependent DFT was used to simulate electronic absorption spectra of the two series.

Mo[SNS]$_2$Cu(dppe). To a 100-mL Schlenk flask, Mo[SNS]$_2$ (279 mg, 0.456 mmol, 1.00 equiv.) was dissolved in dry THF (~7 mL) and frozen in a liquid nitrogen cold well. To the frozen purple solution was added a freshly-prepared, chilled solution of sodium naphthalide (59 mg $C_{10}H_8$, 0.46 mmol, 1.0 equiv.). The resulting brown reaction mixture was stirred to room temperature. To the brown solution was added Cu(dppe)Cl (228 mg, 0.456 mmol, 1.00 equiv.) as a solution in THF (~10 mL) and the reaction mixture was stirred for two hours. The pink/purple reaction mixture was concentrated to roughly 4 mL and precipitation was induced using pentane. The solid was filtered and washed with pentane (2 x 10 mL), Et_2O (2 x 20 mL), and MeCN (3 x 20 mL). The solid was collected as a dark powder (397 mg, 81%). X-ray quality crystals were obtained by diffusion of heptane into a THF solution of the complex. MS (ESI$^+$) *m/z*: 1074.69 ([M]$^+$). UV-vis (THF) λ_{max}/nm (ε / M^{-1} cm^{-1}): 490 (14,400).

Mo[SNS]$_2$Cu(bpytBu$_2$). To a 100-mL Schlenk flask, potassium metal (20 mg, 0.50 mmol, 2.0 equiv.) and graphite (48 mg, 0.50 mmol, 2.0 equiv.) were heated to generate two equiv. of KC_8 as a bronze powder. KC_8 was suspended in 10 mL of dry THF and frozen in a liquid nitrogen cold well. Mo[SNS]$_2$ (153 mg, 0.250 mmol, 1.00 equiv.) was added to the frozen suspension and the reaction mixture was stirred to room temeprature to generate K_2[Mo[SNS]$_2$] *in situ* as a dark solution with a yellow hue around the rim. After 10 minutes, Cu(bpytBu$_2$)Cl$_2$ (101 mg, 0.250 mmol, 1.00 equiv.) was added to the solution and stirred at room temperature for two hours. The solution was filtered through a Celite plug to remove graphite and KCl and yield a maroon filtrate. The filtrate was concentrated to roughly 4 mL and precipitation was induced using 10 ml of pentane. The solid was filtered and washed with pentane (2 x 10 mL), Et_2O (2 x 20 mL), and lastly with MeCN (2 x 20 ml). The solid was collected as a dark powder (118 mg, 50%). X-ray quality crystals were obtained by diffusion of pentane into a THF solution of the complex at ambient temperature. Anal. Calcd. (Found) for

$C_{46}H_{48}CuMoN_4S_4$ (%): C, 58.49 (58.90); H, 5.12 (5.22); N, 5.93 (5.74). MS (ESI^+) *m/z*: 944.67 ($[M]^+$). UV-vis (THF) λ_{max}/nm (ε / M^{-1} cm^{-1}): 490 (14,410), 660 (5,120).

[K(THF)][Mo[SNS]$_2$]. To a 100-mL Schlenk flask, KC_8 (20.5 mg, 0.152 mmol, 1.00 equiv.) was combined with Mo[SNS]$_2$ (93 mg, 0.152 mmol, 1.00 equiv.) in dry THF (~8 mL) to yield a dark maroon-brown reaction mixture. After stirring for ~30 minutes, the reaction mixture was filtered through a plug of Celite to remove graphite, and the filtrated was concentrated down to roughly 3 mL, and Et_2O was used to induce precipitation and wash the product, [K(THF)][Mo[SNS]$_2$] (99 mg, 90%), collected by vacuum filtration and dried *in vacuo*. X-ray quality crystals were obtained by diffusion of Et_2O into a THF solution of the complex at ambient temperature. MS (ESI^-) *m/z*: 614.9 ($[M]^-$). UV-vis (THF) λ_{max}/nm (ε / M^{-1} cm^{-1}): 477 (11,300).

Table 3.5. Crystal data and structure refinement for Mo[SNS]$_2$Cu(dppe), Mo[SNS]$_2$Cu(bpytBu$_2$), and [K(THF)][Mo[SNS]$_2$].

Identity	Mo[SNS]$_2$Cu(dppe)	Mo[SNS]$_2$Cu(bpytBu$_2$)	[K(THF)][Mo[SNS]$_2$]
Empirical formula	$C_{54}H_{48}CuMoN_2P_2S_4$	$C_{46}H_{48}CuMoN_4S_4$	$C_{32}H_{32}KMoN_2OS_4$
Formula weight (g/mol)	1074.60	944.60	723.87
Crystal system	Monoclinic	Tetragonal	Orthorhombic
Space group	$P2_1/c$	$I4_1/a$	$Pna2_1$
T (K)	88(2)	133(2)	133(2)
a (Å)	15.0982(5)	38.9791(19)	15.8139(10)
b (Å)	17.3565(6)	38.9791(19)	12.7598(8)
c (Å)	24.2384(9)	11.5041(6)	15.5060(10)
α (º)	90	90	90
β (º)	103.9254(4)	90	90
ɣ (º)	90	90	90
V (Å3)	6165.0(4)	17479.0(19)	3128.8(3)
Z	4	16	4
Refl. collected	76082	73995	35822
Indep. refl.	15847	9635	7652
R1 ($I > 2\sigma$)[a]	0.0247	0.0301	0.0246
wR2 (all data)[b]	0.0628	0.0726	0.0573

[a]$R1 = \Sigma||F_o|-|F_c|| / \Sigma|F_o|$, [b]$wR2 = [\Sigma[w(F_o^2-F_c^2)^2] / \Sigma[w(F_o^2)^2]]^{1/2}$

3.6 References

(1) Lindahl, P. A. *J. Inorg. Biochem.* **2012**, *106*, 172–178.

(2) Gnida, M.; Ferner, R.; Gremer, L.; Meyer, O.; Meyer-Klaucke, W. *Biochem.* **2003**, *42*, 222–230.

(3) Dobbek, H.; Gremer, L.; Kiefersauer, R.; Huber, R.; Meyer, O. *Proc. Natl. Acad. Sci. U.S.A.* **2002**, *99*, 15971–15976.

(4) Groysman, S.; Majumdar, A.; Zheng, S.-L.; Holm, R. H. *Inorg. Chem.* **2009**, *49*, 1082–1089.

(5) Eames, E. V.; Hernández Sánchez, R.; Betley, T. A. *Inorg. Chem.* **2013**, *52*, 5006–5012.

(6) Eisenhart, R. J.; Carlson, R. K.; Clouston, L. J.; Young Jr, V. G.; Chen, Y.-S.; Bill, E.; Gagliardi, L.; Lu, C. C. *Inorg. Chem.* **2015**, *54*, 11330–11338.

(7) Eisenhart, R. J.; Clouston, L. J.; Lu, C. C. *Acc. Chem. Res.* **2015**, *48*, 2885–2894.

(8) Kuppuswamy, S.; Bezpalko, M. W.; Powers, T. M.; Wilding, M. J. T.; Brozek, C. K.; Foxman, B. M.; Thomas, C. M. *Chem. Sci.* **2014**, *5*, 1617–1626.

(9) Krogman, J. P.; Thomas, C. M. *Chem. Comm.* **2014**, *50*, 5115–5127.

(10) Clouston, L. J.; Siedschlag, R. B.; Rudd, P. A.; Planas, N.; Hu, S.; Miller, A. D.; Gagliardi, L.; Lu, C. C. *J. Am. Chem. Soc.* **2013**, *135*, 13142–13148.

(11) Che, C.; Mao, Z.; Miskowski, V. M.; Tse, M.; Chan, C.; Cheung, K.; Phillips, D. L.; Leung, K. *Angew. Chem. Int. Ed.* **2000**, *112*, 4250–4254.

(12) Pyykkö, P. *Chem. Rev.* **1997**, *97*, 597–636.

(13) Katz, M. J.; Sakai, K.; Leznoff, D. B. *Chem. Soc. Rev.* **2008**, *37*, 1884–1895.

(14) Che, C.-M.; Wong, W.-T.; Lai, T.-F.; Kwong, H.-L. *J. Chem. Soc., Chem. Comm.* **1989**, 243–244.

(15) Schmidbaur, H. *Chem. Soc. Rev.* **1995**, *24*, 391–400.

(16) Harvey, P. D.; Gray, H. B. *J. Am. Chem. Soc.* **1988**, *110*, 2145–2147.

(17) Shaffer, D. W.; Szigethy, G.; Ziller, J. W.; Heyduk, A. F. *Inorg. Chem.* **2013**, *52*, 2110–2118.

(18) Rosenkoetter, K. E.; Ziller, J. W.; Heyduk, A. F. *Inorg. Chem.* **2016**, *55*, 6794–6798.

(19) Rosenkoetter, K. E.; Ziller, J. W.; Heyduk, A. F. *Dalton Trans.* **2017**, *46*, 5503–5507.

(20) Stiefel, E. I.; Eisenberg, R.; Rosenberg, R. C.; Gray, H. B. *J. Am. Chem. Soc.* **1966**, *88*, 2956–2966.

(21) Stiefel, E. I.; Dori, Z.; Gray, H. B. *J. Am. Chem. Soc.* **1967**, *89*, 3353–3354.

(22) Cordero, B.; Gómez, V.; Platero-Prats, A. E.; Revés, M.; Echeverría, J.; Cremades, E.; Barragán, F.; Alvarez, S. *Dalton Trans.* **2008**, 2832–2838.

(23) Takuma, M.; Ohki, Y.; Tatsumi, K. *Inorg. Chem.* **2005**, *44*, 6034–6043.

(24) Smee, J. J.; Miller, M. L.; Grapperhaus, C. A.; Reibenspies, J. H.; Darensbourg, M. Y. *Inorg. Chem.* **2001**, *40*, 3601–3605.

(25) Stibrany, R. T.; Fox, S.; Bharadwaj, P. K.; Schugar, H. J.; Potenza, J. A. *Inorg. Chem.* **2005**, *44*, 8234–8242.

(26) Herebian, D.; Bothe, E.; Bill, E.; Weyhermüller, T.; Wieghardt, K. *J. Am. Chem. Soc.* **2001**, *123*, 10012–10023.

(27) Sproules, S.; Wieghardt, K. *Coord. Chem. Rev.* **2011**, *255*, 837–860.

(28) Ghosh, P.; Begum, A.; Herebian, D.; Bothe, E.; Hildenbrand, K.; Weyhermüller, T.; Wieghardt, K. *Angew. Chem. Int. Ed.* **2003**, *42*, 563–567.

(29) Sproules, S.; Banerjee, P.; Weyhermüller, T.; Yan, Y.; Donahue, J. P.; Wieghardt, K. *Inorg. Chem.* **2011**, *50*, 7106–7122.

(30) Darensbourg, D. J.; Chao, C. S.; Reibenspies, J. H.; Bischoff, C. J. *Inorg. Chem.* **1990**, *29*, 2153–2157.

(31) Tsuboyama, A.; Kuge, K.; Furugori, M.; Okada, S.; Hoshino, M.; Ueno, K. *Inorg. Chem.*

2007, *46*, 1992–2001.

(32) Awad, D. J.; Schilde, U.; Strauch, P. *Inorganica Chim. Acta* **2011**, *365*, 127–132.

(33) Chisholm, M. H.; Huffman, J. C.; Rothwell, I. P.; Bradley, P. G.; Kress, N.; Woodruff, W. H. *J. Am. Chem. Soc.* **1981**, *103*, 4945–4947.

(34) Bock, H.; Lehn, J.; Pauls, J.; Holl, S.; Krenzel, V. *Angew. Chem. Int. Ed.* **1999**, *38*, 952–955.

(35) Gore-Randall, E.; Irwin, M.; Denning, M. S.; Goicoechea, J. M. *Inorg. Chem.* **2009**, *48*, 8304–8316.

(36) Scarborough, C. C.; Wieghardt, K. *Inorg. Chem.* **2011**, *50*, 9773–9793.

(37) Rosenkoetter, K. E.; Wojnar, M. K.; Charette, B. J.; Ziller, J. W.; Heyduk, A. F. *Inorg. Chem.* **2018**, *57*, 9728–9737.

(38) Cotton, F. A.; Murillo, C. A.; Walton, R. A. *Multiple bonds between metal atoms*; Springer Science & Business Media: **2005**.

(39) Kölle, U.; Kossakowski, J.; Klaff, N.; Wesemann, L.; Englert, U.; Herberich, G. E. *Angew. Chem. Int. Ed. Engl.* **1991**, *30*, 690–691.

(40) Gardner, J. K.; Pariyadath, N.; Corbin, J. L.; Stiefel, E. I. *Inorg. Chem.* **1978**, *17*, 897–904.

(41) Kwik, W. L.; Stiefel, E. I. *Inorg. Chem.* **1973**, *12*, 2337–2342.

(42) Wu, B.; Wilding, M. J.; Kuppuswamy, S.; Bezpalko, M. W.; Foxman, B. M.; Thomas, C. M. *Inorg. Chem.* **2016**, *55*, 12137–12148.

(43) De, S.; Mahata, K.; Schmittel, M. *Chem. Soc. Rev.* **2010**, *39*, 1555–1575.

(44) Riesgo, E.; Hu, Y.-Z.; Bouvier, F.; Thummel, R. P. *Inorg. Chem.* **2001**, *40*, 2541–2546.

(45) Pianet, I.; Vincent, J.-M. *Inorg. Chem.* **2004**, *43*, 2947–2953.

(46) Wojnar, M. K.; Ziller, J. W.; Heyduk, A. F. *Eur. J. Inorg. Chem.* **2017**, *2017*, 5571–5575.

(47) McMillin, D. R.; Buckner, M. T.; Ahn, B. T. *Inorg. Chem.* **1977**, *16*, 943–945.

(48) McMillin, D. R.; McNett, K. M. *Chem. Rev.* **1998**, *98*, 1201–1220.

(49) Harkins, S. B.; Peters, J. C. *J. Am. Chem. Soc.* **2005**, *127*, 2030–2031.

(50) Kutal, C. *Coord. Chem. Rev.* **1990**, *99*, 213–252.

(51) Wenger, O. S. *J. Am. Chem. Soc.* **2018**, *140*, 13522–13533.

(52) Czerwieniec, R.; Leitl, M. J.; Homeier, H. H. H.; Yersin, H. *Coord. Chem. Rev.* **2016**, *325*, 2–28.

(53) Mara, M. W.; Fransted, K. A.; Chen, L. X. *Coord. Chem. Rev.* **2015**, *282–283*, 2–18.

(54) Cariati, F.; Naldini, L. *Gazz. Chim. Ital.* **1965**, *95*, 3.

(55) Marsich, N.; Camus, A.; Cebulec, E. *J. Inorg. Nucl. Chem.* **1972**, *34*, 933–946.

(56) Fife, D. J.; Moore, W. M.; Morse, K. W. *Inorg. Chem.* **1984**, *23*, 1545–1549.

(57) Mohr, F.; Binfield, S. A.; Fettinger, J. C.; Vedernikov, A. N. *J. Org. Chem.* **2005**, *70*, 4833–4839.

(58) Schäfer, A.; Huber, C.; Ahlrichs, R. *J. Chem. Phys.* **1992**, *97*, 2571–2577.

(59) Schäfer, A.; Huber, C.; Ahlrichs, R. *J. Chem. Phys.* **1994**, *100*, 5829–5835.

Chapter 4

Interrogation of Heterotrimetallic Systems Incorporating Late First-Row Transition Metals Bridged by a Redox-Active Mo[SNS]$_2$ Metalloligand

4.1 Introduction

Metallic cluster synthesis remains an attractive platform to model metalloenzyme active sites, interrogate fundamental interactions between transition metal ions, activate small molecules, and investigate multi-electron redox processes.[1-3] The deliberate positioning of multiple metals in close proximity to allow for metal-metal interactions remains a bottleneck in synthetic inorganic chemistry due to the lack of synthetic approaches. The primary manifolds to accomplish this include dinucleating ligand manifolds which allow for the encapsulation of multiple ions, with the main disadvantage being unselective metal incorporation i.e. homobimetallic synthetic complexes.[4] One method to bypass this is through the utilization of metalloligands. These complexes are comprised of a single metal ion, with the ability to bind to other metal centers. While both of these methods have advantages and disadvantages, metalloligands incorporating a *cis*-dithiolate bridging moiety are especially attractive due to the similarities to metalloenzyme active sites in biological systems, such as hydrogenase and nitrogenase.[5]

The study of bonding between metal ions remains an area of interest in chemistry due to the complex electronic phenomena involved in these systems. One method to understand the intricate electronic structure of these multimetallic systems is through variation of a metal ion and observance of the changes in spectroscopic, electrochemical, and structural properties of these isostructural systems. This has been accomplished by the Thomas and Lu groups to justify how energy differences between metal centers, upon varying metal identity (and, consequently, electron count), leads to polarization of metal-metal molecular orbitals. [6-13] This leads to systematic changes in bond orders, which manifests itself in distinct changes in electronic structure. While this has been investigated thoroughly in bimetallic systems, the next level of complexity (heterotrimetallic systems) has received less attention.

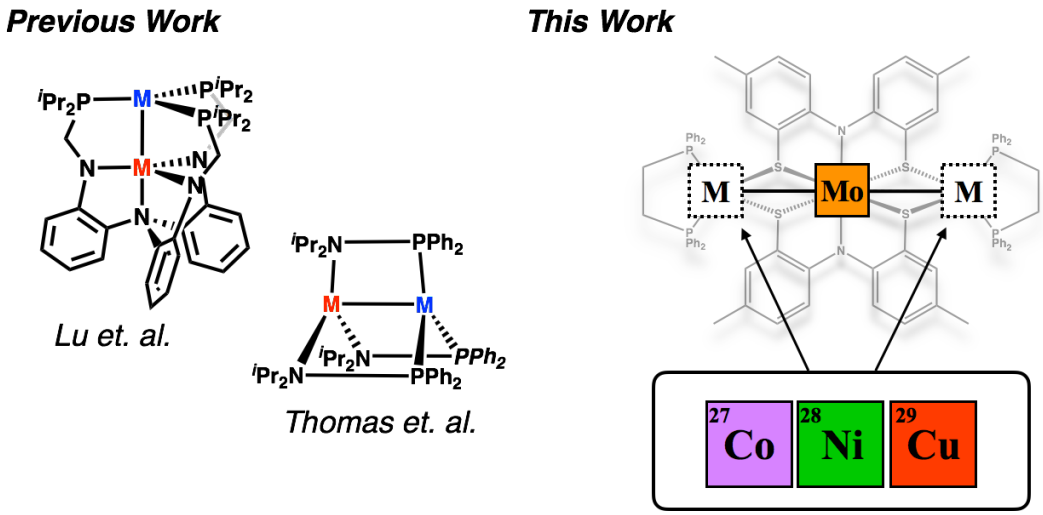

Figure 4.1. Heterometallic ligand platforms used to investigate metal-metal interactions (left) and metalloligand platform used to bridge two metal centers and study metal-metal bonds in linear trimetallic systems.

The tridentate [SNS] ligand platform has allowed for the synthesis of a metalloligand that can bind via the extra lone pairs on the thiolate arms.[14] Previous research of the complexes suggests a highly covalent structure in which electrons are shared among the ligand and the metal.[15] This manifests itself in modest reduction potentials, a distortion from octahedral geometry (to either pseudo-octahedral or trigonal prismatic), and ambiguous intraligand bond lengths. Specifically, we have taken advantage of the reductions to yield a dianionic $[M[SNS]_2]^{2-}$ metalloligand that can act as a terminal or bridging ligand to various metal centers (i.e. nickel, palladium, platinum, and copper).[16] The aim in this chapter is to observe the effects of exterior late transition metal identity on metal-metal bond distance and its corresponding electronic structure. Heterotrimetallic architectures of the type, $Mo[SNS]_2\{M(dppe)\}_2$, represent a three-center bond with electron occupations of two, four, and six, for the cobalt, nickel, and copper metal centers, respectively. This will lead to distinct electronic changes which manifest in differences in metal-metal bond lengths, as well as spectroscopic and electrochemical characteristics.

4.2 Results

4.2.1 Synthesis of Heterotrimetallic $Mo[SNS]_2\{M(dppe)\}_2$ Systems Incorporating Late Transition Metals (M = Co, Ni, Cu)

To synthesize the heterotrimetallic systems incorporating late transition metal centers, reduction of two equivalents of $M(dppe)Cl_2$ (with four equivalents of reductant) in the presence of one equivalent of the $Mo[SNS]_2$ metalloligand leads to the generation of $Mo[SNS]_2\{M(dppe)\}_2$ (M = Co, Ni, Cu) in 78%-82% yield (Scheme 4.1).[17] Specifically, to a chilled dark purple THF solution of $Mo[SNS]_2$ is added KC_8 or sodium naphthalide ($[Na][C_{10}H_8]$), followed by addition of $M(dppe)Cl_x$ (M = Co, x = 2; M = Cu, x = 1). Reaction times for these syntheses range from two to eight hours, although it appears that the reaction occurs immediately upon introduction of the late transition metal ions. Synthesis of the CuMoCu coordination complex involves the reduction of $Mo[SNS]_2$ to $K_2[Mo[SNS]_2]$, followed by salt metathesis upon addition of two equivalents of Cu(dppe)Cl. Both the CoMoCo and CuMoCu products were characterized by a parent ion peak at 1527.9 *m/z* and 1534.9 *m/z*, respectively, in the electrospray mass spectrum. Due to the reducing conditions of the reaction, all isolated $Mo[SNS]_2\{M(dppe)\}_2$ complexes are washed with diethyl ether to remove $M^0(dppe)_2$, the main side product of the reaction. In the synthesis of the CuMoCu system, either $Cu^{II}(dppe)Cl_2$ or $Cu^{I}(dppe)Cl$ can be utilized as starting materials; it was observed that less $Cu^0(dppe)_2$ byproduct was generated with $Cu^{I}(dppe)Cl$. Attempts to generate the Fe analogue led to the isolation of $Fe^{II}(dppe)_2(solvent)_2$ and a non-coordinating dianionic $Mo[SNS]_2^{2-}$ metalloligand counterion, while the Zn analogue led to intractable mixtures.

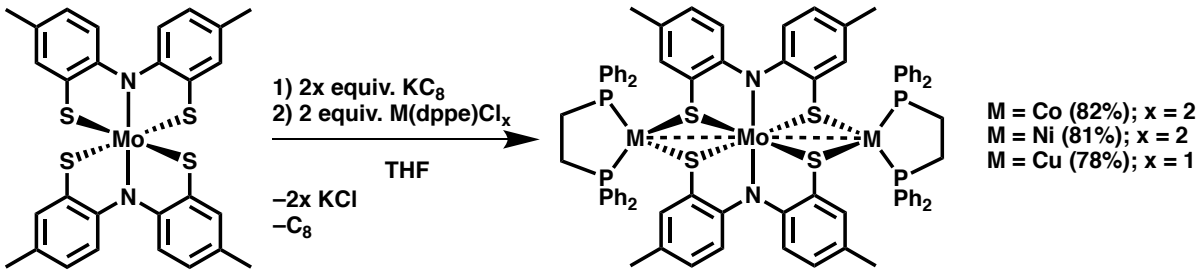

Scheme 4.1. Synthesis of the $Mo[SNS]_2\{M(dppe)\}_2$ heterotrimetallic systems (M = Co, Ni, Cu).

4.2.2 Structural Analysis of Heterotrimetallic Mo[SNS]$_2${M(dppe)}$_2$ Systems

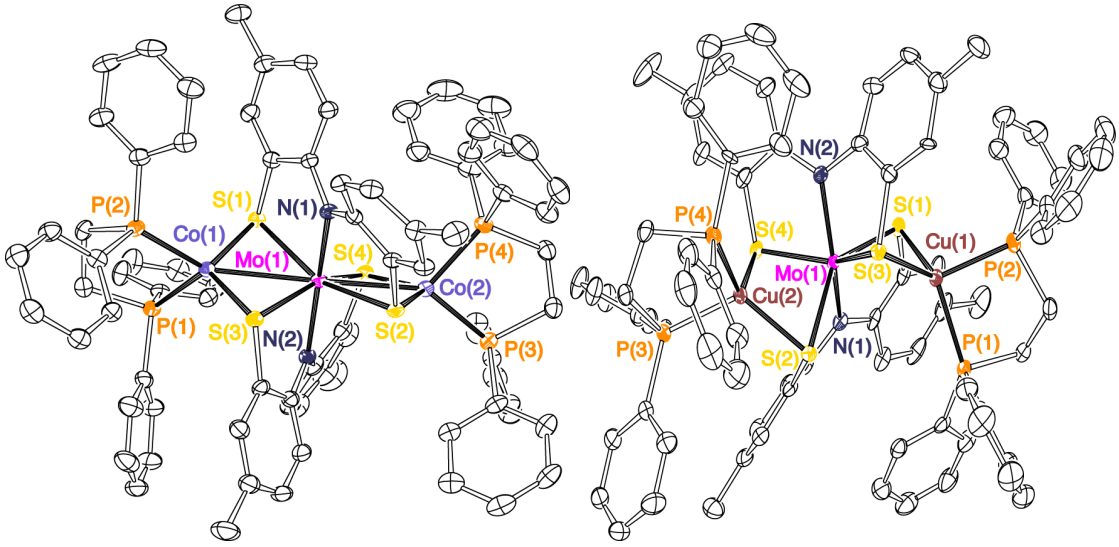

Figure 4.2. ORTEP diagram for Mo[SNS]$_2${Co(dppe)}$_2$ (left) and Mo[SNS]$_2${Cu(dppe)}$_2$ (right) with thermal ellipsoids shown at 50% probability. Hydrogen atoms and solvent molecules (THF) have been omitted for clarity.

The structures of Mo[SNS]$_2${Co(dppe)}$_2$ and Mo[SNS]$_2${Cu(dppe)}$_2$ were determined in the solid state, from single crystals obtained via diffusion of a THF solution of the complex into pentane. Table 4.1 shows the relevant metal–ligand bond lengths and angles for the CoMoCo and CuMoCu systems, while Table 4.2 and Table 4.3 lists the intraligand bond variables and coordination geometries around the metal ions, respectively. The intraligand bond distances are most consistent with two fully-reduced [SNS^{cat}]$^{3-}$ in all three heterotrimetallic complexes. Mo[SNS]$_2${M(dppe)}$_2$ (M = Co, Cu, Ni) have average intraligand C–S and C–N bond distances of 1.76 Å-1.77 Å and 1.41 Å, respectively, along with minimal localization of double bond character in the C–C bonds of the aryl rings ($(\Delta C–C)_{avg}$ = 0.026 Å-0.027 Å), consistent with the ligand oxidation state assignment of [SNS^{cat}]$^{3-}$. Comparison of these values with analogous bidentate derivatives, ortho-amidothiophenolates, are in agreement with C–S and C–N single bonds.[18-22]

The geometry around the Mo metalloligand experiences a substantial distortion upon moving from a Group IX to a Group XI metal. This distortion is less dramatic upon moving from Group IX cobalt to Group X nickel. For the CoMoCo system, the geometry around Mo can best be described as pseudo-octahedral, lying between an ideal octahedron and trigonal prism. X–Mo–X trans angles range from 156°-167°, with a perfect octahedron displaying trans angle values of 180°. For the CuMoCu

complex, these values deviate even further from 180°, ranging from 137°-147°, demonstrating the further distortion from an octahedral geometry to a trigonal prismatic geometry. These parameters are supported by the Bailar twist angles (θ), which quantify the distortion from an octahedron to a trigonal prism.[23] In order to quantify a Bailar twist, two trigonal faces are defined and the C3 rotation from eclipsed to staggered is measured (Figure 4.3).[24,25] The two trigonal faces for the CoMoCo and NiMoNi systems are defined as S(1), S(3), and N(1) (for the first trigonal face), and S(2), S(4), and N(2) (for the second trigonal face). For CuMoCu, the two trigonal faces are S(1), S(3), and N(2) (for the first trigonal face), and S(2), S(4), and N(1) (for the second trigonal face). While a trigonal prism shows a perfect eclipsed geometry of the two faces (θ = 0°), a trigonal antiprism (octahedron) displays a staggered orientation of trigonal faces (θ = 60°). In agreement with the trans angle measurements, $Mo[SNS]_2\{Co(dppe)\}_2$ has θ values that range from 19° to 45°, while $Mo[SNS]_2\{Cu(dppe)\}_2$ values are much closer to a trigonal prism, θ = 2°-15°. In fact, the copper derivative approaches the geometry of an almost perfect trigonal prism. The trans angles and Bailar twist values for $Mo[SNS]_2\{Ni(dppe)\}_2$ are analogous to the cobalt derivative (Figure 4.3, right). The metal–ligand bond distances for the metalloligand generally decrease upon moving from Co to Ni to Cu. The average Mo–S bond lengths of the $Mo[SNS]_2$ bridge for cobalt, nickel, and copper is 2.44 Å, 2.41 Å, and 2.40 Å respectively; the average Mo–N bond distances are 2.12 Å, 2.11 Å, and 2.10 Å respectively.

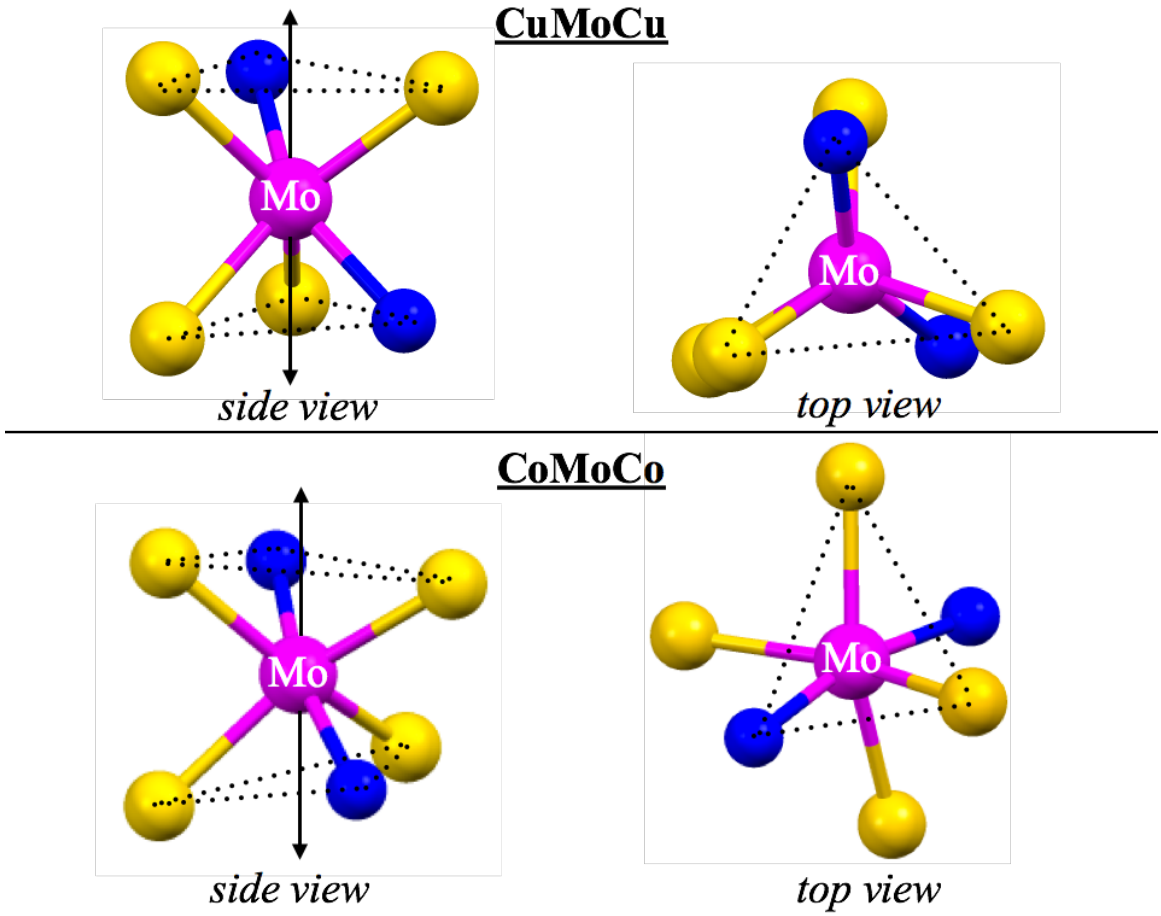

Figure 4.3. Isolation of the $Mo[SNS]_2$ metalloligand in $Mo[SNS]_2\{Cu(dppe)\}_2$ (top) and $Mo[SNS]_2\{Co(dppe)\}_2$ demonstrating the Bailar twist and coordination geometry around the Mo ion. (M(dppe) and aryl rings of [SNS] ligand removed for clarity).

Accommodating Bailar twist distortions are significant differences in metal–metal bond distances. As a means to measure the strength of metal-metal interactions, the covalent ratio (*r*) is calculated, which is the ratio of the metal–metal bond length of interest, normalized to the sum of the covalent radii of the two metal ions being considered.[26] For $Mo[SNS]_2\{Co(dppe)\}_2$, the Mo–Co bond distances are 2.77 Å and 2.79 Å**,** while the sum of the covalent radii of molybdenum and cobalt is 2.80 Å (1.54 Å + 1.26 Å). This leads to covalent ratio values of 0.99 and 1.00, in agreement with the presence of Mo–Co metal-metal interactions. On the other hand, in $Mo[SNS]_2\{Cu(dppe)\}_2$, the Mo–Cu bond lengths are elongated, at 2.94 Å and 2.95 Å, and lead to covalent ratio values of 1.03 for each ($r_{Mo} + r_{Cu}$ = 2.86 Å). This is indicative of no interaction between the molybdenum and copper centers. In comparison to the cobalt and copper systems, $Mo[SNS]_2\{Ni(dppe)\}_2$ exemplifies the shortest metal-metal bonds, with covalent ratio values of 0.96 (at 2.66 Å to 2.67 Å). The shorter

metal-metal bond distance (> 0.1 Å, in comparison to CoMoCo) does not have an impact on the coordination geometry of the molybdenum metalloligand, as evidenced by the similar bond metrics and angles between CoMoCo and NiMoNi (Figure 4.4).

The exterior late transition metal ions all exhibit four-coordinate ligand environments (excluding the metal-metal bond) that are tetrahedral coordination geometries (Table 4.3). These environments can be quantified using the $\boldsymbol{\tau}_4$ geometry index value with the following equation:

$$\boldsymbol{\tau}_4 = (360° - (\alpha + \beta)) / (360° - 2\theta)$$

where α and β are the two greatest valence angles of the coordination center, and θ is the value of a perfect angle in a tetrahedron (109.5°).[27] $\boldsymbol{\tau}_4$ values range from 0 (square plane) to 1 (tetrahedron). For the CoMoCo system, $\boldsymbol{\tau}_4$ values of 0.89 and 0.91 were calculated for the two cobalt ions (Table 4.3). The Co–S_{avg} and Co–P_{avg} values are 2.19 Å and 2.20 Å, respectively. There is a dearth of examples of 4/5-coordinate cobalt complexes in thiolate/phosphine environments. The heterotrimetallic cobalt complex exhibits similar bond metrics to a Mo_2Co_2 cluster compound incorporating bridging sulfides and capping bidentate phosphine ligands (for which oxidation state assignments were not proposed).[28] $Mo[SNS]_2\{Co(dppe)\}_2$ and $[Co(dppe)_2]^{-1}$ both contain reduced cobalt ions in tetrahedral environments, but with different Co–P_{avg} bond distances (2.11 Å in $[Co(dppe)_2]^{-1}$; 2.20 Å in CoMoCo).[29] Similar cobalt–phosphine bond distances to the CoMoCo system are observed in the tetrahedral zero-valent cobalt complexes, $Co(PhNCO)(PMe_3)_3$ (Co–P_{avg} = 2.24 Å) and Co(benzo-[c]-cinnoline)$(PMe_3)_3$ (Co–P_{avg} = 2.21 Å).[30] In the CuMoCu system, $\boldsymbol{\tau}_4$ values of 0.78 and 0.80 were quantified for the CuS_2P_2 coordination geometries. The Cu–S_{avg} and Cu–P_{avg} values are long, in comparison to the cobalt analogue, at 2.32 Å and 2.29 Å, respectively. The copper phosphine bond lengths are consistent with other copper ions in the monovalent oxidation state.[31-33] The Cu(S_2P_2) coordination sphere (bond lengths and geometry) are similar to other Cu(dppe) synthons coordinated to bridging thiolates/sulfides.[34] In fact, the only examples of copper coordinated to a diphenylphosphinoethane (dppe) ligand in the Cambridge Crystallographic Data Center (CCDC) are in the monovalent oxidation state, likely owing to the "soft" nature of the ligand.[35-37] In terms of both

bond metrics and coordination geometries, $Mo[SNS]_2\{Co(dppe)\}_2$ is most similar to $Mo[SNS]_2\{Ni(dppe)\}_2$ with a distinct increase in metal–metal bond distances.

Table 4.1. Selected Bond Distances and Angles of $Mo[SNS]_2\{Co(dppe)\}_2$, $Mo[SNS]_2\{Cu(dppe)\}_2$, and $Mo[SNS]_2\{Ni(dppe)\}_2$.

	$Mo[SNS]_2\{Co(dppe)\}_2$	**$Mo[SNS]_2\{Cu(dppe)\}_2$**	**$Mo[SNS]_2\{Ni(dppe)\}_2$**
Mo(1)–M(1)	2.7684(5)	2.9375(7)	2.6755(6)
Mo(1)–M(2)	2.7876(5)	2.9483(7)	2.6635(6)
M(1)–S(1)	2.4285(8)	2.352(1)	2.409(1)
M(1)–S(2)	2.4365(8)	2.447(1)	2.419(1)
M(1)–S(3)	2.4382(7)	2.447(1)	2.412(1)
Mo(1)–S(4)	2.4421(7)	2.352(1)	2.414(1)
Mo(1)–N(1)	2.118(2)	2.104(3)	2.120(4)
Mo(1)–N(2)	2.120(2)	2.106(3)	2.109(3)
M(1)–S(1)	2.1781(8)	2.346(1)	2.176(1)
M(1)–S(3)	2.1962(8)	2.307(1)	2.196(1)
M(1)–P(1)	2.197(1)	2.277(1)	2.182(1)
M(1)–P(2)	2.1868(6)	2.281(1)	2.229(1)
M(2)–S(2)	2.2087(7)	2.305(1)	2.199(1)
M(2)–S(4)	2.1818(9)	2.342(1)	2.170(1)
M(2)–P(3)	2.1902(6)	2.284(1)	2.185(1)
M(2)–P(4)	2.2323(8)	2.272(1)	2.211(1)
M(1)–Mo(1)–M(2)	173.05(2)	135.83(2)	168.77(2)
S(1)–Mo(1)–S(3)	97.90(2)	90.00(4)	98.41(4)
S(2)–Mo(1)–S(4)	97.27(2)	89.92(4)	98.97(4)
S(1)–Mo(1)–S(2)	156.82(3)	138.10(4)	156.38(4)
S(3)–Mo(1)–S(4)	156.75(3)	137.49(4)	156.59(4)
N(1)–Mo(1)–N(2)	166.61(8)	146.6(1)	162.5(1)
S(1)–M(1)–S(3)	114.07(3)	93.66(4)	113.19(4)
P(1)–M(1)–P(2)	88.21(3)	90.36(4)	90.75(5)
S(2)–M(1)–S(4)	113.01(3)	93.75(4)	114.49(5)
P(3)–M(2)–P(4)	88.00(3)	90.92(4)	91.27(5)

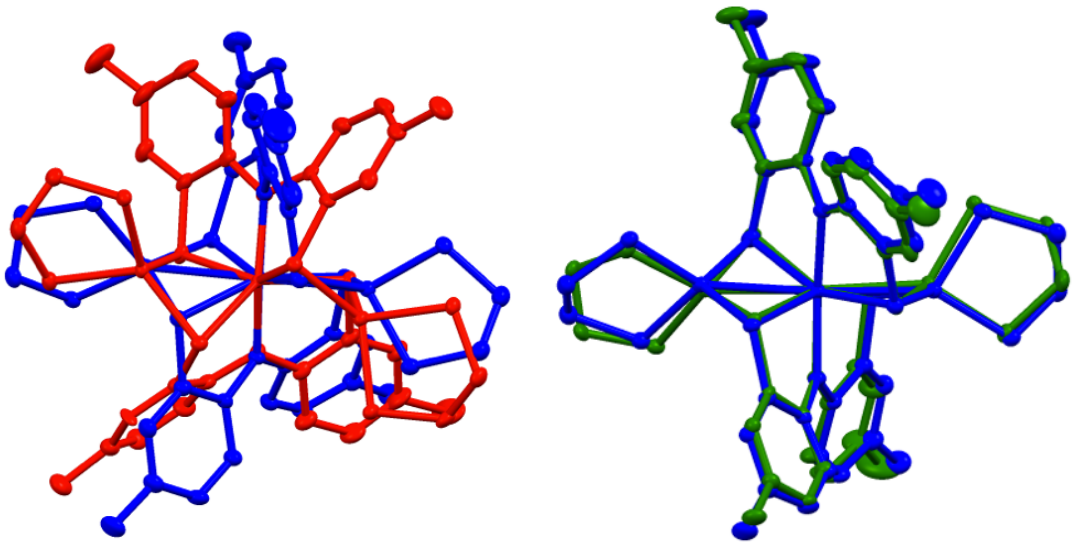

Figure 4.4. Overlay of the solid-state structure of Mo[SNS]$_2${Co(dppe)}$_2$ (blue) with Mo[SNS]$_2${Cu(dppe)}$_2$ (red) (left) and Mo[SNS]$_2${Co(dppe)}$_2$ (blue) with Mo[SNS]$_2${Ni(dppe)}$_2$ (green) (right). The phenyl substituents on the bidentate phosphine ligands have been omitted for clarity.

Table 4.2. Intraligand bond metrics for Mo[SNS]$_2${Co(dppe)}$_2$, Mo[SNS]$_2${Cu(dppe)}$_2$, and Mo[SNS]$_2${Ni(dppe)}$_2$.

	Mo[SNS]$_2${Co(dppe)}$_2$	**Mo[SNS]$_2${Cu(dppe)}$_2$**	**Mo[SNS]$_2${Ni(dppe)}$_2$**
S–C$_{avg}$	1.77	1.76	1.76
N–C$_{avg}$	1.41	1.41	1.41
(ΔC–C)$_{avg}$	0.026	0.027	0.030

Table 4.3. τ_4 Geometry index values, covalent ratio (r), and Bailar twist (θ) values of Mo[SNS]$_2${Co(dppe)}$_2$, Mo[SNS]$_2${Cu(dppe)}$_2$, and Mo[SNS]$_2${Ni(dppe)}$_2$.

	Mo[SNS]$_2${Co(dppe)}$_2$	**Mo[SNS]$_2${Cu(dppe)}$_2$**	**Mo[SNS]$_2${Ni(dppe)}$_2$**
τ_4 M(1)	0.91	0.80	0.86
τ_4 M(2)	0.89	0.78	0.88
$r_{Mo(1)–M(1)}$	0.99	1.03	0.96
$r_{Mo(1)–M(2)}$	1.00	1.03	0.96
θ$_{S,N}$	43.4	14.9	41.6
θ$_{S,S}$	19.3	2.4	17.5
θ$_{S,N}$	44.8	14.3	41.6

4.2.3 Spectroscopic Analysis of $M[SNS]_2\{M(dppe)\}_2$ Systems

It has previously been shown that $Mo[SNS]_2\{Ni(dppe)\}_2$ is diamagnetic and has been characterized by both ^1H and ^{31}P NMR spectroscopy. It was surprising to discover that the CuMoCu complex was also diamagnetic in solution, despite the fact that the "two-electron reduced" analogue of the nickel congener would lead to an occupation of two electrons on the molybdenum metalloligand. This would lead to an occupation of two electrons in the non-bonding t_2 set of d orbitals of molybdenum.[38] Yet, $Mo[SNS]_2\{Cu(dppe)\}_2$ exhibits C_2 symmetry in solution, with two sets of chemically inequivalent resonances for both the aromatic backbone and the methyl groups on the [SNS] ligand backbone. The neutral metalloligand and $Mo[SNS]_2\{Ni(dppe)\}_2$ both show D_2 symmetry in solution with one set of resonances that demonstrate that all aromatic and aliphatic protons are equivalent in solution. In $Mo[SNS]_2\{Cu(dppe)\}_2$, one signal is observed by ^{31}P NMR at –8 ppm (referenced to H_3PO_4), which confirms that both copper ions are in identical electronic environments. $Mo[SNS]_2\{Co(dppe)\}_2$ is a paramagnetic system which showed broad signals by NMR. Evan's method was employed for the cobalt complex, with a solution magnetic moment of 2.89 μ_B in C_6D_6. This is in agreement with an S=1 ground state for the cobalt analogue.

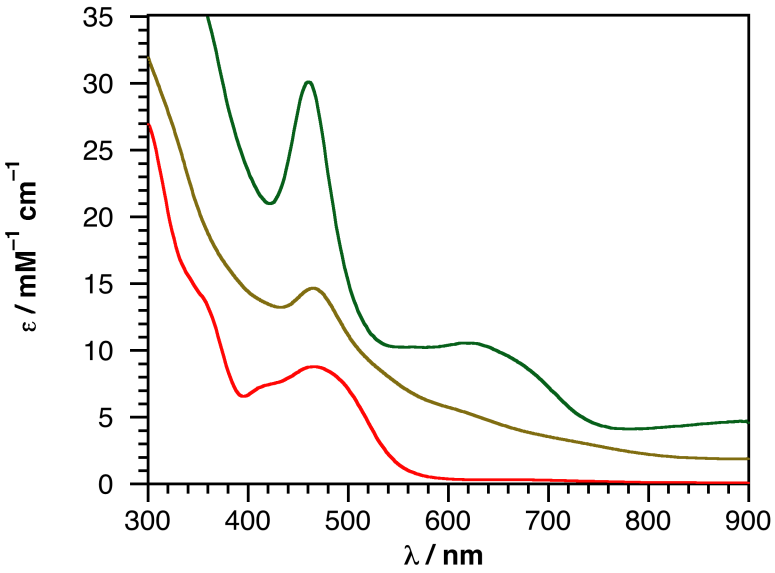

Figure 4.5. Electronic absorption spectra of $Mo[SNS]_2\{M(dppe)\}_2$ obtained in THF (M = Co (light brown), M = Cu (red), and M = Ni (green)).

Electronic absorption spectroscopy was utilized to aid in the understanding of the electronic structure of these heterotrimetallic systems. All three complexes demonstrate a primary transition at λ_{max}=~460 nm. As observed in Figure 4.5, the CuMoCu system only exhibits this main transition at λ_{max}=465 nm. For both CoMoCo and NiMoNi, the growth of low energy transitions is observed. $Mo[SNS]_2\{Ni(dppe)\}_2$ exhibits two relatively well-defined lower energy absorption maxima at 622 nm and 918 nm; $Mo[SNS]_2\{Co(dppe)\}_2$ demonstrates a single absorption maximum at 465 nm, with a broad absorption that extends into the near infrared (NIR).

4.2.4 Electrochemical Analysis of $Mo[SNS]_2\{M(dppe)\}_2$ Systems

The heterotrimetallic systems were also studied electrochemically to assess their redox properties and aid in assigning oxidation state. $Mo[SNS]_2\{Co(dppe)\}_2$ exhibits a similar voltammetric profile to $Mo[SNS]_2\{Ni(dppe)\}_2$ (Figure 4.6) in which multiple reductions and oxidations are observed. Referenced to the $FeCp_2^{+/0}$ redox couple in THF solvent, the cobalt derivative displays two reversible reductions (i_{pa}/i_{pc} ~ 1) at negative potentials (–1.79 V and –2.5 V), along with multiple irreversible oxidations (Table 4.4). In the case of cobalt, the irreversibility of the anodic redox events indicates a significant rearrangement of the multimetallic system upon oxidation. $Mo[SNS]_2\{Cu(dppe)\}_2$ displays two reversible oxidations, at –0.70 V and 0.00 V that are shifted anodically in comparison to $Mo[SNS]_2\{Co(dppe)\}_2$ (shifted by 0.2 V for the first oxidation). No reduction for the CuMoCu complex was observed in the THF solvent window. While the nickel derivative demonstrates two reductions at similar potentials (differing by ~380 mV), as well as oxidations (differing by ~300 mV), the heterotrimetallic cobalt complex shows evenly spaced redox events, with separation ranging from 760 mV to 890 mV. $Mo[SNS]_2\{Cu(dppe)\}_2$ exhibits a separation of 700 mV between the first and second oxidation.

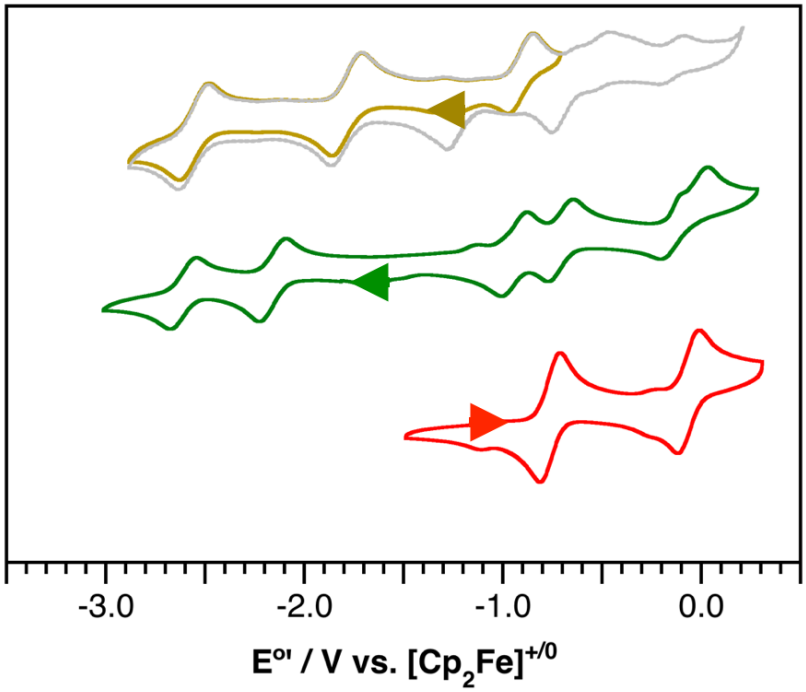

Figure 4.6. Cyclic voltammograms of $[Mo[SNS]_2\{Co(dppe)\}_2]$ (top, light brown/gray), $Mo[SNS]_2\{Cu(dppe)\}_2$ (middle, red), and $Mo[SNS]_2\{Ni(dppe)\}_2$ (bottom, green) dissolved in THF. Measurements were made under N_2 using a scan rate of 200 mV sec^{-1} on 1.0 mM analyte solutions containing 0.10 M $[Bu_4N][PF_6]$ as the supporting electrolyte. Potentials were referenced to $[Cp_2Fe]^{+/0}$ using an internal standard. The asterisk (arrowhead) denotes the open circuit potential. Voltammetric data were collected using three electrodes: glassy carbon working, platinum counter, and silver wire pseudo-reference.

Table 4.4. Electrochemical potentials of $[Mo[SNS]_2\{M(dppe)\}_2]$ M = Co (light brown/gray), M = Cu (red), and M = Ni, obtained in THF (right). obtained in THF containing 0.1 M $[NBu_4][PF_6]$, referenced to the $[Cp_2Fe]^{+/0}$.

	$[M]^{-1/-2}$	$[M]^{0/-1}$	$[M]^{0/+1}$	$[M]^{+1/+2}$	$[M]^{+2/+3}$
$Mo[SNS]_2\{Co(dppe)\}_2$	–2.55	–1.79	–0.90	–	–
$Mo[SNS]_2\{Ni(dppe)\}_2$	–2.50	–2.12	–0.80	–0.50	0.00
$Mo[SNS]_2\{Cu(dppe)\}_2$	–	–	–0.70	0.00	–

4.2.5 Computational Investigations of the $M[SNS]_2\{M(dppe)\}_2$ Systems

In order to further understand the underlying electronic factors underpinning these heterotrimetallic $Mo[SNS]_2\{M(dppe)\}_2$ systems, density functional theory (DFT) calculations were performed. Geometry optimizations were performed on the isolated X-ray crystal structures as the starting points and all computations were employed using the TPSS functional at the TZVP level of

theory. $Mo[SNS]_2\{Co(dppe)\}_2$ was optimized as an open-shell unrestricted Hartree-Fock (UHF) triplet system, with geometry optimizations yielding molybdenum–cobalt bond distances of 2.76 Å and 2.78 Å, analogous to those derived experimentally. Metal–heteroatom bond distances fell within 0.02 Å of the solid-state values. The CoMoCo system displays overlap of the cobalt 3d and molybdenum 4d orbitals. The total spin density plot shows that most of the spin (70%) resides on the cobalt transition metal ions, with contribution from the central molybdenum center (24%) (Figure 4.7).

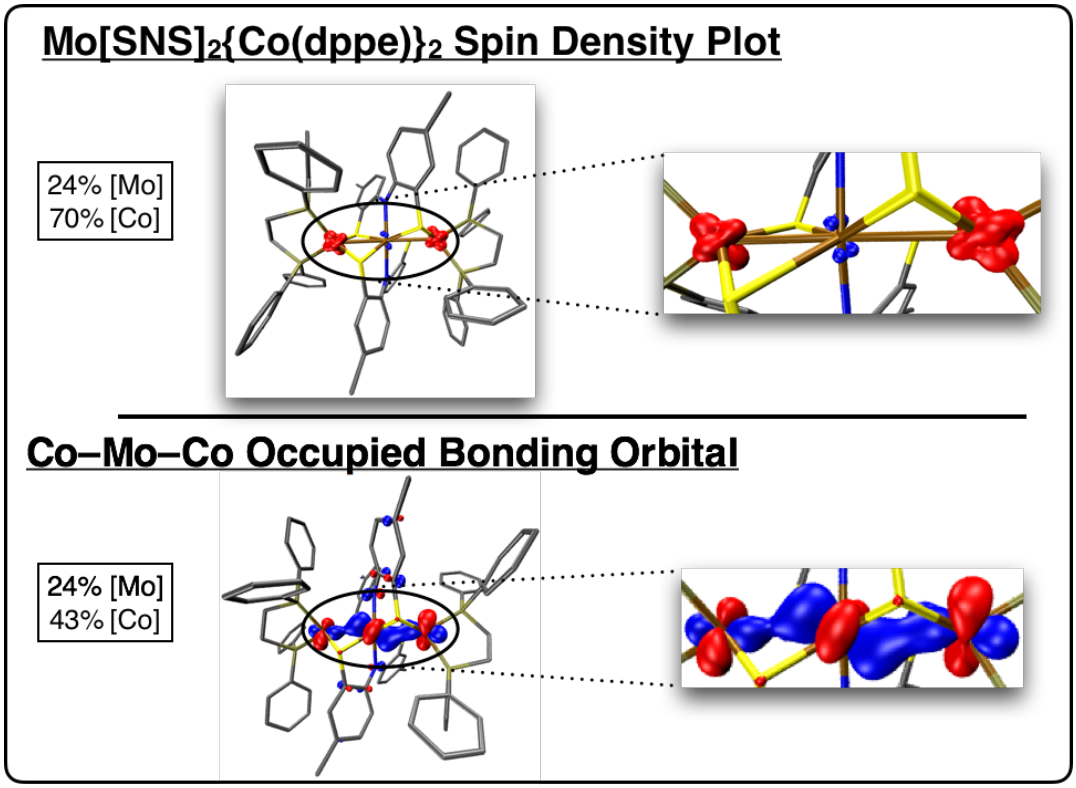

Figure 4.7. Spin density plot of $Mo[SNS]_2\{Co(dppe)\}_2$ (top) and metal-metal bonding Kohn-Sham molecular orbital (bottom).

$Mo[SNS]_2\{Cu(dppe)\}_2$ was optimized as an S=0 system (based on the ^1H NMR data), using a spin-restricted DFT computational scheme. Geometry optimizations yielded molybdenum–copper bond distances of 2.99 Å for both metal-metal bond lengths. The metal–heteroatom and intraligand bond distances were in good agreement with the solid-state experimental data. No overlap of molybdenum and copper d orbitals was observed. Figure 4.8 (left) shows the highest-occupied Kohn-Sham molecular orbital in the case of the copper system: a dz^2 orbital on the molybdenum metalloligand. Time-dependent DFT (TD-DFT) calculations predict one main transition for the

CuMoCu complex, which corresponds to a HOMO–1 → LUMO+1 transition. This charge transfer band is attributed to promotion of an electron from an [SNS]-ligand-based orbital to a $d_{xy}/d_{x^2-y^2}$ orbital localized on the metalloligand.

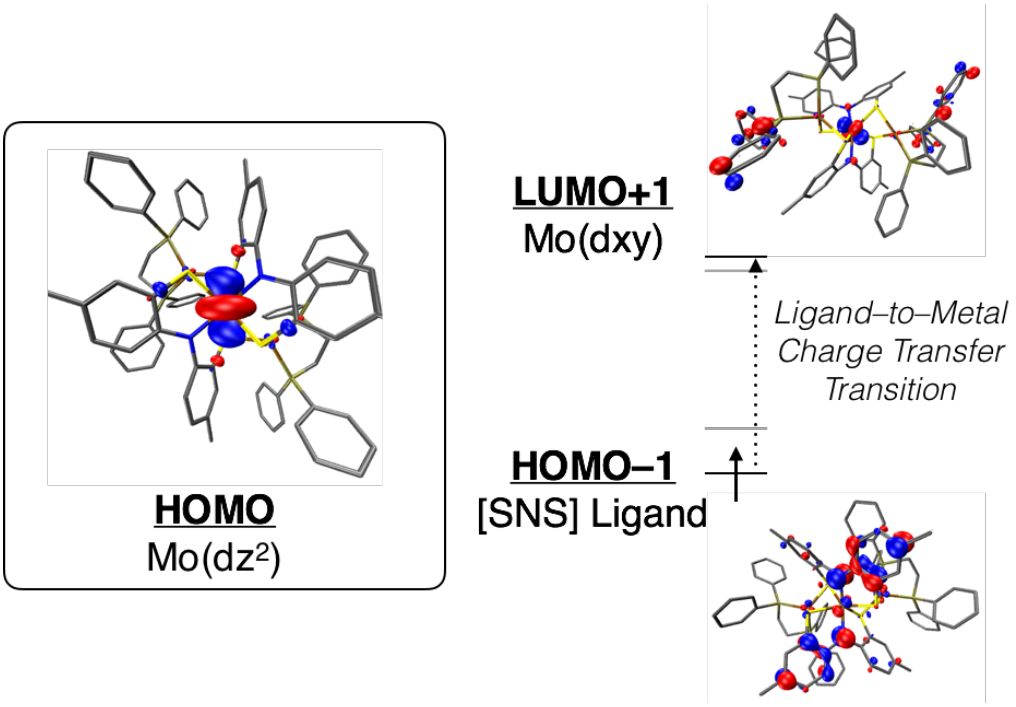

Figure 4.8. Highest occupied molecular orbital (HOMO) in $Mo[SNS]_2\{Cu(dppe)\}_2$ (left) and time-dependent density functional theory (TD-DFT) calculation of the dominant transition in $Mo[SNS]_2\{Cu(dppe)\}_2$ (right).

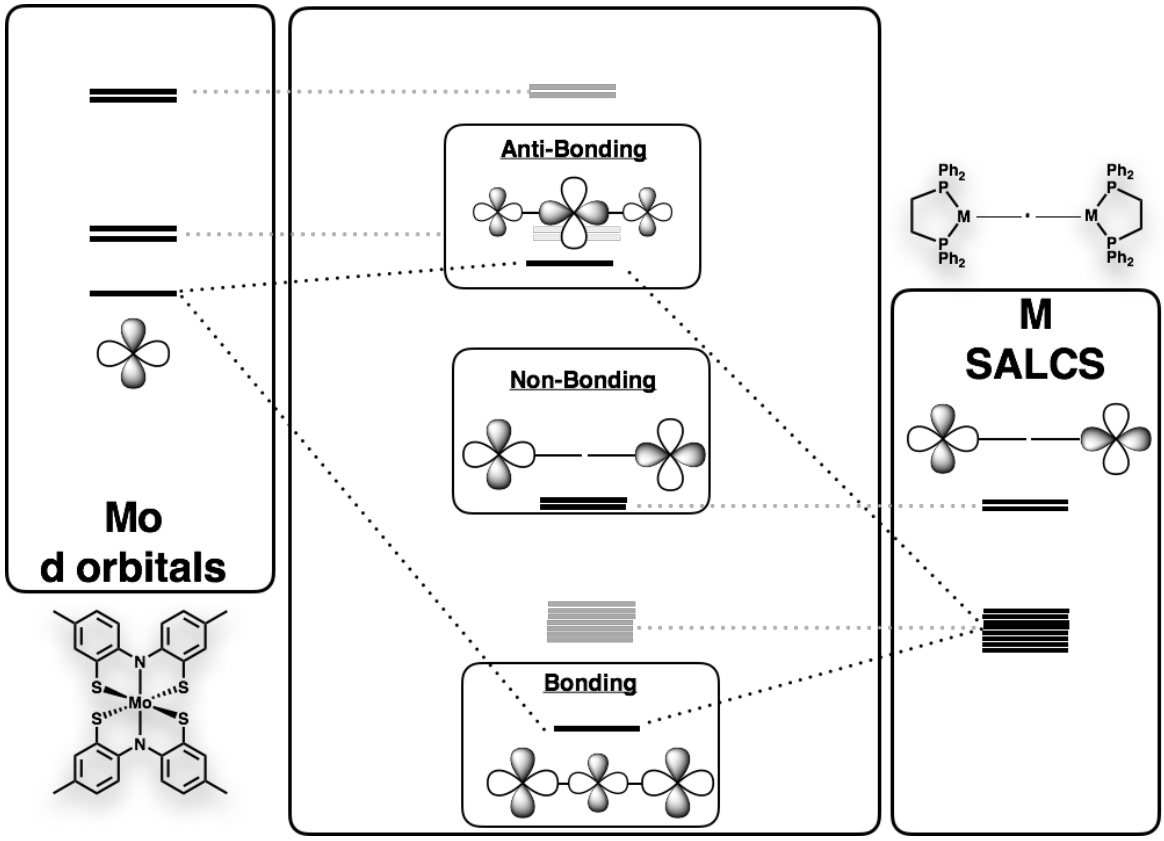

Figure 4.9. General molecular orbital diagram for $Mo[SNS]_2\{Ni(dppe)\}_2$, illustrating the three-center bonding scheme found in these $Mo[SNS]_2\{M(dppe)\}_2$ heterotrimetallic systems.

4.3 Discussion

The $Mo[SNS]_2\{M(dppe)\}_2$ heterotrimetallic coordination complexes were synthesized under reducing conditions, in the presence of the divalent (or monovalent, in the case of copper) M(dppe) salts. These syntheses can be viewed as reduction of both $Mo[SNS]_2$ and M(dppe) synthons *in situ* to generate the final trimetallic product. While four equivalents of reductant are added to the solution of Mo metalloligand, it is hypothesized that the metalloligand is not reduced to $[Mo]^{4-}$. This is consistent with the electrochemistry of $Mo[SNS]_2$, which undergoes two reversible metal-based reduction events in THF at –0.50 V and –1.53 V vs. $[FeCp_2]^{+/0}$. Due to the redox-inactivity of Zn^{II}, heterotrimetallic design of $Mo[SNS]_2\{Zn(dppe)\}_2$ would need to yield $[Mo]^{4-}$ tetra-anion, an oxidation state not achievable for Mo in the N_2S_4 ligand pocket, making the Zn analogue inaccessible.

X-ray crystallography confirmed the connectivity of these multimetallic systems. While the [SNS] ligand platform has demonstrated redox noninnocence in other metal complexes, the

$Mo[SNS]_2\{M(dppe)\}_2$ systems maintain the tridentate ligand in its fully-reduced, trianionic oxidation state.[39] Thus, the organic frameworks incorporated here ([SNS], dppe) can be viewed solely as a means to stabilize interactions between metal ions without complicating oxidation state assignment. Most importantly, it is demonstrated that this bridging metalloligand can host a wide range of metal-metal bond distances and does not naturally bring in the two metals in close proximity, a common problem associated with multinucleating ligands.[40] For $Mo[SNS]_2\{Ni(dppe)\}_2$, it was previously demonstrated that short molybdenum–nickel contacts of ~2.66 Å and ~2.67 Å (r = 0.96) were observed in the solid-state. Upon variation of the exterior late transition metal ion from nickel to cobalt, short metal-metal bond distances of 2.76 Å and 2.78 Å (r = 0.99, 1.00) were also present. However, incorporation of Cu(dppe) synthons led to longer molybdenum–copper bond lengths of 2.94 Å and 2.95 Å (r = 1.03), consistent with metal-metal bond scission. With concomitant cleavage of metal-metal bonds was observed a distinct variation in the coordination geometry of the $Mo[SNS]_2$ metalloligand bridge. Both the nickel and cobalt systems demonstrated a pseudo-octahedral coordination geometry around the metalloligand (θ = 19°-45°), with similar metal–ligand bond lengths. The CuMoCu system, on the other hand, adopted an ideal trigonal prismatic geometry (θ = 2°-15°). It is this Bailar twist that leads to double occupation of the non-bonding dz^2 orbital of the $Mo[SNS]_2$ metalloligand, and a consequent S=0 diamagnetic ground state in the case of $Mo[SNS]_2\{Cu(dppe)\}_2$. The tetrahedral geometry around the exterior late transition metal ions indicates a more reduced form of the synthon. In the case of copper, a tetrahedral coordination geometry is associated with copper in its monovalent oxidation state, while Cu^{2+} ions typically adopt square-planar or distorted octahedral geometries. Nickel phosphine complexes in the monovalent or zero oxidation states are known to adopt a tetrahedral geometry, with divalent nickel complexes arranging its ligands in a square plane. Cobalt phosphine coordination compounds exhibit a wide variety of coordination geometries that range in coordination number and kinetic stability.

The spectroscopic properties of the heterotrimetallic complexes aided in the characterization and comparison of their electronic structures. Both the NiMoNi and the CuMoCu complexes

exhibited well-resolved resonances by both ^{1}H and $^{31}P\{^{1}H\}$ NMR. While the nickel analogue was *D*2 symmetric in a C_6D_6 solution, the copper derivative demonstrated a lowering of symmetry, to a *C*2 symmetric coordination complex. The lowering of symmetry can be attributed to the significant Bailar twist observed in the molybdenum metalloligand of the CuMoCu complex toward a trigonal prism in the solid state. $Mo[SNS]_2\{Co(dppe)\}_2$ was paramagnetic, with a solution magnetic moment in agreement with an S=1 ground state system. For the electronic absorption spectra, it is noted that in multimetallic cluster compounds, low energy transitions are observed and are typically delineated as charge transfer between metal ions. If the transfer or delocalization of charge is impeded (for example, through metal-metal bond scission), these transitions will decrease in intensity (i.e. lower probability of transition). This was observed for $Mo[SNS]_2\{Cu(dppe)\}_2$, in which one main transition at ~460 nm was observed. This transition, in agreement with previous studies of these complexes incorporating the $Mo[SNS]_2$ metalloligand, was confirmed by TD-DFT calculations as an intrametalloligand transition, from the [SNS] ligand to the Mo ion. The lack of metal-metal bonding (in conjunction with the soft phosphine donors maintaining copper in its +1 oxidation state) in the case of CuMoCu is hypothesized to prohibit electronic communication between metal centers, leading to a UV-vis spectrum dominated by metalloligand transitions. In other heteromultimetallic systems incorporating metal-metal bonds involving copper ions, the same phenomenon is observed in which interactions with copper ions are weak to nonexistent, due to the location of the Group XI metal on the periodic table (large differences in electronegativity and more d electrons, which can potentially populate antibonding orbitals).[13] For both the nickel and cobalt systems, lower energy transitions are observed, which is consistent with the X-ray crystallographic data, buttressed by computational evidence, that metal-metal interactions exist in these compounds. Further experimental work is required to identify the nature of these low-energy transitions.

Electrochemical assessment of the heterotrimetallic systems was consistent with the spectroscopic and structural data. As mentioned previously, the soft nature of the bidentate phosphine maintains copper in its monovalent oxidation state. As a result, the late transition metal ions can be

considered redox-inactive in the case of $Mo[SNS]_2\{Cu(dppe)\}_2$. This would lead to the electrochemical assignment of the oxidations as $Mo[SNS]_2^{-1/-2}$ and $Mo[SNS]_2^{0/-1}$, which is in line with the reversible nature of the redox events (i.e. electron removal from a non-bonding dz^2 orbital). These two redox couples have been shown to be reversible i.e. demonstrate minimal geometric rearrangement upon redox, in the case of the neutral $Mo[SNS]_2$ metalloligand.[41] The anodic shift, in comparison to the monomeric $Mo[SNS]_2$, can be attributed to the dianionic nature of the metalloligand bridge ($Mo[SNS]_2^{2-}$ coordinated to two $[Cu(dppe)]^{+1}$ ions). While the assignment of redox events is relatively facile in the case of the CuMoCu system, the covalency associated with the cobalt system (as well as the nickel analogue, $Mo[SNS]_2\{Ni(dppe)\}_2$) makes the locus of electron placement inherently more difficult. The reversibility of the reductions intimates that these are localized on the molybdenum-based bridge (in keeping with the electrochemical profiles of CuMoCu, as well as the neutral $Mo[SNS]_2$). One of the main geometric rearrangements for the metal–phosphine systems is a tetrahedral → square planar twist. Typically, these rearrangements occur upon moving from a d^9 to a d^8 electron count. From these data, it is hypothesized that $Mo[SNS]_2\{Co(dppe)\}_2$ consists of two cobalt(0) d^9 synthons in tetrahedral coordination environments, that upon oxidation, rearrange to adopt a square planar geometry to accommodate the new d^8 electron configuration. This is in line with the irreversible oxidations observed via cyclic voltammetry.

An understanding of the electronic structure of these $Mo[SNS]_2\{M(dppe)\}_2$ systems is best accomplished through a three-center bonding scheme, with the NiMoNi system being an example of a three-center four-electron bond.[42,43] As a simplification, the cobalt and copper derivatives can be viewed as the two-electron oxidized and reduced versions of this bonding scheme, respectively (as a result of their position on the periodic table). In terms of electron count, $Mo[SNS]_2\{Ni(dppe)\}_2$ has 20 valence electrons distributed among the three metal ions; $Mo[SNS]_2\{Co(dppe)\}_2$ has 18 valence electrons to be distributed among the CoMoCo core, and $Mo[SNS]_2\{Cu(dppe)\}_2$ 22 valence electrons. Note that these structures do not truly represent redox partners of the nickel analogue, as metal identity leads to variations in orbital energies (as dictated by their inherent electronegativity

values) and size (variation from cobalt to nickel to copper leads to a covalent radii range of 0.08 Å). As a result, direct comparisons between this series of clusters should be viewed with caution. Nonetheless, the results are in accord with what is to be expected in a three-center bonding manifold.

$Mo[SNS]_2\{Cu(dppe)\}_2$ is an example of adding two electrons to the general bonding scheme in Figure 4.10 (red)**.** Formally, these electrons will be added to a M–M–M antibonding orbital that would lead to cleavage of the metal-metal bonds (a three-center six-electron bond). The long metal–metal bond length can also be justified as a filled-filled interaction between the d^{10} Cu(I) ions and the d^2 Mo(IV) ion. Furthermore, due to the energetic difference of the molybdenum and copper d orbitals, this antibonding molecular orbital will be dominated by contributions from the molybdenum metalloligand: the electrons from this "two-electron reduction" are hypothesized be localized on the molybdenum metal center. Crystal field splitting arguments for this six-coordinate octahedral metalloligand suggest that this would lead to occupation of two electrons in the non-bonding t_2 set of orbitals, and in accordance with the Pauli exclusion principle, lead to an S=1 triplet ground state. Further investigations into the coordination geometry of $Mo[SNS]_2\{Cu(dppe)\}_2$ demonstrate an almost perfect trigonal prismatic geometry with the following crystal field splitting: dz^2 (non–bonding) ≤ dxy, $dx^2–y^2$ (π-antibonding) ≤ dxz, dyz (σ-antibonding). A double occupation of the dz^2 orbital would yield an S=0 complex, which is what is observed both in the solid state and in solution.[44] All of these data result in an unambiguous oxidation state assignment for the CuMoCu system as $[Cu^{I}–Mo^{IV}–Cu^{I}]$.

The electronic structure of CoMoCo can be viewed as the "two-electron oxidized" version of $Mo[SNS]_2\{Ni(dppe)\}_2$ – this would lead to depopulation of the non-bonding molecular orbital, while two electrons still occupy the bonding molecular orbital (Figure 4.10, green). Based on the three-center two-electron bonding scheme, the metal-metal interactions should still be maintained in CoMoCo. While the three-center bonding scheme for the CoMoCo system in Figure 4.10 suggests an S=0 ground state, it is important to recognize that there are d orbitals on the cobalt center that are orthogonal to this three-center bonding, and thus do not participate in the interaction (it is these

orthogonal orbitals that result in the S=1 system!). This is what is observed experimentally, although there is an elongation of the metal-metal bonds (the covalent ratio value increases from 0.96 for the nickel analogue, to 0.99-1.00 for the cobalt analogue). The current hypothesis for this elongation is that, in terms of oxidation state assignment and d electron count, $Mo[SNS]_2\{Ni(dppe)\}_2$ is nominally a $[Ni^0–Mo^{VI}–Ni^0]$ system, and the formal two-electron oxidation would be based on the exterior late transition metal (according to Figure 4.9), leading to an electronic assignment of $[Co^0–Mo^{VI}–Co^0]$. Ni^0 refers to a d^{10} fully-occupied d orbital manifold, and Co^0 refers to a d^9 electronic configuration. As a result, $Mo[SNS]_2\{Co(dppe)\}_2$ has open-shell character associated with the late transition metal ions, which manifests in an $S\neq0$ ground state. This d^9 electron configuration is confirmed experimentally through Evan's method, as well as through DFT computations, with the spin density plot of the CoMoCo system demonstrating the majority of the spin in this triplet system residing on the exterior cobalt ions. Moreover, it is well known that for d^9 electron configurations, these metal ions undergo a Jahn-Teller distortion, which would manifest in longer metal-metal bonds. Another hypothesis is that these metal-metal bonds are dynamic and flexible, with X-ray crystallography providing a "snapshot" of this dynamic behavior.

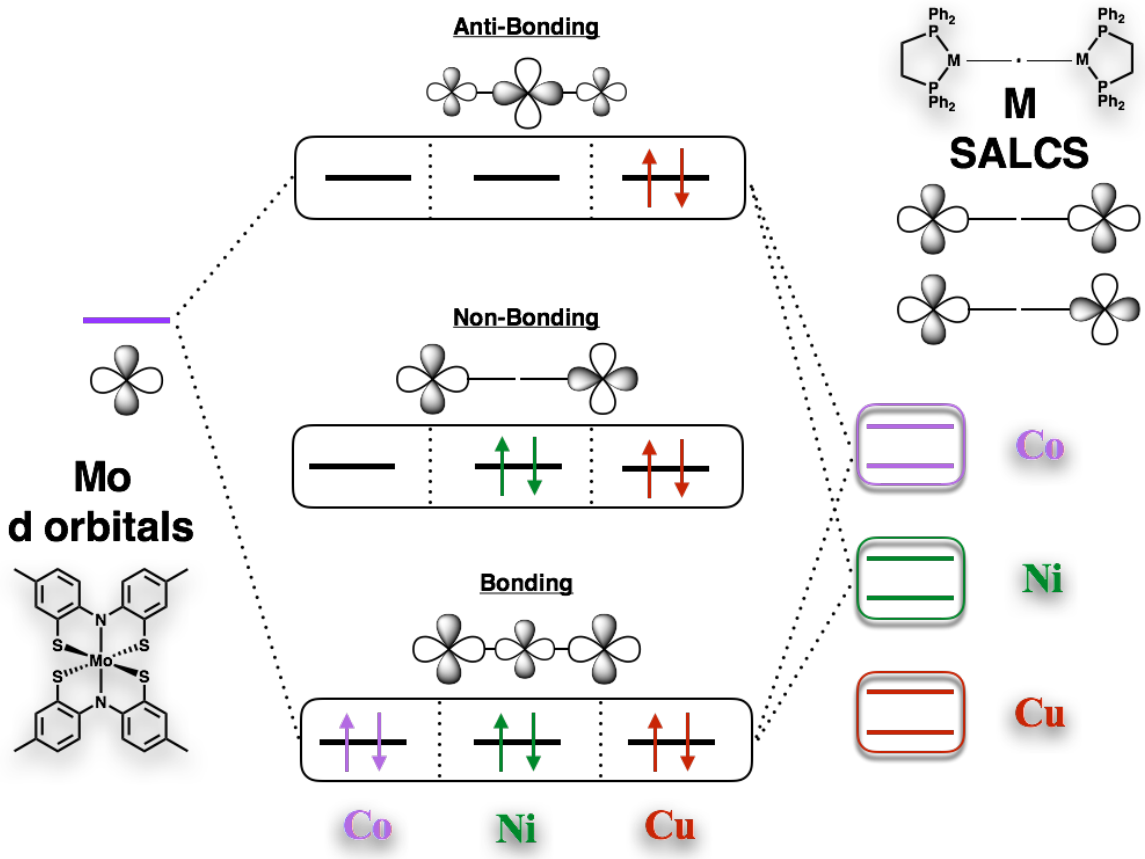

Figure 4.10. Three-center metal-metal bonding scheme for Mo[SNS]2{M(dppe}2 (M = Co (light purple), Ni (green), Cu (red).

4.4 Conclusion

A set of heterotrimetallic complexes was generated that involved modular replacement of the exterior ancillary metal ions, while maintaining the identity of the central metalloligand. This was accomplished to understand the electronic structure and bonding as a function of metal identity, redox, and metal-metal overlap (spatial and energetic). It was demonstrated that heterotrimetallic architectures of the type, $Mo[SNS]_2\{M(dppe)\}_2$, can be explained as a three-center bond with a varying electron count of two, four, and six upon variation of metal ion source from cobalt, to nickel, and copper, respectively. Consequently, $Mo[SNS]_2\{Co(dppe)\}_2$ (3-center 2-electron bond) maintains a metal-metal bonding network with de-occupation of a non-bonding orbital. The 3-center 6-electron bonding scheme for $Mo[SNS]_2\{Cu(dppe)\}_2$ leads to occupation of the metal-metal antibonding orbital and scission of the molybdenum–copper bonds. Placement of those electrons in a dz^2 orbital on the molybdenum metalloligand bridge yields a diamagnetic ground state.

4.5 Experimental

General Considerations. All compounds and reactions reported below show varied degrees of air- and moisture-sensitivity, therefore all manipulations were carried out using standard vacuum-line, Schlenk-line and glovebox techniques. Solvents were sparged with argon before being deoxygenated and dried by passage through Q5 and activated alumina columns, respectively. To test for effective oxygen and water removal, aliquots of each solvent were treated with a few drops of a purple solution of sodium benzophenone ketyl radical in THF. $Mo[SNS]_2\{Ni(dppe)\}_2$ was synthesized following literature procedures from commercially available precursors.

Spectroscopic Measurements. NMR spectra were collected at 298 K on a Bruker Avance 500 MHz spectrometer in dry, degassed $CDCl_3$. ^1H NMR spectra were referenced to tetramethylsilane (TMS) using the residual proteo impurities of the solvent (7.26 ppm). All chemical shifts are reported using the standard δ notation in parts per million; positive chemical shifts are to a higher frequency from the given reference. Electronic absorption spectra were recorded with a Jasco V-670 absorption spectrometer UV-vis-NIR spectrophotometer using 1-cm path-length cells at ambient temperature (20-24 °C).

Electrochemical Methods. Electrochemical experiments were performed on a Gamry Series G300 potentiostat/galvanostat/ZRA (Gamry Instruments, Warminster, PA) using a 3.0 mm glassy carbon working electrode, a platinum wire auxiliary electrode, and a silver wire pseudo-reference electrode. Electrochemical experiments were performed at ambient temperature (20-24°C) in a nitrogen-filled glovebox. Sample concentrations were 1.0 mM in analyte in a THF solution containing 100 mM $[NBu_4][PF_6]$ as the supporting electrolyte. All potentials are referenced to $[Cp_2Fe]^{+/0}$ as an internal standard. Ferrocene was purified by sublimation under reduced pressure and tetrabutylammonium hexafluorophosphate (Acros) was recrystallized from ethanol three times and dried under vacuum.

Crystallographic Methods. X-ray diffraction data for all complexes were collected on single crystals mounted on a glass fiber using paratone oil. Data was acquired using a Bruker SMART APEX II diffractometer equipped with a CCD detector at 88 K using Mo Kα radiation (λ = 0.71073 Å), which

was wavelength selected with a single-crystal graphite monochromator. The SMART program package was used to determine unit-cell parameters and for data collection. The raw frame data were processed using SAINT and SADABS to yield the reflection data file. Subsequent calculations were carried out using the SHELXTL program suite. The structures were solved by direct methods and refined on F2 by full-matrix least-squares techniques. Analytical scattering factors for neutral atoms were used throughout the analyses. Hydrogen atoms were generated in calculated positions and refined using a riding model. ORTEP diagrams were generated using ORTEP-3 for Windows.

Computational Methods. All calculations were performed employing the non-empirical tpss density functional theory using the quantum chemistry program package TURBOMOLE. For computational efficiency, initial geometry optimizations were performed using moderate split-valence plus polarization basis sets (def2-SVP).[45] Structures were refined using basis sets of triple zeta valence plus polarization (def2-TZVP) quality.[46] Crystal structures obtained from X-ray diffraction experiments were used as starting points for the geometry optimization; no molecular symmetry was imposed. Energies and minimum energy structures were evaluated self-consistently to tight convergence criteria (energy converged to 0.1 μHartree, maximum norm of the Cartesian gradient $\leq 10^{-4}$ a.u.). Linear-response time-dependent DFT was used to simulate electronic absorption spectra of the two series.

$Mo[SNS]_2\{Co(dppe)\}_2$. In a 20-mL Schlenk flask, $Mo[SNS]_2$ (137 mg, 0.223 mmol, 1.00 equiv.) was dissolved in THF (~10 mL). The purple reaction mixture was added to a freshly-prepared suspension of KC_8 (0.035 g K, 0.895 mmol, 4.00 equiv.) in THF (~4 mL). After stirring for ~15 min, the resulting dark brown reaction mixture with a vibrant yellow rim was chilled. To the chilled reaction was added the green solid $Co(dppe)Cl_2$ (236 mg, 0.448 mmol, 2.00 equiv.) as a solution in THF (~5 mL) and the resulting brown reaction mixture was stirred for 8 hours. The brown reaction mixture was then filtered through a plug of Celite (to remove graphite and KCl) and solvent was removed *in vacuo*. The residue was suspended in diethyl ether (~20 mL) and filtered via vacuum filtration to yield a dark solid. The solid was washed with diethyl ether (3 x 20 mL) to yield $Mo[SNS]_2\{Co(dppe)\}_2$ (172 mg, 82%).

Anal. Calcd. (Found) for $C_{80}H_{72}Co_2MoN_2P_4S_4$ (%): C, 62.91 (62.85); H, 4.75 (4.76); N, 1.83 (1.85). MS (ESI^+) *m/z*: 1527.9 ($[M]^+$). UV-vis (THF) λ_{max}/nm (ε / M^{-1} cm^{-1}): 465 (14,800).

$Mo[SNS]_2\{Cu(dppe)\}_2$. In a 100-mL Schlenk flask, $Mo[SNS]_2$ (154 mg, 0.250 mmol, 1.00 equiv.) was dissolved in THF (~10 mL). To the purple reaction mixture was added a freshly-prepared dark green solution of sodium naphthalide (64 mg $C_{10}H_8$, 0.50 mmol, 2.0 equiv.) in THF (~4 mL). To the resulting dark brown reaction with a vibrant yellow rim was added the white solid Cu(dppe)Cl (249 mg, 0.500 mmol, 2.00 equiv.) as a solution in THF (~5 mL) and the resulting vibrant maroon reaction mixture was stirred for 8 hours. The orange-red reaction mixture was then filtered through a plug of Celite (to remove NaCl) and solvent was removed *in vacuo*. The red residue was suspended in diethyl ether (~20 mL) and filtered via vacuum filtration to yield a vibrant red solid. The red solid was washed with diethyl ether (3 x 20 mL) to remove $C_{10}H_8$, to yield $Mo[SNS]_2\{Cu(dppe)\}_2$ (300 mg, 78%). Anal. Calcd. (Found) for $C_{80}H_{72}Cu_2MoN_2P_4S_4$ (%): C, 62.91 (62.89); H, 4.75 (4.78); N, 1.83 (1.84). ^1H NMR (400 MHz; C_6D_6) δ/ppm: 7.59 (d, J = 8.16 Hz, 2H, aryl–H), 7.43 (s, 2H, aryl–H), 7.32 (m, 10H, aryl–H), 6.89 (d, J = 7.76 Hz, 2H, aryl–H), 6.73 (d, J = 8.48 Hz, 2H, aryl–H), 6.32 (d, J = 8.60 Hz, 2H, aryl–H), 6.10 (s, 2H, aryl–H), 2.12 (s, 6H, $–CH_3$), 1.79 (s, 6H, $–CH_3$), 1.25 (m, 4H, $–CH_2$). ^{31}P $\{^1H\}$-NMR (162 MHz, $CDCl_3$) δ/ppm: –8. MS (ESI^+) *m/z*: 1534.9 ($[M]^+$). UV-vis (THF) λ_{max}/nm (ε / M^{-1} cm^{-1}): 466 (8,790).

Table 4.5. Crystal data and structure refinement for $Mo[SNS]_2\{Co(dppe)\}_2$ and $Mo[SNS]_2\{Cu(dppe)\}_2$.

Identity	$Mo[SNS]_2\{Co(dppe)\}_2$	$Mo[SNS]_2\{Cu(dppe)\}_2$
Empirical formula	$C_{80}H_{72}Co_2MoN_2P_4S_4 \bullet C_4H_8O$	$C_{80}H_{72}N_2P_4S_4Cu_2Mo \bullet (C_4H_8O)_5$
Formula weight (g/mol)	1599.42	1897.05
Crystal system	Triclinic	Monoclinic
Space group	P-1	$P2_1/n$
T (K)	133(2)	128(2)
a (Å)	14.5688(19)	18.7328(12)
b (Å)	16.168(2)	26.1541(17)
c (Å)	20.008(3)	18.7932(12)
α (º)	66.1792(14)	90
β (º)	87.3203(16)	97.9759(9)
ɣ (º)	66.0385(14)	90
V ($Å^3$)	3900.8(9)	9118.5(10)
Z	2	4
Refl. collected	45635	99127
Indep. refl.	17982	18657
R1 ($I > 2\sigma$)[a]	0.0308	0.0592
wR2 (all data)[b]	0.0804	0.1759

[a]$R1 = \Sigma||F_o|-|F_c|| / \Sigma|F_o|$, [b]$wR2 = [\Sigma[w(F_o^2-F_c^2)^2] / \Sigma[w(F_o^2)^2]]^{1/2}$

4.6 References

(1) Heyduk, A. F.; Macintosh, A. M.; Nocera, D. G. *J. Am. Chem. Soc.* **1999**, *121*, 5023–5032.

(2) Carroll, M. E.; Barton, B. E.; Gray, D. L.; Mack, A. E.; Rauchfuss, T. B. *Inorg. Chem.* **2011**, *50*, 9554–9563.

(3) Brogden, D. W.; Berry, J. F. *Inorg. Chem.* **2014**, *53*, 11354–11356.

(4) Gavrilova, A. L.; Bosnich, B. *Chem. Rev.* **2004**, *104*, 349–384.

(5) Denny, J. A.; Darensbourg, M. Y. *Chem. Rev.* **2015**, *115*, 5248–5273.

(6) Thomas, C. M. *Comments Inorg. Chem.* **2011**, *32*, 14–38.

(7) Kuppuswamy, S.; Bezpalko, M. W.; Powers, T. M.; Wilding, M. J. T.; Brozek, C. K.; Foxman, B. M.; Thomas, C. M. *Chem. Sci.* **2014**, *5*, 1617–1626.

(8) Krogman, J. P.; Thomas, C. M. *Chem. Comm.* **2014**, *50*, 5115–5127.

(9) Rudd, P. A.; Liu, S.; Gagliardi, L.; Young Jr, V. G.; Lu, C. C. *J. Am. Chem. Soc.* **2011**, *133*, 20724–20727.

(10) Clouston, L. J.; Siedschlag, R. B.; Rudd, P. A.; Planas, N.; Hu, S.; Miller, A. D.; Gagliardi, L.; Lu, C. C. *J. Am. Chem. Soc.* **2013**, *135*, 13142–13148.

(11) Eisenhart, R. J.; Clouston, L. J.; Lu, C. C. *Acc. Chem. Res.* **2015**, *48*, 2885–2894.

(12) Clouston, L. J.; Bernales, V.; Cammarota, R. C.; Carlson, R. K.; Bill, E.; Gagliardi, L.; Lu, C. C. *Inorg. Chem.* **2015**, *54*, 11669–11679.

(13) Eisenhart, R. J.; Carlson, R. K.; Clouston, L. J.; Young Jr, V. G.; Chen, Y.-S.; Bill, E.; Gagliardi, L.; Lu, C. C. *Inorg. Chem.* **2015**, *54*, 11330–11338.

(14) Shaffer, D. W.; Szigethy, G.; Ziller, J. W.; Heyduk, A. F. *Inorg. Chem.* **2013**, *52*, 2110–2118.

(15) Rosenkoetter, K. E.; Ziller, J. W.; Heyduk, A. F. *Inorg. Chem.* **2016**, *55*, 6794–6798.

(16) Rosenkoetter, K. E.; Ziller, J. W.; Heyduk, A. F. *Dalton Trans.* **2017**, *46*, 5503–5507.

(17) Wojnar, M. K.; Ziller, J. W.; Heyduk, A. F. *Eur. J. Inorg. Chem.* **2017**, 5571–5575.

(18) Herebian, D.; Bothe, E.; Bill, E.; Weyhermüller, T.; Wieghardt, K. *J. Am. Chem. Soc.* **2001**, *123*, 10012–10023.

(19) Ghosh, P.; Begum, A.; Herebian, D.; Bothe, E.; Hildenbrand, K.; Weyhermüller, T.; Wieghardt, K. *Angew. Chem. Int. Ed.* **2003**, *42*, 563–567.

(20) Sproules, S.; Banerjee, P.; Weyhermüller, T.; Yan, Y.; Donahue, J. P.; Wieghardt, K. *Inorg. Chem.* **2011**, *50*, 7106–7122.

(21) Sproules, S.; Wieghardt, K. *Coord. Chem. Rev.* **2011**, *255*, 837–860.

(22) Roy, N.; Sproules, S.; Weyhermüller, T.; Wieghardt, K. *Inorg. Chem.* **2009**, *48*, 3783–3791.

(23) Bailar Jr, J. C. *J. Inorg. Nucl. Chem.* **1958**, *8*, 165–175.

(24) Tenderholt, A. L.; Szilagyi, R. K.; Holm, R. H.; Hodgson, K. O.; Hedman, B.; Solomon, E. I. *Inorg. Chem.* **2008**, *47*, 6382–6392.

(25) Ashley, D. C.; Jakubikova, E. *Inorg. Chem.* **2018**, *57*, 5585–5596.

(26) Cordero, B.; Gómez, V.; Platero-Prats, A. E.; Revés, M.; Echeverría, J.; Cremades, E.; Barragán, F.; Alvarez, S. *Dalton Trans.* **2008**, 2832–2838.

(27) Yang, L.; Powell, D. R.; Houser, R. P. *Dalton Trans.* **2007**, 955–964.

(28) Curnow, O. J.; Curtis, M. D.; Kampf, J. W. *Organometallics* **1997**, *16*, 2523–2529.

(29) Brennessel, W. W.; Young, J., Victor G; Ellis, J. E. *Angewandte Chemie* **2002**, *114*, 1259–1263.

(30) Klein, H. F.; Karsch, H. H. *Inorg. Chem.* **1975**, *14*, 473–477.

(31) Darensbourg, D. J.; Chao, C. S.; Reibenspies, J. H.; Bischoff, C. J. *Inorg. Chem.* **1990**, *29*, 2153–2157.

(32) Comba, P.; Katsichtis, C.; Nuber, B.; Pritzkow, H. *Eur. J. Inorg. Chem.* **1999**, 777–783.

(33) Tsuboyama, A.; Kuge, K.; Furugori, M.; Okada, S.; Hoshino, M.; Ueno, K. *Inorg. Chem.* **2007**, *46*, 1992–2001.

(34) Takuma, M.; Ohki, Y.; Tatsumi, K. *Inorg. Chem.* **2005**, *44*, 6034–6043.

(35) Babashkina, M. G.; Safin, D. A.; Bolte, M.; Klein, A. *CrystEngComm.* **2010**, *12*, 134–143.

(36) Dou, J.; Zhang, D.; Li, D.; Wang, D. *Inorg. Chem. Commun.* **2006**, *9*, 1099–1102.

(37) Stylidou, V.; Kavaratzi, K.; Papazoglou, I.; Hatzidimitriou, A. G.; Papadopoulos, A. G.; Angaridis, P.; Aslanidis, P. *Eur. J. Inorg. Chem.* **2018**, 2915–2926.

(38) Sproules, S. *Prog. Inorg. Chem.* **2014**, *58*, 1–144.

(39) Rosenkoetter, K. E.; Wojnar, M. K.; Charette, B. J.; Ziller, J. W.; Heyduk, A. F. *Inorg. Chem.* **2018**, *57*, 9728–9737.

(40) Cotton, F. A.; Murillo, C. A.; Walton, R. A. *Multiple bonds between metal atoms*; Springer Science & Business Media: **2005**.

(41) Zanello, P. *Inorganic electrochemistry: theory, practice and application*; Royal Society of Chemistry: **2007**.

(42) Berry, J. F. *Dalton Trans.* **2012**, *41*, 700–713.

(43) Chipman, J. A.; Berry, J. F. *Chem. Eur. J.* **2018**, *24*, 1494–1499.

(44) Cremades, E.; Echeverría, J.; Alvarez, S. *Chem. Eur. J.* **2010**, *16*, 10380–10396.

(45) Schäfer, A. *J. Chem. Phys.* **1992**, *97*, 2571–2577.

(46) Schäfer, A.; Huber, C.; Ahlrichs, R. *J. Chem. Phys.* **1994**, *100*, 5829–5835.

Chapter 5

Synthesis and Characterization of a Library of $M[SNS]_2$ Metalloligands Incorporating Group IV, V, VI Metals

5.1 Introduction

The controlled and tunable synthesis of heteromultimetallic systems is sought after to model metalloenzyme active sites, and more importantly, emulate their performances in catalytic multielectron chemistry. However, the generation of these systems typically involves multinucleating ligands[1-4] or cluster self-assembly processes[5,6] which both have disadvantages around design and control of the cluster. A way to circumvent this problem is through the use of metalloligands, consisting of stable coordination compounds that can bind to other metal centers.[7-9] The quintessential metalloligand is the Ni(N_2S_2) family of complexes, which have shown to bind to a variety of metal ions, leading to a library of multimetallic complexes.[10] It has also been hypothesized that the Ni(N_2S_2) metalloligand in the active site in acetyl-coenzyme A synthetase (ACS) stabilizes a reduced form of the bimetallic system through metal-metal interactions, the two-electron-reduction leading to formation of a Ni-Ni bond where the electrons reside (Figure 5.1 (left)).[11] Moreover, the hemilability of these metalloligands, coupled to the redox properties of the secondary metal it is appended to, is postulated to be a primary reason for these systems being active electrocatalysts for H_2 production (Figure 5.1 (right)).[12,13]

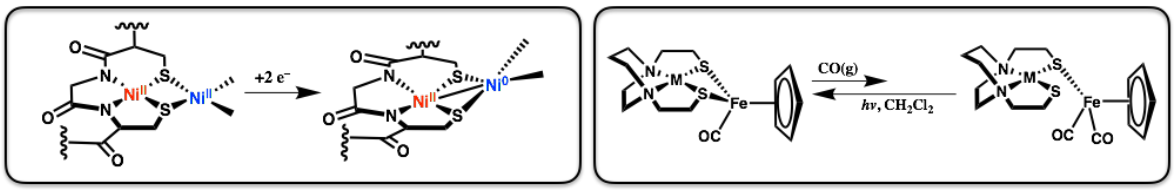

Figure 5.1. Active site of acetyl-coenzyme A synthetase (ACS) upon reduction (left) and M(N_2S_2)Fe hemilability (right).

Recently, it has been shown that M[SNS]$_2$ coordination compounds, encapsulating high-valent Group VI metals Mo and W within a fully-reduced [SNS]$^{3-}$ pocket, can bind to secondary, and also tertiary metal centers, with the M[SNS]$_2$ metalloligand functioning as a bridge.[14,15] The M[SNS]$_2$ metalloligand can engender new reactivity to the secondary metal center, making it an active catalyst for proton reduction.[16] Moreover, the M[SNS]$_2$ complexes can also lead to the generation of mixed-valent complexes, allowing for the preparation of redox species in near identical coordination environments, in which electronic communication through metal-metal bonds between metal centers can be investigated. In order to fully understand the electronic structure of these multimetallic

systems, it is imperative to understand the electronic structure of the $M[SNS]_2$ metalloligand bridge. As has been shown previously, chemical understanding of the bridge framework and the molecular orbitals involved with the mixed-valent complexes is crucial to understanding the degree of electronic communication between redox sites.[17-19]

It is well known that oxidation state assignment may be difficult due to the covalency involved in molecular systems.[20] In these systems, "molecular redox" may better describe the one-electron reactions because the redox event is occurring in a molecular orbital that is distributed over the entire molecule.[21] Covalency leads to a variety of different properties, from optical and electrochemical (as will be described below), as well as magnetic properties, due to the fact that magnetic anisotropy is directly correlated to electronic structure.[22,23] These electronic structure-function relationships have implications toward reactivity: it has been hypothesized that the covalency involved in the interaction of the axial thiolate with the iron center in cytochrome P450s leads to distinct reactivity[24], and the redox isomerism in Betley's high-spin ferric imido/iminyl complexes encourages C–H bond functionalization.[25] Covalency also lends itself for unique applications as well, including metal chalcogenide interactions for photovoltaics and batteries[26], and even as catalysts for CO_2 reduction.[27] A battery of techniques has been utilized to understand the fundamental interactions in these systems, from electron paramagnetic resonance spectroscopy (EPR), X-ray absorption spectroscopy (XAS), to computations.[28-30]

To understand covalency in these metalloligand systems, a library of $M[SNS]_2$ complexes has been synthesized in which the central metal ion has been systematically varied. By changing the central metal ion from more electronegative Group VI metals to more electropositive Group IV metals, one can begin to understand the interaction between the soft [SNS] ligands and the transition metal, which can, in turn, lead to a better understanding of the multimetallic systems.

5.2 Results

5.2.1 Synthesis of $M[SNS]_2$ Metalloligands

The metalloligands $K_x[M[SNS]_2]$ (M = Hf, Zr, Ti, x = 2; Ta, Nb, V, x = 1) were prepared via a

salt metathesis strategy by adding two equivalents of fully-deprotonated K_3[SNS] ligand to one equivalent of the corresponding commercially-available metal halide, $MCl_y(THF)_z$ ($HfCl_4$ (**1**), $ZrCl_4$ (**2**), $TiCl_4$ (**3**), z=2; $TaCl_5$ (**4**), $NbCl_5$ (**5**), (z=0); VCl_3 (**6**) (z=3)). To a stirring suspension of potassium hydride (KH) in dry tetrahydrofuran was added via cannula transfer a yellow solution of [SNS]H_3. After dihydrogen evolution, to the putative fully-deprotonated K_3[SNS] was added $MCl_y(THF)_z$ to generate the K_x[M[SNS]$_2$] metalloligands in yields ranging from 51%-71%. The reaction mixtures were filtered to remove KCl. The Group VI metalloligands W[SNS]$_2$ and Mo[SNS]$_2$ have been previously synthesized.[14,15] Formation of the desired complex was signified by a change of color, which is dependent on the choice of the central metal ion (*vide infra*). Electrospray mass spectrometry (in negative ion mode) exhibited a parent mass ion peak for the anionic Group IV and V metalloligands. Synthetic caution was taken in preparing "valence isoelectronic" (d^0) metalloligand derivatives for comparison purposes.

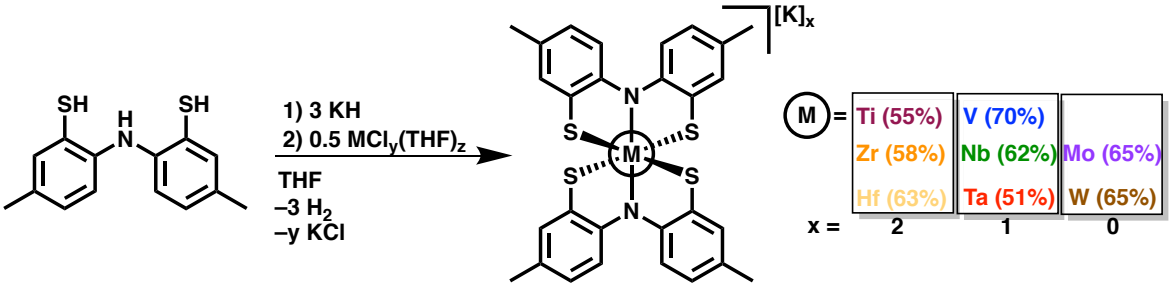

Scheme 5.1. Synthesis of K_x[M[SNS]$_2$] metalloligands. Percent yields for Mo[SNS]$_2$ and W[SNS]$_2$ taken from references 15 and 14, respectively.

5.2.2 Structural Analysis of M[SNS]$_2$ Metalloligands

X-ray crystallography was employed to confirm connectivity and geometric structure of the metalloligands (Figure 5.2). [Ta[SNS]$_2$]$^{-1}$ was crystallized as the triethylbenzylammonium complex, [N(Et)$_3$Bn][Ta[SNS]$_2$] and crystallizes in the triclinic space group, P-1. [Nb[SNS]$_2$]$^{-1}$ was crystallized as the [K(18-Crown-6)][M[SNS]$_2$] complex in the monoclinic space group, C2/*c*. [V[SNS]$_2$]$^{-1}$ was crystallized with the [K(18-Crown-6)(12-Crown-4)] countercation in the monoclinic space group, P2$_1$/*n*. Although X-ray quality crystals of Group IV dianions could not be obtained, preliminary diffraction experiments of the complexes demonstrate the stoichiometry (two [K(18-Crown-6)] countercations per one M[SNS]$_2$) and connectivity of the Group IV metalloligands. All of the struc-

tures are six-coordinate and exhibit a coordination geometry that falls on the spectrum between an ideal trigonal prism and trigonal antiprism (octahedron). To quantitatively determine the geometry of these geometries, the twist angle and the X–M–X trans angles were calculated. The twist angle (or Bailar twist) refers to the torsion angle between the vertices of the trigonal plane.[31] For a trigonal prism, the twist angle is 0°. For a trigonal antiprism, the twist angle is 60°. Between these two extremes lies a pseudo-octahedral molecular geometry. The two trigonal planes defined for the $M[SNS]_2$ metalloligands consisted of two atoms from the same [SNS] ligand and a single atom from the other ligand; both trigonal planes are made up of two sulfur atoms (from different [SNS] ligands) and a nitrogen atom (Figure 5.3). For M = Mo, W, Nb, and Ta, the first trigonal plane is composed of S(1), S(3), and N(1), while the second trigonal face is S(2), S(4), N(2). For M = V, the first trigonal plane is composed of S(1), S(4), and N(2), while the second trigonal face is S(2), S(3), N(1). As can be seen in Table 5.1, the twist angle for the metalloligands ($0° < \theta < 60°$) puts this class of molecules in the pseudo-octahedral regime of geometries, with $V[SNS]_2^{-1}$ (θ_{avg}=45.0°) lying the closest to an octahedron and Mo[SNS] (θ_{avg}=9.3°) to a trigonal prism. Additionally, the X–Mo–X angle of atoms trans to each other is 180° for a perfect octahedron and less than 180° for a distortion to a trigonal prism. In agreement with the twist angle parameters, $V[SNS]_2^{-1}$ ($\angle_{avg}$=158°) exhibits X–Mo–X angles closest to 180° and $Mo[SNS]_2$ ($\angle_{avg}$=139°) furthest from 180° but with all values indicative of pseudo-octahedral geometries.

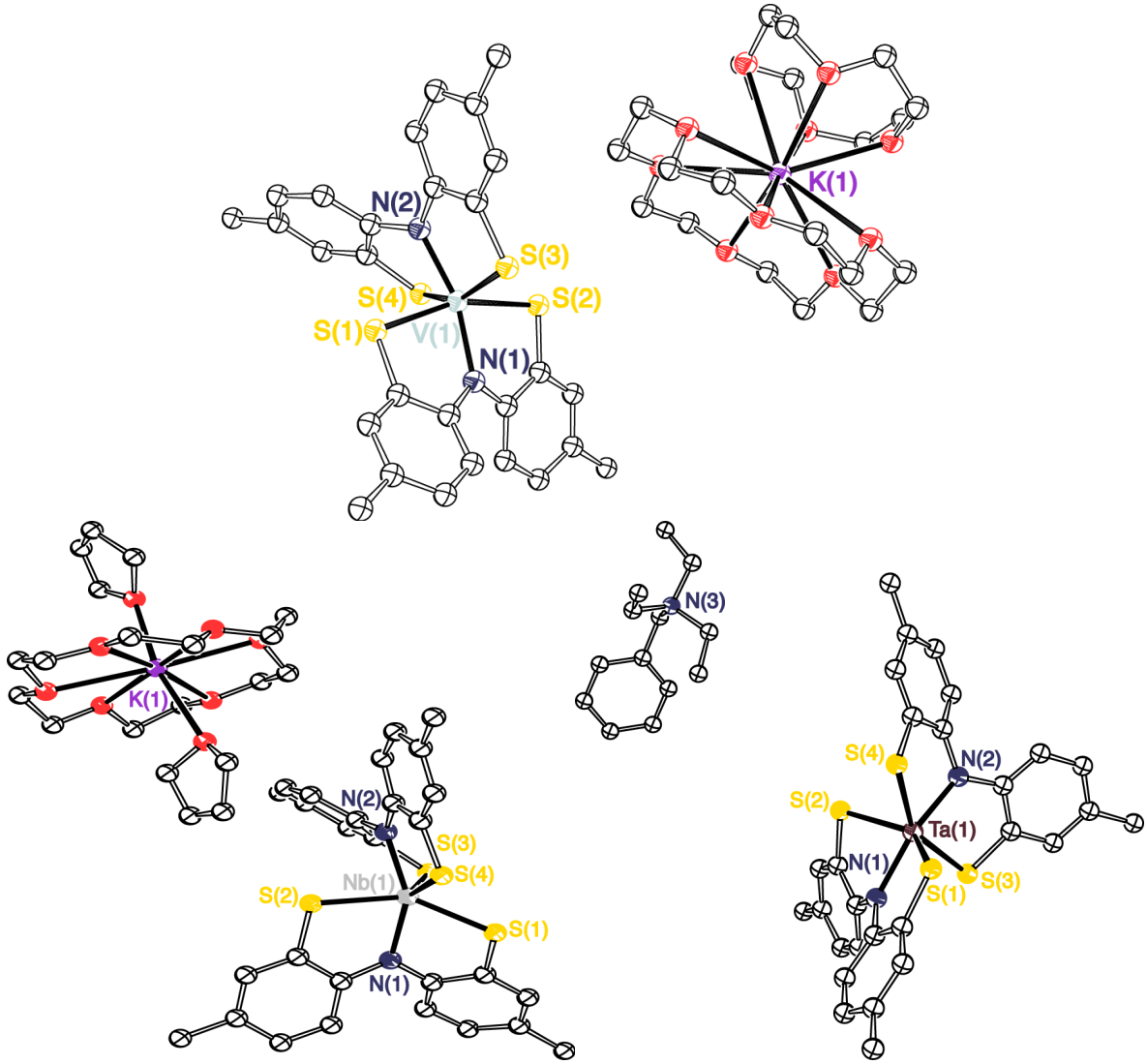

Figure 5.2. X-ray crystal structures of $[M[SNS]_2]^-$ (M = V, Nb, Ta) with thermal ellipsoids shown at 50% probability. Hydrogen atoms (and three THF molecules in $[Ta[SNS]_2]^{-1}$ have been removed for clarity.

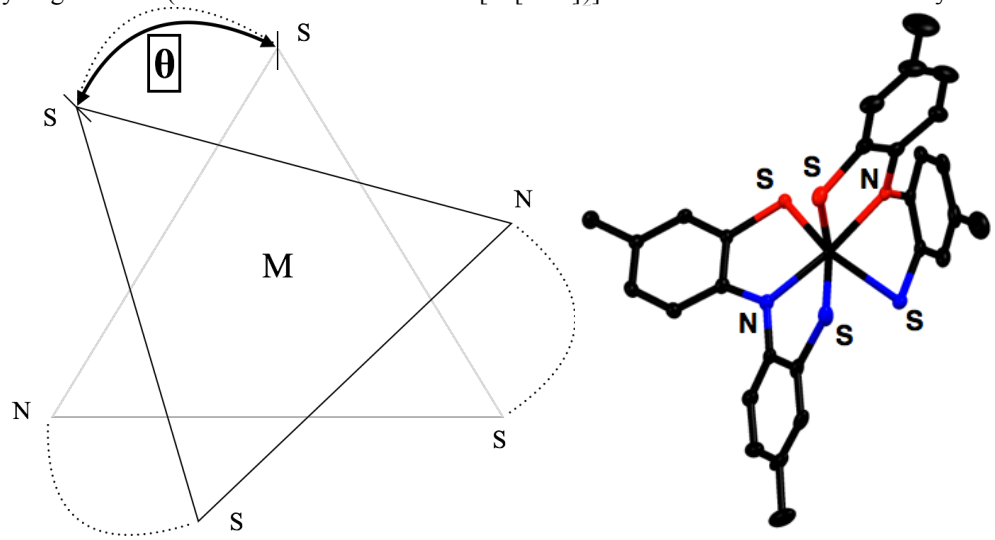

Figure 5.3. Bailar twist (θ) demonstrating the geometric constraints of a trigonal prism and trigonal antiprism (left) and definition of the two trigonal faces in $M[SNS]_2$ metalloligands, denoted by red and blue colors (right).

Table 5.1. Bailar twist (θ) values for $K_x[M[SNS]_2]$ metalloligands.

	$Mo[SNS]_2$	$W[SNS]_2$	$V[SNS]_2^{-1}$	$Nb[SNS]_2^{-1}$	$Ta[SNS]_2^{-1}$
$\theta_{S,S}$	4.2	9.3	27.7	3.6	2.90
$\theta(1)_{N,S}$	10.7	27.3	46.4	25.7	18.9
$\theta(2)_{N,S}$	13.0	33.2	60.9	14.6	34.1

The bond distances for the metalloligands are consistent with a fully-reduced [SNS] ligand set (Table 5.4). In the primary coordination sphere, the metal–sulfur and metal–nitrogen bond lengths increase in size on going from the Group VI to the Group V metalloligands and are consistent with the covalent radii of the respective metal ions (Table 5.2).[32] The V–S[33], Nb–S[34], and Ta–S[35] bond lengths are similar to complexes incorporating those metal ions in other six-coordinate sulfur-containing-ligand environments. In bidentate ortho-aminothiophenolate ligands, the ligand in the fully-reduced catecholate oxidation state contains C–S and C–N bond distances of 1.76 Å and 1.41 Å, respectively. The semiquinonate oxidation state is characterized by C–S and C–N bond distances of 1.72 Å and 1.36 Å, respectively.[36-39] Another signifier of an oxidized [SNS] ligand set is partial localization of double-bond character within the aryl rings with differences between the longest and shortest C–C bonds of about 0.06 Å. Besides the molybdenum-containing metallolloligand, there is minimal localized double bond character within the phenyl rings, so the ligands can still be described as fully-reduced trianionic ligands. C–C bond contractions are also hypothesized to be less prominent in sulfur-containing non-innocent ligands, as the primary locus of oxidation is at the sulfur atom or the sulfur-carbon molecular orbital.[40] Upon moving from Ta to Mo, a slight oxidation of the [SNS] ligand set is seen by contraction of the C–N and C–S bond metrics. While the Group VI metalloligands have mean C–S and C–N bond lengths of 1.74 Å and 1.39 Å-1.40 Å, respectively, the values slightly (although consistently) increase upon shifting to the Group V metalloligands, affording average C–S and C–N bond lengths of 1.75 Å and 1.40 Å-1.41 Å. This trend in ligand oxidation has been observed in systems concerning the tris(dithiolene) family of complexes.[41] The changes in bond metrics for

$Mo[SNS]_2$, in contrast to the rest of the metalloligands, coincides with [SNS] ligand oxidation observed in $[SNS]Ni^{II}PR_3$ systems, which also displays average C–S and C–N of 1.74 Å and 1.39 Å.[42]

Table 5.2. Selected bond distances of $K_x[M[SNS]_2]$ metalloligands.

	$Mo[SNS]_2$	$W[SNS]_2$	$V[SNS]_2^{-1}$	$Nb[SNS]_2^{-1}$	$Ta[SNS]_2^{-1}$
M(1)–S(1)	2.3411(6)	2.3942(4)	2.341(1)	2.4300(9)	2.419(1)
M(1)–S(2)	2.3975(6)	2.3718(4)	2.387(1)	2.4173(8)	2.453(1)
M(1)–S(3)	2.3816(6)	2.3296(4)	2.335(1)	2.4427(8)	2.4157(8)
M(1)–S(4)	2.3791(6)	2.3732(4)	2.358(1)	2.4604(9)	2.4270(9)
M(1)–N(1)	2.099(2)	2.0592(14)	2.012(3)	2.153(2)	2.103(3)
M(1)–N(2)	2.048(2)	2.0843(13)	2.014(4)	2.104(3)	2.120(3)

Table 5.3. Selected bond angles of $K_x[M[SNS]_2]$ metalloligands.

	$Mo[SNS]_2$	$W[SNS]_2$	$V[SNS]_2^{-1}$	$Nb[SNS]_2^{-1}$	$Ta[SNS]_2^{-1}$
N(1)–M(1)–S(1)	78.96(5)	78.76(4)	80.5(1)	77.06(7)	77.44(9)
N(1)–M(1)–S(2)	77.41(5)	79.41(4)	80.23(9)	77.21(7)	78.62(9)
N(2)–M(1)–S(3)	80.87(5)	80.09(4)	81.8(1)	79.17(7)	77.40(8)
N(1)–M(1)–N(2)	151.19(7)	155.27(5)	161.1(1)	150.50(9)	153.9(1)
S(1)–M(1)–S(2)	131.26(2)	145.17(1)	159.97(5)	142.93(3)	135.64(3)
S(3)–M(1)–S(4)	135.57(2)	152.65(1)	153.59(5)	133.25(3)	149.96(3)

Table 5.4. Average intraligand bond distances for $K_x[M[SNS]_2]$ metalloligands.

	$Mo[SNS]_2$	$W[SNS]_2$	$V[SNS]_2^{-1}$	$Nb[SNS]_2^{-1}$	$Ta[SNS]_2^{-1}$
$S–C_{avg}$	1.74	1.74	1.74	1.76	1.75
$N–C_{avg}$	1.39	1.41	1.40	1.41	1.42
$(\Delta C–C)_{avg}$	0.07	0.04	0.04	0.04	0.03

5.2.3 Spectroscopic Analysis of $M[SNS]_2$ Metalloligands

All homoleptic metal complexes have diamagnetic ground states and were analyzed by ^1H NMR in CD_3CN for the Group IV and Group V metal ions. In CD_3CN, all complexes exhibit D_2 symmetry, with one singlet in the aliphatic region between 2.15 ppm and 2.28 ppm, which can be assigned to the methyl group on the [SNS] ligand backbone, as well as two doublets and a singlet in

the aromatic region between 6.50 ppm and 7.60 ppm, which can be attributed to the twelve aromatic protons of the [SNS] ligands.

UV-vis spectroscopy proved crucial in elucidating the electronic structure of the metalloligands (Figure 5.4). The color of the metalloligand complex was shown to depend on the identity of the central metal: hafnium (yellow), zirconium (orange), titanium (maroon), tantalum (dark red), niobium (yellow-green), vanadium (dark blue), tungsten (purple-brown), molybdenum (purple). By varying the central metal, the energies of the transitions shift. Group IV metals (Hf, Zr, Ti) show transitions between 300 nm and 600 nm. Group V metals (Ta, Nb, V) exhibited red-shifted charge-transfer transitions between 300 nm and 800 nm. Group VI metals demonstrated transitions to lower energies, as far as 1000 nm. Table 5.5 includes the values for the transitions. Previous assignment of the [Mo] metalloligand as $Mo^{VI}[SNS]^{3-}_2$ (consisting of fully-reduced ligands and a fully-oxidized metal) dictates that these transitions must be ligand-to-metal charge-transfer bands.

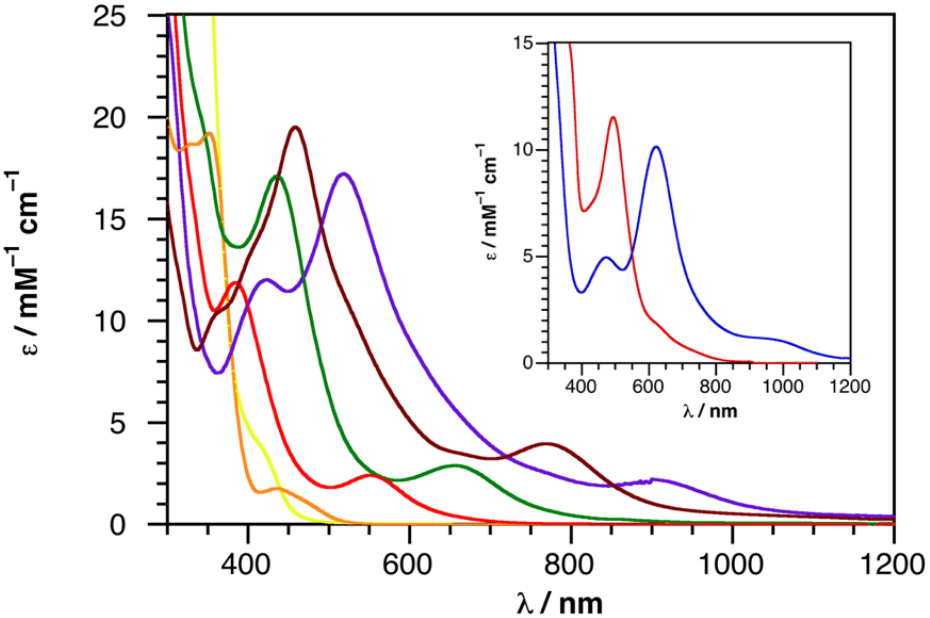

Figure 5.4. Electronic absorption spectra of $K_x[M[SNS]_2]$ metalloligands in THF (M = Hf (yellow); Zr (orange); Ta (red); Nb (green); W (brown); Mo (purple) (Inset contains absorption spectra of $K_2[Ti[SNS]_2]$ (maroon) and $K[V[SNS]_2]$ (blue)).

Table 5.5. Optical transitions of the $K_x[M[SNS]_2]$ metalloligands.

	Transitions with $\varepsilon > 5$ mM^{-1} cm^{-1}	Transitions with $\varepsilon < 5$ mM^{-1} cm^{-1}
$K_2[Hf[SNS]_2]$	< 400 nm	~408 nm (shoulder, 4.25)
$K_2[Zr[SNS]_2]$	< 400 nm	436 nm (1.76)
$K_2[Ti[SNS]_2]$	< 400 nm, 494 nm (11.55)	~625 nm (shoulder, 1.82)
$K[Ta[SNS]_2]$	384 nm (11.88)	552 nm (2.41)
$K[Nb[SNS]_2]$	436 nm (17.11)	656 nm (2.89)
$K[V[SNS]_2]$	472 nm (4.96), 621 nm (10.16)	~1000 nm (broad shoulder, 1.02)
$W[SNS]_2$	461 nm (19.3)	766 nm (3.62)
$Mo[SNS]_2$	424 nm (7.41), 520 nm (10.6)	900 nm (2.21)

5.2.4 Electrochemical Analysis of $M[SNS]_2$ Metalloligands

Electrochemical experiments were performed on the metalloligands to probe the electronic properties of these systems. For all of the metalloligands, from Hf to Mo, two characteristic features are observed in the cyclic voltammograms: 1) an irreversible oxidation 2) one to two reversible or quasi-reversible reductions. All electrochemical experiments were performed in THF, and all redox events were referenced to the Fc/Fc^+ redox couple (Table 5.6). While Hf and Zr show no reductive events within the solvent window, one-electron reductions were observed starting with titanium. The Ti- and Ta-based metalloligands demonstrated one quasi-reversible reduction. Upon reaching Nb, two reductions were observed, and these reductions shifted anodically upon moving to V, W, and Mo (in that order). The potential difference between the first oxidation and first reduction varied as a function of metal identity. The gap between the first oxidation and first reduction is a method to gauge the separation between the HOMO ([SNS] ligand orbitals) and the LUMO (central metal d orbitals) at equilibrium.[43,44] This equilibrium HOMO-LUMO gap measurement was better assessed via differential pulse voltammetry (DPV), due to the irreversible nature of the oxidations (Figure 5.5). A notable characteristic is the strong dependence of the reduction ($[M]^{0/1-}$) potentials on the identity of the central metal. While varying the metal did lead to variations in the potential of the first oxidation (~700 mV variation from Ti to Mo, according to DPV), the reduction potentials exhibited a much more substan-

tial change (~2.0 V). For the metalloligands that showed two reductions (not illustrated in Figure 5.5), the separation between the first and second reduction increased when the metal was varied, in the order Mo (0.83 V) < W (0.94 V) < V (1.44 V) < Nb (1.66 V).

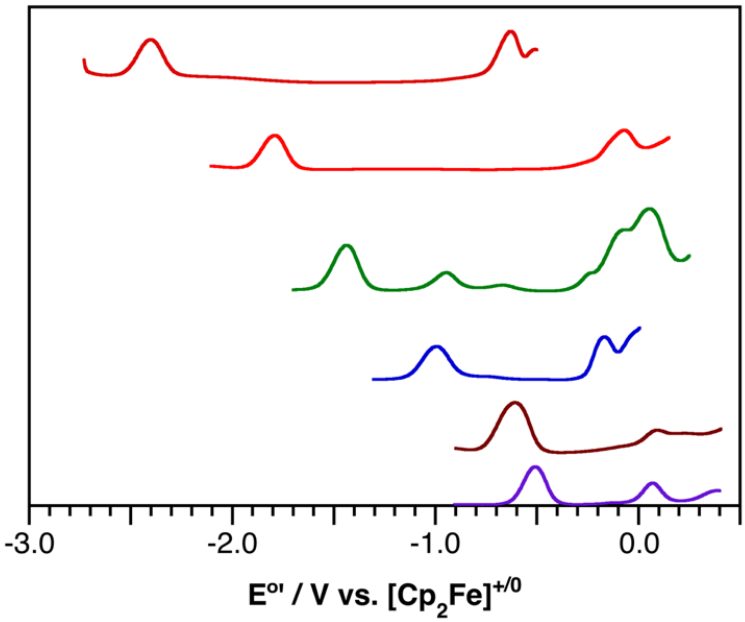

Figure 5.5. Differential pulse voltamograms of $K_x[M[SNS]_2]$ metalloligands (M (top to bottom) = Ti (maroon); Ta (red); Nb (green); V (blue); W (brown); Mo (purple)).

Table 5.6. Electrochemical potentials of the first oxidation, first/second reductions, and difference in potential of $K_x[M[SNS]_2]$ metalloligands, collected by differential pulse voltammetry experiments in THF.

	$E_1°'$ ($[M]^{+1/0}$)	$E_2°'$ ($[M]^{0/1-}$)	$E_3°'$ ($[M]^{1-/2-}$)		$E_1°' - E_2°'$	$E_2°' - E_3°'$
$K_2[Ti[SNS]_2]$	–0.63	–2.40	–		1.77	–
$K[Ta[SNS]_2]$	–0.07	–1.79	–		1.72	–
$K[Nb[SNS]_2]$	–0.07	–1.43	–3.09		1.36	1.66
$K[V[SNS]_2]$	–0.16	–0.99	–2.43		0.83	1.44
$W[SNS]_2$	0.09	–0.61	–1.55		0.70	0.94
$Mo[SNS]_2$	0.07	–0.51	–1.34		0.58	0.83

5.2.5 Computational Analysis of $M[SNS]_2$ Metalloligands

To support the frontier molecular orbital picture provided by experiment, density functional theory (DFT) computations were employed. The X-ray crystal structures were used as the starting point for geometry minimizations, which were refined at the TPSS/TZVP level of theory. All complexes were refined as closed-shell, S=0, ground-state species. The purpose of the computations was

three-fold: to ascertain the energies of the HOMO and LUMO, and as a result, the energy difference (HOMO-LUMO gap); to quantify the contributions of the metal and ligand orbitals to the HOMO and LUMO molecular orbitals; to utilize time-dependent DFT (TD-DFT) to rationalize the experimental spectroscopic observations. First, DFT confirms the relative energies of the HOMO and LUMO, and the HOMO-LUMO gap (provided in Table 5.7). With regards to each Group of the periodic table analyzed (IV, V, VI), it is shown that the more electronegative elements (1st row > 2nd row > 3rd row) are lower in energy and lead to a smaller HOMO-LUMO gap (Figure 5.6). More drastically, upon moving from left to right across the periodic table, the electronegativity values of the elements increase (Group IV < Group V < Group VI), leading to a net lowering of the metal orbitals.[45] For the eight distinct metalloligands, it is observed that the HOMO is predominantly [SNS]-ligand-based and the LUMO mainly of metal character. As the orbital energies approach each other, the HOMO adopts more metal character and the LUMO adopts more ligand character. As a result, with variation in metal identity, the metal contribution to the HOMO varies in the order: Mo (15.55%) > W (12.49%) > V (10.07%) > Nb (7.99%) > Ti (7.65%) > Ta (7.14%) > Zr (5.57%) > Hf (5.27%). Table 5.8 provides the amount of metal and ligand character for both molecular orbitals. Lastly, TD-DFT confirms the observed optical properties of the metalloligands. In all cases, the lowest energy transition corresponds to a HOMO–1 → LUMO transition. Due to the fact that the HOMO–1 is ligand-based, while the LUMO is metal-based, this transition can be assigned as a ligand-to-metal charge transfer (LMCT) transition. The two main transitions (higher energy transition and lower energy transition) are calculated and listed in Table 5.9.

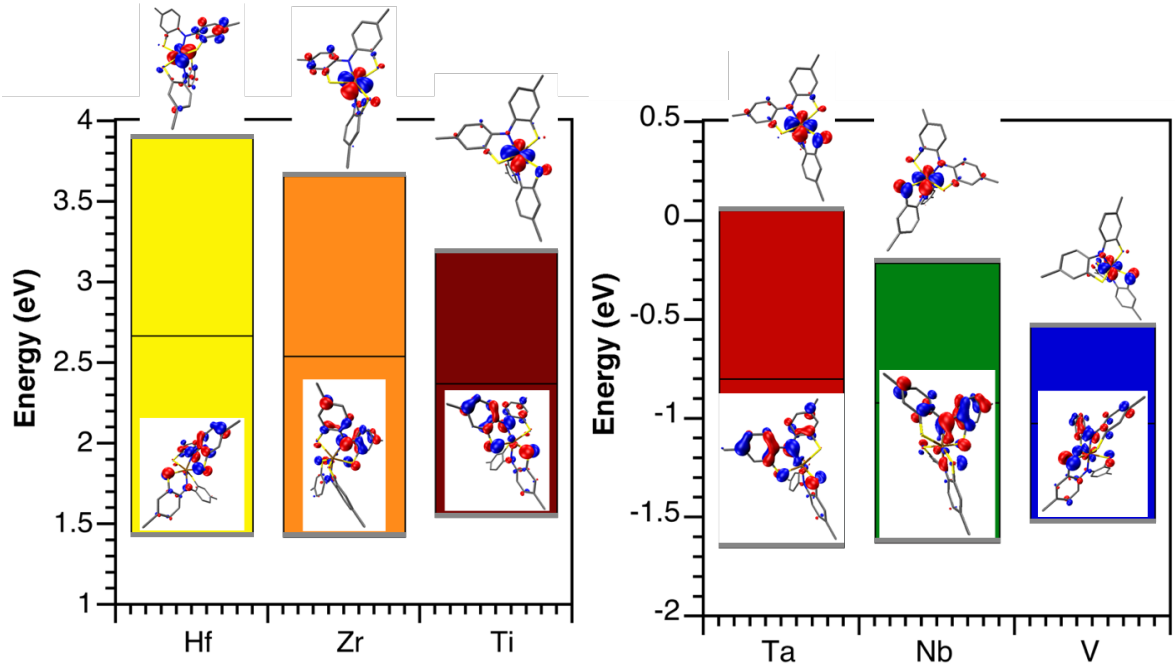

Figure 5.6. HOMO-LUMO gap energies for the Group IV (left) and Group V (right) metalloligands, calculated with the TPSS functional at the TZVP level of theory.

Table 5.7. HOMO-LUMO gap Kohn-Sham energies of $K_x[M[SNS]_2]$ metalloligands, calculated with the TPSS functional at the TZVP level of theory.

	Energy of HOMO (eV)	Energy of LUMO (eV)	HOMO–LUMO Gap Energy Difference
$K_2[Hf[SNS]_2]$	+1.43	+3.91	2.48
$K_2[Zr[SNS]_2]$	+1.42	+3.66	2.24
$K_2[Ti[SNS]_2]$	+1.54	+3.20	1.66
$K[Ta[SNS]_2]$	–1.65	+0.05	1.70
$K[Nb[SNS]_2]$	–1.63	–0.21	1.42
$K[V[SNS]_2]$	–1.52	–0.53	0.99
$W[SNS]_2$	–4.77	–3.61	1.16
$Mo[SNS]_2$	–4.77	–3.68	1.09

Table 5.8. Kohn-Sham Mulliken population analyses of $K_x[M[SNS]_2]$ metalloligands, calculated with the TPSS functional at the TZVP level of theory.

	Character of HOMO	Character of LUMO
$K_2[Hf[SNS]_2]$	5.27% Metal 94.73% [SNS]	45.99% Metal 54.01% [SNS]
$K_2[Zr[SNS]_2]$	5.57% Metal 94.43% [SNS]	61.62% Metal 38.38% [SNS]
$K_2[Ti[SNS]_2]$	7.65% Metal 92.35% [SNS]	77.81% Metal 22.19% [SNS]
$K[Ta[SNS]_2]$	7.14% Metal 92.86% [SNS]	63.67% Metal 36.33% [SNS]
$K[Nb[SNS]_2]$	7.99% Metal 92.01% [SNS]	63.73% Metal 36.27% [SNS]
$K[V[SNS]_2]$	10.07% Metal 89.93% [SNS]	67.65% Metal 32.35% [SNS]
$W[SNS]_2$	12.49% Metal 87.51% [SNS]	48.95% Metal 51.05% [SNS]
$Mo[SNS]_2$	15.55% Metal 84.45% [SNS]	49.31% Metal 50.69% [SNS]

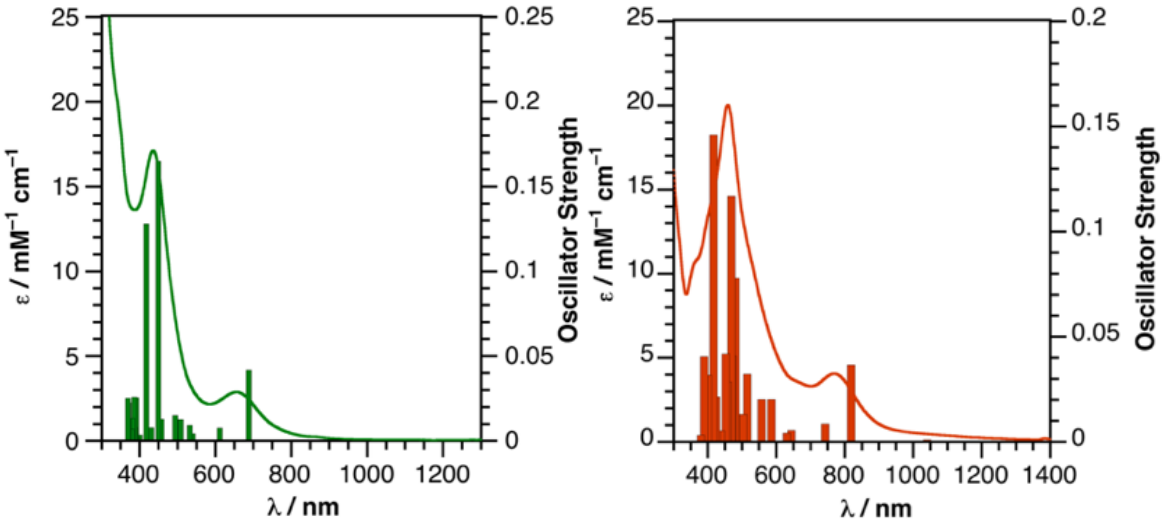

Figure 5.7. Time-dependent density functional theory (TD-DFT) calculations performed for $K[Nb[SNS]_2]$ (left) and $W[SNS]_2$ (right), calculated with the TPSS functional at the TZVP level of theory.

Table 5.9. Nature of the transitions for the time-dependent density functional theory (TD-DFT) calculations of $K_x[M[SNS]_2]$ metalloligands, calculated with the TPSS functional at the TZVP level of theory.

	High Energy/Intensity Transition	Low Energy/Intensity Transition
$K_2[Hf[SNS]_2]$	HOMO–3 → LUMO (λ_{max}=373 nm)	HOMO–1 → LUMO (λ_{max}=452 nm)
$K_2[Zr[SNS]_2]$	HOMO–5 → LUMO (λ_{max}=364 nm)	HOMO–1 → LUMO (λ_{max}=492 nm)
$K_2[Ti[SNS]_2]$	HOMO–1 → LUMO+1 (λ_{max}=474 nm)	HOMO–1 → LUMO (λ_{max}=633 nm)
$K[Ta[SNS]_2]$	HOMO → LUMO+2 (λ_{max}=411 nm)	HOMO–1 → LUMO (λ_{max}=602 nm)
$K[Nb[SNS]_2]$	HOMO → LUMO+2 (λ_{max}=449 nm)	HOMO–1 → LUMO (λ_{max}=687 nm)
$K[V[SNS]_2]$	HOMO–1 → LUMO+1 (λ_{max}=541 nm)	HOMO–1 → LUMO (λ_{max}=909 nm)
$W[SNS]_2$	HOMO–1 → LUMO (λ_{max}=415 nm)	HOMO–1 → LUMO (λ_{max}=818 nm)
$Mo[SNS]_2$	HOMO–5 → LUMO+1 (λ_{max}=436 nm)	HOMO–1 → LUMO (λ_{max}=900 nm)

5.3 Discussion

The electronic structure of the $M[SNS]_2$ metalloligands is best exemplified in Figure 5.8.[46] The metalloligands all exhibit a pseudo-octahedral geometry, with the following metal d orbital splitting: dz^2 < dxy, $dx^2–y^2$ < dxz, dyz. Differences in energy between the degenerate e sets (dxy, $dx^2–y^2$ and dxz, dyz) can be explained by the lack of symmetry imposed on the geometry optimizations. The area of focus is the frontier energetic region where the ligand orbitals end and the metal orbitals begin, labeled as $\Delta E_{HOMO–LUMO}$. It is this area that can be probed by chemical means, including inducing optical excitations that directly interrogate the difference in energy between molecular orbitals, as well as electrochemical means, by oxidizing and reducing the two prominent orbitals (Figure 5.9). Ligand oxidation, investigated via X-ray crystallography, also gives a measure of how close in energy the metal and ligand orbitals reside thereby providing a "reporter"[47] to look at the HOMO-LUMO gap in these metalloligand systems. Computations confirm this phenomenon structurally, energetically, and optically via geometry optimizations, Mulliken population analyses, and TD-DFT calculations, respectively.

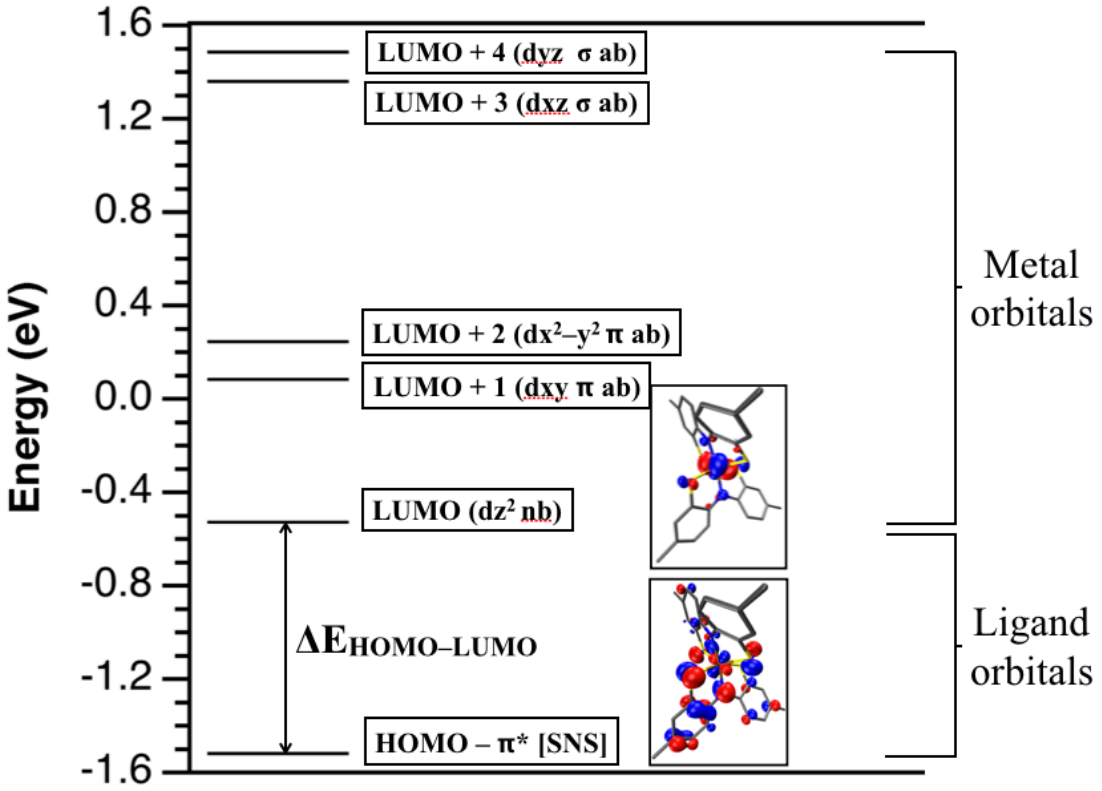

Figure 5.8. Electronic structure of $M[SNS]_2$ metalloligands.

X-ray crystallography establishes the connectivity and coordination geometry of the $M[SNS]_2$ metalloligands, with the redox non-innocent [SNS] ligands acting as "reporters" for ligand oxidation state. The Group V and VI metalloligands exhibited coordination geometries between that of a perfect trigonal prism and octahedron, a common geometry in multidentate sulfur-containing ligands. Interactions between the metal d orbitals and the π systems on the sulfur-atoms/aromatic backbones have been hypothesized to support these sterically less favorable geometries.[48] The intraligand bond metrics for this ligand are less diagnostic of ligand oxidation state (in comparison to redox-active ligands like catechol or aminophenol) due to small changes in C–S, C–N, and C–C bond distances. These minor bond length fluctuations upon redox can be attributed to poor overlap between the large p orbitals on sulfur and the p orbitals of carbon and nitrogen, leading to less delocalization of charge into the π backbone. Investigations of the [SNS] ligand coordinated to a nickel ion in a square planar environment confirmed the redox-active nature of this ligand. Specifically, upon formal oxidation of the fully-reduced [SNS] ligand, a ligand-based radical is generated, with average C–S and C–N bond dis-

tance contractions from 1.76 Å to 1.74 Å, and 1.40 Å to 1.39 Å, respectively.[42] For the metalloligand systems, these intraligand bond distance changes reflect the covalency, or energetic and spatial overlap of metal and ligand orbitals. For the more electronegative elements (i.e. Mo, W, and V), partial oxidation of the [SNS] ligands are observed (i.e. π back-bonding). Upon moving to the less electronegative Nb/Ta, the bond distances elongate, consistent with separation of metal and ligand orbitals.

This covalency as a function of metal identity is evident in the spectroscopy of these metalloligand systems. As has already been stated, the $M[SNS]_2$ coordination complexes are best described as d^0 electron configurations with two fully-reduced trianionic [SNS] ligands. Due to where the electrons are polarized (toward the ligand), the transitions observed by UV-vis spectroscopy are ligand-to-metal charge-transfer transitions. As the metal is varied from the more electronegative Group VI metal ions to the most electropositive Group IV ions, the energy of light absorbed blue shifts. This is consistent with a frontier molecular orbital scheme in which the highest occupied molecular orbital, HOMO (and all of the filled orbitals that are lower in energy) are ligand-based, while the lowest unoccupied molecular orbital, LUMO (and all of the unfilled orbitals that are higher in energy) are metal-based. As the metal ion becomes progressively more electropositive, the ligand and metal orbitals separate energetically. It is this energetic separation that electronic absorption spectroscopy probes. For $Mo[SNS]_2$, the metal and ligand orbitals are closest in energy, leading to the lowest energy light absorbed, with a charge-transfer transition at 900 nm. Switching out Mo for W leads to a blue-shift of this low energy transition to 766 nm. Incorporation of Group V metals shifts the transition to even higher energy, consistent with a greater degree of metal and ligand orbital separation. The vibrant yellow and orange colors of $K_2[Hf[SNS]_2]$ and $K_2[Zr[SNS]_2]$ are attributed to the absorption of high energy light, at the limit of the visible spectrum (400 nm). While the second- and third-row transition metals exhibit the same spectroscopic profile, $[Ti[SNS]_2]^{2-}$ and $[V[SNS]_2]^{-}$ demonstrate different absorption signatures. This is attributed to the weaker metal-ligand bonds for the 3d metal ions, with this weaker ligand-field splitting affording lower energy metal-centered states.[49-51]

This hypothesis of a ligand-based HOMO and a metal-based LUMO was consistent with the voltammetry data of these metalloligands. In general, cyclic voltammograms of these coordination complexes displayed an irreversible oxidation and 1-2 reversible/quasi-reversible reductions. These voltammetric profiles are consistent with electrochemical studies on Group VI tris(dithiolene) complexes. The irreversibility of the oxidations was attributed to ligand-localized redox, with the radical character on the unprotected sulfur atoms leading to substantial rearrangement. In other complexes containing this ligand, this was observed chemically. For K{[SNS]Ni(PPh_3)}, oxidation of the [SNS] ligand led to dimerization of the complex, {[SNS]Ni(PPh_3)}$_2$.[42] The reversible reductions are hypothesized to be metal-based, in which input of an electron into a non-bonding d orbital of the M[SNS]$_2$ metalloligand should require minimal geometric distortion. The dependence of the first reduction on metal choice corroborates this electrochemical assignment as well. Moving from the Group VI analogues Mo[SNS]$_2$ to W[SNS]$_2$ saw a 20 mV shift in the oxidation, with a 100 mV shift in the reduction. The Group V metalloligands had oxidations that ranged 90 mV, with first reductions that ranged 800 mV. The comparison between the three groups of the periodic table is flawed because the Group VI metalloligands exist as neutral species, the Group V analogues as anions, and the Group IV systems as dianions. This difference in overall charge of the complex is observed in the first oxidation of the metalloligands: a dianion (K_2[Ti[SNS]$_2$]) is easier to oxidize than a monoanion (K[V[SNS]$_2$]), which is easier to oxidize than the corresponding neutral complex (Mo[SNS]$_2$). Electrostatic contributions to redox potentials, which includes counterion[52] and medium[53] choice, have previously been quantified in mixed-valent multi-ferrocenyl heterocycles.[54]

With this in mind, the electrochemistry still can provide a handle to assess HOMO-LUMO gaps (at equilibrium) of these systems. The potentials of the events give information on localization of redox, and the difference in potential between the first oxidation and first reduction speaks to the separation in the frontier molecular orbitals. Strong correlations between charge transfer transitions and electrochemical potential differences between first oxidation and first reduction have been observed previously.[55,56] In agreement with the spectroscopy, differential pulse voltammetry displayed an in-

creasing separation between the ligand-based orbitals (HOMO) and metal-based orbitals (LUMO). As the transition metals were varied from electronegative Group VI metals to electropositive Group IV metals, the electrochemical gap increased (larger separation between first oxidation and first reduction), and this was manifested spectroscopically, with transitions increasing in energy. The Hf and Zr metalloligands did not exhibit first reductions in the THF solvent window, which is consistent with the trend: the gap is so large that it cannot be observed under these electrochemical conditions. This trend in HOMO-LUMO gap/covalency measurements of Group IV, V, and VI metal complexes is in agreement with recent work on metallocene systems of Mo, V, and Ti incorporating dithiolenes.[57,58]

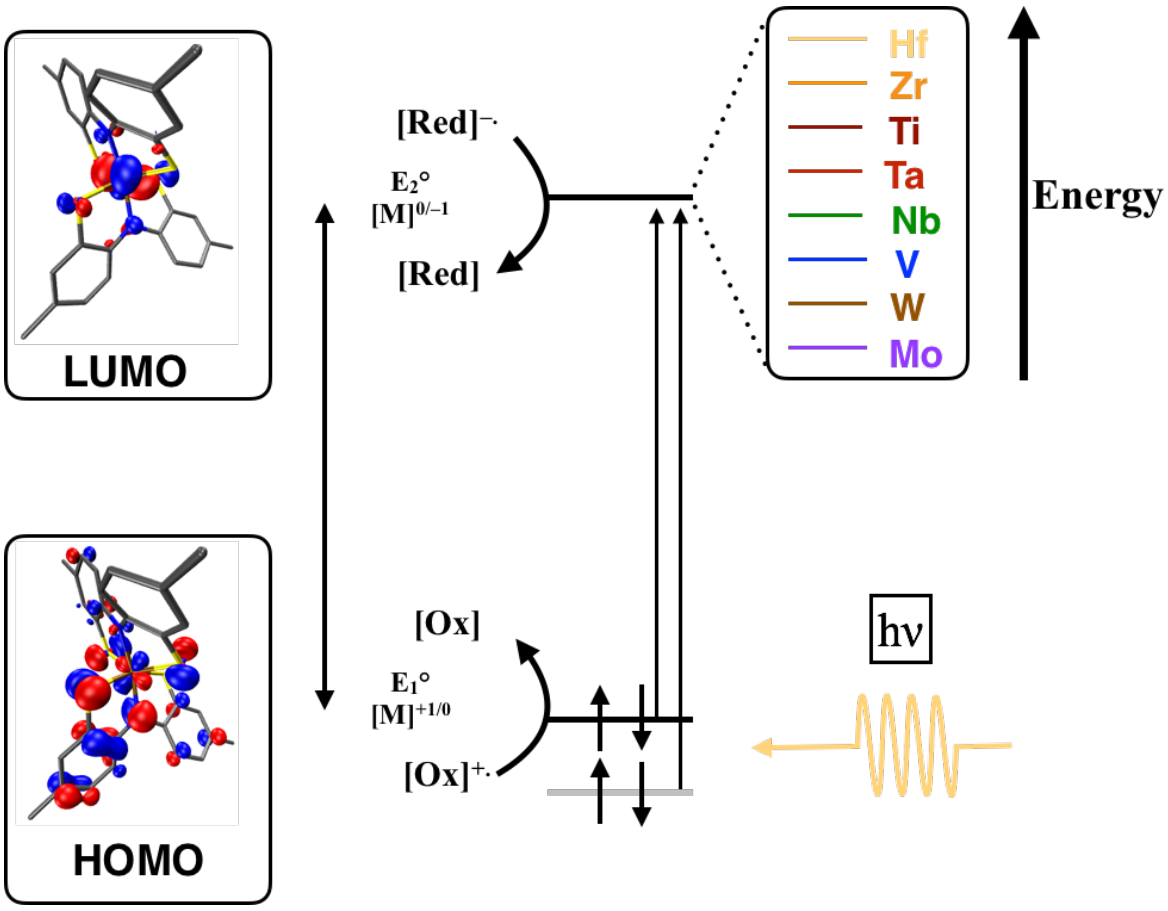

Figure 5.9. Variation of HOMO-LUMO gap as a function of metal choice.

The separation between the first and second reduction also provide a gauge to measure covalency in the M[SNS]$_2$ systems. This separation measures the electronic communication between metal and ligand redox sites. The stronger the communication (i.e. electron delocalized over a molecular orbital with both metal and ligand contribution), the smaller the separation between reductions.[59,60]

As the metal and ligand orbitals begin to separate energetically on going from Mo, W, V, and Nb (as observed by both the difference in first oxidation and first reduction, as well as the UV-vis spectra of the metalloligands), the separation between the first and second reduction increases. This separation is indicative of the reduction becoming more metal-localized. For covalent systems with delocalization over both metal and ligand, electron-electron repulsion is minimized, which is observed as a smaller separation between reductions in the electrochemistry. As the metal and ligand orbitals energetically diverge, delocalization is curtailed and electron-electron repulsion becomes a more substantial factor, leading to a greater separation between reduction events.

These characterization methods were in agreement with DFT calculations, which confirmed the notion of a ligand-based HOMO and a metal-based LUMO, as well as the separation between them. Mulliken population analysis (MPA) on the HOMO had [SNS] ligand contributions ranging from 84% (for the Group VI metalloligands) to 95% (for the Group IV metalloligands). MPA of the LUMO yielded metal contributions of 46% to 78%. The smaller metal ion contributions from $K_2[Hf[SNS]_2]$ and $K_2[Zr[SNS]_2]$ are based on the metal d orbitals being much more electropositive (higher in energy) that calculations compute contributions from a π^* orbital to the LUMO of the [SNS] ligand. The difference in energy between the HOMO and LUMO was also confirmed computationally within each group, with the gap increasing as one goes down the column (decreasing electronegativity). While the absolute values (based on gas-phase calculations) between groups could not be compared due to the overall charge of the complex, the relative separation still generally held the trend: V< Mo < W < Nb < Ta ≤ Ti < Zr < Hf. DFT calculations compute the smallest HOMO-LUMO gap for $K[V[SNS]_2]$, although it is relatively close in energy to the Group VI analogues. TD-DFT calculations are in agreement with the spectroscopic data as well, affirming both the energy and relative intensity of the two main transitions observed by electronic absorption spectroscopy. For both transitions, the electron is calculated to come from a ligand-based orbital, to be transferred to a metal-based orbital.

5.4 Conclusion

To understand the complete electronic structure of the $M[SNS]_2$ metalloligands, a library was synthesized that involves the insertion of high-valent Group IV, Group V, and Group VI metals into the hexa-anionic pocket of the tetrathiolato-bis-amido framework. HOMO-LUMO gap measurements were conducted optically and electrochemically, and confirmed computationally, to identify the character of the frontier molecular orbitals. Solid-state- and solution-based measurements confirm the oxidation state assignment of the metalloligands as $K_x[M^{VI-x}[SNS^{cat}]_2]$. The highest molecular orbital is mainly ligand-based in character, with the lowest unoccupied molecular orbital consisting mostly of metal character. Upon electing more electronegative elements for the bis-[SNS] cavity, the HOMO-LUMO gap decreases in energy, and as a result, covalency yields FMO's of significant metal and ligand character. Variation of metal ion with distinct differences in electronegativity provides a direct probe to understand covalency in six-coordinate $M[SNS]_2$-based systems. Electronic assignment of these $M[SNS]_2$ metalloligands is imperative in order to interrogate these systems as molecular bridges in heteromultimetallic mixed-valent cluster compounds. Tuning covalency of the metalloligand bridge can lead to variations in electronic coupling between exterior metal centers in the corresponding heterotrimetallic systems.

5.5 Experimental

General Considerations. All compounds and reactions reported below show varied degrees of air- and moisture-sensitivity, therefore all manipulations were carried out using standard vacuum-line, Schlenk-line and glovebox techniques. Solvents were sparged with argon before being deoxygenated and dried by passage through Q5 and activated alumina columns, respectively. To test for effective oxygen and water removal, aliquots of each solvent were treated with a few drops of a purple solution of sodium benzophenone ketyl radical in THF. $HfCl_4(THF)_2$, $ZrCl_4(THF)_2$, and $TiCl_4(THF)_2$, and $VCl_3(THF)_3$ were synthesized following literature procedures from commercially available precursors.[61] $TaCl_5$ and $NbCl_5$ were purchased from Alfa-Aesar and used as received.

Spectroscopic Measurements. NMR spectra were collected at 298 K on a Bruker Avance 400 MHz

spectrometer in dry, degassed CD_3CN. ^1H NMR spectra were referenced to tetramethylsilane (TMS) using the residual proteo impurities of the solvent (7.26 ppm). All chemical shifts are reported using the standard δ notation in parts per million; positive chemical shifts are to a higher frequency from the given reference. Electronic absorption spectra were recorded with a Jasco V-670 absorption spectrometer UV-vis-NIR spectrophotometer using 1-cm path-length cells at ambient temperature (20-24°C).

Electrochemical Methods. Electrochemical experiments were performed on a Gamry Series G300 potentiostat/galvanostat/ZRA (Gamry Instruments, Warminster, PA) using a 3.0 mm glassy carbon working electrode, a platinum wire auxiliary electrode, and a silver wire pseudo-reference electrode. Electrochemical experiments were performed at ambient temperature (20-24°C) in a nitrogen-filled glovebox. Sample concentrations were 1.0 mM in analyte in a THF solution containing 100 mM $[NBu_4][PF_6]$ as the supporting electrolyte. All potentials are referenced to $[Cp_2Fe]^{+/0}$ using ferrocene as an internal standard. Ferrocene was purified by sublimation under reduced pressure and tetrabutylammonium hexafluorophosphate (Acros) was recrystallized from ethanol three times and dried under vacuum.

Crystallographic Methods. X-ray diffraction data for all complexes were collected on single crystals mounted on a glass fiber using paratone oil. Data was acquired using a Bruker SMART APEX II diffractometer equipped with a CCD detector at 88 K using Mo Kα radiation (λ = 0.71073 Å), which was wavelength selected with a single-crystal graphite monochromator. The SMART program package was used to determine unit-cell parameters and for data collection. The raw frame data were processed using SAINT and SADABS to yield the reflection data file. Subsequent calculations were carried out using the SHELXTL program suite. The structures were solved by direct methods and refined on F2 by full-matrix least-squares techniques. Analytical scattering factors for neutral atoms were used throughout the analyses. Hydrogen atoms were generated in calculated positions and refined using a riding model. ORTEP diagrams were generated using ORTEP-3 for Windows.

Computational Methods. All calculations were performed employing the non-empirical tpss density

functional theory using the quantum chemistry program package TURBOMOLE. For computational efficiency, initial geometry optimizations were performed using moderate split-valence plus polarization basis sets (def2-SVP).[62] Structures were refined using basis sets of triple zeta valence plus polarization (def2-TZVP) quality.[63] Crystal structures obtained from X-ray diffraction experiments were used as starting points for the geometry optimization; no molecular symmetry was imposed. Energies and minimum energy structures were evaluated self-consistently to tight convergence criteria (energy converged to 0.1 μHartree, maximum norm of the Cartesian gradient $\leq 10^{-4}$ a.u.). Linear-response time-dependent DFT was used to simulate electronic absorption spectra of the two series.

$[SNS^{cat}]H_3$. The $[SNS^{cat}]H_3$ ligand platform was synthesized according to a four-step procedure from a literature preparation. All compounds were verified using ^{1}H NMR and obtained in comparable yields throughout all synthetic steps.[14]

General Synthesis of $K_x[M[SNS]_2]$ (M = Hf, Zr, Ti, Ta, Nb; x = 1-2). To a chilled flask containing potassium hydride (KH) was added a golden-yellow solution of $[SNS]H_3$ in dry THF via cannula transfer to yield a golden-yellow solid suspension in THF stirred to room temperature. Via a solid addition funnel was added the appropriate metal chloride and the reaction mixture was stirred overnight. The next day, the reaction mixture was filtered through a plug of Celite to remove KCl. The reaction solution was concentrated to a minimum of solvent and pentane was used to crash out a solid powder, which was subsequently washed with diethyl ether and dried in vacuo to yield the desired $[K(THF)_x][M[SNS]_2]$ complex.

$K_2[Hf[SNS]_2]$. To the golden-yellow suspension of the putative $K_3[SNS]$, generated from $[SNS]H_3$ (255 mg, 0.975 mmol, 2.00 equiv.) and KH (119 mg, 2.98 mmol, 6.1 equiv.), was added $HfCl_4$ (156 mg, 0.488 mmol, 1.00 equiv.) via solid addition funnel to yield a homogeneous vibrant yellow solution that was stirred overnight, filtered, washed with diethyl ether, and dried *in vacuo* to yield $K_2[Hf[SNS]_2]$ (238 mg, 63%). MS (ESI$^-$) *m/z*: calcd for $[C_{28}H_{24}N_2S_4HfK]$, 735.0; found 736.9 ($[M+H]^-$). ^{1}H NMR (400 MHz; CD_3CN) δ/ppm: 7.13 (d, *J* = Hz, 4H, aryl–H), 6.87 (s, 4H, aryl–H),

6.5 (d, *J* = Hz, 4H, aryl–H), 2.15 (s, 12H, –CH_3). UV-vis (THF) λ_{max}/nm (ε / M^{-1} cm^{-1}): < 400 (> 20,000), 408 (< 5,000).

K_2[Zr[SNS]$_2$]. To the golden-yellow suspension of the putative K_3[SNS], generated from [SNS]H_3 (578 mg, 2.21 mmol, 2.00 equiv.) and KH (268 mg, 6.69 mmol, 6.05 equiv.), was added $ZrCl_4(THF)_2$ (417 mg, 1.10 mmol, 1.00 equiv.) via solid addition funnel to yield a homogeneous vibrant orange solution that was stirred overnight, filtered, washed with diethyl ether, and dried *in vacuo* to yield K_2[Zr[SNS]$_2$] (438 mg, 58%). MS (ESI$^-$) *m/z*: calcd for [$C_{28}H_{24}N_2S_4ZrK$], 645.0; found 646.8 ([M+H]$^-$). ^{1}H NMR (400 MHz; CD_3CN) δ/ppm: 7.17 (d, *J* = Hz, 4H, aryl–H), 6.87 (s, 4H, aryl–H), 6.51 (d, *J* = Hz, 4H, aryl–H), 2.15 (s, 12H, –CH_3). UV-vis (THF) λ_{max}/nm (ε / M^{-1} cm^{-1}): < 400 (> 20,000), 436 (1,760).

K_2[Ti[SNS]$_2$]. To the golden-yellow suspension of the putative K_3[SNS], generated from [SNS]H_3 (279 mg, 1.07 mmol, 2.00 equiv.) and KH (129 mg, 3.23 mmol, 6.05 equiv.), was added $TiCl_4(THF)_2$ (178 mg, 0.533 mmol, 1.00 equiv.) via solid addition funnel to yield a homogeneous dark red/maroon solution that was stirred overnight. The next day, the reaction mixture was filtered and washed with diethyl ether to yield K_2[Ti[SNS]$_2$] (188 mg, 55%**)**. MS (ESI$^-$) *m/z*: calcd for [$C_{28}H_{24}N_2S_4TiK$], 602.0; found 603.9 ([M+H]$^-$). ^{1}H NMR (400 MHz; CD_3CN) δ/ppm: 7.18 (d, *J* = Hz, 4H, aryl–H), 6.78 (s, 4H, aryl–H), 6.54 (d, *J* = Hz, 4H, aryl–H), 2.17 (s, 12H, –CH_3). UV-vis (THF) λ_{max}/nm (ε / M^{-1} cm^{-1}): 494 (11,600), 625 (1,820).

K[Ta[SNS]$_2$]. To the golden-yellow suspension of the putative K_3[SNS], generated from [SNS]H_3 (209 mg, 0.800 mmol, 2.00 equiv.) and KH (98 mg, 2.4 mmol, 6.1 equiv.), was added $TaBr_5$ (232 mg, 0.400 mmol, 1.00 equiv.) via solid addition funnel to yield a homogeneous dark red solution that was stirred overnight, filtered, and solvent was removed in vacuo. The remaining residue was suspended in diethyl ether, filtered, washed with diethyl ether, and dried in vacuo to yield K[Ta[SNS]$_2$] (150 mg, 51%). Crystals were obtained by addition of [$NBnEt_3$][Cl] to a solution of $K(THF)_x$[Ta[SNS]$_2$] in THF, and diffusion of this THF solution into pentane. MS (ESI$^-$) *m/z*: calcd for [$C_{28}H_{24}N_2S_4Ta$], 698.0; found 698.0 ([M]$^-$). ^{1}H NMR (400 MHz; CD_3CN) δ/ppm: 7.46 (d, *J* = 8.40 Hz, 4H, aryl–H),

7.02 (s, 4H, aryl–H), 6.85 (d, J = 7.92 Hz, 4H, aryl–H), 2.28 (s, 12H, –CH_3). UV-vis (THF) λ_{max}/nm (ε / M^{-1} cm^{-1}): 384 (11,900), 552 (2,410).

K[Nb[SNS]$_2$]. To the golden-yellow suspension of the putative K_3[SNS], generated from [SNS]H_3 (270 mg, 1.03 mmol, 2.00 equiv.) and KH (126 mg, 3.15 mmol, 6.10 equiv.), was added $NbCl_5$ (140 mg, 0.518 mmol, 1.00 equiv.) via solid addition funnel to yield a homogeneous dark olive-green solution that was stirred overnight, filtered, and solvent was removed in vacuo. The remaining residue was suspended in diethyl ether, filtered, washed with diethyl ether, and dried in vacuo to yield K[Nb[SNS]$_2$] **(**208 mg, 62%**)**. Crystals were obtained by addition of 18-Crown-6 to a THF solution of K(THF)$_x$[Nb[SNS]$_2$], and diffusion of the THF solution into pentane. ^{1}H NMR (400 MHz; CD_3CN) δ/ ppm: 7.52 (d, J = 8.40 Hz, 4H, aryl–H), 7.04 (s, 4H, aryl–H), 6.87 (d, J = 8.40 Hz, 4H, aryl–H), 2.28 (s, 12H, –CH_3). MS (ESI$^-$) *m/z*: calcd for [$C_{28}H_{24}N_2S_4Nb$], 608.7; found 609.0 ([M]$^-$). UV-vis (THF) λ_{max}/nm (ε / M^{-1} cm^{-1}): 436 (17,100), 656 (2,890) .

K[V[SNS]$_2$]. To the golden-yellow suspension of the putative K_3[SNS], generated from [SNS]H_3 (343 mg, 1.31 mmol, 2 equiv.) and KH (159 mg, 3.97 mmol, 6.05 equiv.), was added $VCl_3(THF)_3$ (245 mg, 0.660 mmol, 1.00 equiv.) with $PhICl_2$ (180 mg, 0.660 mmol, 1.00 equiv.) via solid addition funnel to yield a homogeneous dark blue-green solution. After stirring for ~15 minutes, the reaction mixture was exposed to air, yielding a dark blue reaction mixture, which was stirred for ~12 hours. The next day, the reaction mixture was filtered and solvent was removed in vacuo. The remaining residue was suspended in diethyl ether, filtered, washed with diethyl ether, and dried in vacuo to yield K[V[SNS]$_2$] **(**280 mg, 70%**)**. Crystals were obtained by addition of 18-Crown-6 to a THF solution of K(THF)$_x$[V[SNS]$_2$], and diffusion of the THF solution into pentane. MS (ESI$^-$) *m/z*: calcd for [$C_{28}H_{24}N_2S_4V$], 567.0; found 567.1 ([M]$^-$). ^{1}H NMR (400 MHz; CD_3CN) δ/ppm: 7.17 (d, J = 8.48 Hz, 4H, aryl–H), 6.92 (s, 4H, aryl–H), 6.72 (d, J = 8.40 Hz, 4H, aryl–H), 2.35 (s, 12H, –CH_3). UV-vis (THF) λ_{max}/nm (ε / mM^{-1} cm^{-1}): 472 (4,960), 621 (10,200).

Table 5.10. Crystal data and structure refinement for [K(18-Crown-6)(12-Crown-4)][$V[SNS]_2$], [K(18-Crown-6)$(THF)_2$] [$Nb[SNS]_2$], and [$N(Et)_3(Bn)$][$Ta[SNS]_2$].

Identity	[K(18-Crown-6)(12-Crown-4)][$V[SNS]_2$]	[K(18-Crown-6)$(THF)_2$] [$Nb[SNS]_2$]	[$N(Et)_3(Bn)$][$Ta[SNS]_2$]
Empirical formula	$C_{48}H_{64}KN_2O_{10}S_4V$	$C_{48}H_{64}KN_2NbO_8S_4$	$C_{53}H_{70}N_3O_3S_4Ta$
Formula weight (g/mol)	1047.29	1057.26	1105.38
Crystal system	Monoclinic	Monoclinic	Triclinic
Space group	$P2_1/n$	$C2/c$	P-1
T (K)	133(2)	88(2)	133(2)
a (Å)	13.6433(18)	24.8476(11)	9.9854(7)
b (Å)	18.632(3)	11.8823(5)	14.3609(10)
c (Å)	20.197(3)	34.1671(15)	19.4976(13)
α (°)	90	90	73.4581(8)
β (°)	94.5879(17)	92.7653(6)	75.7667(8)
ɣ (°)	90	90	73.1133(8)
V ($Å^3$)	5117.6(12)	10076.0(8)	2523.8(3)
Z	4	8	2
Refl. collected	39150	60745	28950
Indep. refl.	9724	12661	11069
R1 ($I > 2\sigma$)[a]	0.0703	0.0498	0.0358
wR2 (all data)[b]	0.2245	0.1278	0.0903

[a]$R1 = \Sigma||F_o|-|F_c|| / \Sigma|F_o|$, [b]$wR2 = [\Sigma[w(F_o^2-F_c^2)^2] / \Sigma[w(F_o^2)^2]]^{1/2}$

5.6 References

(1) Greenwood, B. P.; Forman, S. I.; Rowe, G. T.; Chen, C.-H.; Foxman, B. M.; Thomas, C. M. *Inorg. Chem.* **2009**, *48*, 6251–6260.

(2) Rudd, P. A.; Liu, S.; Gagliardi, L.; Young Jr, V. G.; Lu, C. C. *J. Am. Chem. Soc.* **2011**, *133*, 20724–20727.

(3) Manz, D. H.; Duan, P. C.; Dechert, S.; Demeshko, S.; Oswald, R.; John, M.; Mata, R. A.; Meyer, F. *J. Am. Chem. Soc.* **2017**, *139*, 16720–16731.

(4) Zhou, Y. Y.; Hartline, D. R.; Steiman, T. J.; Fanwick, P. E.; Uyeda, C. *Inorg. Chem.* **2014**, *53*, 11770–11777.

(5) Long, J. R.; Williamson, A. S.; Holm, R. H. *Angew. Chem. Int. Ed. Engl.* **1995**, *34*, 226–229.

(6) Tulsky, E. G.; Long, J. R. *Inorg. Chem.* **2001**, *40*, 6990–7002.

(7) Flowers, S. E.; Cossairt, B. M. *Organometallics* **2014**, *33*, 4341–4344.

(8) Li, F.; Carpenter, S. H.; Higgins, R. F.; Hitt, M. G.; Brennessel, W. W.; Ferrier, M. G.; Cary, S. K.; Lezama-Pacheco, J. S.; Wright, J. T.; Stein, B. W.; Shores, M. P.; Neidig, M. L.; Kozimor, S. A.; Matson, E. M. *Inorg. Chem.* **2017**, *56*, 7065–7080.

(9) Lau, N.; Sano, Y.; Ziller, J. W.; Borovik, A. S. *Dalton Trans.* **2018**, *47*, 12362–12372.

(10) Denny, J. A.; Darensbourg, M. Y. *Chem. Rev.* **2015**, *115*, 5248–5273.

(11) Lindahl, P. A. *J. Inorg. Biochem.* **2012**, *106*, 172–178.

(12) Ding, S.; Ghosh, P.; Lunsford, A. M.; Wang, N.; Bhuvanesh, N.; Hall, M. B.; Darensbourg,

M. Y. *J. Am. Chem. Soc.* **2016**, *138*, 12920–12927.

(13) Ding, S.; Ghosh, P.; Darensbourg, M. Y.; Hall, M. B. *Proc. Natl. Acad. Sci. U.S.A.* **2017**, *114*, E9775–E9782.

(14) Shaffer, D. W.; Szigethy, G.; Ziller, J. W.; Heyduk, A. F. *Inorg. Chem.* **2013**, *52*, 2110–2118.

(15) Wojnar, M. K.; Ziller, J. W.; Heyduk, A. F. *Eur. J. Inorg. Chem.* **2017**, *2017*, 5571–5575.

(16) Rosenkoetter, K. E.; Ziller, J. W.; Heyduk, A. F. *Inorg. Chem.* **2016**, *55*, 6794–6798.

(17) Kubiak, C. P. *Inorg. Chem.* **2013**, *52*, 5663–5676.

(18) Glover, S. D.; Kubiak, C. P. *J. Am. Chem. Soc.* **2011**, *133*, 8721–8731.

(19) Lear, B. J.; Chisholm, M. H. *Inorg. Chem.* **2009**, *48*, 10954–10971.

(20) Eisenberg, R.; Gray, H. B. *Inorg. Chem.* **2011**, *50*, 9741–9751.

(21) Morsing, T. J.; MacMillan, S. N.; Uebler, J. W. H.; Brock-Nannestad, T.; Bendix, J.; Lancaster, K. M. *Inorg. Chem.* **2015**, *54*, 3660–3669.

(22) Craven, M.; Nygaard, M. H.; Zadrozny, J. M.; Long, J. R.; Overgaard, J. *Inorg. Chem.* **2018**, *57*, 6913–6920.

(23) Fataftah, M. S.; Zadrozny, J. M.; Rogers, D. M.; Freedman, D. E. *Inorg. Chem.* **2014**, *53*, 10716–10721.

(24) Dey, A.; Jiang, Y.; Ortiz de Montellano, P.; Hodgson, K. O.; Hedman, B.; Solomon, E. I. *J. Am. Chem. Soc.* **2009**, *131*, 7869–7878.

(25) Wilding, M. J. T.; Iovan, D. A.; Wrobel, A. T.; Lukens, J. T.; MacMillan, S. N.; Lancaster, K. M.; Betley, T. A. *J. Am. Chem. Soc.* **2017**, *139*, 14757–14766.

(26) Cook, B. J.; Di Francesco, G. N.; Ferreira, R. B.; Lukens, J. T.; Silberstein, K. E.; Keegan, B. C.; Catalano, V. J.; Lancaster, K. M.; Shearer, J.; Murray, L. J. *Inorg. Chem.* **2018**, *57*, 11382–11392.

(27) Lim, H. K.; Shin, H.; Goddard, W. A.; Hwang, Y. J.; Min, B. K.; Kim, H. *J. Am. Chem. Soc.* **2014**, *136*, 11355–11361.

(28) Sarangi, R.; DeBeer George, S.; Rudd, D. J.; Szilagyi, R. K.; Ribas, X.; Rovira, C.; Almeida, M.; Hodgson, K. O.; Hedman, B.; Solomon, E. I. *J. Am. Chem. Soc.* **2007**, *129*, 2316–2326.

(29) Szilagyi, R. K.; Lim, B. S.; Glaser, T.; Holm, R. H.; Hedman, B.; Hodgson, K. O.; Solomon, E. I. *J. Am. Chem. Soc.* **2003**, *125*, 9158–9169.

(30) Banerjee, P.; Sproules, S.; Weyhermüller, T.; Debeer George, S.; Wieghardt, K. *Inorg. Chem.* **2009**, *48*, 5829–5847.

(31) Tenderholt, A. L.; Szilagyi, R. K.; Holm, R. H.; Hodgson, K. O.; Hedman, B.; Solomon, E. I. *Inorg. Chem.* **2008**, *47*, 6382–6392.

(32) Cordero, B.; Gómez, V.; Platero-Prats, A. E.; Revés, M.; Echeverría, J.; Cremades, E.; Barragán, F.; Alvarez, S. *Dalton Trans.* **2008**, 2832–2838.

(33) Sproules, S.; Weyhermüller, T.; DeBeer, S.; Wieghardt, K. *Inorg. Chem.* **2010**, *49*, 5241–5261.

(34) Petrov, P. A.; Kuratieva, N. V.; Naumov, D. Y.; Konchenko, S. N. *Acta. Cryst. E* **2005**, *61*, m1138–m1139.

(35) Martin, J. L.; Takats, J. *Inorg. Chem.* **1975**, *14*, 1358–1364.

(36) Herebian, D.; Bothe, E.; Bill, E.; Weyhermüller, T.; Wieghardt, K. *J. Am. Chem. Soc.* **2001**, *123*, 10012–10023.

(37) Sproules, S.; Banerjee, P.; Weyhermüller, T.; Yan, Y.; Donahue, J. P.; Wieghardt, K. *Inorg. Chem.* **2011**, *50*, 7106–7122.

(38) Ghosh, P.; Begum, A.; Herebian, D.; Bothe, E.; Hildenbrand, K.; Weyhermüller, T.; Wieghardt, K. *Angew. Chem. Int. Ed.* **2003**, *42*, 563–567.

(39) Roy, N.; Sproules, S.; Weyhermüller, T.; Wieghardt, K. *Inorg. Chem.* **2009**, *48*, 3783–3791.

(40) Bachler, V.; Olbrich, G.; Neese, F.; Wieghardt, K. *Inorg. Chem.* **2002**, *41*, 4179–4193.

(41) Cowie, M.; Bennett, M. J. *Inorg. Chem.* **1976**, *15*, 1584–1589.

(42) Rosenkoetter, K. E.; Wojnar, M. K.; Charette, B. J.; Ziller, J. W.; Heyduk, A. F. *Inorg. Chem.* **2018**, *57*, 9728–9737.

(43) Cummings, S. D.; Eisenberg, R. *J. Am. Chem. Soc.* **1996**, *118*, 1949–1960.

(44) Juris, A.; Balzani, V.; Barigelletti, F.; Campagna, S.; Belser, P. L.; Von Zelewsky, A. *Coord. Chem. Rev.* **1988**, *84*, 85–277.

(45) Li, K.; Xue, D. *J. Phys. Chem. A* **2006**, *110*, 11332–11337.

(46) Ranis, L. G.; Werellapatha, K.; Pietrini, N. J.; Bunker, B. A.; Brown, S. N. *Inorg. Chem.* **2014**, *53*, 10203–10216.

(47) Wolczanski, P. T. *Organometallics* **2017**, *36*, 622–631.

(48) Wu, B.; Wilding, M. J.; Kuppuswamy, S.; Bezpalko, M. W.; Foxman, B. M.; Thomas, C. M. *Inorg. Chem.* **2016**, *55*, 12137–12148.

(49) Büldt, L. A.; Wenger, O. S. *Angew. Chem. Int. Ed.* **2017**, *56*, 5676–5682.

(50) Büldt, L. A.; Wenger, O. S. *Dalton Trans.* **2017**, *46*, 15175–15177.

(51) Wenger, O. S. *J. Am. Chem. Soc.* **2018**, *140*, 13522–13533.

(52) Barrière, F.; Geiger, W. E. *J. Am. Chem. Soc.* **2006**, *128*, 3980–3989.

(53) Barrière, F.; Camire, N.; Geiger, W. E.; Mueller-Westerhoff, U. T.; Sanders, R. *J. Am. Chem. Soc.* **2002**, *124*, 7262–7263.

(54) Hildebrandt, A.; Lang, H. *Organometallics* **2013**, *32*, 5640–5653.

(55) Lever, A. B. P. *Inorg. Chem.* **1990**, *29*, 1271–1285.

(56) Shepard, S. G.; Fatur, S. M.; Rappé, A. K.; Damrauer, N. H. *J. Am. Chem. Soc.* **2016**, *138*, 2949–2952.

(57) Joshi, H. K.; Cooney, J. J. A.; Inscore, F. E.; Gruhn, N. E.; Lichtenberger, D. L.; Enemark, J. H. *Proc. Natl. Acad. Sci. U.S.A.* **2003**, *100*, 3719–3724.

(58) Stein, B. W.; Yang, J.; Mtei, R.; Wiebelhaus, N. J.; Kersi, D. K.; LePluart, J.; Lichtenberger, D. L.; Enemark, J. H.; Kirk, M. L. *J. Am. Chem. Soc.* **2018**, *140*, 14777–14788.

(59) Zanello, P. *Inorganic electrochemistry: theory, practice and application*; Royal Society of Chemistry: **2007**.

(60) Winter, R. F. *Organometallics* **2014**, *33*, 4517–4536.

(61) Manxzer, L. E.; Deaton, J.; Sharp, P.; Schrock, R. R. *Inorg. Synth.* **1982**, *21*, 135–140.

(62) Schäfer, A.; Huber, C.; Ahlrichs, R. *J. Chem. Phys.* **1992**, *97*, 2571–2577.

(63) Schäfer, A.; Huber, C.; Ahlrichs, R. *J. Chem. Phys.* **1994**, *100*, 5829–5835.

Chapter 6

Mixed Valency in Heterotrimetallic $V[SNS]_2\{Ni(dppe)\}_2$

6.1 Introduction

Coordination complexes that contain two (or more) redox centers in different oxidation states are termed mixed-valence complexes. Such mixed-valence complexes have received considerable attention from synthetic, spectroscopic, and theoretical researchers because they present an ideal framework for studying the impact that thermodynamic driving force, reorganization energy, and electronic delocalization have on intramolecular electron-transfer reactions.[1-6] The lessons learned from these simple systems improve our understanding of the optical properties of charge-transfer chromophores as well as the behavior of metalloenzyme active sites and conductive materials. Prussian blue ($C_{18}N_{18}Fe_7$), which is perhaps the best known and oldest example of a mixed-valence complex, is an extended material comprising octahedral iron(II) and iron(III) centers bridged by cyanide ligands.[7] The mixed-valence nature of the complex is responsible for the intense, deep blue color of the material. The simplest and most elegant small-molecule mixed valence complex is the Creutz-Taube ion, $[(NH_3)_5Ru–NC_4H_4N–Ru(NH_3)_5]^{5+}$, comprising two $Ru(NH_3)_5$ fragments bridged by 1,4-pyrazine.[8] The +5 charge on the ion renders the complex mixed-valent, and the simplicity and symmetry of the ion have rendered it ideal for both experimental and theoretical investigations.

In a general mixed-valent system of the form, $M^n–M^{n+1}$, the itinerant odd electron can be localized on a single metal center, or be evenly distributed among both redox sites. The degree of electronic delocalization (or electron hopping) between sites relies on the amount of electronic communication between the metal ions. Electronic communication, or coupling, can be assessed electrochemically (comproportionation constant, K_c), spectroscopically (intervalence charge transfer band, IVCT), or magnetically (magnetic coupling, J). These values allow for the classification of the mixed-valent system depending on how trapped or detrapped the valence is. This classification system was developed by Peter Day and Melvin Robin (after who it was named) and is comprised of three classes.[9,10] Class I (valence trapped) refers to systems in which an odd electron is localized on a single redox site ($M^n–M^{n+1}$). These mixed-valent molecules will exhibit properties of the individual redox sites. Class III (valence detrapped) is comprised of systems in which the odd electron is

delocalized over both redox sites ($M^{n+0.5}$–$M^{n+0.5}$). Valence-detrapping will lead to distinct properties that are different from the separate ions (conductivity, IVCT transitions). Between these two extremes lies Class II molecules (intermediate coupling) which define systems in which localization is contingent on solvent reorganization. These complexes contain *almost* identical sites, with the odd electron localized. Electronic assignment relies on various tools in the synthetic inorganic chemist's toolbox, such as single-crystal X-ray diffraction (XRD), UV-vis and IR spectroscopy, cyclic voltammetry, electron paramagnetic resonance (EPR) spectroscopy, and computation. There are a plethora of cases where these characterization methods are not in agreement with one another and several techniques are needed to converge on a single electronic description. Cyclic voltammetry and the associated half-wave potential splittings $\Delta E_{1/2}$ are known to demonstrate discrepancies between those electrochemical values and the true electronic coupling, H_{ab}, and charge distribution in the ground state of mixed-valent (MV) systems.[11]

One motif in the field of mixed-valency is the presence of two metal ions that can electronically communicate through a tertiary metal ion; the means of communications aren't necessarily coordinate-covalent bonds found in metal-ligand systems or close proximity of redox sites. Instead, the communication stems from direct interactions between metal centers, or metal-metal bonds.[12-16] As discussed in Chapter 2, heterotrimetallic systems can be constructed under reducing conditions, in which the four electrons derived from the reductant are stored among three metal ions as two formal metal-metal bonds.[17] Well-defined coordination complexes with metal-metal interactions can serve as models for heterogeneous catalysts and semiconductors. These platforms, in which a variety of metal ions can be incorporated, can also be used to model dopants in transition metal dichalcogenides (TMDCs).[18,19] Detailed studies of the electronic properties of such systems can offer insight into the electrical, optical, and structural properties of bulk systems (Figure 6.1).

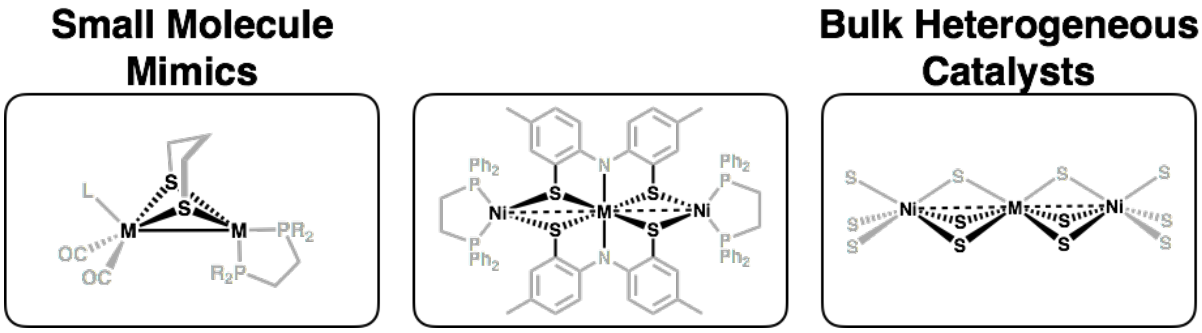

Figure 6.1. Relevance of $M[SNS]_2\{Ni(dppe)\}_2$ (center) to small molecule mimics of the hydrogenase active site (left) and bulk heterogeneous catalysts, such as transition metal dichalcogenides (TMDCs) (right).

This chapter presents the synthesis of the heterotrimetallic cluster complex $V[SNS]_2\{Ni(dppe)\}_2$, and its characterization as a Class I mixed-valence species. Generation of the mixed-valent heterotrimetallic system was accomplished through the reduction of Ni^{2+}(dppe) synthons in the presence of the $[K][V[SNS]_2]$ metalloligand, and was characterized by X-ray crystallography, EPR spectroscopy, as well as cyclic voltammetry. These systems offer information about sulfur-supported metal-metal bonds between 3d transition metals. Insights gained from these complexes are directly relevant to multimetallic metalloenzyme active sites, such as the [FeNi] hydrogenase or the [FeMo] or [FeV] cofactors found in nitrogenase. These heterotrimetallic systems described below also relate to the transition metal sulfide, VS_4 in the patronite mineral structure, which has been shown to demonstrate metal-metal bonding throughout the extended linear chain.[20]

6.2 Results

6.2.1 Synthesis

Generation of $[K][V[SNS]_2\{Ni(dppe)\}_2]$ occurs through reduction of the Ni^{II}-phosphine metal complex in the presence of the redox-active metalloligand, $[V[SNS]_2]^-$. To a chilled solution of $K[V[SNS]_2]$ was added four equivalents of potassium graphite, followed by two equivalents of $Ni(dppe)Cl_2$. After filtration to remove KCl, the addition of pentane to the filtrate induced the precipitation of the product as a dark green powder. This isolation strategy is critical because it allows for the ready removal of the byproduct $Ni^0(dppe)_2$, which is generated under the reducing conditions of the reaction. $[K][V[SNS]_2\{Ni(dppe)\}_2]$ was characterized by a parent ion peak at $[M]^- = 1479.2$ *m/z* in the negative mode electrospray mass spectrum. Synthetic efforts to prepare $V[SNS]_2\{Ni(dppe)\}_2$

involve the addition of three equivalents of KC_8 to the metalloligand, $K[V[SNS]_2]$, followed by the addition of two equivalents of $Ni(dppe)Cl_2$, all performed in THF under an inert atmosphere of N_2 (Scheme 6.1). The neutral NiVNi system demonstrates a parent ion peak at $[M^+]$ = 1480.2 *m/z* in the electrospray mass spectrum (positive ion mode).

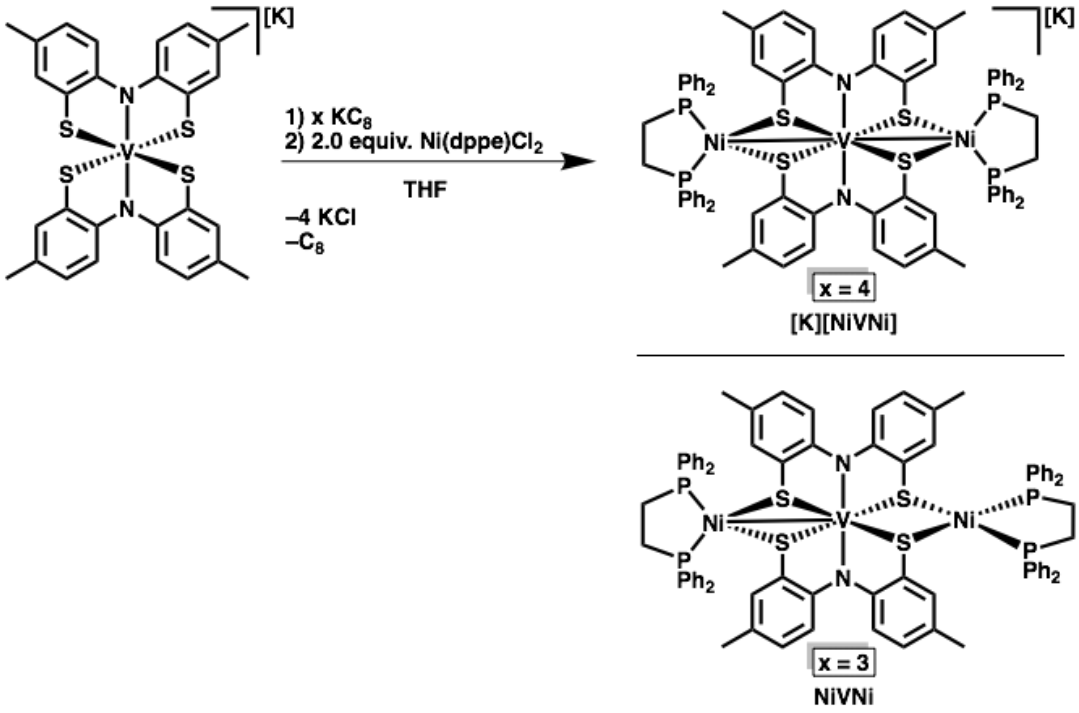

Scheme 6.1. Synthesis of $V[SNS]_2\{Ni(dppe)\}_2$ and $[K][V[SNS]_2\{Ni(dppe)\}_2]$.

6.2.2 Structural Characterization of $[K][V[SNS]_2\{Ni(dppe)\}_2]$ and $V[SNS]_2\{Ni(dppe)\}_2$

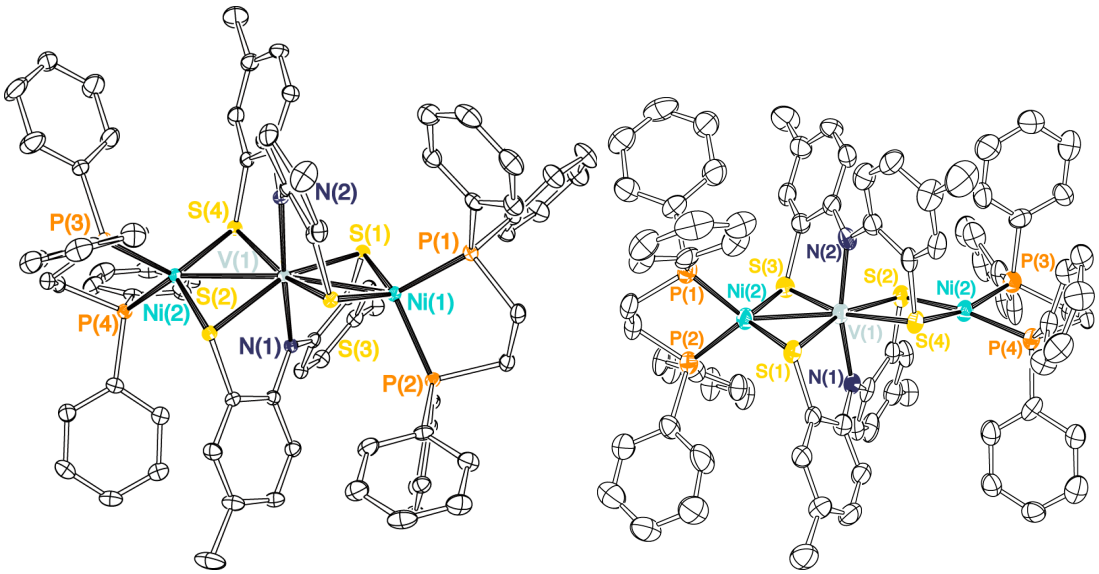

Figure 6.2. ORTEP diagram of $[K(18\text{-Crown-6})(THF)_2][V[SNS]_2\{Ni(dppe)\}_2]$ (left) and $V[SNS]_2\{Ni(dppe)\}_2$ (right) with thermal ellipsoids shown at 50% probability. Hydrogen atoms, solvent molecules (THF and diethyl ether), and $[K(18\text{-Crown-6})(THF)_2]$ counterion have been omitted for clarity.

Table 6.1. Selected bond distances and angles of [K][V[SNS]$_2${Ni(dppe)}$_2$] and V[SNS]$_2${Ni(dppe)}$_2$.

	[K][V[SNS]$_2${Ni(dppe)}$_2$]	**V[SNS]$_2${Ni(dppe)}$_2$**
V(1)–Ni(1)	2.7912(8)	2.603(2)
V(1)–Ni(2)	2.7793(8)	3.450(2)
V(1)–S(1)	2.4293(7)	2.340(3)
V(1)–S(2)	2.4332(7)	2.457(3)
V(1)–S(3)	2.4360(7)	2.331(3)
V(1)–S(4)	2.4115(7)	2.489(3)
V(1)–N(1)	2.039(2)	2.02(1)
V(1)–N(2)	2.045(2)	2.031(8)
Ni(1)–S(1)	2.2100(7)	2.213(3)
Ni(1)–S(3)	2.1880(7)	2.200(3)
Ni(1)–P(1)	2.1695(8)	2.200(3)
Ni(1)–P(2)	2.2261(7)	2.215(3)
Ni(2)–S(2)	2.1931(7)	2.242(3)
Ni(2)–S(4)	2.1942(7)	2.264(3)
Ni(2)–P(3)	2.1965(7)	2.158(3)
Ni(2)–P(4)	2.1941(7)	2.183(3)
S(1)–V(1)–S(3)	96.96(2)	105.4(1)
S(2)–V(1)–S(4)	98.38(2)	81.2(1)
S(1)–V(1)–S(2)	160.22(3)	163.8(1)
S(3)–V(1)–S(4)	161.63(3)	164.0(1)
N(1)–V(1)–N(2)	171.05(7)	164.2(4)
S(1)–Ni(1)–S(3)	111.84(3)	114.7(1)
P(1)–Ni(1)–P(2)	92.18(2)	89.9(1)
S(2)–Ni(1)–S(4)	113.39(3)	91.2(1)
P(3)–Ni(2)–P(4)	91.34(2)	85.2(1)

Table 6.2. τ_4 geometry index values and Bailar twist (θ) values of [K][V[SNS]$_2${Ni(dppe)}$_2$] and V[SNS]$_2${Ni(dppe)}$_2$.

	[K][V[SNS]$_2${Ni(dppe)}$_2$]	**V[SNS]$_2${Ni(dppe)}$_2$**
τ_4 Ni(1)	0.86	0.84
τ_4 Ni(2)	0.82	0.19
$\theta_{S(1),N(1)}$	47.9	52.8
$\theta_{S(2),S(3)}$	23.1	33.9
$\theta_{S(4),N(2)}$	47.6	53.1

The identities of complexes [K][NiVNi] and NiVNi were confirmed by single-crystal X-ray diffraction (Figure 6.2). Crystals were grown by diffusion of a green solution of the complexes in THF into pentane. [K][V[SNS]$_2${Ni(dppe)}$_2$] crystallized in the monoclinic space group P$2_1/c$ and V[SNS]$_2${Ni(dppe)}$_2$ in the orthorhombic space group P$na2_1$. In both cases, the asymmetric unit is comprised of the entire cluster compound. The vanadium metalloligand bridge adopts a pseudo-octahedral geometry for both [K][NiVNi] and NiVNi, similar to its monometallic form. This is reflected in the trans angles X–V–X which range from 160.2°-171.0° (Table 6.1). As an ideal octahedron is adopted, these values should approach 180°. The Bailar twist angle of the molecular bridge reflects this, with θ ranging from 23.1°-52.1° ($\theta_{\text{trigonal prism}}$= 0°; $\theta_{\text{octahedron}}$= 60°).[21,22] The coordination geometry around the two nickel centers demonstrates the location of oxidation in the cluster. Quantification of these coordination geometries can be accomplished with the geometry index, τ_4. These geometry index values range from 0 (an ideal square planar geometry) to 1 (an ideal tetrahedral geometry). For the monoanionic complex, the nickel phosphine synthons adopt tetrahedral coordination environments, reflected in the τ_4 values of 0.86 and 0.82 (Table 6.2). The nickel centers in neutral NiVNi, however, are in distinctly different geometries, ranging from pseudo-tetrahedral to square planar. The τ_4 values for V[SNS]$_2${Ni(dppe)}$_2$ are 0.84 and 0.19, illustrating the different geometries adopted by the two nickel centers with equivalent ligand environments. Additionally, these two nickel centers show varying metal-metal bond distances for the two clusters. In V[SNS]$_2${Ni(dppe)}$_2$, the vanadium–nickel metal-metal bond distances are relatively short, at 2.79 Å and 2.78 Å. [K][V[SNS]$_2${Ni(dppe)}$_2$] exhibits drastically different metal-metal bond metrics. For the

nickel center in the pseudo-tetrahedral environment, the V–Ni bond distance is 2.61 Å; the nickel center enclosed in a square planar geometry yields a vanadium–nickel distance of 3.45 Å. As a means to normalize the metal-metal bond lengths to their respective covalent radii, covalent ratio (*r*) values were calculated to be 1.00 and 1.01 in [K][NiVNi], and 0.94 and 1.25 in NiVNi, demonstrating the existence of metal-metal interactions (although weak) in the case of the reduced metal centers in tetrahedral environments in both the monoanion and neutral complexes, and the lack of a metal-metal bond in the NiVNi complex.[23-25] Upon oxidation and scission of a V–Ni metal-metal bond, it is observed that while one metal-metal bond distance significantly lengthens (consistent with bond breakage), the other metal-metal bond decreases substantially in length. The distortions in metal-metal bond lengths accompany consistent trends in V–S bond lengths: for [K][V[SNS]$_2${Ni(dppe)}$_2$], all V–S bond distances range from 2.41 Å to 2.44 Å. For V[SNS]$_2${Ni(dppe)}$_2$, to accommodate the square-planar geometry around one of the nickel centers, large V–S bond distances are observed, between 2.46 Å and 2.49 Å. The other nickel ion, with a shorter V–Ni metal-metal bond length, exhibits short V–S bond distances of 2.33 Å to 2.34 Å.

In terms of intra-metalloligand bond lengths, bond metrics are consistent with a slight bond lengthening of the individual K[V[SNS]$_2$] metalloligand upon cluster formation, due to additional bridging steric interactions as well as further reduction of the ligand. The intraligand metrical information in [K][NiVNi] and NiVNi is in accordance with two fully-reduced [SNS^{cat}]$^{3-}$ ligands, with long average S–C and N–C bond lengths of 1.77 Å and 1.40 Å for [K][NiVNi], and 1.79 Å and 1.39 Å for NiVNi, respectively.[26-30] In conjunction with the metal geometries, the bond metrics are in agreement with the neutral NiVNi as a mixed-valent molecule in which the nickel centers are in identical ligand environments but in different oxidation states. For the metal–ligand bond lengths, the nickel center with $\boldsymbol{\tau}_4$ value of 0.19 in V[SNS]$_2${Ni(dppe)}$_2$ shows longer average Ni–S bonds, compared to the tetrahedral nickel centers in both the monoanion and neutral systems (2.25 Å for the nickel ion in the square planar geometry; 2.20 Å for the nickel ions in the pseudo-tetrahedral geometry), possibly due to steric interactions between the phenyl rings on the phosphine ligand and

the metalloligand, imposed by the square planar arrangement. These Ni–S values are consistent with other S_2Ni(dppe) bond distances in square planar environments.[31-33] The average Ni–P distances in the square planar environment of NiVNi (2.17 Å) are shorter compared to the nickel ions in the tetrahedral geometry of [K][NiVNi] and NiVNi (2.20 Å), consistent with a more-oxidized metal center (the covalent radii of a more reduced metal ion should be slightly larger than that for a more oxidized one). The Ni–P bond distances of the nickel ion in the square planar coordination environment are congruent to divalent nickel ions in S_2P_2 coordination environments.[32,34,35] The longer Ni–P bond lengths of the nickel ions in tetrahedral S_2P_2 geometries are also analogous to heterobimetallic low-valent nickel-phosphine coordination complexes that invoke metal-metal bonding.[36,37]

6.2.3 Spectroscopy

Electronic absorption spectra of [K][NiVNi] and NiVNi in THF were obtained and demonstrate two prominent transitions at 350 nm-400 nm and at ~630 nm (Figure 6.3). No transitions are observed at lower energy. Based on separate syntheses of K[V[SNS]$_2$] and Ni^0(dppe)$_2$ and related UV-vis data, comparison of the optical data suggests that these transitions arise from the disparate synthons used to generate the heterotrimetallic system. [K][V[SNS]$_2${Ni(dppe)}$_2$] is the valence isoelectronic analogue of Mo[SNS]$_2${Ni(dppe)}$_2$, and has an S=0 ground state. ^{1}H NMR spectroscopy (in THF-d_8) demonstrated broad resonances at 298 K. Upon cooling the system down to 208 K, a single broad resonance at 2.09 ppm was observed, which is assigned as the methyl group on the [SNS] ligand backbone. The aromatic resonances of the [SNS] and dppe ligands were observed between 6 ppm and 8 ppm. The dynamic behavior was evident by ^{31}P{^{1}H} NMR, in which broad resonances between 29 ppm and 32 ppm were observed at room temperature. At 208 K, a single sharp resonance at 44 ppm emerges, while the peaks around 30 ppm become more resolved and decrease in intensity.

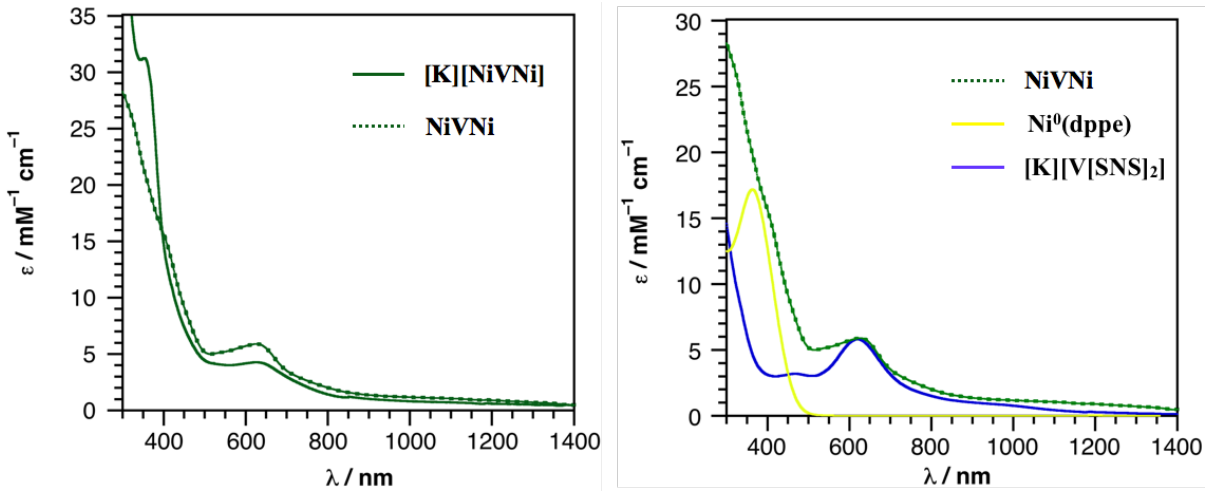

Figure 6.3. Electronic absorption spectra of $[K][V[SNS]_2\{Ni(dppe)\}_2]$ (solid green) and $V[SNS]_2\{Ni(dppe)\}_2$ (dotted green) (left); Optical spectra of $V[SNS]_2\{Ni(dppe)\}_2$ (dotted green) $[K][V[SNS]_2]$ (blue), and $Ni^0(dppe)_2$ (yellow) obtained in THF (right).

$V[SNS]_2\{Ni(dppe)\}_2$ is the one-electron-oxidized analogue of the diamagnetic [K][NiVNi], and therefore contains an odd number of electrons. Consequently, the neutral NiVNi was further characterized by EPR spectroscopy. Figure 6.4 shows the EPR spectra of the complex in THF at 298 K (left) and 77 K (right). At room temperature in THF, the complex exhibits an axial signature with an eight-line hyperfine signal at g = 1.952, 1.958 (A_1 = 217 MHz; A_2 = 175 MHz). The overlaid simulation is modeled for a vanadium-based radical (I=7/2, ^{51}V, 100% natural abundance) as an S=1/2 spin center. When the solution is cooled down to 77 K, the signal becomes rhombic, with the glassy THF solution coinciding with another eight-line vanadium-based hyperfine with a rhombic signal centered at g = 1.95 (Table 6.3). The parameters give information about the environment around the unpaired electron and the electronic structure of the complex.[38] These values are consistent with V(IV) six-coordinate systems in sulfur-rich ligand environments.[39-41]

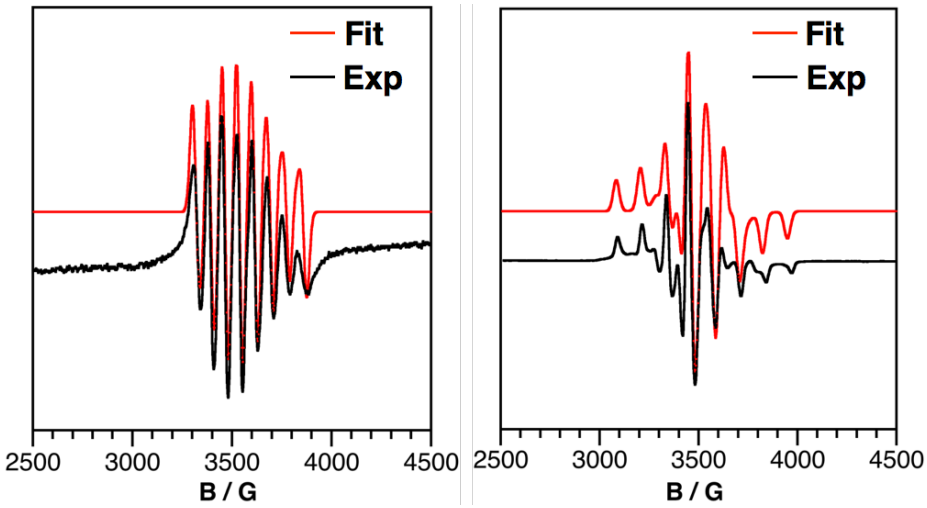

Figure 6.4. X-band Cw-EPR spectra of $V[SNS]_2\{Ni(dppe)\}_2$ taken in THF at 298 K (left) and 77 K (right). The red lines are simulated spectra.

To give a more informed description of the degree of valence trapping vs. detrapping in this class of multimetallic systems, the corresponding $[K]_2[V^{IV}[SNS]_2]$ was synthesized by adding one equivalent of KC_8 to $[K][V^{V}[SNS]_2]$ (Scheme 6.2); the putative $V^{IV}(d^1)$ system was analyzed by EPR spectroscopy (Figure 6.5). In comparison to $V[SNS]_2\{Ni(dppe)\}_2$, $[K]_2[V^{IV}[SNS]_2]$ would lead to an unpaired electron that is localized on the vanadium ion (with minimal covalency or backbonding to the fully-reduced [SNS] ligands), based on previous electron structure arguments of the metalloligand. Table 6.3 compares the associated g and A values for NiVNi and the putative $[K]_2[V^{IV}[SNS]_2]$ at 298 K and 77 K. At 77 K, NiVNi exhibits g values that are shifted to slightly lower values, along with smaller A values. The same trend is observed at 298 K, with larger differences in both g and A values.

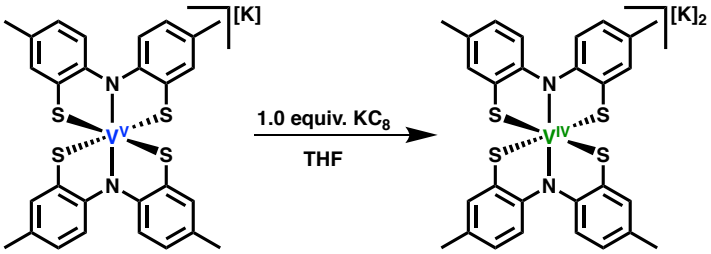

Scheme 6.2. Reduction of $K[V^{V}[SNS]_2]$ to generate the EPR-active $[K]_2[V^{IV}[SNS]_2]$.

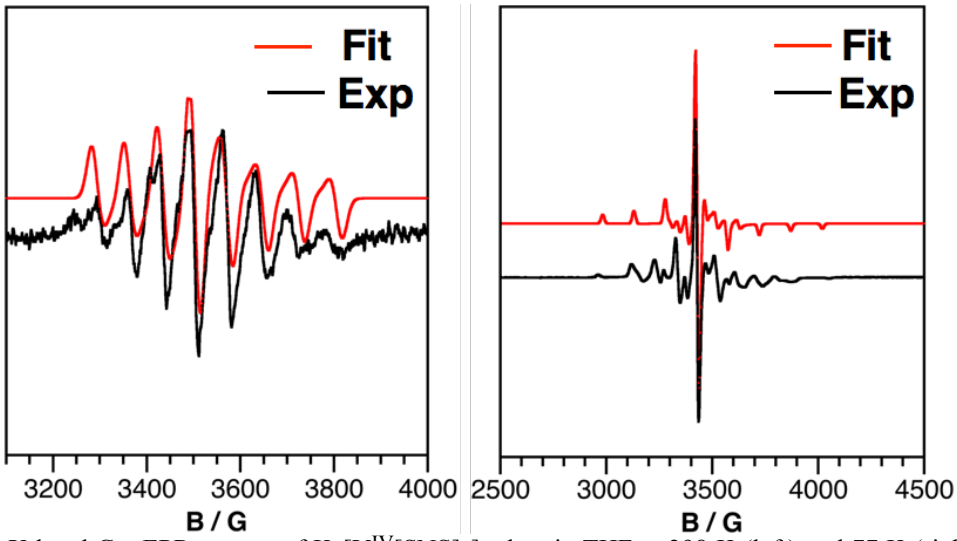

Figure 6.5. X-band Cw-EPR spectra of $K_2[V^{IV}[SNS]_2]$ taken in THF at 298 K (left) and 77 K (right). The red lines are simulated spectra.

Table 6.3. EPR parameters for $V[SNS]_2\{Ni(dppe)\}_2$ and $K_2[V^{IV}[SNS]_2]$ obtained in THF.

	g_1	g_2	g_3	A_1 (MHz)	A_2 (MHz)	A_3 (MHz)
$V[SNS]_2\{Ni(dppe)\}_2$ 77 K	1.954	1.960	1.938	338	157	84
$K_2[V^{IV}[SNS]_2]$ 77 K	1.963	1.981	1.983	407	125	18
$V[SNS]_2\{Ni(dppe)\}_2$ 298 K	1.952	1.958	–	217	175	–
$K_2[V^{IV}[SNS]_2]$ 298 K	1.99	2.01	–	422	118	–

6.2.4 Electrochemical Analysis of Heterotrimetallic $V[SNS]_2\{Ni(dppe)\}_2$ Systems

Voltammetric experiments were conducted on the neutral NiVNi complex in a THF solution with $[NBu_4][PF_6]$ as the supporting electrolyte (Figure 6.6). All potentials were referenced to the reversible redox couple $[Cp_2Fe]^{+/0}$. $V[SNS]_2\{Ni(dppe)\}_2$ exhibited multiple reversible/quasi-reversible redox events ($i_{pa}/i_{pc} \simeq 1$), consistent with the cluster compound incorporating three redox-active transition metal centers and two redox-active [SNS] ligands. Importantly, in the comparison of the cyclic voltammograms of NiVNi and [K][NiVNi], the electrochemical profile remains the same but demonstrates a shift in the open circuit potential. Table 6.4 lists the various potentials associated with the redox events. Voltammetry measurements show that NiVNi can undergo a single quasi-

reversible reduction at –2.42 V vs. $[Cp_2Fe]^{+/0}$. Attributed to the reduced nature of the molecule ([K][NiVNi] and NiVNi are synthesized under an environment of potassium graphite), $[K][V[SNS]_2\{Ni(dppe)\}_2]$ can undergo four reversible to quasi-reversible oxidations. The open circuit potentials range between –1.6 V and –2.1 V (for [K][NiVNi]) and –1.0 V and –1.4 V (for NiVNi) further confirms the "reducing" nature of the complexes. The redox event at –1.44 V that corresponds to the one-electron conversion between [K][NiVNi] and NiVNi is reversible.

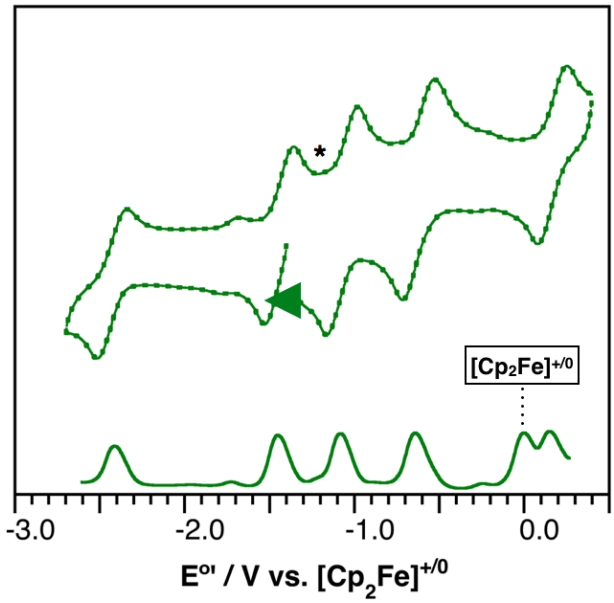

Figure 6.6. Cyclic voltammogram (top) and differential pulse voltammogram (bottom) of $V[SNS]_2\{Ni(dppe)\}_2$ in THF containing 0.1 M $[NBu_4][PF_6]$, referenced to the $[Cp_2Fe]^{+/0}$. Data were collected using a glassy carbon working electrode and a 200 mV s^{-1} scan rate. The asterisk denotes the open circuit potential and the arrow denotes the direction of the scan. The dotted grey voltammogram represents an expansion of the voltammetric window of the experiment.

Table 6.4. Electrochemical potentials of V[SNS]2{Ni(dppe)}$_2$ obtained in THF containing 0.1 M $[NBu_4][PF_6]$, referenced to the $[Cp_2Fe]^{+/0}$.

	$[M]^{-1/-2}$	$[M]^{0/-1}$	$[M]^{0/+1}$	$[M]^{+1/+2}$	$[M]^{+2/+3}$
$V[SNS]_2\{Ni(dppe)\}_2$	–2.42	–1.44	–1.06	–0.62	+0.17

Comparison of the potentials of the vanadium-containing cluster compounds and the free metalloligand, $[K][V[SNS]_2]$, provides information on the oxidation state of the bridge. Figure 6.7 shows an overlay of $V[SNS]_2\{Ni(dppe)\}_2$ and $[K][V[SNS]_2]$, both obtained in THF and referenced to $[Cp_2Fe]^{+/0}$. Inspection of the redox events and open circuit potentials intimates a formal one-electron reduction of the metalloligand bridge, to generate $[V^{IV}[SNS]_2]^{-1}$. The redox event at –2.42 V for

$V[SNS]_2\{Ni(dppe)\}_2$ overlays with the second reduction of the metalloligand. The quasi-reversible anodic features for both $[V[SNS]_2\{Ni(dppe)\}_2]^{0/-1}$ and $K[V[SNS]_2]$ between –0.10 V and 0.0 V is maintained.

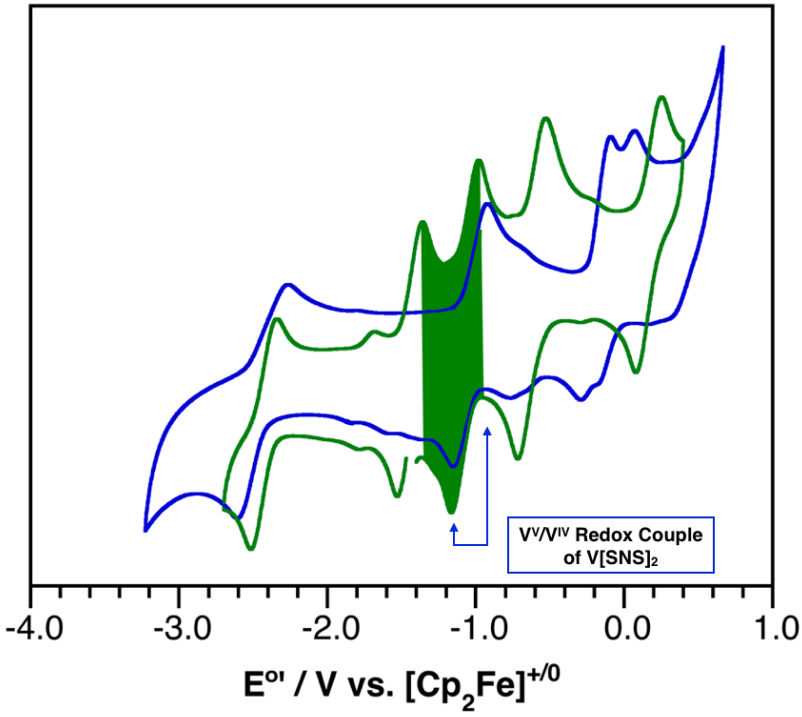

Figure 6.7. Overlay of the cyclic voltammograms of $V[SNS]_2\{Ni(dppe)\}_2$ (green) and $K[V[SNS]_2]$ (blue), demonstrating the degree of reduction of the metalloligand bridge. The shaded green region delineates the open circuit potential of $V[SNS]_2\{Ni(dppe)\}_2$.

6.2.6 Computations of Electronic Structure of Heterotrimetallic $V[SNS]_2\{Ni(dppe)\}_2$ System

To further analyze the electronic structure of the mixed-valent NiVNi**,** density functional theory was employed. Atomic coordinates were derived from the X-ray crystal structure data and geometry optimizations (utilizing the TPSS functional at the TZVP level of theory) yielded metal–ligand and metal–metal bond distances that agree reasonably well with experimental values. For an S=1/2 system, computational analysis modeled NiVNi as an open-shell doublet Kohn-Sham DFT solution, using a spin-unrestricted (unrestricted Hartree–Fock, UHF) scheme. According to Mulliken population analysis (MPA) of the singly-occupied molecular orbital (SOMO) of $V[SNS]_2\{Ni(dppe)\}_2$, the unpaired electron is localized on the metalloligand bridge, with Ni(dppe) ion contributions of 1% each (Figure 6.8). Focus on the frontier molecular orbitals underscores the mixed valency of this system. The singly-unoccupied molecular orbital (SUMO) resides on the

vanadium ion in a square planar environment (Ni_{sp}). Occupation of the SOMO–3/SOMO–4 delineates the overlap of the metal orbitals from V and Ni, demonstrating the presence of a formal metal-metal bond. The contribution from the nickel ion (24%) is exactly double the contribution from the vanadium ion (12%), illustrating a polarization of electron density in this metal-metal interaction. This computational result is consistent with base metal → Lewis acid dative bonds in similar bimetallic manifolds.[42]

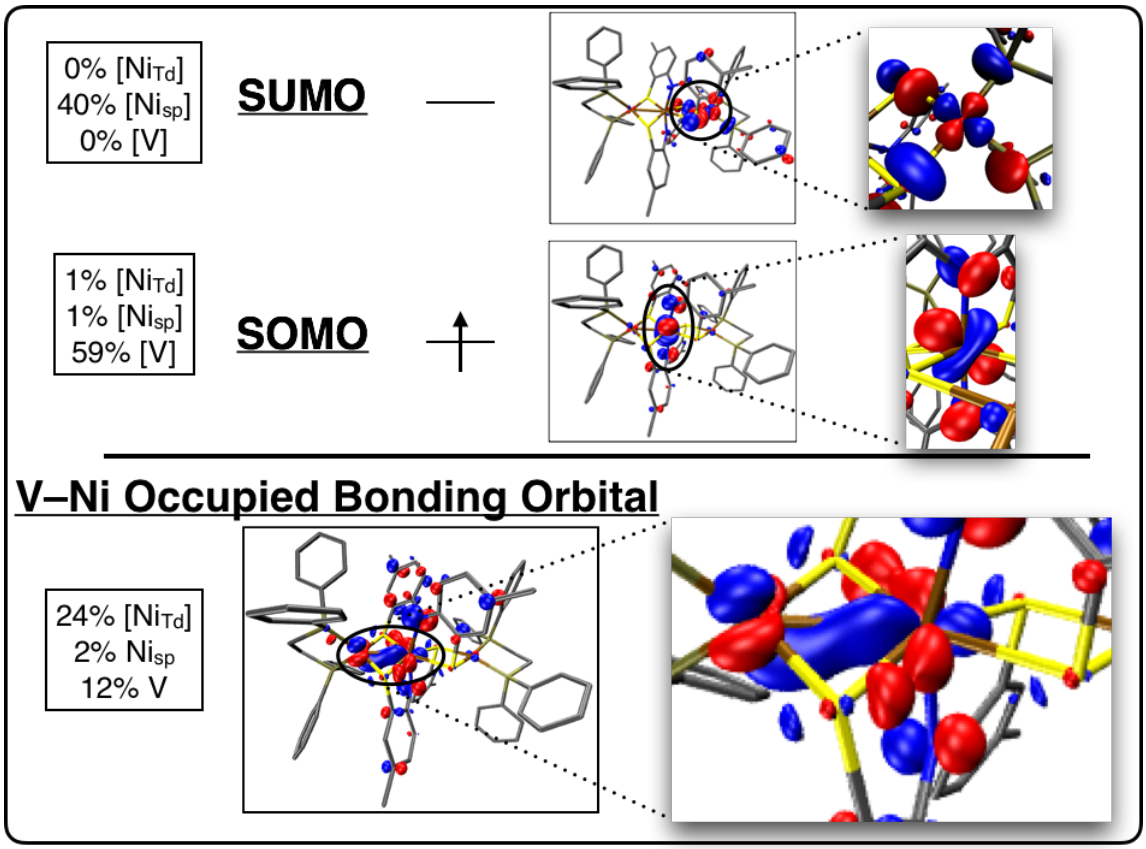

Figure 6.8. Frontier molecular orbital diagram with Kohn-Sham molecular orbitals for NiVNi (bottom). Orbital rendering was performed using VMD.

6.3 Discussion

Having a library of synthesized metalloligands in hand has allowed for the synthesis of a mixed-valent coordination complex, $V[SNS]_2\{Ni(dppe)\}_2$. Generation of the desired vanadium trimetallic complexes involved reduction of $Ni(dppe)Cl_2$ in the presence of the $V[SNS]_2^{-1}$ metalloligand. The complexes were characterized by various techniques, including XRD, UV-vis and EPR spectroscopy as well as voltammetry, to determine the degree of coupling between the nickel centers,

with the characterization methods suggesting that the two nickel centers are valence-trapped and strongly decoupled (despite large half-wave potential splitting values). Structural data shows the two nickel centers in two distinct geometries, indicating localized charge. Nickel is an optimal choice in determining oxidation state because the geometry of this particular metal center is dependent on the oxidation state. For electronic reasons, it is known that nickel in the +2 oxidation state typically adopts a square planar geometry. As the nickel center is reduced to the +1 or 0 oxidation state, electrons are added into antibonding orbitals, eliminating electronic considerations from the coordination geometry. Sterics dictates that the nickel center adopts a tetrahedral geometry for Ni^{+1} and Ni^{0} oxidation states, respectively. In NiVNi, the coordination geometry around the two nickel centers is distinct and consistent with nickel in two different oxidation states. $\boldsymbol{\tau}_4$ values quantify these ligand geometries (0.84 and 0.19) and illustrate that, upon oxidation of one nickel center, the metal changes to a Ni^{2+} oxidation state with concomitant metal-metal bond cleavage, while the other nickel center maintains a pseudo-tetrahedral coordination geometry and a metal-metal bond (that contracts from 2.78 Å-2.79 Å to 2.61 Å). Heterobimetallic manifolds involving nickel typically are comprised of dative single bonds between metal centers, due to the location of nickel on the periodic table and its associated spatial and electronic overlap properties.[43-46]

Both EPR and UV-vis spectroscopies are in agreement with a localized electron/electron-hole, due to the metalloligand-localized radical in the EPR spectra and lack of IVCT bands in the electronic absorption spectrum. One of the most informative techniques to determine the degree of electronic coupling in MV systems is UV-vis-NIR spectroscopy. Generally, spectroscopic techniques are ideal in terms of allocating charge in a mixed-valent system, due to the timescale of the experiment relative to the timescale of electron movement. While the time scale of ^{1}H NMR is $1\text{-}10^{-5}$ s, it is $10^{-5}\text{-}10^{-9}$ s for EPR spectroscopy. For UV-vis spectroscopy, the time scale is 3×10^{-14} or less.[47] Low energy charge transfer bands are invoked to explain the movement of electrons/holes between the associated metal centers (in this case, the two nickel centers). This is referred to as the intervalence charge transfer (IVCT) band.[48-50] The energy of the band varies from case to case but is typically found at lower en-

ergies than 900 nm. Electronic absorption spectroscopy elucidated two main transitions, associated with charge transfer transitions of the disparate $V[SNS]_2$ and Ni(dppe) fragments. Previous spectroscopic and electronic structure analysis of $K[V^{V}[SNS^{cat}]_2]$ establishes the transition at ~630 nm as an intra-metalloligand ligand-to-metal charge transfer (LMCT) transition. The transition between 350 nm-400 nm is characteristic of low-valent metal phosphine MLCT transitions.[51,52] No evidence of charge transfer from the nickel ion to the metalloligand bridge is observed. EPR spectroscopy is a useful method to determine any degree of delocalization, which would manifest in spectra that exhibit complex splittings due to the various components involved in the delocalization, which is not observed in the neutral NiVNi. Comparison of the spectra of NiVNi and a formally V^{IV} vanadium-localized unpaired electron yields a slightly more delocalized electron in $V[SNS]_2\{Ni(dppe)\}_2$ (smaller A value) in an electronically different environment (smaller g value). Both experiments support the locus of the resulting unpaired electron on the metalloligand. Previous spectroscopic characterization of the chemically-oxidized $[Mo[SNS]_2\{Ni(dppe)\}_2]^{+}$ complex also exhibited metalloligand-based hyperfine interactions in the S=1/2 system. The trend observed by EPR is in agreement with an unpaired electron formally localized on a single metal ion in the case of $K_2[V^{IV}[SNS]_2]$, as opposed to the more delocalized electron in a chemically different environment for the neutral NiVNi complex.

The open circuit potential is also in the potential domain that maintains fully-reduced $[SNS^{cat}]^{3-}$ ligands (justified via intraligand solid-state characterization) and, as a result, can be considered "innocent" in the redox chemistry. The redox events at ~0 V are also consistent with the oxidizing potentials necessary to remove electron density from the [SNS] ligands. The redox event at –1.44 V that corresponds to the one-electron conversion between [K][NiVNi] and NiVNi is reversible, which, on the electrochemical timescale, indicates minimal geometric rearrangement upon redox. This nickel-localized oxidation (based on the structural data) is in disagreement with the isolated structures of [K][NiVNi] and NiVNi, which demonstrate a large rearrangement of the molecule upon redox. The current hypothesis is that the geometry change from square planar to tetrahedral is slower (or faster)

than the time scale of the voltammetric experiment, responsible for equal current in both the cathodic and anodic peaks.

The only data to suggest electronic coupling between the metal centers is the potential splittings in the voltammetry experiments conducted. Qualitatively, the amount of charge delocalization can be illustrated via cyclic voltammetry: two metal centers in equivalent environments but negligible electronic coupling will be manifested as a single two-electron redox event because the two metal centers will not "see each other" and, consequently, be oxidized or reduced at the exact same potential. On the other side of the spectrum, two metal centers in equivalent environments but with a large degree of electronic coupling will manifest itself in two distinct redox events that are separated by large potential values. After the initial redox event, the second metal center "feels" that first redox event, and, consequentially, shifts to a different potential.[53] Quantitatively, the electrochemical events for $V[SNS]_2\{Ni(dppe)\}_2$ are separated by 380 mV, illustrating that the two metal centers "feel" each other and are, consequently, coupled. The stability of this mixed-valent state can be expressed with the following equation:

$$K_c = e^{nF\Delta E_{1/2}/RT}$$

The comproportionation constant describes the relative free energy changes upon redox ($-\Delta G_c = nFE^{1/2}$). While it is assumed that the stability of the mixed-valent state is strictly due to electronic coupling, there are a plethora of variables that factor into ΔG_c[54-57]:

$$\Delta G_c = \Delta G_{stat} + \Delta G_{ind} + \Delta G_{ex} + \Delta G_{el} + \Delta G_{res}$$

(ΔG_{stat} = statistical contribution; ΔG_{ind} = inductive contribution; ΔG_{ex} = magnetic exchange contribution; ΔG_{el} = electrostatic contribution; ΔG_{res} = resonance contribution due to electronic coupling). A result of electronic coupling, defined as mixing of metal-based nickel orbitals with orbitals of the appropriate symmetry with the metalloligand bridge, is that the associated charge (electron/hole) should be delocalized over both nickel centers. However, as shown by structural assessment, as well as by EPR and electronic absorption spectroscopies, the charge is localized on one nickel center. This suggests the large potential splitting is due to a combination of statistics, inductive effects, magnetic ex-

change, and electrostatics, as opposed to electronic coupling. Plugging in 380 mV for $\Delta E_{1/2}$ yields a value of 2.7×10^6, specifying that the equilibrium,

$$2[V[SNS]_2\{Ni(dppe)\}_2] \rightleftarrows [V[SNS]_2\{Ni(dppe)\}_2]^- + [V[SNS]_2\{Ni(dppe)\}_2]^+$$

lies far to the left. The mixed-valent NiVNi is stable with respect to disproportionation to its monoanionic and monocationic forms.

This lack of electronic coupling from metal-metal bond scission is observed in similar bimetallic systems integrating third-row 3d transition metal ions. Specifically, the oxidatively-induced tetrahedral → square-planar twist associated with nickel ions involved in metal-metal bonding has been observed in small molecule mimics of the [FeNi] hydrogenase.[37,58] Although the reduced, tetrahedral system is classified as Fe^I (d^7) and Ni^I (d^9), it is hypothesized that the S=1/2 ions couple antiferromagnetically via a strong covalent metal-metal bond to give a closed-shell system, a common theme in metal-metal bond formation.[59,60] Furthermore, these systems are dynamic and fluctuate between the Fe(I)-Ni(I) ⟷ Fe(0)-Ni(II) isomers with concomitant formation and breakage of metal-metal bonds, shown by density functional theory calculations.[61] This phenomenon has also been observed in Rh_2 bimetallic systems as well.[62] Interestingly enough, these exact properties of dynamic behavior and covalent metal-metal bonding is invoked in the $[Mo[SNS]_2\{Ni(dppe)\}_2]$ systems. In the H_2ase mimics incorporating a Ni(dppe) building block, upon oxidation, the covalent Fe(I)-Ni(I) bond is cleaved, yielding a Ni(II) ion in a square planar geometry, with the other electron from the metal-metal bond localizing on the Fe center (Scheme 6.3). For these three-center four-electron systems, it was initially anticipated that oxidation would occur in a symmetry-adapted-linear combination (SALC) centered on the nickel ions that is non-bonding with respect to the metal-metal bonding network. By virtue of the poor spatial overlap between two 3d metal centers, the metal-metal bond scission is predicted to occur.

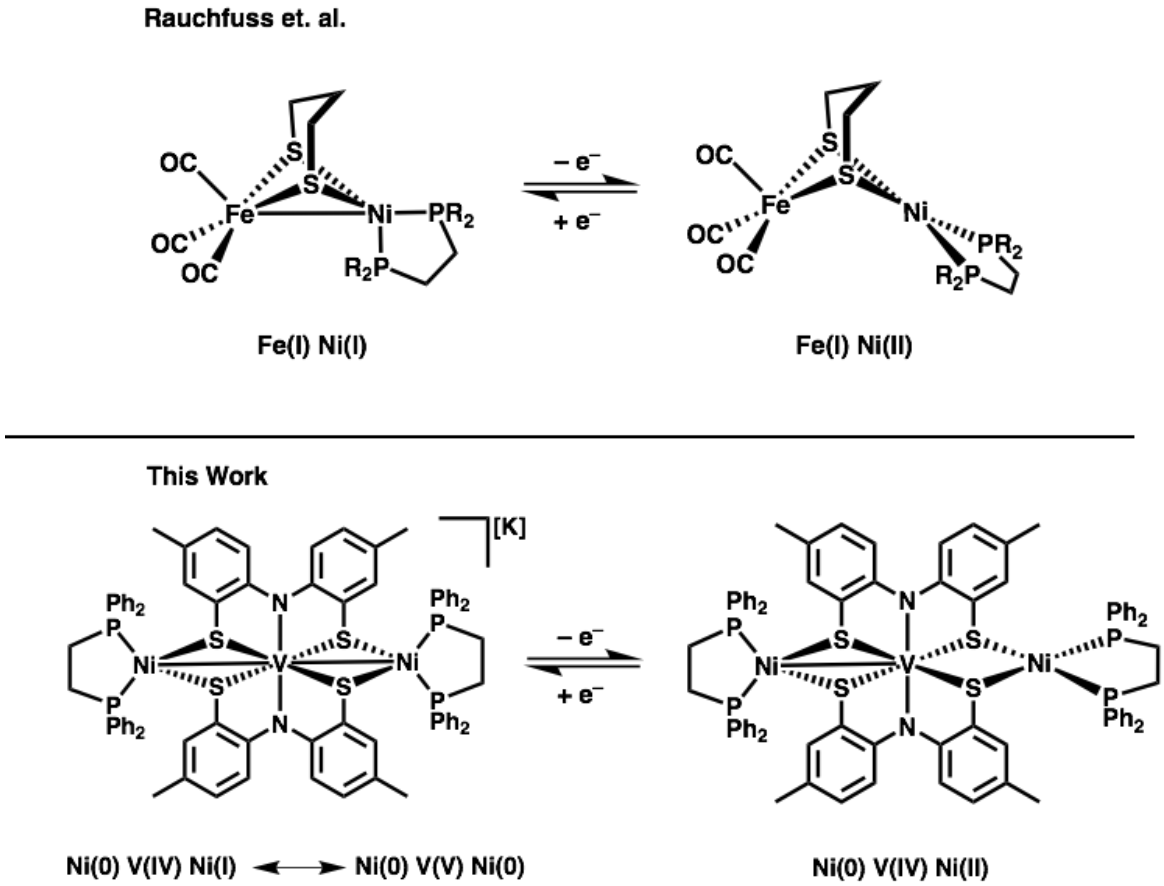

Scheme 6.3. Tetrahedral → square-planar twist in bimetallic FeNi metal-metal bonding motifs from Rauchfuss et. al. (top) and in NiVNi metal-metal bonding networks in this work (bottom).

The current hypothesis is that $V[SNS]_2\{Ni(dppe)\}_2$ represents an example of a two-electron mixed-valent molecule.[63-65] It should be noted that further discussions into localization of electrons in an inherently delocalized system may be futile with current instrumental techniques – actual assessment of electron locality will need other spectroscopies that differentiate on the time scale of electron movement. Previous assignment of formal oxidation states of $Mo[SNS]_2\{Ni(dppe)\}_2$ as Ni^{I}–Mo^{IV}–Ni^{I} and $V[SNS]_2\{Ni(dppe)\}_2$ as Ni^{II}–V^{IV}–Ni^{0} was based on the concept that, through the extraction of one electron from the heterotrimetallic manifold by way of substitution of Mo for V, one nickel center clearly underwent an oxidation state change in which one of the Ni ions adopts a Ni(II) d^8 electronic configuration. EPR spectroscopy, in conjunction with open circuit potential measurements, confirms the localization of a single electron on the vanadium ion of the metalloligand bridge. In terms of electron count, this leaves two electrons to be allocated to the tetrahedral nickel center, yielding a Ni(0) d^{10} electronic configuration. Consequently, the metal-metal bond in NiVNi can be labeled as a

dative interaction, which is confirmed by DFT calculations. The V(IV)–Ni(0) metal-metal bond can be described by another resonance structure, [V(III)–Ni(I)]. Electrochemical measurements suggest this resonance structure is not a major contribution to the full electronic description: the $V^{IV/III}$ redox couple occurs at a substantially negative potential, acknowledgment that further reduction of the vanadium metalloligand will not occur.

6.4 Conclusion

A pair of cluster compounds was synthesized that differ by a single electron, leading to the generation of a formally mixed-valent molecule. The neutral $V[SNS]_2\{Ni(dppe)\}_2$ contains two nickel ions in identical S_2P_2 ligand environments but in different oxidation states. Based on a battery of spectroscopic, electrochemical, and structural techniques, $V[SNS]_2\{Ni(dppe)\}_2$ is classified as a valence-trapped two-electron mixed-valent system. This is corroborated by an X-ray crystal structure demonstrating the localization of charge, as well as through the lack of an IVCT band in the optical spectra and localized behavior via EPR spectroscopy. The justification of this Class I designation is still under investigation. The current hypothesis is that the dative character of the V-Ni bonds (polarized toward the more electronegative nickel ions) leads to minimal electronic coupling with the metalloligand bridge, which in turn, leads to lower coupling between metal ions. According to Marcus theory, the large geometric rearrangement upon oxidation will also contribute to the trapping of charge on a single nickel ion.

6.5 Experimental

General Considerations. All compounds and reactions reported below show varied degrees of air- and moisture-sensitivity, therefore all manipulations were carried out using standard vacuum-line, Schlenk-line and glovebox techniques. Solvents were sparged with argon before being deoxygenated and dried by passage through Q5 and activated alumina columns, respectively. To test for effective oxygen and water removal, aliquots of each solvent were treated with a few drops of a purple solution of sodium benzophenone ketyl radical in THF. $(dppe)NiCl_2$ and $Ni^0(dppe)_2$ were synthesized following literature procedures from commercially available precursors.[66,67]

Spectroscopic Measurements. NMR spectra were collected at 298 K on a Bruker Avance 500 MHz spectrometer in dry, degassed THF-d_8. ^{1}H NMR spectra were referenced to tetramethylsilane (TMS) using the residual proteo impurities of the solvent (1.72 ppm and 3.58 ppm). All chemical shifts are reported using the standard δ notation in parts per million; positive chemical shifts are to a higher frequency from the given reference. Electronic absorption spectra were recorded with a Jasco V-670 absorption spectrometer UV-vis-NIR spectrophotometer using 1-cm path-length cells at ambient temperature (20-24°C).

Electrochemical Methods. Electrochemical experiments were performed on a Gamry Series G300 potentiostat/galvanostat/ZRA (Gamry Instruments, Warminster, PA) using a 3.0 mm glassy carbon working electrode, a platinum wire auxiliary electrode, and a silver wire pseudo-reference electrode. Electrochemical experiments were performed at ambient temperature (20-24°C) in a nitrogen-filled glovebox. Sample concentrations were 1.0 mM in analyte in a THF solution containing 100 mM $[NBu_4][PF_6]$ as the supporting electrolyte. All potentials are referenced to $[Cp_2Fe]^{+/0}$ using ferrocene as an internal standard. Ferrocene was purified by sublimation under reduced pressure and tetrabutylammonium hexafluorophosphate (Acros) was recrystallized from ethanol three times and dried under vacuum.

Crystallographic Methods. X-ray diffraction data for all complexes were collected on single crystals mounted on a glass fiber using paratone oil. Data was acquired using a Bruker SMART APEX II diffractometer equipped with a CCD detector at 88 K using Mo Kα radiation (λ = 0.71073 Å), which was wavelength selected with a single-crystal graphite monochromator. The SMART program package was used to determine unit-cell parameters and for data collection. The raw frame data were processed using SAINT and SADABS to yield the reflection data file. Subsequent calculations were carried out using the SHELXTL program suite. The structures were solved by direct methods and refined on F2 by full-matrix least-squares techniques. Analytical scattering factors for neutral atoms were used throughout the analyses. Hydrogen atoms were generated in calculated positions and refined using a riding model. ORTEP diagrams were generated using ORTEP-3 for Windows.

Computational Methods. All calculations were performed employing the non-empirical tpss density functional theory using the quantum chemistry program package TURBOMOLE. For computational efficiency, initial geometry optimizations were performed using moderate split-valence plus polarization basis sets (def2-SVP).[68] Structures were refined using basis sets of triple zeta valence plus polarization (def2-TZVP) quality.[69] Crystal structures obtained from X-ray diffraction experiments were used as starting points for the geometry optimization; no molecular symmetry was imposed. Energies and minimum energy structures were evaluated self-consistently to tight convergence criteria (energy converged to 0.1 μHartree, maximum norm of the Cartesian gradient $\leq 10^{-4}$ a.u.). Linear-response time-dependent DFT was used to simulate electronic absorption spectra of the two series.

[K(18-Crown-6)(THF)$_2$][V[SNS]$_2${Ni(dppe)}$_2$]. In a 100-mL Schlenk flask was added a blue solution of K(THF)$_4$[V[SNS]$_2$] (135 mg, 0.151 mmol, 1.00 equiv.) to a freshly-prepared sample of KC_8 (102 mg, 1.04 mmol, 6.01 equiv.) in dry THF (~20 mL). In this time, the reaction turns green (indicative of the putative K_2[V[SNS]$_2$]) followed by a brown-black color. The reaction mixture was chilled in a cold well and solid Ni(dppe)Cl_2 (159 mg, 0.301 mmol, 2.00 equiv.) was added to the reaction mixture and rinsed in with dry THF (~10 mL) and stirred for 8 hours. The next day, the vibrant green solution was filtered through a plug of Celite. 18-Crown-6 (44 mg, 0.17 mmol, 1.0 equiv) was added to the solution, which was subsequently concentrated down to a minimum amount of solvent (~2 ml). Pentane was used to precipitate a dark solid, collected by vacuum filtration and washed with pentane (~20 mL) and Et_2O (~20 mL) to remove Ni^0(dppe)$_2$. A dark solid green powder was isolated (205 mg, 70% yield). ^{1}H NMR (500 MHz, 208 K, THF-d_8) δ/ppm: 6-8 (*m*, 52H, aryl–H), 2.09 (*s*, 12H, –CH_3). ^{31}P{^{1}H} NMR (162 MHz, 208 K, THF-d_8) δ/ ppm: 44.6 (*s*). UV-vis (THF) λ_{max}/ nm (ε / M^{-1} cm^{-1}): 353 nm (31,200), 631 nm (4700). MS (ESI$^-$) *m/z*: 1479.2 ([M]).

V[SNS]$_2${Ni(dppe)}$_2$. In a 100-mL Schlenk flask was added a blue solution of K(THF)$_4$[V[SNS]$_2$] (152 mg, 0.170 mmol, 1.00 equiv.) to a freshly-prepared sample of KC_8 (21 mg K, 0.54 mmol, 3.2 equiv.) in dry THF (~20 mL). In this time, the reaction turns green (indicative of the putative

$K_2[V[SNS]_2)$ followed by a brown-black color. The reaction mixture was chilled in a cold well and solid Ni(dppe)Cl_2 (180 mg, 0.340 mmol, 2.00 equiv.) was added to the reaction mixture and rinsed in with dry THF (~10 mL) and stirred for 3 hours. The next day, the bright forest green solution was filtered through a plug of Celite and subsequently concentrated down to a minimum amount of solvent (~3 ml). Pentane was used to crash out a dark solid, collected by vacuum filtration and washed with pentane (~20 mL) and Et_2O (~20 mL) to isolate $Ni^0(dppe)_2$. A dark solid green powder was isolated (170 mg, 67% yield). Anal. Calcd. (Found) for $C_{80}H_{72}N_2Ni_2P_4S_4V$ (%): C, 64.84 (64.62); H, 4.90 (4.88); N, 1.89 (2.02). UV-vis (THF) λ_{max}/nm (ε / M^{-1} cm^{-1}): 410 nm (14,300), 627 nm (6000). MS (ESI^+) *m/z*: 1480.2 ([M+H]).

Table 6.5. Crystal data and structure refinement for [K(18-Crown-6)$(THF)_2$][V[SNS]$_2${Ni(dppe)}$_2$] and V[SNS]$_2${Ni(dppe)}$_2$.

Identity	[K(18-Crown-6)$(THF)_2$] [V[SNS]$_2${Ni(dppe)}$_2$]	V[SNS]$_2${Ni(dppe)}$_2$
Empirical formula	$C_{92}H_{96}KN_2Ni_2O_6P_4S_4V{\cdot}3(C_4H_8O){\cdot}1(C_4H_{10}O)$	$C_{80}H_{72}N_2Ni_2P_4S_4V{\cdot}4(C_4H_8O)$
Formula weight (g/mol)	2075.71	1770.36
Crystal system	Monoclinic	Orthorhombic
Space group	$P2_1/c$	P $na2_1$
T (K)	88(2)	88(2)
a (Å)	22.900(3)	17.422(3)
b (Å)	17.985(2)	28.908(5)
c (Å)	25.266(3)	19.809(3)
α (°)	90	90
β (°)	98.9874(16)	90
ɣ (°)	90	90
V ($Å^3$)	10278(2)	9976(3)
Z	4	8
Refl. collected	126089	94889
Indep. refl.	26108	20498
R1 ($I > 2\sigma$)[a]	0.0396	0.0842
wR2 (all data)[b]	0.0985	0.2648

[a]$R1 = \Sigma||F_o|-|F_c|| / \Sigma|F_o|$, [b]$wR2 = [\Sigma[w(F_o^2-F_c^2)^2] / \Sigma[w(F_o^2)^2]]^{1/2}$

6.6 References

(1) Gray, H. B.; Winkler, J. R. *Chem. Phys. Lett.* **2009**, *483*, 1–9.

(2) Winkler, J. R.; Gray, H. B. *Chem. Rev.* **2013**, *114*, 3369–3380.

(3) Gray, H. B.; Winkler, J. R. *Proc. Natl. Acad. Sci. U.S.A.* **2005**, *102*, 3534–3539.

(4) Kasack, V.; Kaim, W.; Binder, H.; Jordanov, J.; Roth, E. *Inorg. Chem.* **1995**, *34*, 1924–1933.

(5) Kaim, W.; Kasack, V. *Inorg. Chem.* **1990**, *29*, 4696–4699.

(6) Kaim, W.; Lahiri, G. K. *Angew. Chem. Int. Ed.* **2007**, *46*, 1778–1796.

(7) Dunbar, K. R.; Heintz, R. A. *Prog. Inorg. Chem.* **1996**, 283–391.

(8) Creutz, C.; Taube, H. *J. Am. Chem. Soc.* **1969**, *91*, 3988–3989.

(9) Kubiak, C. P. *Inorg. Chem.* **2013**, *52*, 5663–5676.

(10) Robin, M. B.; Day, P. *Adv. Inorg. Chem. Radiochem.* **1968**, *60*, 247–422.

(11) Winter, R. F. *Organometallics* **2014**, *33*, 4517–4536.

(12) Chisholm, M. H.; D'Acchioli, J. S.; Pate, B. D.; Patmore, N. J.; Dalal, N. S.; Zipse, D. J. *Inorg. Chem.* **2005**, *44*, 1061–1067.

(13) Chisholm, M. H. *Philos. Trans. Royal Soc. A* **2008**, *366*, 101–112.

(14) Clerac, R.; Cotton, F. A.; Dunbar, K. R.; Murillo, C. A.; Pascual, I.; Wang, X. *Inorg. Chem.* **1999**, *38*, 2655–2657.

(15) Clerac, R.; Cotton, F. A.; Daniels, L. M.; Dunbar, K. R.; Kirschbaum, K.; Murillo, C. A.; Pinkerton, A. A.; Schultz, A. J.; Wang, X. *J. Am. Chem. Soc.* **2000**, *122*, 6226–6236.

(16) Cotton, F. A.; Daniels, L. M.; Murillo, C. A.; Pascual, I. *J. Am. Chem. Soc.* **1997**, *119*, 10223–10224.

(17) Wojnar, M. K.; Ziller, J. W.; Heyduk, A. F. *Eur. J. Inorg. Chem.* **2017**, *2017*, 5571–5575.

(18) Wagenhofer, M. F.; Baráth, E.; Gutiérrez, O. Y.; Lercher, J. A. *ACS Catal.* **2017**, *7*, 1068–1076.

(19) Ji, Q.; Li, C.; Wang, J.; Niu, J.; Gong, Y.; Zhang, Z.; Fang, Q.; Zhang, Y.; Shi, J.; Liao, L. *Nano. Lett.* **2017**, *17*, 4908–4916.

(20) Britto, S.; Leskes, M.; Hua, X.; Hébert, C.-A.; Shin, H. S.; Clarke, S.; Borkiewicz, O.; Chapman, K. W.; Seshadri, R.; Cho, J. *J. Am. Chem. Soc.* **2015**, *137*, 8499–8508.

(21) Stiefel, E. I.; Eisenberg, R.; Rosenberg, R. C.; Gray, H. B. *J. Am. Chem. Soc.* **1966**, *88*, 2956–2966.

(22) Stiefel, E. I.; Dori, Z.; Gray, H. B. *J. Am. Chem. Soc.* **1967**, *89*, 3353–3354.

(23) Pauling, L. *J. Am. Chem. Soc.* **1947**, *69*, 542–553.

(24) Cordero, B.; Gómez, V.; Platero-Prats, A. E.; Revés, M.; Echeverría, J.; Cremades, E.; Barragán, F.; Alvarez, S. *Dalton Trans.* **2008**, 2832–2838.

(25) Cotton, F. A.; Murillo, C. A.; Walton, R. A. *Multiple bonds between metal atoms*; Springer Science & Business Media: **2005**.

(26) Herebian, D.; Bothe, E.; Bill, E.; Weyhermüller, T.; Wieghardt, K. *J. Am. Chem. Soc.* **2001**, *123*, 10012–10023.

(27) Sproules, S.; Wieghardt, K. *Coord. Chem. Rev.* **2011**, *255*, 837–860.

(28) Ghosh, P.; Begum, A.; Herebian, D.; Bothe, E.; Hildenbrand, K.; Weyhermüller, T.; Wieghardt, K. *Angew. Chem. Int. Ed.* **2003**, *42*, 563–567.

(29) Sproules, S.; Banerjee, P.; Weyhermüller, T.; Yan, Y.; Donahue, J. P.; Wieghardt, K. *Inorg. Chem.* **2011**, *50*, 7106–7122.

(30) Roy, N.; Sproules, S.; Weyhermüller, T.; Wieghardt, K. *Inorg. Chem.* **2009**, *48*, 3783–3791.

(31) Schilter, D.; Rauchfuss, T. B.; Stein, M. *Inorg. Chem.* **2012**, *51*, 8931–8941.

(32) Carroll, M. E.; Barton, B. E.; Gray, D. L.; Mack, A. E.; Rauchfuss, T. B. *Inorg. Chem.* **2011**, *50*, 9554–9563.

(33) Barton, B. E.; Rauchfuss, T. B. *J. Am. Chem. Soc.* **2010**, *132*, 14877–14885.

(34) Zhu, W.; Marr, A. C.; Wang, Q.; Neese, F.; Spencer, D. J. E.; Blake, A. J.; Cooke, P. A.; Wilson, C.; Schröder, M. *Proc. Natl. Acad. Sci. U.S.A.* **2005**, *102*, 18280–18285.

(35) Redin, K.; Wilson, A. D.; Newell, R.; DuBois, M. R.; DuBois, D. L. *Inorg. Chem.* **2007**, *46*, 1268–1276.

(36) Chambers, G. M.; Mitra, J.; Rauchfuss, T. B.; Stein, M. *Inorg. Chem.* **2014**, *53*, 4243–4249.

(37) Huynh, M. T.; Schilter, D.; Hammes-Schiffer, S.; Rauchfuss, T. B. *J. Am. Chem. Soc.* **2014**, *136*, 12385–12395.

(38) Schweiger, A.; Jeschke, G. *Principles of pulse electron paramagnetic resonance*; Oxford University Press on Demand: **2001**.

(39) Atzori, M.; Morra, E.; Tesi, L.; Albino, A.; Chiesa, M.; Sorace, L.; Sessoli, R. *J. Am. Chem. Soc.* **2016**, *138*, 11234-11244.

(40) Zadrozny, J. M.; Niklas, J.; Poluektov, O. G.; Freedman, D. E. *ACS Cent. Sci.* **2015**, *1*, 488–492.

(41) Yu, C.-J.; Graham, M. J.; Zadrozny, J. M.; Niklas, J.; Krzyaniak, M. D.; Wasielewski, M. R.; Poluektov, O. G.; Freedman, D. E. *J. Am. Chem. Soc.* **2016**, *138*, 14678–14685.

(42) Napoline, J. W.; Kraft, S. J.; Matson, E. M.; Fanwick, P. E.; Bart, S. C.; Thomas, C. M. *Inorg. Chem.* **2013**, *52*, 12170–12177.

(43) Rudd, P. A.; Liu, S.; Gagliardi, L.; Young Jr, V. G.; Lu, C. C. *J. Am. Chem. Soc.* **2011**, *133*, 20724–20727.

(44) Clouston, L. J.; Siedschlag, R. B.; Rudd, P. A.; Planas, N.; Hu, S.; Miller, A. D.; Gagliardi, L.; Lu, C. C. *J. Am. Chem. Soc.* **2013**, *135*, 13142–13148.

(45) Clouston, L. J.; Bernales, V.; Cammarota, R. C.; Carlson, R. K.; Bill, E.; Gagliardi, L.; Lu, C. C. *Inorg. Chem.* **2015**, *54*, 11669–11679.

(46) Vollmer, M. V.; Xie, J.; Cammarota, R. C.; Young Jr, V. G.; Bill, E.; Gagliardi, L.; Lu, C. C. *Angew. Chem. Int. Ed.* **2018**, *57*, 7815–7819.

(47) Demadis, K. D.; Hartshorn, C. M.; Meyer, T. J. *Chem. Rev.* **2001**, *101*, 2655–2686.

(48) Hush, N. S. *Prog. Inorg. Chem.* **1967**, 391–444.

(49) Marcus, R. A.; Sutin, N. *Biochim. Biophys. Acta* **1985**, *811*, 265–322.

(50) Sutin, N. *Prog. Inorg. Chem.* **1983**, 441–498.

(51) Frem, R. C. G.; Massabni, A. C.; Massabni, A. M. G.; Mauro, A. E. *Inorg. Chim. Acta* **1997**, *255*, 53–58.

(52) Tolman, C. A.; Seidel, W. C.; Gosser, L. W. *J. Am. Chem. Soc.* **1974**, *96*, 53–60.

(53) Zanello, P. *Inorganic electrochemistry: theory, practice and application*; Royal Society of Chemistry: **2007**.

(54) Richardson, D. E.; Taube, H. *Coord. Chem. Rev.* **1984**, *60*, 107–129.

(55) Evans, C. E. B.; Naklicki, M. L.; Rezvani, A. R.; White, C. A.; Kondratiev, V. V.; Crutchley, R. J. *J. Am. Chem. Soc.* **1998**, *120*, 13096–13103.

(56) Crutchley, R. J. *Adv. Inorg. Chem.* **1994**, *41*, 273–325.

(57) Lin, Y.-C.; Chen, W.-T.; Tai, J.; Su, D.; Huang, S.-Y.; Lin, I.; Lin, J.-L.; Lee, M. M.; Chiou, M. F.; Liu, Y.-H. *Inorg. Chem.* **2009**, *48*, 1857–1870.

(58) Schilter, D.; Nilges, M. J.; Chakrabarti, M.; Lindahl, P. A.; Rauchfuss, T. B.; Stein, M. *Inorg. Chem.* **2012**, *51*, 2338–2348.

(59) Heyduk, A. F.; Macintosh, A. M.; Nocera, D. G. *J. Am. Chem. Soc.* **1999**, *121*, 5023–5032.

(60) Esswein, A. J.; Dempsey, J. L.; Nocera, D. G. *Inorg. Chem.* **2007**, *46*, 2362–2364.

(61) Zhu, W.; Marr, A. C.; Wang, Q.; Neese, F.; Spencer, D. J. E.; Blake, A. J.; Cooke, P. A.; Wilson, C.; Schröder, M. *Proc. Natl. Acad. Sci. U.S.A.* **2005**, *102*, 18280–18285.

(62) Kang, S. K.; Albright, T. A.; Wright, T. C.; Jones, R. A. *Organometallics* **1985**, *4*, 666–675.

(63) Bachmann, J.; Nocera, D. G. *J. Am. Chem. Soc.* **2004**, *126*, 2829–2837.
(64) Gray, T. G.; Nocera, D. G. *Chem. Commun.* **2005**, 1540–1542.
(65) Rosenthal, J.; Bachman, J.; Dempsey, J. L.; Esswein, A. J.; Gray, T. G.; Hodgkiss, J. M.; Manke, D. R.; Luckett, T. D.; Pistorio, B. J.; Veige, A. S. *Coord. Chem. Rev.* **2005**, *249*, 1316–1326.
(66) Standley, E. A.; Smith, S. J.; Müller, P.; Jamison, T. F. *Organometallics* **2014**, *33*, 2012–2018.
(67) Staudaher, N. D.; Arif, A. M.; Louie, J. *J. Am. Chem. Soc.* **2016**, *138*, 14083–14091.
(68) Schäfer, A. *J. Chem. Phys.* **1992**, *97*, 2571–2577.
(69) Schäfer, A.; Huber, C.; Ahlrichs, R. *J. Chem. Phys* **1994**, *100*, 5829–5835.